

## Special Issue: European Perspectives

Knaack, U.; Klein, T.

**DOI**

[10.7480/jfde.2020.1](https://doi.org/10.7480/jfde.2020.1)

**Publication date**

2020

**Document Version**

Final published version

**Published in**

Journal of Facade Design and Engineering

**Citation (APA)**

Knaack, U., & Klein, T. (Eds.) (2020). Special Issue: European Perspectives. *Journal of Facade Design and Engineering*, 8(1). <https://doi.org/10.7480/jfde.2020.1>

**Important note**

To cite this publication, please use the final published version (if applicable).  
Please check the document version above.

**Copyright**

Other than for strictly personal use, it is not permitted to download, forward or distribute the text or part of it, without the consent of the author(s) and/or copyright holder(s), unless the work is under an open content license such as Creative Commons.

**Takedown policy**

Please contact us and provide details if you believe this document breaches copyrights.  
We will remove access to the work immediately and investigate your claim.

# JOURNAL OF FACADE DESIGN & ENGINEERING

VOLUME 8 / NUMBER 1 / 2020

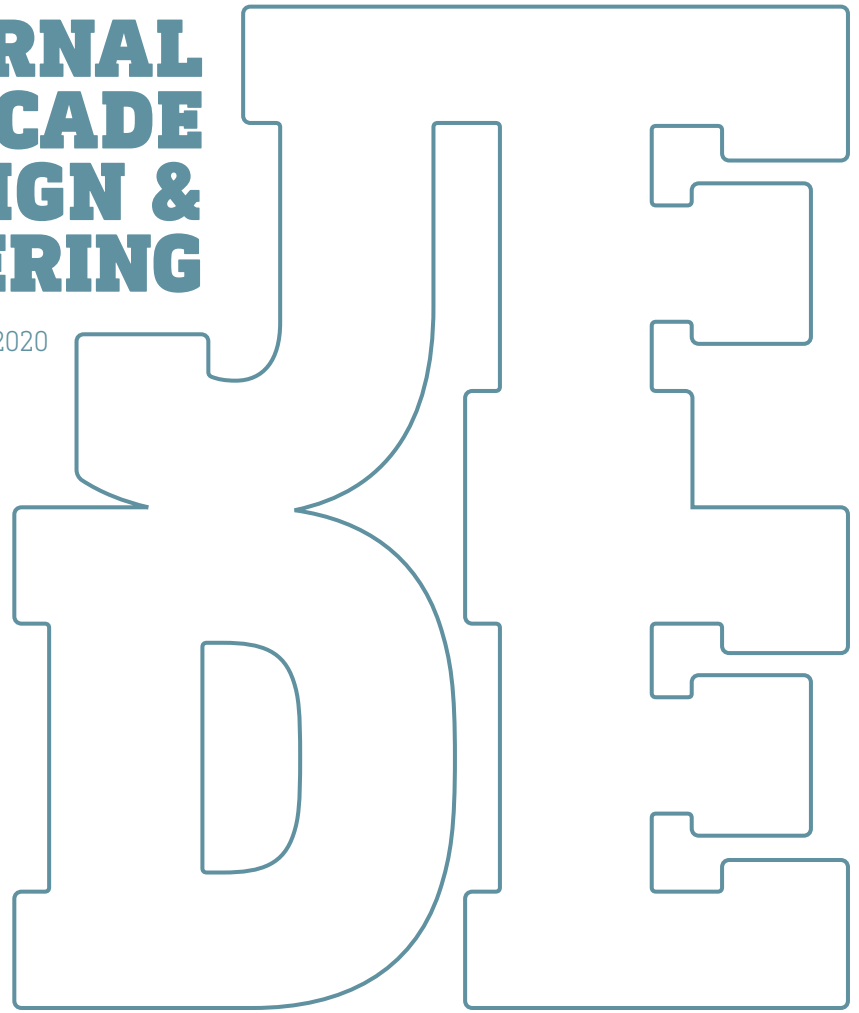
## SPECIAL ISSUE EUROPEAN PERSPECTIVES

**EDITORS IN CHIEF ULRICH KNAACK AND TILLMANN KLEIN**  
SUPPORTED BY THE EUROPEAN FACADE NETWORK



**JOURNAL  
OF FACADE  
DESIGN &  
ENGINEERING**

VOLUME 8 / NUMBER 1 / 2020



**EDITORS IN CHIEF ULRICH KNAACK AND TILLMANN KLEIN**  
SUPPORTED BY THE EUROPEAN FACADE NETWORK

**SPECIAL ISSUE**  
EUROPEAN  
PERSPECTIVES

## JFDE Journal of Facade Design and Engineering

JFDE presents new research results and new proven practice of the field of facade design and engineering. The goal is to improve building technologies, as well as process management and architectural design. JFDE is a valuable resource for professionals and academics involved in the design and engineering of building envelopes, including the following disciplines:

- Architecture
- Building Engineering
- Structural design
- Climate design
- Building Services Engineering
- Building Physics
- Design Management
- Facility Management

JFDE will – initially - be directed at the scientific community, but it will also feature papers that focus on the dissemination of science into practice and industrial innovations. In this way, readers explore the interaction between scientific developments, technical considerations and management issues.

### Publisher

TU Delft Open  
TU Delft / Faculty of Architecture and the Built Environment  
Julianalaan 134, 2628 BL Delft, The Netherlands

### Contact

Alejandro Prieto  
JFDE-BK@tudelft.nl  
<http://jfde.tudelft.nl/>

### Policies

**Peer Review Process** – The papers published in JFDE are double-blind peer reviewed.

**Open Access** – JFDE provides immediate Open Access (OA) to its content on the principle that making research freely available to the public supports a greater global exchange of knowledge.

Licensed under a Creative Commons Attribution 4.0 International License (CC BY 4.0).

**Indexation** – JFDE is indexed in the Directory of Open Access Journals (DOAJ), Google Scholar, Inspec IET and Scopus.

**Publication Ethics** – Editors, authors and publisher adopt the guidelines, codes to conduct and best practices developed by the Committee on Publication Ethics (COPE).

**Copyright Notice** – Author(s) hold their copyright without restrictions.

### Design & layout

**Design** – Sirene Ontwerpers, Rotterdam

**Layout** – Nienke Blaauw, TU Delft

ISSN 2213-302X (Print)  
ISSN 2213-3038 (Online)  
ISBN 978-94-6366-336-6

### Editorial board

#### Editors in Chief

Ulrich Knaack  
Tillmann Klein  
*Delft University of Technology, The Netherlands*

#### Editors

Alejandro Prieto  
Thaleia Konstantinou  
*Delft University of Technology, The Netherlands*

#### Editorial Board

Daniel Aelenei (Universidade Nova de Lisboa, Lisbon, Portugal), Enrico de Angelis (Polytechnico Milano, Milan, Italy), Julen Astudillo (TECNALIA Research & Innovation, San Sebastian, Spain), Carlo Battisti (IDM Südtirol - Alto Adige, Italy), Anne Beim (Royal Danish Academy of Fine Arts, Copenhagen, Denmark, Denmark), Jan Belis (Ghent University, Belgium), Jan Cremers (Hochschule für Technik Stuttgart (HFT), Germany), Andy van den Dobbelsteen (Delft University of Technology, Delft, the Netherlands), Paul Donnelly (Washington University, St. Louis, USA), Chris Geurts (TNO, Delft, Netherlands), Mikkel K. Kragh (University of Southern Denmark, Odense, Denmark), Klaus Kreher (Lucerne University of Applied Sciences and Art, Lucerne, Switzerland), Bert Lieverse (Association of the Dutch Façade Industry, Nieuwegein, The Netherlands), Steve Lo (University of Bath, Bath, United Kingdom), Andreas Luible (Lucerne University of Applied Sciences and Art, Lucerne, Switzerland), Enrico Sergio Mazzucchelli (Politecnico di Milano ABC Department, Italy), David Metcalfe (Centre for Window and Cladding Technology, United Kingdom), Mauro Overend (University of Cambridge, Cambridge, United Kingdom), Uta Pottgiesser (University of Antwerp, Antwerp, Belgium), Josemi Rico-Martinez (University of the Basque Country, Donostia- San Sebastian, Spain), Paolo Rigone (UNICMI, Milan, Italy), Holger Strauss (Hartmann&Hauss, Germany), Jens Schneider (University of Darmstadt, Darmstadt, Germany), Holger Techen (University of Applied Sciences Frankfurt, Frankfurt, Germany), Nil Turkeri (Istanbul Technical University, Istanbul, Turkey), Claudio Vásquez-Zaldívar (Pontificia Universidad Católica de Chile, Santiago, Chile), Aslihan Ünlü Tavlil (Istanbul Technical University, Istanbul, Turkey), Stephen Wittkopf (Lucerne University of Applied Sciences and Art, Lucerne, Switzerland).

#### Submissions

All manuscripts and any supplementary material should be submitted to the Editorial Office (JFDE-BK@TUDelft.nl), through the Open Journal System (OJS) at the following link: <http://jfde.tudelft.nl/>

#### Author Guidelines

Detailed guidelines concerning the preparation and submission of manuscripts can be found at the following link: <https://journals.open.tudelft.nl/index.php/jfde/about/submissions>

# Contents

- v **Editorial**
- 001 **Additive Manufacturing of Ceramic Components for Façade Construction**  
Paulo J.S. Cruz, Bruno Figueiredo, João Carvalho, Tatiana Campos
- 021 **Fire Safety Façade Design and Modelling**  
Enrico Sergio Mazzucchelli, Paolo Rigone, Blanca Judith De la Fuente, Paolo Giussani
- 043 **A Novel Approach to Shape Memory Alloys Applied to Passive Adaptive Shading Systems**  
Lorenzo Vercesi, Alberto Speroni, Andrea Giovanni Mainini, Tiziana Poli
- 065 **Small-scale Field Study of Window Films' Impact on Daylight Availability under Clear Sky Conditions**  
Júlia Pereira, M. Glória Gomes, A. Moret Rodrigues, Henriqueta Teixeira, Manuela Almeida
- 085 **Daylight Transmittance Through Expanded Metal Shadings**  
Jose Miguel Rico-Martinez, Marcin Brzezicki, Carlos Gabriel Ruiz-Mugica, Jakub Lech
- 115 **Assessing Self-shading Benefits of Twisting Towers**  
Nebojsa Jakica, Mikkel K. Kragh
- 131 **Design and Experimental Proof-of-concept of a Façade-integrated Solar Thermal Venetian Blind with Heat Pipes**  
Simon Frederik Haeringer, Paul-Rouven Denz, Puttakhun Vongsingha, Bruno Bueno, Tilmann E. Kuhn, Christoph Maurer



# Editorial

Welcome to this new issue of our Journal of Façade Design and Engineering. We are very pleased to be able to release a new issue under the current global circumstances, to keep supporting research and the engineering of new technologies, materials, and methods for the design of our envelopes.

This special issue features a wide range of topics, stemming from research activities of members from the European Façade Network (EFN). The EFN seeks to advance and promote façade design and engineering at a European level and beyond, through inclusive collaboration between European Research centres, Universities, and alumni, resulting in skills and knowledge transfer in education, research, and development. Consequently, this special issue showcases a selection of research experiences presented at two scientific events sponsored by the EFN.

The first scientific event was the Conference "FACADES19" held in Lisbon on November 22<sup>nd</sup>, 2019, which was organised by Dr. Daniel Aelenei from the Department of Civil Engineering at NOVA School of Science and Technology. The second scientific event refers to a special "EFN session" hosted at the Façade Tectonics 2020 World Congress, held online in August 2020. This session within the larger congress was coordinated by Daniel Artzmann, Mikkel Kragh, Annalisa Andoloro, and Ulrich Knaack. The selection of the papers from both events was based on their relevance to the scope of our journal and went through the double-blind peer review process of the JFDE.

We thank all supporters and contributors who made these events a success and especially the authors of the articles compiled in this issue.

The Editors in Chief,

Ulrich Knaack  
Tillmann Klein



# Additive Manufacturing of Ceramic Components for Façade Construction

**Paulo J.S. Cruz\*, Bruno Figueiredo, João Carvalho, Tatiana Campos**

\* Corresponding author  
Lab2PT, University of Minho, School of Architecture, Guimarães, Portugal, pcruz@arquitetura.uminho.pt

## **Abstract**

*Additive Manufacturing (AM) opens new fields of research and development in the architectural design and construction industry, enabling a geometric freedom that can result in the design of components with specific requirements and multifunctional behaviours.*

*This work explores the integration of digital design tools and AM extrusion processes on the production of ceramic architectural components for façade construction, reshaping and expanding the boundaries of what is possible to achieve with masonry construction in a wide range of applications (opaque walls, ventilated sunscreens, and shading systems).*

*Several stoneware prototypes were developed, encompassing different challenges such as the morphology customisation, the versatility of use, the exploitation of the maximum degree of curvature, and the optimisation of structural patterns.*

## **Keywords**

*Additive manufacturing, 3D-printing, digital fabrication, ceramic components, façade construction*

DOI 10.7480/jfde.2020.1.4725

# 1 INTRODUCTION

One of the first references to the potential of Additive Manufacturing (AM) in Architecture arose in the mid-1990s under the term 'Incremental Forming' (Mitchell & McCullough, 1997). Often referred to as 3D printing, AM consists of the production of objects through the successive addition of layered material, resulting in a sustainable and a very cost effective method, due to the fact that material is deposited only where required. This is in contrast to subtractive processes or traditional casting and moulding techniques, which, in addition to producing a high degree of waste of raw material, do not benefit customisation.

The advent of AM opened new areas of research in architectural design, construction materials, and in the building industry. Moreover, when combined with computational design and simulation tools, their potential is exponential, namely by enabling a broad geometrical freedom that can result from specific design requirements, design optimisation, and challenging functions (Sarakinoti et al., 2020).

Regardless, the debate between the direct application of AM on site and the production of discretised architectural components for subsequent assembly on site, the commercialisation of houses built through AM is already a reality (Castañeda, Lauret, Lirola, & Ovando, 2015). Just as AM was highlighted as a key technology that accelerated the transformation of the manufacturing industry towards Industry 4.0, it is expected that within the next decade an increase in successful integrations of AM in the building industry will constitute a revolution in development strategies in the built environment.

A first set of experiments in AM for the building industry was mainly focused in cementitious materials (Khoshnevis, 2004). The ability of transposing AM techniques to the scale of the building represents a major issue for its application to the construction industry. In this sense, the main constraints are the dimensions and mechanisms of the extrusion apparatus and the reaction of the material. The principle of depositing the layered material assumes that the manufactured object fits within the working area of the 3D printer. For this reason there are two approaches that can be taken: (i) Continuous deposition manufacturing – Scaling the printing apparatus; (ii) Manufacture of discrete elements – Scaling the components to the available print area.

In a report entitled 'Shaping the Future of Construction', the World Economic Forum discussed the 'future impact' and the 'likelihood of new technologies', based on the results of the 'Future of Construction Survey' (World Economic Forum, 2016). According to this study, the 'contour crafting of buildings' is not likely to occur and its impact is considered low. The likelihood and impact of '3D printing of components' and 'advanced building materials' is considered to be moderate and that of 'prefabricated building components' is extremely high. This fact justifies why many research groups and corporations interested in testing AM technologies in the construction industry end up following a line of thinking that is based on discrete elements. In this approach, instead of requiring a machine that provides a larger work area than the building to be built, it is proposed to adjust the size of the different parts according to the physical characteristics of the machinery (the 3D printer work area, the size of the kiln if necessary, etc.).

As Mario Carpo (2019) points out, 'instead of printing bigger and bigger monoliths, it may conceivably be easier to start with any number of parts, as many and as small as needed', leaving the correct positioning and assembly of the parts to another machine.

In this way, there is an approximation of traditional building systems based on three factors: (i) the various constituent components of the building are prefabricated with smaller dimensions; (ii) transportation to the work site; (iii) assembly in their positions, creating larger structures.

Ceramic materials are a natural resource with unique properties whose application goes back to the prehistoric age, to the first attempts of man to provide his own shelter. Features such as hardness, density, durability, and the possibility of having a vast number of shapes and finishes, make the application of this material in buildings widespread. The history of architecture and construction is inseparable from the history of ceramics, a key material for the manufacturing of masonry, cladding, and pavement and roof components.

Several protagonists of the architectural vanguards of the twentieth century explored the use of ceramic materials in a multiple range of innovative design languages.

The striking façade of the Fagus-Werk Factory, in Alfeld an der Leine, Germany, an early expression of Modern Architecture, designed in the 1910s by Walter Gropius and Adolf Meyer, masterfully combined brick masonry walls with steel-glass curtain walls, a harbinger of the later so-called 'new objectivity' of Bauhaus architecture (Ramcke, 2001).

With the modernist movement in the early twentieth century, ornament went out of fashion among many architects. However, in the 1920s, primarily in Germany and in the Netherlands, the 'brick expressionism architecture' used bricks and tiles as the main visible building material to create ornamented buildings with a rounded or organic appearance that was simultaneously completely modern (Boëthius, 2019).

In the middle of the twentieth century, Alvar Aalto recurrently used brick masonry: Baker Dormitory in Cambridge, 1947-48; or the Saynatsalo town hall, 1949-52. His predilection for ceramic materials was extended to the design of ceramic glazed tiles to solve specific functional aspects, formation of corners and skirtings, such as the round curved tiles used for pillar cladding in the Helsinki University of Technology (1953-66) or the wedge-shape brick that he devised for the wall of the House of Culture in Helsinki of 1952-58 (Pallasma, 1998).

In the post-war period, a critical examination of the Modern Movement will find an important resource through the observation of local architecture. Kenneth Frampton (1980) celebrated it as critical regionalism due to the dialogue between Modern abstract forms and traditional construction techniques. One of Frampton's references is the work of José Antonio Coderch, namely the 'modern brick vernacular first formulated in his eight-storey ISM apartment block built in Barcelona' in 1951. Yet, in Ugalde House, built in 1952 at Caldas de Estrac, one of the most renowned projects of the Catalan architect, the local cultural identity was introduced through the use of the traditional *baldoşin* ceramic tiles in the floors (internal and external) and roofs combined with a more abstract expression of curved white walls.

Frampton also considers the work of Mario Botta an expression of critical regionalism. The Swiss architect, who worked for Louis Kahn for a short period, is known for his draughtsmanship that manipulates geometry at small and large scales. He often uses bricks as a covering material to poetically underline the severity of strong volumes, yet which are based on very simple shapes.

It is worth mentioning the proposals of Eladio Dieste, in the 1960s and 1970s, for thin shell vaulted systems made from brick and ceramic tiles. The use of this 'reinforced masonry' structure in Gaussian vaulted roofs allows for the achievement of spans up to 50 metres (Dieste, 1996). In this period, the Uruguayan engineer and architect designed several buildings in Montevideo (warehouses, a gymnasium, and silos plant) and a Market in Porto Alegre (Brazil) that even today represents some of the most challenging applications of ceramic building components in structural design.

In the 1960s, Marcel Breuer, despite being one of the masters of brutalist expressionism in concrete, designed terra-cotta flue tiles to produce sunscreens for Hunter College's uptown campus façades, today known as Lehman College (Bergdoll & Massey, 2011).

Louis Kahn, often called 'the brick whisperer', believed that materials had a stubborn sense of their own destiny. His design for the Indian Institute of Management in Ahmedabad, built between the 1960s and 1970s, embodies this notion of geometry as a key principle for the consistent and systematic quality of his work and provided an order for the formal expressions that encompass both composition and construction (Park & Baldanchoijil, 2014).

The possibility of additively producing ceramic components brings new opportunities for the architecture and building industry, opening new compromises between the use of a low-cost high performance material and the execution of complex geometries and multifunctional products, impossible to obtain using any other traditional production process (Cruz, Knaack, Figueiredo & Witte, 2017).

One of the merits of AM is the rediscovery of some of the functions that ceramic products had in traditional construction systems. An example of this is the use of binder-jetting ceramic powder for the development of a nonstandard ceramic brick system, similar to cinder blocks, for the assembly of freeform ventilated façades whose connections were inspired in traditional wood joinery techniques requiring no additional adhesives or mortar (Sabin, Miller, Cassab, & Lucia, 2014).

In this context, also deserving of a mention is the porous 3D-printed ceramic masonry system for passive evaporative cooling in buildings. Inspired by the Muscatese evaporative cooling window, it combines a wood screen and a ceramic vessel filled with water (Rael & San Fratello, 2018).

The potential for producing a customised design with a standard desktop 3D printer with a modified extrusion head for earthenware ceramics has been illustrated with a series of ceramic modular block systems for interior and exterior walls, columns, vaults, and sun shading (Peters, 2014).

The work presented in this article aims to enhance the exploration of morphological, technological and functional aspects of ceramic façade components, encompassing the following objectives: delving into different approaches for the discretisation of irregular surfaces in uniform and nonuniform components; assessing the potential of AM techniques; expanding the functionalities of ceramic components beyond their conventional architectural uses; proposing new systems and developing innovative architectural components.

The fulfilment of these objectives provided new insights to be integrated into the project practice and contributed to add value to ceramic products and the ceramic industry.

## 2 METHODOLOGY

This work follows a methodology centred on three key aspects that are interrelated and fundamental to an effective application in a real context: (1) controlling the ceramic material properties critical to AM processes; (2) optimising the extrusion process of ceramic materials; (3) exploring the restrictions to free-form geometries.

### 2.1 MATERIALS

Ceramic can be considered the first human-designed material, as opposed to materials directly extracted from nature and shaped for specific uses such as wood and stone. The word derives from the Greek words *keramos* or *keramikos*, meaning the product of the potter's art.

The most common clay bodies for architectural ceramics - mixes of different clays and additives - are earthenware, stoneware, and porcelain.

Earthenware, including terra cotta, is a low-fire clay body with relatively large particle sizes that is frequently used for tiles and bricks. A wide range of raw materials can be added to the clay body in order to improve workability, such as: quartz sand, shells, calcite, mica, crushed rocks, and volcanic ash.

Stoneware is composed of finer particles and exhibits better mechanical properties and a lower porosity (Martín-Márquez, Rincón & Romero, 2008; Gualtieri et al., 2018). It is commonly used for architectural tile applications and for façade elements (Gualtieri et al., 2018; Rambaldi, Pabst, Gregorová, Prete & Bignozzi, 2017; Ribeiro, Ferreira & Labrincha, 2005). Porcelain is a white kaolinite body, fired at the highest temperatures, and usually fully vitrified, resulting in a non-porous homogenous product with extremely low water absorption. Table 1 presents a basic comparison of the most common clay bodies for architectural ceramics.

TABLE 1 Basic comparison of most common clay bodies for architectural ceramics.

CLAY BODY	DESCRIPTION	FIRING TEMPERATURE
Earthenware	Porous, soft paste; contains added raw materials to improve workability and firing	500 - 1200°C
Stoneware	Hard and compact, not porous. Rough texture and usually grey in colour	1200-1350°C
Porcelain	Very hard and compact. Glass like, white to bluish white in colour	1300-1450°C

Earthenware is less dense than stoneware, which in turn is less dense than porcelain. The density is related to the amount of water that can be absorbed and consequently determines the absorption range of the unglazed fired ceramic. The less dense the ceramic the higher the absorption rate and the greater the porosity. Usually, low-density clays do not vitrify when fired. Clays of high densities can become vitreous and resistant to water infiltration, increasing the resistance to freeze-thaw cycles.

The transformation from clay - predominantly composed of alumina, silica, and water - to ceramic occurs during the firing process. Firing changes the material composition at a micro level as particles are sintered and permanently bonded. Material properties are altered substantially in the process, producing a harder, durable, and water-resistant matter. The process of firing is a complex balance of heating and cooling that must be precisely controlled to achieve the desired quality (da Silva, Feltrin, Dal Bó, Bernardin, & Hotza, 2014; Gültekina, Topatesb, & Kuramac, 2017).

A kiln schedule consists of a ramping-up period in which the temperatures are slowly increased. Following the ramp phase, the ceramic pieces remain at a constant firing temperature for a prescribed duration, then enter a controlled cooling cycle in which the ceramic element returns to room temperature. Rapid temperature fluctuations may result in cracking of the ceramic pieces.

Once the clay body has been formed it dries to the 'green state', either naturally or through more controlled, machine-based drying processes such as with universal ovens. During drying and subsequent firing, shrinkage occurs as moisture is removed (Ribeiro, Ferreira & Labrincha, 2005; Oummadi et al., 2019; da Silva, Feltrin, Dal Bó, Bernardin & Hotza, 2014). Raw material properties such as particle size and moisture content impact shrinkage rates. The smaller the particle size and greater the moisture content the higher the shrinkage rate.

Industrial clay extrusion is a medium to high volume manufacturing process that, compared to dry-pressing, offers better potential for shape customisation. It is a 'wet' process used to form clays with a moisture content ranging between 16% and 23% (Ribeiro, Ferreira, & Labrincha, 2005). During extrusion, a large lead screw system forces clay through a vacuum chamber and through a shaping die, resulting in linear parts that have a constant cross-section (Ribeiro, Blackburn & Labrincha, 2009; Guilherme, Ribeiro & Labrincha, 2009).

Shrinkage rates vary between clay bodies, from approximately 8% to 12% (to the referenced moisture percentage). Approximately half of the overall shrinkage occurs during drying, when moisture evaporates from the surface (Martín-Márquez, Rincón, & Romero, 2008; Gültekina, Topatesb, & Kuramac, 2017). Water moves from the centre out through capillary action. Additional shrinkage, typically 50% of the overall rate, occurs during firing when particles are sintered or bonded together, and all remaining chemical moisture is released from the clay body. Shrinkage during firing impacts all clay bodies. This causes 'differential shrinkage', which can result in warping and even cracking as outer surfaces dry faster than the core material.

In a flat or linear product the dimensional changes due to shrinkage can be easily compensated by oversizing it. In a product with a complex geometry, this compensation is not straightforward.

Several measuring techniques and devices are available to determine the optimal water content in a clay body required to allow this body to be plastically deformed by shaping. The widely accepted Pfefferkorn method has been extensively used in this research to evaluate and control the plasticity of the stoneware used. It determines the amount of water required to achieve a 30% reduction in height in relation to the initial height of the test body under the action of a standard mass (Pfefferkorn, 1924).

Brittleness and vulnerability to crack propagation should be properly considered when conceiving a ceramic product. Designers should avoid creating areas of high stress concentration, which include drastic changes in wall thickness, sharp edges, openings, localized fasteners, acute corners, and non-filleted intersections.

The mechanical performance can be tailored by combining the appropriate clay body with additives. The addition of cellulose or nylon fibres increases the 'green strength' of the dried clay before firing, reducing or even avoiding shrinkage induced cracks. These fibres have little impact on the properties of the finished part because they burn away during firing.

Usually, clay bodies fired at higher temperatures, up to 1300°C, exhibit higher strengths than those fired at temperatures as low as 1000°C. The strength and porosity of stoneware clay bodies are modified by varying the kiln schedule.

Fig. 1 shows a wide range of specimens recently produced at the Advanced Ceramics R&D Lab (ACLab) of the Design Institute of Guimarães (IDEGUI) using a wide range of ceramic pastes (stoneware, porcelain, and refractory clays), fired at different maximum temperatures of 700°C, 900°C, and 1050°C (Ribeiro, 2020). It is perceptible how the firing temperature affects the final colour.

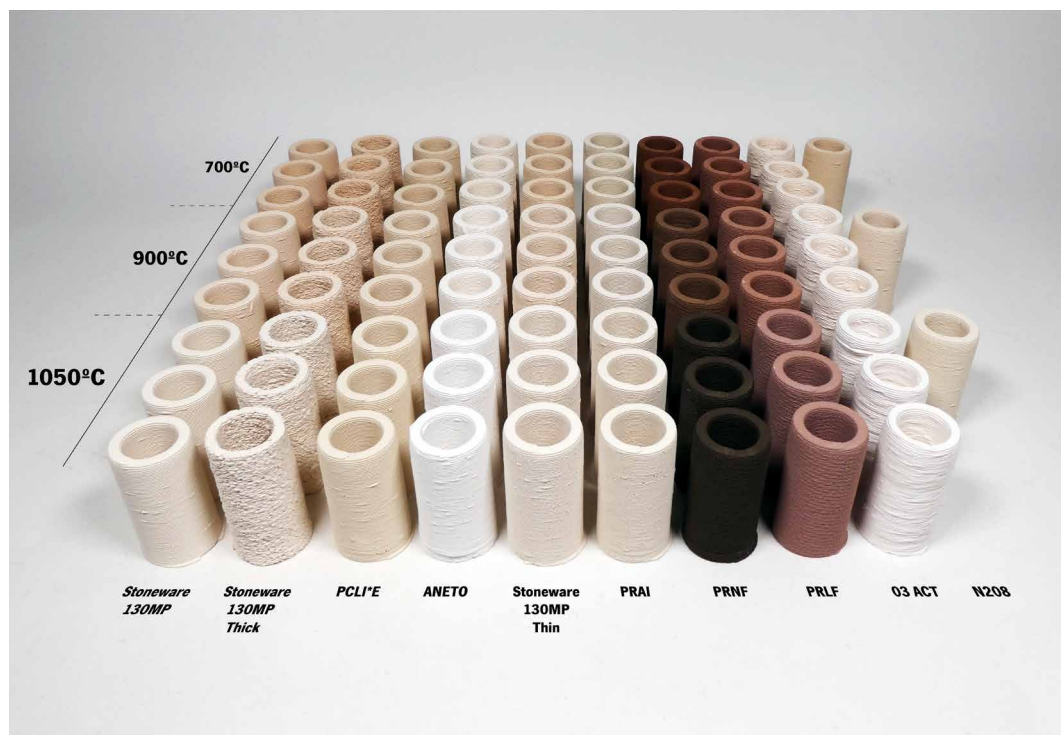


FIG. 1 Specimens produced with stoneware, porcelain and refractory clays after firing at different maximum temperatures of 700°C, 900°C, and 1050°C.

Stoneware usually exhibits a high compressive strength and behaves poorly under tension. A previous experimental research was performed by testing a set of specimens until compression failure, at the Materials Laboratory of the Civil Engineering Department of the University of Minho, using a hydraulic test machine with 5000 kN capacity (Cruz, Camões, Figueiredo, Ribeiro, & Renault, 2019). The tested specimens comprise manually extruded cylindrical pieces (solid) and cylindrical models produced by AM with the same dimensions (from a single thin wall to a solid model). The mean value of the compressive strength of the first set oscillated between approximately 200 MPa, for smaller specimens (60mm height by 30mm diameter), and 100 MPa for the bigger ones (120mm height by 60mm diameter). The second set presented an average compressive strength

that ranged between  $\approx 77$  MPa (for tubular specimens with one thin wall, 60mm height by 30mm diameter) and  $\approx 136$  MPa (for tubular specimens with three concentric walls, 120mm height by 60mm diameter). The lower values obtained for the one-wall specimens makes evident the excessive slenderness of the thin wall.

The research also carried tests on the compressive strength evaluation of a set of bricks produced by AM (Fig. 2) with dimensions of 100 x 200 x 50 mm. Each brick was composed of 34 horizontal layers, 1.5 mm high and approximately 5.0 mm wide. The external and internal brick walls were composed of two parallel extrusion paths; since the extrusion nozzle has a diameter of 3 mm, the walls thickness is approximately 6 mm. The goal of these tests was to infer the influence of the internal structural design for similar void ratios. Nevertheless, this study concluded that the obtained compressive strength ranges (between  $\approx 87$  to 111 MPa) denote proper mechanical behaviour for the architectural ceramic bricks wall construction.

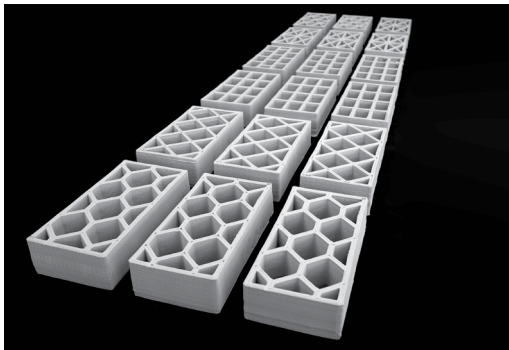


FIG. 2 Different internal structural patterns.

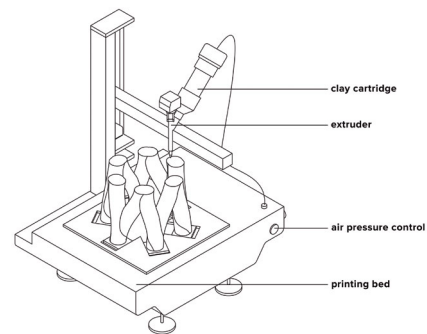


FIG. 3 Lutum® ceramic printers available at the Advanced Ceramics R&D Lab (ACLab).

## 2.2 PASTE EXTRUSION

The stages of industrial production processes related to architectural ceramics include the creation of the clay body, followed by shaping, drying, firing, post-processing, and packaging. High-tech industrial automation may boost/improve productivity by combining those stages.

Clay is usually extruded through a die in a final cross-sectional shape. A medium production volume, in the thousands of units, is typically needed to offset the costs of designing and making the dies (Bechthold, Kane, & King, 2015). Once shaped, the material is cut to length using an automated wire or blades that move perpendicular to the axis of extrusion.

Although extruded products usually show only one finished surface, some producers prefer to create high-quality surfaces on all sides of the product. To ensure that complex units retain their shape without warping, additional features may be added to unsupported areas. Manual or automated processes after final firing stage may break away additional geometries.

The extruded parts of many architectural applications are usually moulded with engravings, such as slots and grooves, which may help the element to be hooked into metal substructures during installation.

Another manual process is the craft-based extrusion, although it is not commonly used due to the fact that the resulting elements are much less accurate than industrial processed ones. Custom extrusion dies are low cost in terms of tools as they use metal or wood among other materials.

Some factories combine industrial manufacturing with craft-based production methods. Such hybrid production settings have a high potential for customisation of project-specific ceramic systems and often modify their standard clay bodies to meet the performance requirements of a certain project.

The possibility of additively producing ceramic components brings new opportunities for the building industry to explore the possibilities of incorporating components with specific design requirements. The advent of Additive Manufacturing (AM) of ceramic brought unprecedented possibilities for the building industry while exploring and incorporating components with specific design requirements. It definitively reshaped and expanded the boundaries of what it's possible to achieve with masonry construction and opened new domains, with multiple angles of study and experimentation, and with great industrial potential.

Since 2016, clay extruding printers are being intensively used in the ACLab (Fig.3). The extrusion path, material flow, and printing speed of the printing process are digitally defined by a computational model. The movement speed, extrusion flow, and the air pressure can be controlled manually to adapt the specific printing process to the characteristics of the clay during the printing process. Print speeds are tuned, taking into consideration the viscosity of clay, specific object design, and layer/nozzle size, with speeds ranging from 20 mm/s to 100 mm/s.

## 2.3 DESIGN

The integration of AM in the production of architectural ceramic components requires a prior definition of strategies to be adopted in the design process. In the context of ACLab activity, computational design tools perform a key role in the different stages of that methodology.

A first step is the enhancement of the process of morphogenesis, comprising the use and combination of appropriate tools for: the parametric design; the form-finding process; and performance optimisation (Fig. 4 & Fig. 5).

A second feature is the implementation of design rules that automatise the discretisation of building envelopes, from the most conventional rational geometries to the most complex free-form surfaces. This rationalisation of the design processes allows for the definition of customised cladding systems in accordance with functional performance, while also considering material and manufacturing constraints - the Hive Wall (Fig.14) and the Hexashade Vault (Fig.18) exemplify this approach.

Other discretisation design strategies are characterised by the minimisation of the type of architectural components that define a construction system, relying on the combinatorial possibility of connections to configure different architectural objects - S-Brick (Fig.9) and V-Brick (Fig.11) follow those design principles. Their design is focused on the interconnection possibilities that aim for a capability to disassemble and re-assemble the same masonry system in multiple formal configurations.

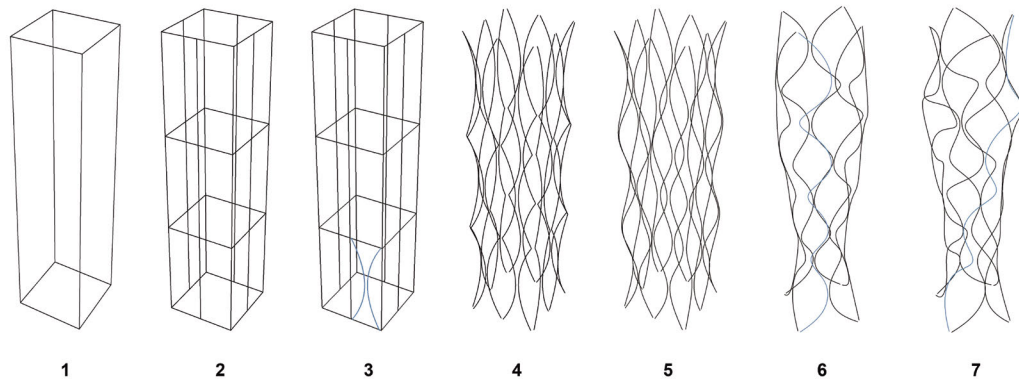


FIG. 4 Ficus Column, different stages from the design process testing different design solutions through the use of parametric design and form-finding techniques. Stages: [1] Base shape. [2] Shape division. [3] Pattern definition. [4] Recursive application. [5] Pattern smoothing. [6] Section variation. [7] Section rotation.

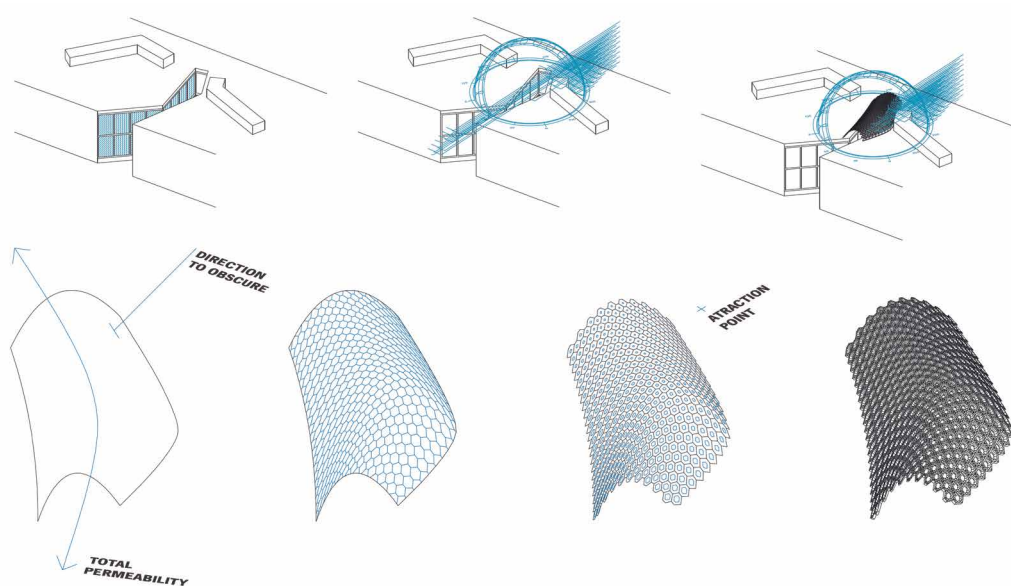


FIG. 5 Hexashade project. Schema of the vault design process considering solar analysis of a glazed surface to optimise a shading hexagonal grid (top illustrations). It also presents the discretisation process of the vault in non-regular hexagonal blocks (bottom illustrations).

Thirdly, the possibility of assembling customised solutions is made possible by the design of adaptable connection systems. In order to accomplish this goal, two design approaches have been tested. In the first, a direct fit of the components is envisaged through interconnecting surfaces. Here, the design of the fitting system is fully parametrised in correlation to the overall shape of the architectural object - Hexashade Vault (see the brick side surfaces, Fig.17). The second approach considers the design of hybrid systems. AM has the potential to allow for the production of complex geometries that are relatively difficult to assemble via conventional methods or interconnections. The integration of external connectors enables the production of complex parts as fully functional assemblies. To create a fully functional prototype, it is possible to manufacture an object up to a certain level, place all the other elements (e.g., polymeric, metallic or other components) and resume the manufacturing process - V-brick wall (Fig.12).

Finally, a seamless framework between the initial design stage and the building stage can be achieved because the design process is developed in a continuous computational environment. Computational models generate the formal definition as well the instructions for the production machinery (G-Code), providing a direct translation of design intentions and avoiding the traditional design interpretation by third parties. This methodology allows for the extension of the morphogenetic design principles to the digital manufacturing technology and respective material constraints. One of the main benefits related to computational design and AM is the enabling of a shift from conventional design methodologies to processes such as Design for Manufacture (DFM) or Design for Assembly (DFA).

### 3 PROTOTYPES

A set of prototypes of free-form stoneware components was developed to illustrate the wide range of possibilities they open for façade construction. They give an insight into the potential conferred by the chance of customising and optimising their shape and function. In fact, the production of most of those free-form components would be impossible with any traditional manufacturing technique, namely by conventional industrial extrusion process, using a die with a regular cross-sectional shape.

The design principles always focus on a clear response to very specific problems that we think are relevant to future works and to the effective implementation of this production method and material. Each developed prototype has a specific purpose of exploring and combining different attributes and challenges related to AM: (1) The noteworthy inclination of some extruded contours, evident in the Wave wall bricks and in the Hexashade blocks; (2) The interlocking possibilities conferred by V-Bricks, Hive wall bricks, and Hexashade blocks; (3) The versatility of some components, allowing their combination in different orientations, highlighted by S-Bricks, V-Bricks, and Kusudama blocks; (4) The customisation of their morphology and functionality, e.g. the optimisation of their permeability and degree of shading (Hive wall bricks, Hexashade blocks, and Kusudama blocks). Table 2 summarises the main characteristics of the six prototypes.

TABLE 2 Prototypes characteristics.

	WAVE	S-BRICK	V-BRICK	HIVE	KUSUDAMA	HEXASHADE
Façade cladding	•	•	•	•	•	
Ventilated sunscreen		•		•	•	•
Opaque wall	•	•				
Vault shading system						•
Maximum degree of vertical curvature	•					•
Customisation of morphology and functionality				•	•	•
Optimisation of internal structural pattern	•				•	•
Layering in different orientations		•	•		•	
Interlocking			•	•		•

### 3.1 WAVE WALL

Wave wall project consists of a computational model and AM prototype that proposes a system of ceramic components for façade masonry. Wave wall has the specificity of formally exploiting the maximum degree of vertical curvature of the external face that stoneware extrusion is able to perform without collapsing.

The research project comprises the design and production of a full-scale prototype of a façade masonry system (100cm x 50cm) with 50 components, all of them different. A block with standard measurements (210x100x50mm) was used as a reference in which a free irregular shape was defined that configures its external surface.

The internal structural pattern was studied and found to be the most efficient pattern possible, allowing the correlation of the heat conduction between the two exposed faces and their mechanical performances. For this end, several patterns were considered and for each some variables were defined that can be parametrically controlled, such as the number of cells in U and V directions, the thickness of the cells walls, and the pattern's ability to adapt or not to the external shape of the brick.

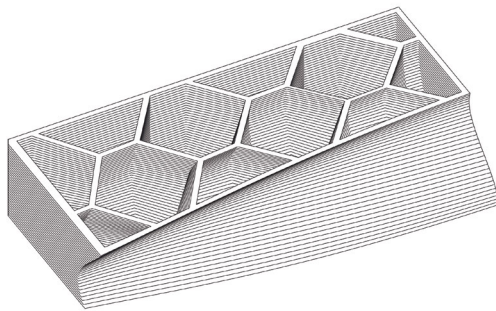


FIG. 6 Wave wall brick extrusion path model.

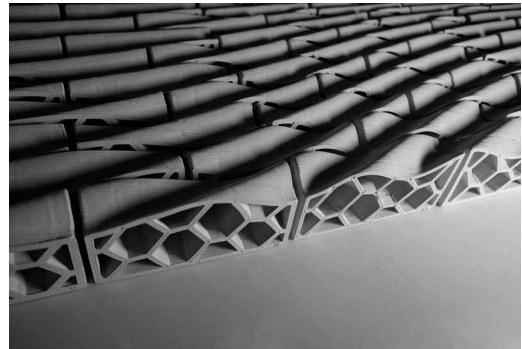


FIG. 7 Wave wall prototype.

## 3.2 S-BRICK WALL

S-Brick prototype explores the design of bricks whose two larger faces are composed of double curved sinusoidal surfaces. It also takes advantage of AM for the customisation of the brick's inner structure by testing s-shaped curved configurations. These features allow its layering to be done in two directions resulting in walls with different design and functions.

If the bricks are assembled in the extrusion direction it might result in an opaque wall with a corrugated pattern. If layered lying down, a ventilated sunscreen wall is obtained. In this solution, the sinusoidal profile also facilitates the connection between the different layers of bricks, blocking each component in its correct position.



FIG. 8 S-Brick extrusion path model.



FIG. 9 S-Brick wall prototype variants.

### 3.3 V-BRICK WALL

V-Brick wall project aimed to explore the discretisation of architectural structures, such as walls, in ceramic blocks through the use of parametric design tools and AM processes. The focus was mainly on the development of innovative design solutions for the joints and interlocking strategy for a freeform design approach.

To augment the degree of morphological freedom, two block types of 50 mm high were developed: block A, which allows the construction of linear walls, and block B which enables a 60° rotation of the walls. The block's design provides a self-interlocked joint which eliminates the need for third-party assembly elements. In fact, there are two grooves on the bottom of the outer wall, seeking a male-female connection, which enabled the structure's construction by simply stacking the blocks.

The external walls of the blocks are composed of two contour surfaces. It was proposed to use a truss-like internal structure to increase the bricks' structural strength, while also optimising the process of continuous material deposition that is performed in AM, and avoiding any undesired superficial deformation.

Finally, as illustrated in Fig. 12, V-Brick blocks have also been used to test the possibility of incorporating AM polymeric reversible fittings, with or without magnets embedded, facilitating quick assembly (Sampaio et al., 2019).

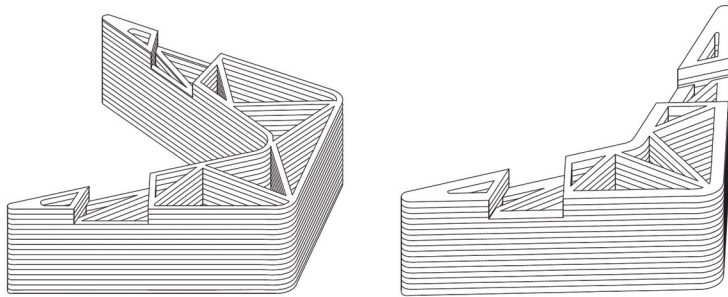


FIG. 10 V-bricks extrusion path models.

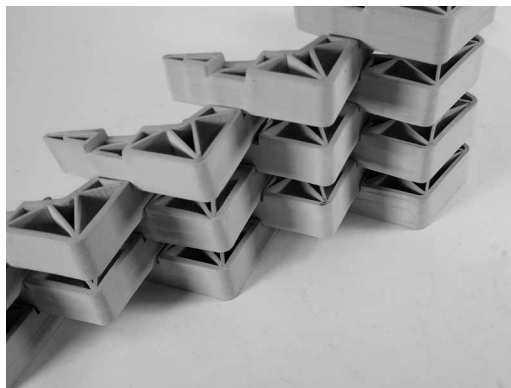


FIG. 11 V-brick wall prototype.

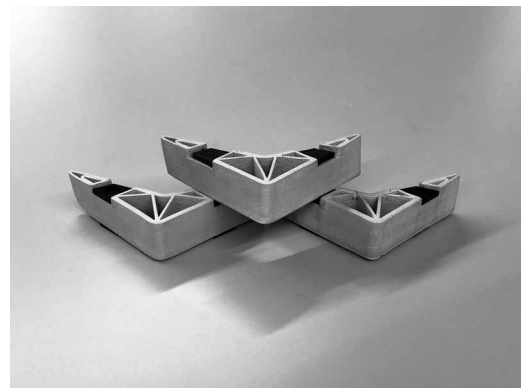


FIG. 12 V-Brick Wall with polymeric connectors and magnets.

### 3.4 HIVE WALL

Hive wall experiments with the capabilities of AM processes to demonstrate the potential of the architectural application of non-standard ceramic components for façade cladding. The challenge was to define a system for ventilated walls in which the size of the openings is customised, allowing wider or narrower openings in accordance with the need for ventilation, shadowing, or desired visual constraints. The blocks' apertures and geometry are composed of three non-uniform truncated pyramids produced with stoneware.

The assembly comprises horizontal layering that is facilitated by the trimmed formal configuration of the bricks that result in a stable interconnecting and docking system. The prototype corresponds to a section of approximately one square metre, composed of 57 bricks of 10 cm depth, in which the central point corresponds to the maximum opening of the wall, which progressively decreases towards its limits.

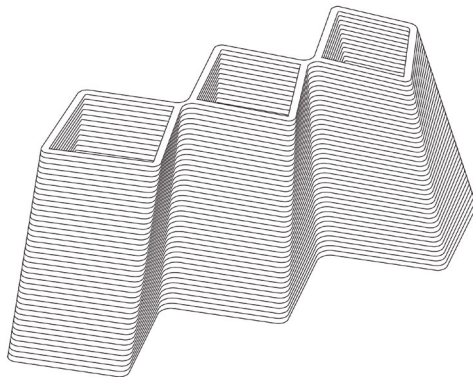


FIG. 13 Hive-brick extrusion path model.

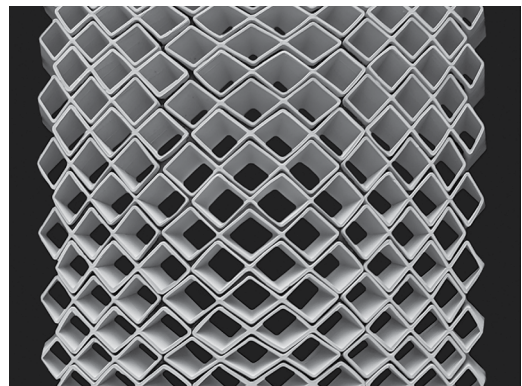
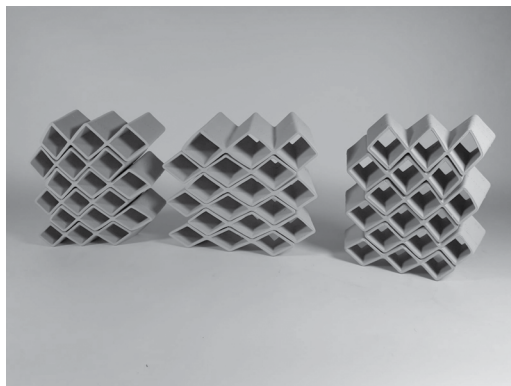


FIG. 14 Hive wall prototype..

### 3.5 KUSUDAMA WALL

Kusudama wall prototype resulted from research that aimed to explore the use of cellulose to produce architectural components by AM. After an initial evaluation of 3D printed specimens produced with cellulose and composite materials, mixing different percentages of cellulose with different percentages of water, starch, sawdust, and ceramic paste, a set of mixtures was selected in order to produce a reliable prototype wall that expressed the different behaviour and tectonics of those materials - the Kusudama wall.

The design solution was achieved through the use of a parametric design model, envisaging a customised set of hexagonal blocks. Two types of blocks were made from a regular hexagonal grid; the first consisted of a triangular interior opening and the second one consisted of a pentagonal interior opening. The heights of the hexagonal external wall and pentagonal internal wall are 50 mm and 100 mm, respectively. The hexagon is circumscribed in a circle with a diameter of 170 mm.

From the material perspective, the use of a small percentage of cellulose, and other additives of stoneware mixtures, shows a substantial improvement in mechanical performance during the drying and firing stages.

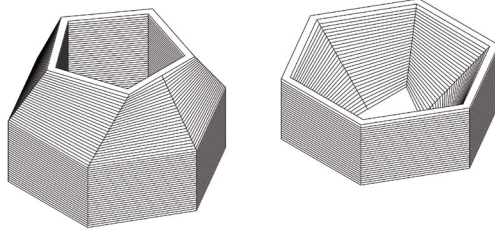


FIG. 15 Kusudama-brick extrusion path models.

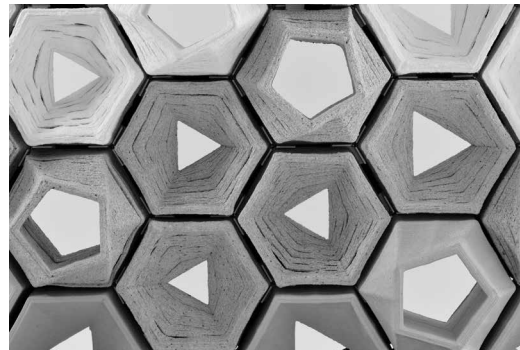


FIG. 16 Kusudama wall prototype.

### 3.6 HEXASHADE

Hexashade prototype explores the use of hexagonal ceramic blocks for the construction of a vault shading system whose geometry and internal structure are defined according to solar incidence. Based on hexagonal blocks, the optimisation takes place through the geometric variation of the internal structure of the blocks.

The design process is mediated by a computational model, taking into account the sun incidence data, resulting in a system that adapts the internal geometry of each one of the blocks through their relative position in the set, making them more or less permeable depending on the space/ time ratio to be shaded.

The prototype is composed of irregular hexagonal blocks with variable internal openings and external configurations. Their dimensions range from 200 mm x 74 mm x 23 mm (the smallest block) and 210 mm x 167 mm x 23 mm (the biggest block).

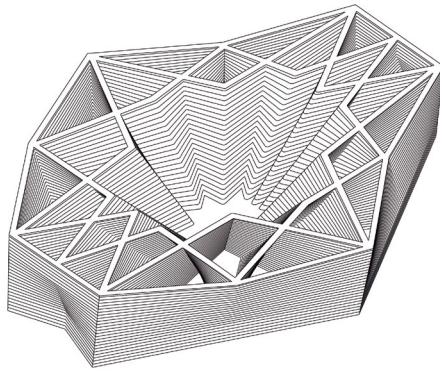


FIG. 17 Hexashade-block extrusion path model.

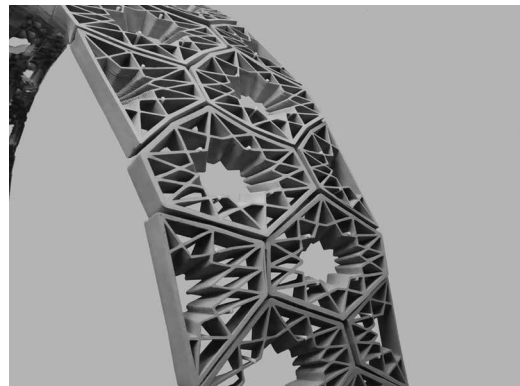


FIG. 18 Hexashade vault prototype.

## 4 CONCLUSIONS

The history of architecture, characterised by its technical and material, as well as aesthetic evolution, is enhanced by the evolution of ceramics. The authors of this paper believe that there is room for achieving significant improvements in the implementation of AM in ceramics, beyond the state-of-the-art in the building industry and in industrial applications.

The production of reduced-scale prototypes helps to dispel doubts about their functionality and the efficacy of the AM process. The manufacturing constraints, recognised by experimentation, must be integrated in the computational models from the design phase, in order to avoid the need for subsequent changes.

The prototypes presented in this work reveal viable architectural and constructional solutions and clearly validate the fulfilment of the objectives proposed. In fact, they wholly demonstrate the potential of AM techniques and the efficient use of resources; they made use of different approaches for the discretization of irregular surfaces; they integrate innovative architectural components with enhanced functionalities.

### Acknowledgements

This work has the financial support of the Project Lab2PT - Landscapes, Heritage and Territory laboratory - AUR/04509 and FCT through national funds and where applicable through the FEDER co-financing, within the aim of the new partnership agreement PT2020 and COMPETE2020 - POCI 01 0145FEDER 007528.

### References

- Bechthold, M., Kane, A. & King, N. (2015). *Ceramic Material Systems: in Architecture and Interior Design*, Birkhäuser, Verlag GmbH, Basel, ISBN 978-3-03821-843-2.
- Bergdoll, B. & Massey, J. (2011). *Marcel Breuer and Postwar America: Drawings from the Marcel Breuer Papers*. Syracuse: Syracuse University School of Architecture.
- Boëthius, J. (2019). *Same, Same but Different - learning from references when designing contemporary brick architecture*. (Master's thesis). Chalmers School of Architecture, Gothenburg.
- Carpo, M. (2019). *The Age of Computational Brutalism. Robotic Building: Architecture in the Age of Automation (1st ed)*, (pp. 8–9). Munich: Detail Business Information GmbH.
- Castañeda, E., Lauret, B., Lirola, J.M., & Ovando, G. (2015). Free-form architectural envelopes: Digital processes opportunities of industrial production at a reasonable price. *Journal of Façade Design and Engineering*, 3(1), 1–13. doi:10.7480/jfde.2015.1.914
- Cruz, P.J.S., Camões, A., Figueiredo, B., Ribeiro, M.J., & Renault, J. (2019). Additive manufacturing effect on the mechanical behaviour of architectural stoneware bricks. *Construction & Building Materials*, 238, Elsevier. doi:10.1016/j.conbuildmat.2019.117690
- Cruz, P.J.S., Knaack, U., Figueiredo, B., & Witte, D. De. (2017). Ceramic 3D printing – The Future of Brick in Architecture. *Proceedings of the IASS Annual Symposium 2017, IASS 2017 – Interfaces: Architecture. Engineering. Science*. Hamburg: HafenCity University.
- Da Silva, A.L., Feltrin, J., Dal Bó, M., Bernardin, A.M., & Hotza, D. (2014). Effect of reduction of thickness on microstructure and properties of porcelain stoneware tiles. *Ceramics International*, 40(9), Part B, 14693–14699.
- Dieste, E. (1996). *Reinforced Masonry. Eladio Dieste 1943-1996*, Jiménez Torrecillas A. (ed), Seville, Consejería de Obras Públicas y Transportes.
- Gualtieri, M.L., Mugoni, C., Guandalini, S., Cattini, A., Mazzini, D., Alboni, C., & Siligardi, C. (2018). Glass recycling in the production of low-temperature stoneware tiles. *Journal of Cleaner Production*, Vol 197, Part 1, 1531–1539.
- Guilherme, P., Ribeiro, M.J., & Labrincha, J.A. (2009). Behaviour of different industrial ceramic pastes in the extrusion process. *Advances in Applied Ceramics*, 108(6), 347–351.
- Gültekina, E.E., Topateşb, G., & Kuramac, S. (2017). The effects of sintering temperature on phase and pore evolution in porcelain tiles. *Ceramics International*, 43(14), 11511–11515.
- Khoshnevis, B. (2004). Automated construction by contour crafting-related robotics and information technologies. *Automation in Construction*, 13(1), 5–19. doi:10.1016/j.autcon.2003.08.012
- Martín-Márquez, J., Rincón, J.M., & Romero, M. (2008). Effect of firing temperature on sintering of porcelain stoneware tiles. *Ceramics International*, 34(8), 1867–1873.
- Mitchell, W. & McCullough, M. (1997). *Digital Design Media*. New York: John Wiley & Sons, Inc.
- Oummedi, S., Nait-Ali, B., Alzina, A., Victor, J.-L., Launay, Y., Mirdrikvand, M., Dreher, W., Rezwan, K., & Smith, D.S. (2019). Distribution of water in ceramic green bodies during drying. *J. Eur. Ceram. Soc.*, 39, 3164–3172.

- Pallasma, J. (1998). Alvar Aalto: Toward a Synthetic Functionalism. *AlvarAalto: Between Humanism and Materialism*, Peter Reed (Ed.). New York: The Museum of Modern Art.
- Park, J. & Baldanchoijil, G. (2014). The Superimposition of Circles Cut into Louis I. Kahn's Building Façades. *Journal of Asian Architecture and Building Engineering*, 13(2), 389-396. DOI: 10.3130/jaabe.13.389
- Peters, B. (2014). Building Bytes: 3D-Printed bricks. *Fabricate 2014: Negotiating Design Making*, Zurich: gta Verlag.
- Pfefferkorn, K. (1924). *Ein Beitrag zur Bestimmung der Plastizität in Tonen und Kaolinen. Sprechsaal* [A contribution to the determination of plasticity in clays and kaolins], 57(25), 297-299.
- Rael, R., & San Fratello, V. (2018). *Printing Architecture: Innovative Recipes for 3D Printing*. Princeton Architectural Press.
- Rambaldi, E., Pabst, W., Gregorová, E., Prete, F., & Bignozzi, M.C. (2017). Elastic properties of porous porcelain stoneware tile. *Ceramics International*, 43(9), 6919-6924.
- Ramcke, R. (2001). *Masonry in architecture. Masonry construction manual*. Gerd Soffker; Philip Thrift, Elizabeth Schwaiger (Eds.). Basel; Boston; Berlin: Birkhauser; Munich: Ed. Detail. (pp. 8-52).
- Ribeiro, M.J., Blackburn, S., & Labrincha, J.A. (2009). Single screw extrusion of mullite-based tubes containing Al-rich anodising sludge. *Ceramics International*, 35(3), 1095-1101.
- Ribeiro, M.J., Ferreira, J.M., & Labrincha, J.A. (2005). Plastic behaviour of different ceramic pastes processed by extrusion. *Ceramics International*, 31(4), 515-519.
- Ribeiro, S. (2020). *Optimization of ceramic pastes for extrusion processes by additive manufacturing and respective characterization of mechanical behaviour*, (Master's thesis). University of Minho, Portugal (in Portuguese).
- Sabin, J.E., Miller, M., Cassab, N., & Lucia, A. (2014). PolyBrick: Variegated Additive Ceramic Component Manufacturing. *ACCM 3D Printing and Additive Manufacturing*, 1(2), 78-84. <https://doi.org/10.1089/3dp.2014.0012>, 2015.
- Sampaio, A.M., Gonçalves, R., Lima, R., Cruz, P.J.S., Figueiredo, B., Carvalho, S., & Pontes, A.J. (2019). Design for Additive Manufacturing of Mechanical Connections Toward Hybrid Products. *Advances in Additive Manufacturing, Modeling Systems and 3D Prototyping, Proceedings of the AHFE 2019 International Conference on Additive Manufacturing, Modeling Systems and 3D Prototyping*, July 24-28, Washington D.C., USA. Springer Nature Switzerland AG 2020, M. Di Nicolantonio et al. (Eds.): AHFE 2019, AISC 975, pp. 418-427.
- Sarakinioti, M-V., Konstantinou, T., Turrin, M., Tenpierik, M., Loonen, R., Klijn-Chevalerias, M. L., & Knaack, U. (2020). Development and prototyping of an integrated 3D-printed façade for thermal regulation in complex geometries. *Journal of Façade Design and Engineering*, 6(2), 029-040. doi:10.7480/jfde.2018.2.2081
- World Economic Forum (2016). *Shaping the Future of Construction - A Breakthrough in Mindset and Technology, Industry Agenda*, Ref. 220416, Prepared in collaboration with The Boston Consulting Group. Switzerland: World Economic Forum.



# Fire Safety Façade Design and Modelling

## The Case Study of the Libeskind Tower

**Enrico Sergio Mazzucchelli<sup>1\*</sup>, Paolo Rigone<sup>1</sup>, Blanca Judith De la Fuente<sup>2</sup>, Paolo Giussani<sup>3</sup>**

\* Corresponding author

1 Department of Architecture, Built environment and Construction engineering, Politecnico di Milano, Italy, [enrico.mazzucchelli@polimi.it](mailto:enrico.mazzucchelli@polimi.it)

2 Sustainability Department, Ariatta Engineering

3 Façade Engineer and Consultant, Studio di Ingegneria Rigone

### Abstract

*Nowadays, the construction industry is characterised by high-rise, multifunctional, and complex buildings with innovative façade systems. Unlike a simple prescriptive approach in accordance with standards and codes, a performance-based design allows us to:*

*define safety levels and goals, evaluate heat transfer to the structure and the structure's response based on fire behaviour, model different fire scenarios using Computational Fluid Dynamics (CFD) software, and personalise the design of any specific project in order to reach the required level of safety. Through a significant case study, the Libeskind Tower in Milan's City Life district, this paper describes the Fire Safety Engineering (FSE) performance-based design approach. The analysis demonstrates consistent results between the CFD fire modelling output and the laboratory test on a full-scale façade mock-up. Moreover, a Finite Element Analysis (FEA) performed on a section of the façade mullion, identifies and highlights the façade system's critical issues in different fire scenarios.*

### Keywords

*Computational fluid dynamics (CFD), finite element analysis (FEA), façade modelling, Fire Safety Engineering (FSE), building façades*

DOI 10.7480/jfde.2020.1.4703

# 1 INTRODUCTION

Nowadays, the construction industry is characterised by high-rise, multifunctional, and complex buildings with innovative façade systems (Fig. 1). The need to comply with European energy efficiency regulations has led to research and design advanced building envelopes (Rigone, & Giussani, 2019; Romano, Aelenei L., Aelenei D., & Mazzucchelli, 2018), for which innovative materials and systems are continuously developed and introduced (Aelenei L., Aelenei D., Brzezicki, Mazzucchelli, Rico Martinez, & Romano, 2018; Mazzucchelli, Alston, Brzezicki, & Doniacovo, 2018), calling for an improvement of regulations and testing standards (Anderson, Boström, McNamee, & Milovanović, 2017).

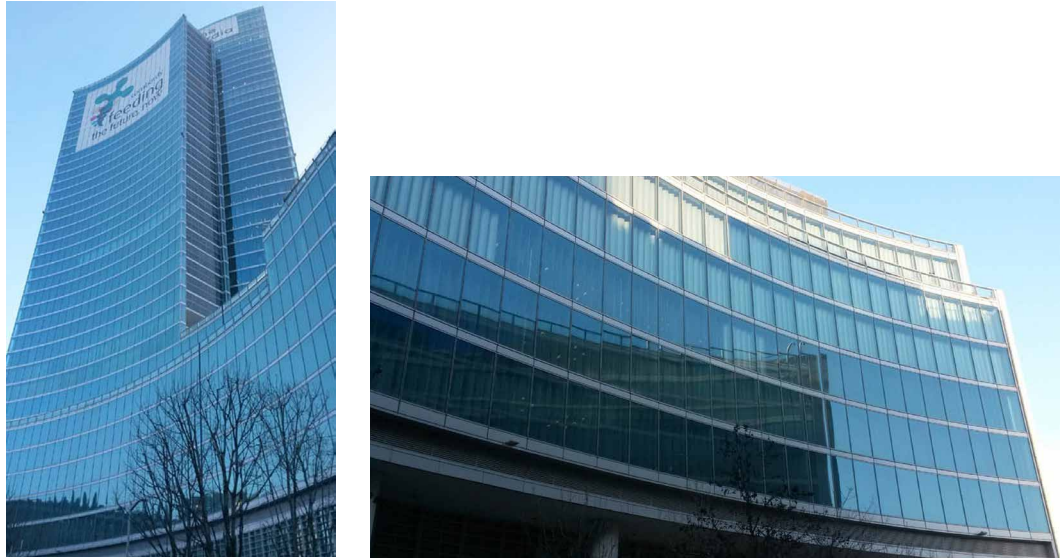


FIG. 1 Example of high-rise building with advanced façades: Palazzo Lombardia, Milan, Italy

However, the architectural quality and thermal performance of a façade system must be in accordance and consistent to guarantee other requirements, such as fire safety. Many recent fire events demonstrate that the need to improve the technical knowledge and practical procedures in high-rise buildings façade systems design, especially those concerning fire vulnerability, is still very strong (Mazzucchelli, Lucchini, & Stefanazzi, 2019). In this regard, unlike a simple prescriptive approach in accordance with standards and codes, a performance-based design allows us to define safety levels and goals, evaluate heat transfer to the structure and the structure's response based on fire behaviour, model different fire scenarios using Computational Fluid Dynamics (CFD) software, and personalise the design of any specific project in order to reach the required level of safety. Therefore, an appropriate selection and use of materials, a Fire Safety Engineering (FSE) analysis, and laboratory tests (Fig. 2) become fundamental (Bjegović, Pečur, Milovanović, Rukavina, & Alagušić, 2016).

The paper, after introducing the general issue of fire safety pertaining to building façades, focuses on a case study where a performance-based FSE design approach has been followed. In particular, the CFD modelling process and the Finite Element Analysis (FEA) analysis, as tools to evaluate different fire scenarios and the façade system's critical issues in case of fire, are described in detail. The analyses carried out demonstrate results consistent with those of a laboratory test on a full scale façade mock-up, showing that such an approach can be conveniently used in assessing the fire performance of façade systems, especially in the case of new buildings with complex shapes.



FIG. 2 Images of laboratory tests to evaluate the fire behaviour of an opaque façade solution: ignition phase (left) and steady phase after 10 minutes (right)

## 2 FIRE SAFETY CONSIDERATIONS

In the construction field, fire events in façades are the less likely to occur. Nevertheless, in Europe many national guidelines regarding opaque façades (Rukavina, Carevic, & Pečur, 2017; Mazzucchelli et al., 2019) are available, while new transparent curtain wall systems undoubtedly call for an improvement in the standards.

In general, the typical scenarios for the fire spread over façades are of three types (Fig. 3):

- spread of an external fire onto a combustible façade by radiation from a neighbouring, separate building;
- spread of an external fire due to radiative effect or due to direct fire effect from a source of fire located next to the façade (for example fire developed on a balcony or fire from a car parked near the façade);
- internal fire, started in a space inside the building, spreading through openings in the façade (windows, doors, etc.) onto upper or lower floors.

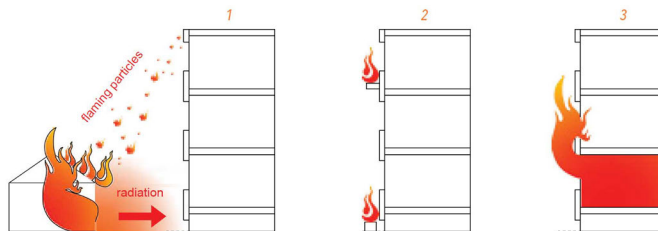


FIG. 3 Typical scenarios of fire spread across façades (Rukavina et al., 2017)

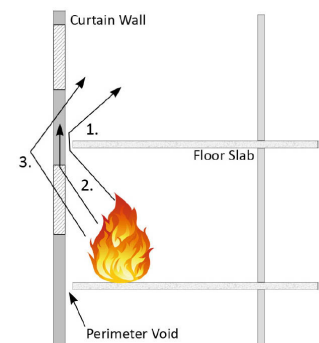


FIG. 4 Curtain wall façades' main fire spread mechanisms (Mazziotti & Cancelliere, 2013)

Considering a curtain wall system, where normally there are no combustible materials on the external surface of the façade, the typical fire spread scenarios are summarised in Fig. 4, where no. 1 represents the fire spread through the space between the slabs and the internal façade surface, no. 2 the fire spread within the façades cavities or ventilation chambers, and no. 3 the fire spread through façade windows and openings.

In any case, many aspects should be considered to guarantee the fire safety in building façades, such as the connection requirements between fire compartments and façade elements, the fire behaviour of materials, the absence of obstacles to the fire spread on the façade and/or to neighbouring façades, the possibility of detachment of burnt façade portions and involvement of still intact portions of the façade, the risk of glass units and façade components to fall, etc. Fire vulnerability can be reduced if the fire load within building compartments is maintained at moderate levels. Moreover, fire protection for buildings can be achieved not only by passive methods, but also by active systems (e.g. sprinklers) that can minimise the risk of fire propagations. Therefore, fire safety is related to many variables and must be assessed, investigated, and solved, case by case, through a specific FSE analysis, taking into account many parameters (e.g. spatial distribution of the combustible materials, development and fire spread over the façades, Heat Release Rate - HRR, temperature distribution, smoke composition, air movement and diffusion or ventilation). Furthermore, fire safety aspects are not limited to the control of fire spread, but also concern the structural safety of the building components.

In the past, the fire resistance performance of components could be determined only by laboratory tests. In recent years however, the use of numerical methods for the fire resistance calculation of various structural components is growing and spreading, since it is far less costly and time consuming, thus significantly contributing to the modern development of fire safety science and engineering. Nowadays, appropriate numerical simulations allow a performance-based approach to be followed in a much faster and more convenient way, in which the modelling is combined with full scale fire tests carried out to evaluate the behaviour of different solutions, materials, and effects due to different geometries and configurations of façade openings (Kotthoff, Hauswaldt, Riese, & Riemesch-Speer, 2016; Northe, Riese, & Zehfuß, 2016; Bjegović et al., 2016).

Thus, numerical modelling is commonly used for a major parameter analysis, especially in the case of buildings characterised by complex façades, such as those of the Libeskind Tower. Moreover, for a large-scale test method, modelling is required for simulations as undergoing a laboratory test can be complex due to factors that can influence the results (e.g. wind direction and speed).

### 3 CASE STUDY: THE LIBESKIND TOWER

The Libeskind Tower is located in the City Life district in Milan (Italy). The main highlighted issues of the office tower are the concave bending of its elevations and the top crown (Fig. 5). The building core is divided into two separate blocks, symmetrical as far as the structure is concerned, but asymmetrical with regards to the location of the escape routes (Fig. 6).



FIG. 5 Render of the Citylife district in Milan (Italy). The Libeskind tower is the one on the left



FIG. 6 Tower layout of the 5<sup>th</sup> floor

From the first to the twenty-eighth floor, indoor spaces are occupied by offices (Fig. 6), while at the twenty-seventh floor a double-height office and conference rooms are located. The crown's façade is characterised by a glass structure, whose geometrical lines complete the building, closing the spherical tendency, which is crucial to the tower concept. It is possible to simplify and to model the façade's design geometry into a toroid and cylinders, relatively simple shapes defined with a limited number of panel families. The façade units have a typical size of about 1500mm x 4100mm (Fig. 7),

although it is not possible to identify a standard module because of the tower's geometry. Despite having the same performance requirements, the different types of façade units differ for geometric characteristics, type of components, and installation method (Fig. 7 and Fig. 8).



FIG. 7 Construction phases of the Libeskind tower façade

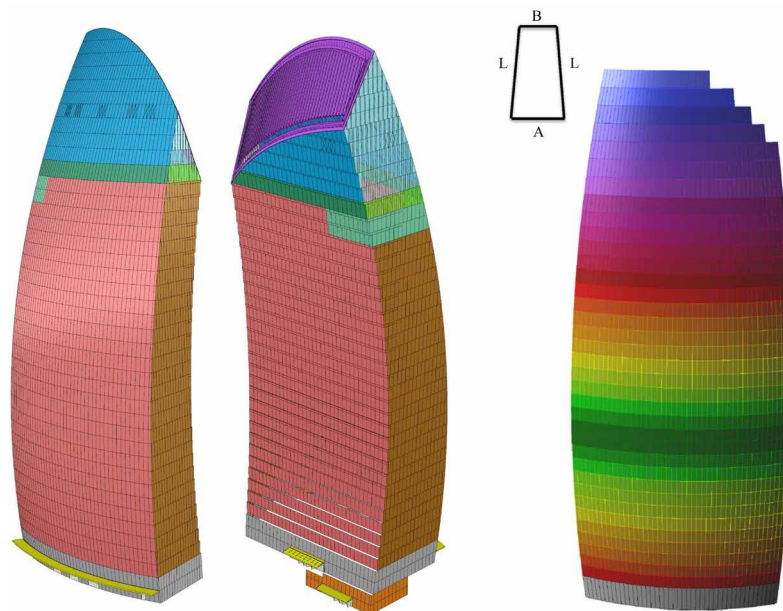


FIG. 8 Façade type and façade module shape. Despite having the same performance requirements, the different types of façade units differ for geometric characteristics, type of components, and installation method

The geometric rules of the module shape generation (Fig. 9 and Fig. 10) are the following:

- north façade: the shape is generated by a portion of spindle with horizontal oriented rotation axis. The center of the toroid is located at the 11<sup>th</sup> floor of the tower, defining a geometric rule that reduces the number of different panels. The horizontal stack joint between the flat units allows the vertical rotation of the panels;
- south façade: the shape is obtained from a portion of cylinder on the horizontal axis, discretised by vertical, inclined, and horizontal flat panels. The centre of the toroid is located at the 14<sup>th</sup> floor of the tower. To reduce the solar radiation of the façade to the public square, the façade module was modified, including the projected windowsill;
- east and west façades: the shape is given by two radial planes that cut the volume of the entire building. The panels are flat, rectangular-shaped, and the “jolly” panels are cut at the edges of the tower.

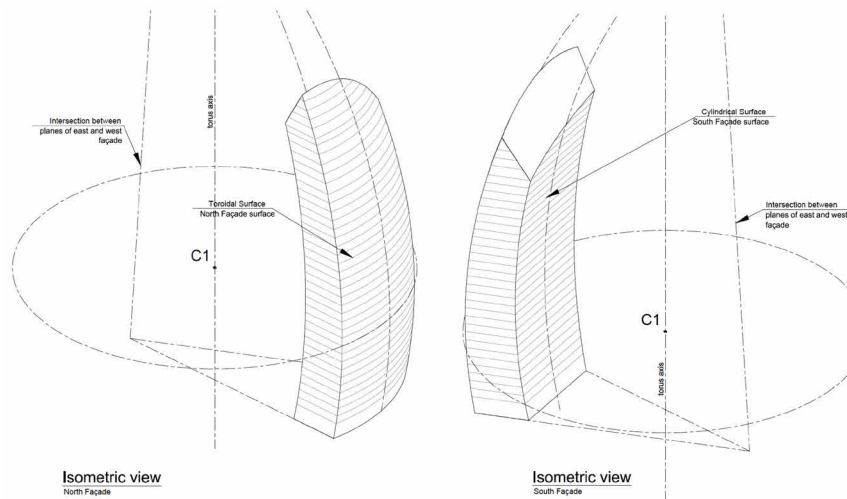


FIG. 9 Geometrical rule of module shape generation (De la Fuente, 2019)

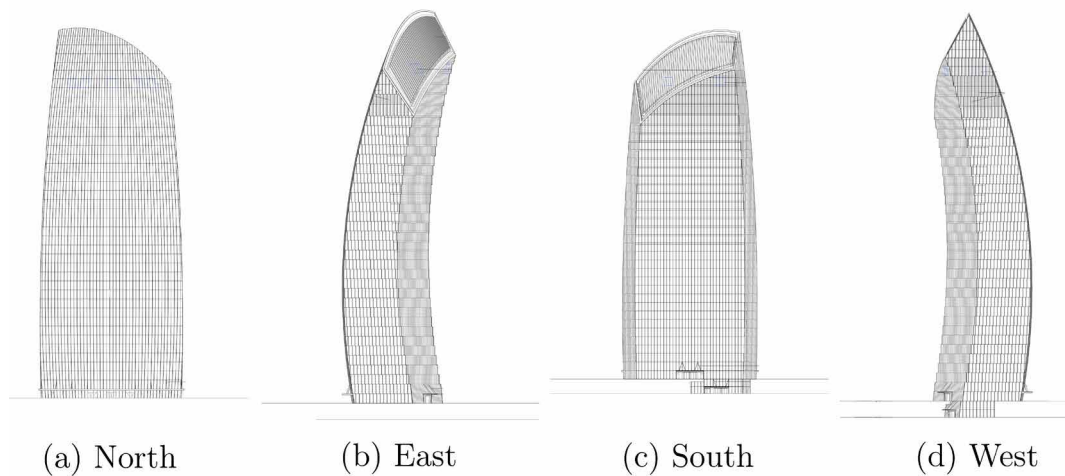


FIG. 10 Elevations of the tower (De la Fuente, 2019)



FIG. 11 Façade - south-east corner, low rise

From a functional point of view, the crown hides the cooling towers, the service lifts, and the façade's Building Maintenance Unit (BMU) system. The triple glazing façade fixed units (Fig. 11) comply with the thermal (overall U-Value  $U_{cw} = 1.1 \div 1.3 \text{ W/m}^2\text{K}$ ), air permeability (class A4 - EN 12152), and acoustic insulation ( $D_{2m,nT,w} = 42 \text{ dB}$ ) performance values required by Italian national standards, as well as the protection from solar radiation in compliance with the current building regulations. Most of the glazing units of the single skin façade are Triple Glazed Units (TGU), with low-E and solar coating, air cavity filled with Argon gas and a "warm edge" spacer type. The connection to the slab is fire resistant and the details include insulating material and specific calcium silicate fire-board installed between the façade and the concrete decking (Fig. 12).

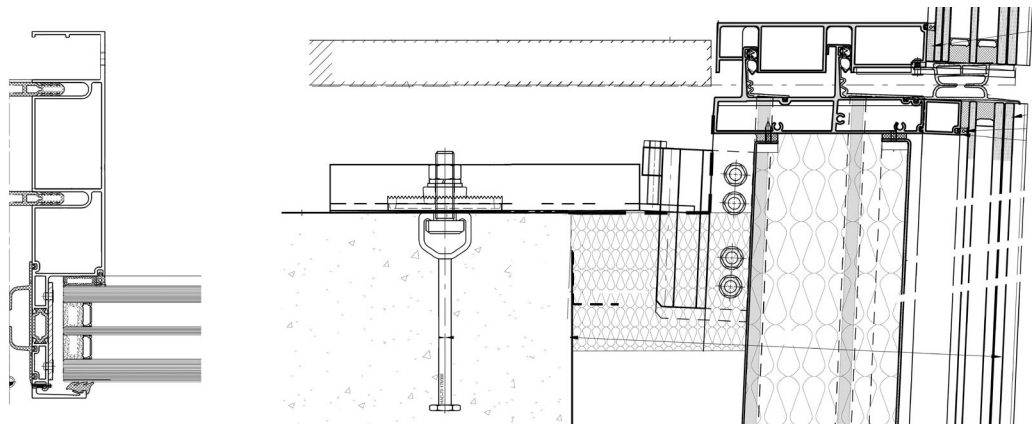


FIG. 12 Typical horizontal section of façade unit – half mullion aluminium frame (on the left) and typical vertical section of stack joint between units (on the right)

The connection joint is also very high performance for acoustic insulation. An internal natural light control system is achieved with automatic blackout roller blinds powered by a step-by-step electric driver controlled by a Building Management System (BMS). The potential overheating of the glass interlayer induced by the roller blind radiant effect is controlled by suitable slow natural ventilation through a perimetral air gap between the curtain walling framing and the roller blind.

### 3.1 METHODOLOGY AND MODELLING

The aim of the analysis here presented is the evaluation of the façade system's behaviour in case of fire, carried out through a CFD simulation (to assess the temperatures reached in a standard room and on the façade surface) and thermal and FEA modelling on a façade mullion (to assess critical issues in case of fire).

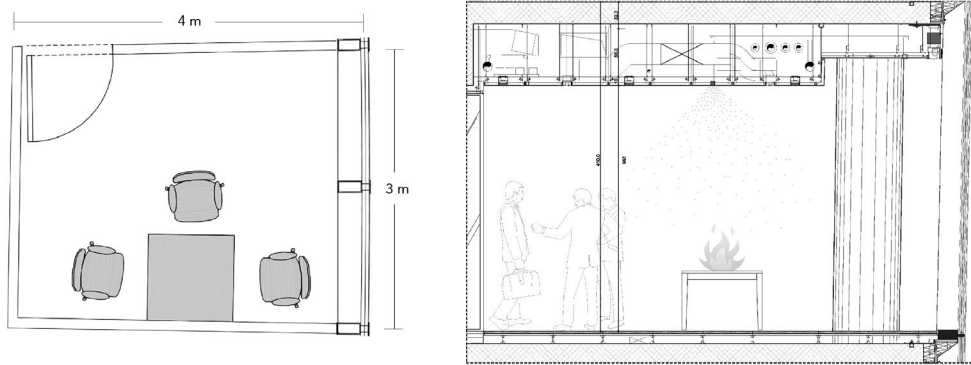


FIG. 13 Layout and vertical section of the analysed 7<sup>th</sup> floor north-facing room

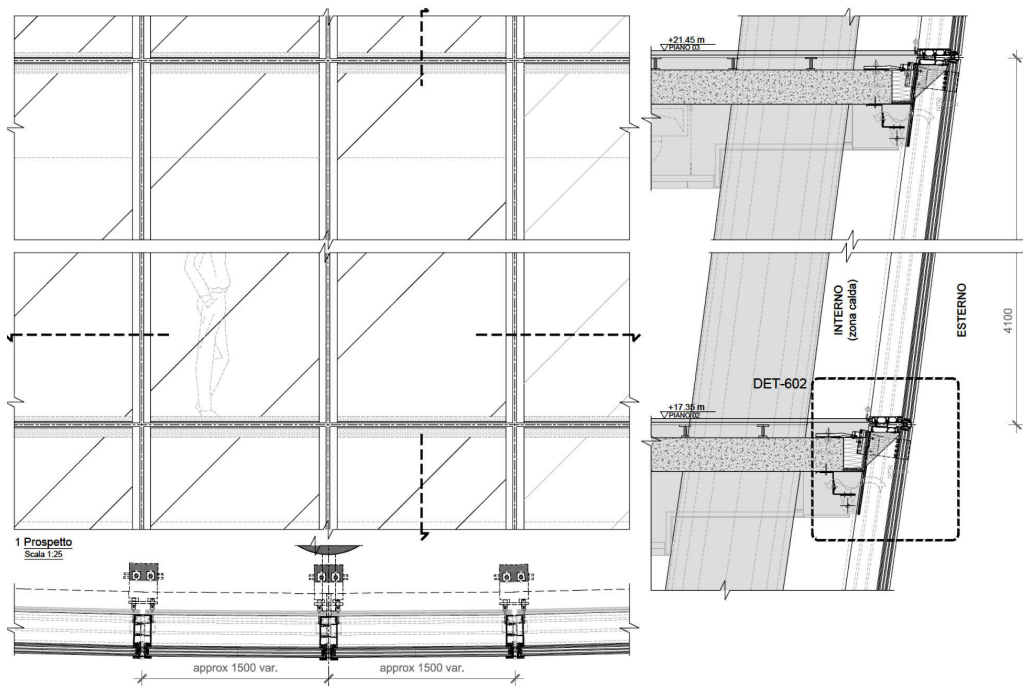


FIG. 14 North façade details: front view, vertical and horizontal sections

Different room configurations on different floors and with different orientations have been analysed (De la Fuente, 2019), but only the results for a north-facing office (Fig. 13) are presented here. This is because the north façade is the most critical due to its architectural curvature (Fig. 14) and where, in case of failure, a façade module is more likely to fall onto pedestrian zones.

The fire simulations allow the identification of the thermal loads acting on a façade and evaluation of the components' performance after flame and smoke propagation. In further detail, fire dynamics take into account physical and chemical interactions, including fluid dynamics, thermodynamics, combustion, and radiation. While in simplified fire models (such as one zone model), the gas temperature of a compartment is considered uniform and it is represented by a temperature-time relationship, without considering smoke movement and fire spread, advanced ones are normally theoretical computer models that simulate the heat and mass transfer process associated with fire in a compartment. This allows gas temperatures to be predicted in a more detailed and precise way, and to provide a space- and time-dependent gas temperature distribution, smoke movement, and fire spread.

In accordance with PD 7974-1 (Application of fire safety principles to the design of buildings, 2003), the design of fire is characterised in terms of HRR, smoke production rate, and time to key events like flashover and fire size or duration. Some preliminary assessments were performed to evaluate the fire scenario (Rigone, Mazzucchelli, & De la Fuente, 2020), such as ventilation conditions and possible variations during the fire (FSC Engineering report Torre Tcc, 2018), automatic suppression systems, and performance of each of the safety measures (De la Fuente, 2019), location, type, quantity, and distribution of combustible materials, materials fire reaction, considering BS 7479 (Application of fire safety principles to the design of buildings - Code of Practice, 2001) as a technical reference.

In the case study, an automatic sprinkler system was considered. The system aims to stabilise the maximum flow rate of the flames, once activated; still, the possibility of a system failure has been studied. Therefore, the following fire scenarios have been analysed:

- SN1: Fire located close to a mullion with a standard response sprinkler. The purpose of the standard response sprinkler is to pre-wet materials around the fire, removing the fuel source. Containing the fire in its original location and suppressing its growth are the main goals;
- SN2: Fire located close to a mullion with a quick response sprinkler. It has similar fire-control benefits as a standard response sprinkler, but it sprinkles more water on walls to control fire growth and to maintain lower temperatures at ceiling level, reducing the likelihood of flashover and slowing the fire growth within the building;
- SN3: Fire located close to a mullion with a sprinkler failing. This scenario aims to assess the behaviour of the room and to investigate the timing failure for the different components of the building façade.

For a typical office room, a fire with a medium growth rate parameter ( $0.012 \text{ kJ/s}^3$ , as recommended in BS 7974 and in accordance with NFPA 92B) is considered (Table 1). The fire is located at 0.5 m distance from one of the mullions, allowing the maximum effect of the fire on the façade structure to be analysed. The interaction between water and air heated by the fire is not directly modelled, but it is assumed that the sprinkler activation interrupts the fire development and stabilises it, maintaining a horizontal growth curve (FSC Engineering report Torre Tcc, 2018). Hence, when the fire growth value becomes constant, it corresponds to the sprinkler system activation. To evaluate the activation time for the two different sprinkler systems, B-Risk software (provided by BRANZ and the University of Canterbury) has been used. The output of this pre-assessment phase is necessary for the definition of the fire curves and the HRR.

TABLE 1 Summary of the main HRR curves inputs

	SPRINKLER STANDARD RESPONSE (SN1)	SPRINKLER QUICK RESPONSE (SN2)	UNCONTROLLED FIRE (SN3)
Room temperature [°C]	20	20	20
Sprinkler activation temperature [°C]	68	68	-
Space height [m]	3.0	3.0	3.0
Fire detector spacing [m]	2.9	2.9	-
Fire growth rate [kW/s <sup>2</sup> ]	0.012	0.012	0.012
Activation time [s]	175	140	300
Heat Release Rate, HRR [kW]	375	225	1,080
Heat Release Rate Per Unit Area, HRRPUA [kW/m <sup>2</sup> ]	284	220	818

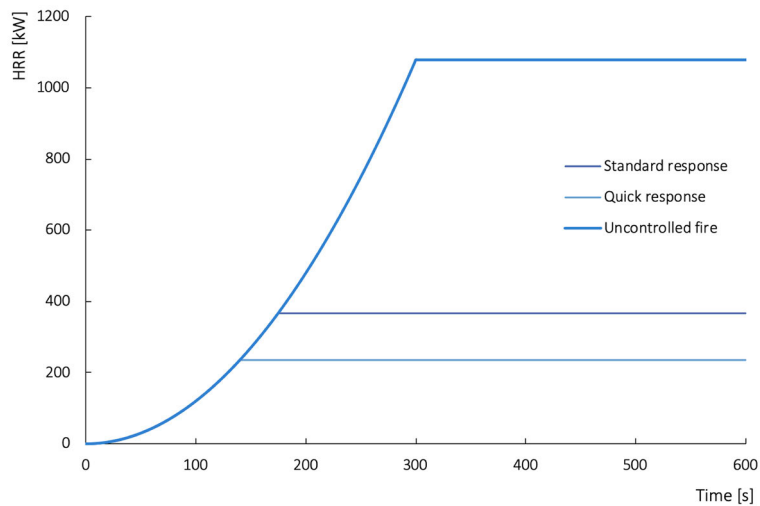


FIG. 15 Input HRR curves for the identified fire scenarios: sprinkler standard response (SN1), sprinkler quick response (SN2), uncontrolled fire (SN3) (De la Fuente, 2019)

The HRR curves for the proposed scenarios were calculated according to the equation of time-squared fire growth curve (specified in PD 7974-1). For SN3, following EN 1991-1-2 (Eurocode 1: Part 1-2: General actions – Actions on structures exposed to fire, 2002), which states that at 300 seconds (from ignition) the maximum rate of heat release is reached in an office occupancy, it is assumed that the curve stabilises at a fully developed fire and the decay phase would follow. The HRR curves for the identified fire scenarios and the main inputs are summarised in Table 1 and Fig. 15 (De la Fuente, 2019). Finally, the HRR curves have been used as a CFD software input, through the specific area (representing a localised fire) and the Heat Release Rate Per Unit Area (HRRPUA).

To analyse the specific façade system performance and to evaluate the temperatures of the framing mullions and glazing within the hypothesised fire scenarios, “Fire Dynamics Simulator” (provided by the National Institute of Standards and Technology - NIST) and “PyroSim 2018” (provided by Thunderhead Engineering), based on the Fire Dynamics Simulator 6.6.0 CFD calculation algorithm (McGrattan, Hostikka, McDermott, Floyd, Weinschenk, & Overholt, 2013), have been used. The modelling is characterised by the subdivision of the area of interest into a large number of much smaller domains, called mesh or cell grid. In this way, complex geometries and time-dependent flows

can be easily managed. The output consists of parametric values of the flows of interest, such as speed, smoke concentration, and the level of radiation calculated in each of the cells of the grid.

The temperature monitoring was carried out through specific detectors positioned on the façade module. The number of sensors, called Adiabatic Surface Temperature (AST), total 95 on the mullions and 208 on the glass panes, giving a total of 303 (Fig. 16). The modelling and the experimental test have been carried out to verify if the temperatures reached within the room could rise up to critical values, compromising the stability of the aluminium structure and the glass panes. In this regard, the CFD modelling output has been used as input for the Transient Thermal Analysis (TTA) of the mullion section, carried out through Straus7 (provided by G+D Computing and HSH Srl) and ANSYS (provided by ANSYS, Inc.) software, taking into account convection, radiation, and conduction effects. Both pieces of software use a finite elements analysis (FEA) method and, for the case study, a non-linear analysis section has been considered. To further elaborate, for the TTA of the mullion, a simplified section (Fig. 17) was analysed, considering the exposure of the mullion for 40 minutes to the natural fire curves obtained by CFD simulations. The triple glazing was modelled in Window and THERM software (provided by Lawrence Berkeley National Laboratory) to analyse the temperatures on each glazing pane surface. Finally, the modelling results were compared with the laboratory test results to evaluate the real model reliability.

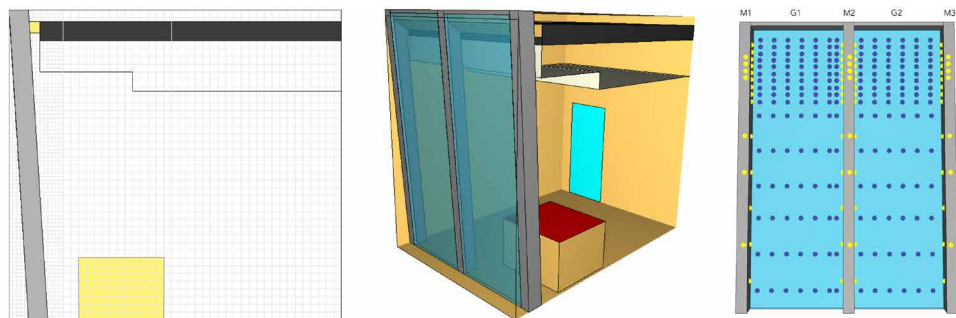


FIG. 16 Office model vertical section (left), 3D view (in the centre), and Adiabatic Surface Temperature (AST) sensors position (on the right, façade indoor view). M1: mullion no. 1, M2: mullion no. 2, M3: mullion no. 3, G1: glazing no. 1, G2: glazing. no. 2

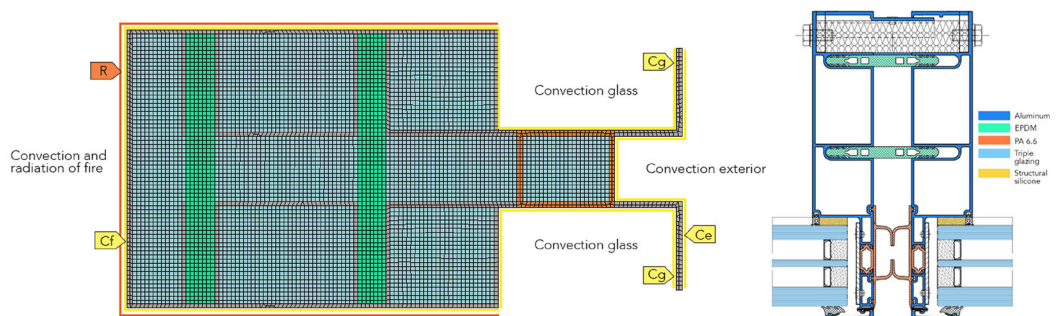


FIG. 17 ANSYS mullion model with mesh and boundary conditions (left) and mullion section with components (right)

## 3.2 NUMERICAL RESULTS

The overall behaviour of the office room proves the benefit of providing the sprinkler system. The temperature distribution on the façade (Fig. 18) reaches its highest values after 600 seconds of fire exposure. As can be seen according to what is detected by AST sensors, the façade is subject to temperatures between 50°C and 600°C, where the ranges differ according to the scenario. Considering SN1 and SN2, the mullions are locally subjected to temperatures equal to or higher than 250°C at the M1 and M2, while having temperatures between 120°C and 250°C in two thirds of the total area, and temperatures lower than 120°C for about one third of each mullion. For SN3, the mullion temperatures drastically increase, approximately doubling.

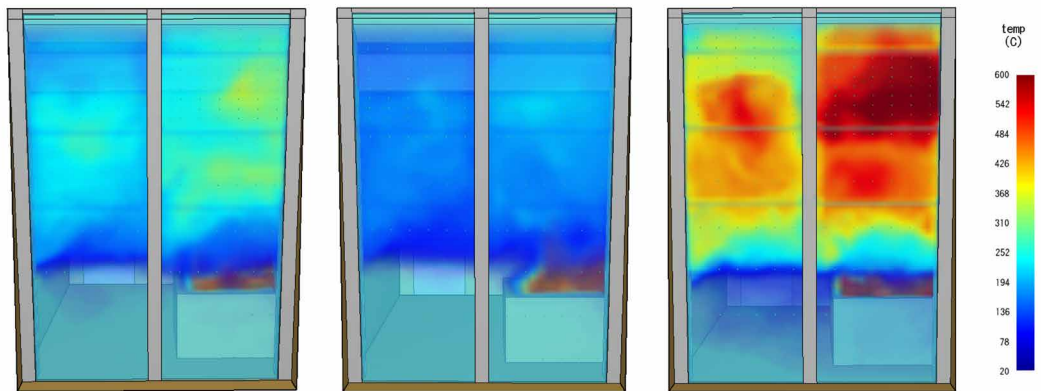


FIG. 18 Temperature distribution on façades for scenario SN1 (on the left), SN2 (in the centre), and SN3 (on the right)

For SN2, temperatures do not exceed 250°C, and for SN1 they reach the highest value of 280°C (Fig. 19 and Fig. 20). Meanwhile, the third case shows an uncontrolled fire (i.e. sprinkler system failure) and flashover (namely the sudden involvement of a room or an area in flames from floor to ceiling caused by thermal radiation feedback) occurrence, reaching temperatures of 600°C (Fig. 21).

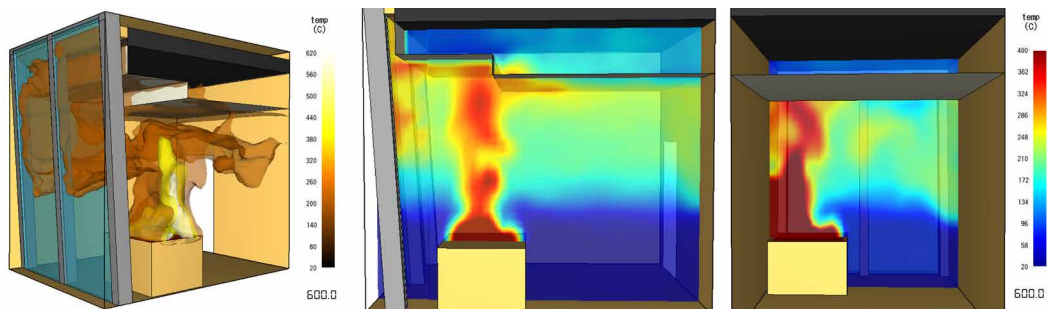


FIG. 19 SN1 - Isosurface at 200-400-600°C (on the left) and temperature of two vertical planes at stationary conditions after 600 seconds (in the centre and on the right)

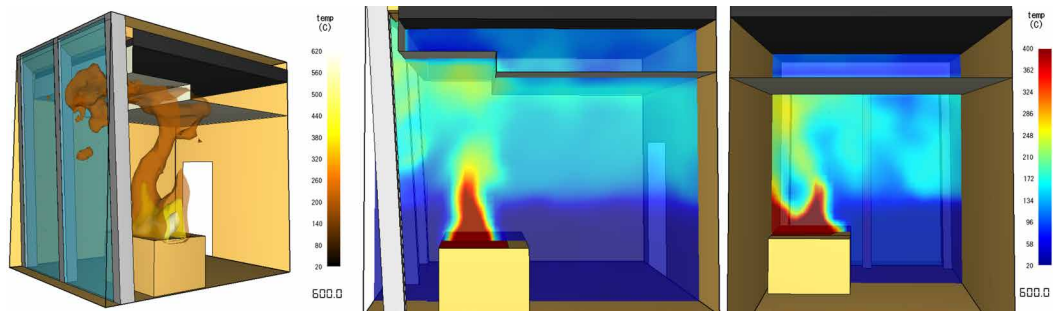


FIG. 20 SN2 - Isosurface at 200-400-600°C (on the left) and temperature of two vertical planes at stationary conditions after 600 seconds (in the centre and on the right)

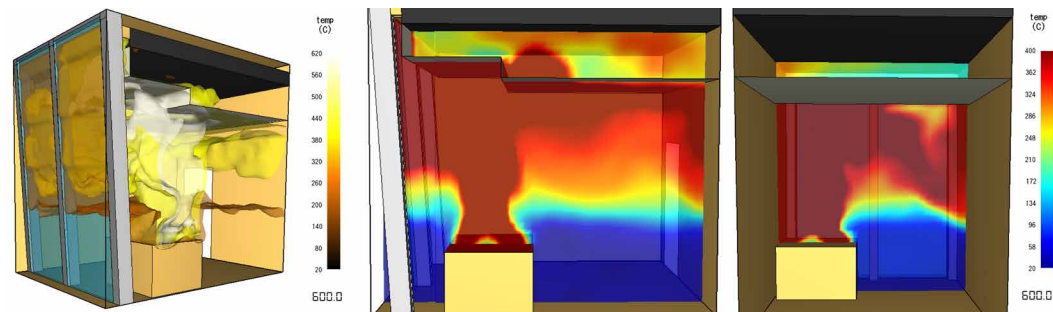


FIG. 21 SN3 - Isosurface at 200-400-600°C (on the left) and temperature of two vertical planes at stationary conditions after 600 seconds (in the centre and on the right)

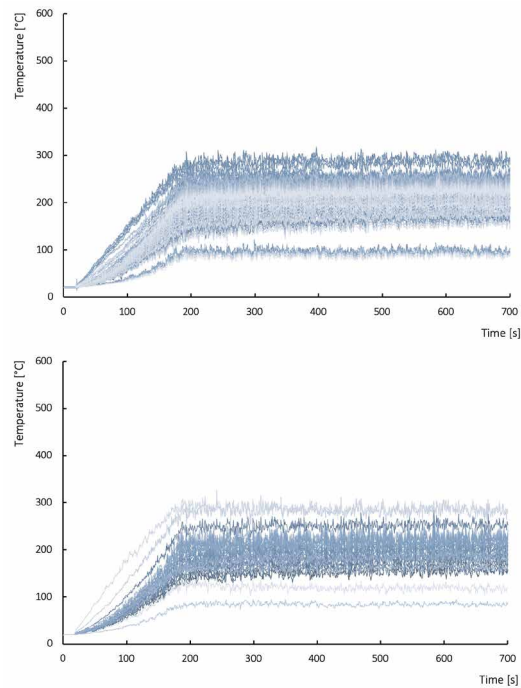


FIG. 22 SN1 – Glazing no. 1 (top) and Mullion no. 1 (bottom) time-temperature chart (data from AST sensors). The temperatures, after a first growth phase, stabilise when the stationary conditions (sprinkler system activation, after about 200 s of simulation) are reached

The temperatures obtained in the CFD analysis along the façade elements by AST sensors are summarised in time-temperature charts (see Fig. 22 for SN1): the temperatures, after a first growth phase, stabilise when the stationary conditions (sprinkler system activation, after about 200 seconds of simulation) are reached. The temperatures recorded on the mullions and the glazing reach a maximum of about 300 °C. The highest temperatures reached are for mullion no. 1 and glazing no. 1 (as identified in Fig. 16), which are the closest to the fire source. The CFD analysis results highlighted that the sprinkler scenario SN1 and the uncontrolled fire SN3 are the most relevant, as they have the higher recorded temperatures.

The CFD results and the temperature distribution have been used as inputs for TTA to estimate and determine the temperatures reached in the whole mullion section, their variation over time and the possibility of a structural failure. In this regard, a study of each façade component has been performed to evaluate the temperature effect from a structural stability point of view (see Fig. 23 and Table 2). For this analysis, some material properties are needed (e.g. specific heat, mass density, etc.) in order to take into account the contribution of their thermal inertia.

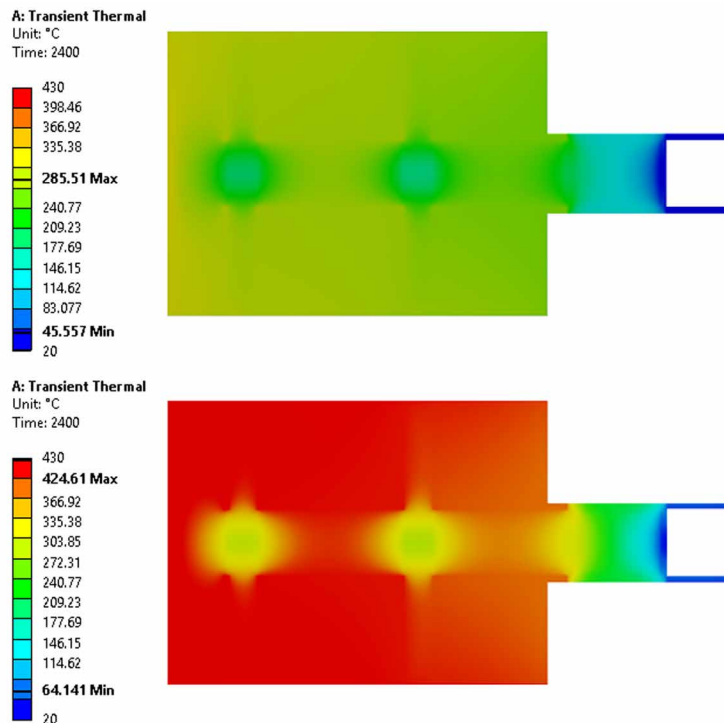


FIG. 23 SN1 (top) and SN3 (bottom) TTA mullion temperatures

As a thermal break, a polyamide 6.6 is used, which offers good insulating properties and excellent mechanical performance. According to the producer technical data sheet, its melting point is between 250°C – 265°C, while the flash point is at 490°C and the ignition temperature is 530°C. In the SN1, the thermal break highest temperature reached is 214°C, therefore melting, heat problems, and ignition phenomena are negligible. Although considering that the service temperature of the polyamide is between 120°C-150°C, a softening phase of the material is expected with a loss of mechanical properties. In the SN3, a temperature of 288 °C is reached, and this could cause the thermal break to melt. The gaskets are made of EPDM, which has a self-ignition temperature

of 279 °C at a standard room percentage of oxygen of 21% (Steinberg, Newton, & Beeson, 2000). Considering SN3, the temperature reached its highest value, higher than the auto-ignition of EPDM, and so the gaskets fail. Since, for the structural calculation of aluminium profiles, the EPDM elements are not taken into account, the softening of the gaskets can be considered irrelevant. Regarding the structural silicone thermal properties, the temperature reached within the mullion in all the scenarios leads to its mechanical failure. To secure the glazing, an aluminium bead was considered (Fig. 17).

TABLE 2 Summary of transient thermal analysis (TTA) mullion temperatures

FIRE SCENARIO	ALUMINIUM	EPDM	POLYAMIDE 6.6
SN1	256 °C	242 °C	214 °C
SN2	226 °C	216 °C	190 °C
SN3	425 °C	415 °C	288 °C

The loads on the structural elements were assumed from the structural report provided by the builder. The mullion numerical verifications (according to EN 1999-1-2: Eurocode 9, Design of aluminium structures, Part 1-2: Structural fire design, 2007) consider only the aluminium section, neglecting the contribution of other materials such as silicones, EPDM, and polyamide. The results show that all the metallic elements on the façade that reach temperatures below 400°C are not affected by a significant mechanical strength reduction and are verified in case of SN1 and SN2 scenarios (see Table 2). For the SN3 scenario, the temperature is above 400°C and a significant mechanical resistance loss occurs, putting the glazing in a potentially dangerous situation.

The triple glazing was modelled in Window software (provided by Lawrence Berkeley National Laboratory) as a triple pane system (internal 13 mm clear float glass pane, 18 mm argon filled cavity, 6 mm middle glass pane, 18 mm argon filled cavity, external 17 mm glazing pane made of heat strengthened glass with PVB interlayer). This model was then exported to THERM software (provided by Lawrence Berkeley National Laboratory) to analyse the temperatures on each glazing pane surface. According to the National Research Council of Canada (Babrauskas, 1998) the range of gradient temperature from exposed to unexposed surfaces that causes cracks on float glass goes from 25°C to 75°C. For the heat strengthened glass, the gradient temperature from inside to outside surfaces should be at least 100°C. Considering SN1 and SN3 scenarios, the minimum gradient temperature from the exposed surface to the unexposed has been calculated as 26 °C. With this value, a failing condition in the inner pane can be considered. Thus, another analysis is required to evaluate the behaviour of the middle heat strengthened pane after the failure of the inner pane. This second analysis has been performed considering the glazing as a double pane configuration. The maximum gradient temperature from the exposed surface to the unexposed one was calculated as 45 °C. From these results, it can be concluded that the middle pane does not break in the different fire scenarios (De la Fuente, 2019).

### 3.3 LABORATORY TEST AND MODEL VALIDATION

A fire resistance test was carried out on a façade mock-up (Fig. 24) at the Istituto Giordano's Fire Resistance Laboratory (Italy). Even if the façade is not subjected to specific fire requirements, except for the horizontal fire stop at slab level (it does not include any fire resisting glazing or fire resisting spandrel panel), the test was performed following the general provision given by the standard EN 1364-3 (Fire resistance tests for non-loadbearing elements - Part 3: Curtain walling - Full configuration - complete assembly, 2014), with a modification of the temperature profile in accordance with the fire analysis carried out. In fact, the temperature curves follow the software simulation with an exposure of 320°C for 60 minutes, and slowly increase for the last 15 minutes to a temperature of 450°C. The increased temperature was imposed to verify the ultimate resistance state of the façade exposed to a fire event. The test duration was evaluated in relation to the evacuation time for the given building and occupancy.

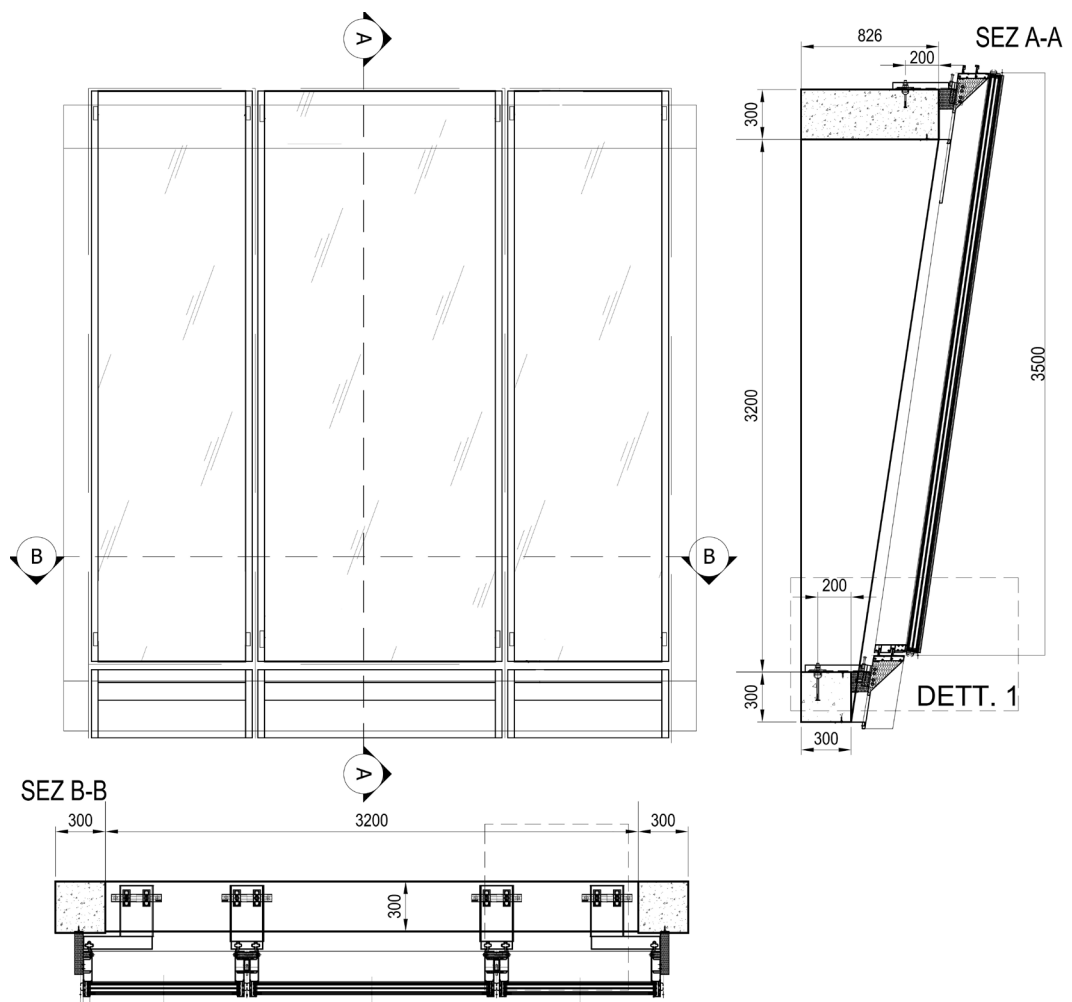


FIG. 24 Laboratory set up configuration of the façade mock-up in accordance with EN 1364-3 standard

The tested sample has shown no damage, except for the deterioration of the PVB layer in the strengthened glass pane. To carry out the test, an experimental oven (internal height of 3200 mm, width of 3200 mm, and depth of 1200 mm), fitted with 8 oil-fired double flame burners, evenly distributed on the vertical side walls, and two fireplaces placed separately, with output section electronically controlled variation valves, was used. The pressure detection system included two pressure detectors connected both to an automatic and a manual pressure reading system.

The temperature detection system included control units located on the vertical sides of the oven (to measure the inside temperatures), "K" type wire thermocouples (Nickel-Chromium/Alumel) connected to a mobile unit, in turn connected to a reader to translate the thermocouples potential difference into temperature values, laser deformation detection system, data acquisition system connected to an electronic computer with a management software. 75 thermocouples and 14 points for the deformation measurement through the laser detection system were placed at the unexposed side of the sample (Fig. 25).



FIG. 25 Façade mock-up after the laboratory test (on the left). Façade mock-up with thermocouples test equipment (on the right)



FIG. 26 Façade mock-up under fire exposure (on the left). Glass interlayer appearance after the laboratory test (on the right)

The test was successful, as the façade element maintained the thermal insulation and integrity for the entire test duration (70 minutes) evaluating the SN1 scenario. The mock-up and the glazing panels did not collapse during the test. Throughout the 70-minute test, there were no significant effects other than a change in colour of the PVB layer, which started 16 minutes after the beginning of the test (Fig. 26).

## 4 DISCUSSION

Different analyses were performed to assess the real behaviour of the façade in case of fire. To evaluate the accuracy of the model and the experimental test, a comparison pertaining to the mullion was done, taking as a base point the experimental test results by the Istituto Giordano laboratory, considering the experimental test conditions after 40 minutes of fire exposure and the scenario SN1, which is the one performed in all the analyses carried out. The thermocouples output of the six mullions are summarised in Fig. 27, which correlates to the experimental test and ANSYS simulation time-temperature charts; for Straus7 TTA, only the final temperatures of the sensors are considered. To avoid peak temperatures and follow the trend behaviour, the time-temperature chart of the laboratory test was traced considering the median values.

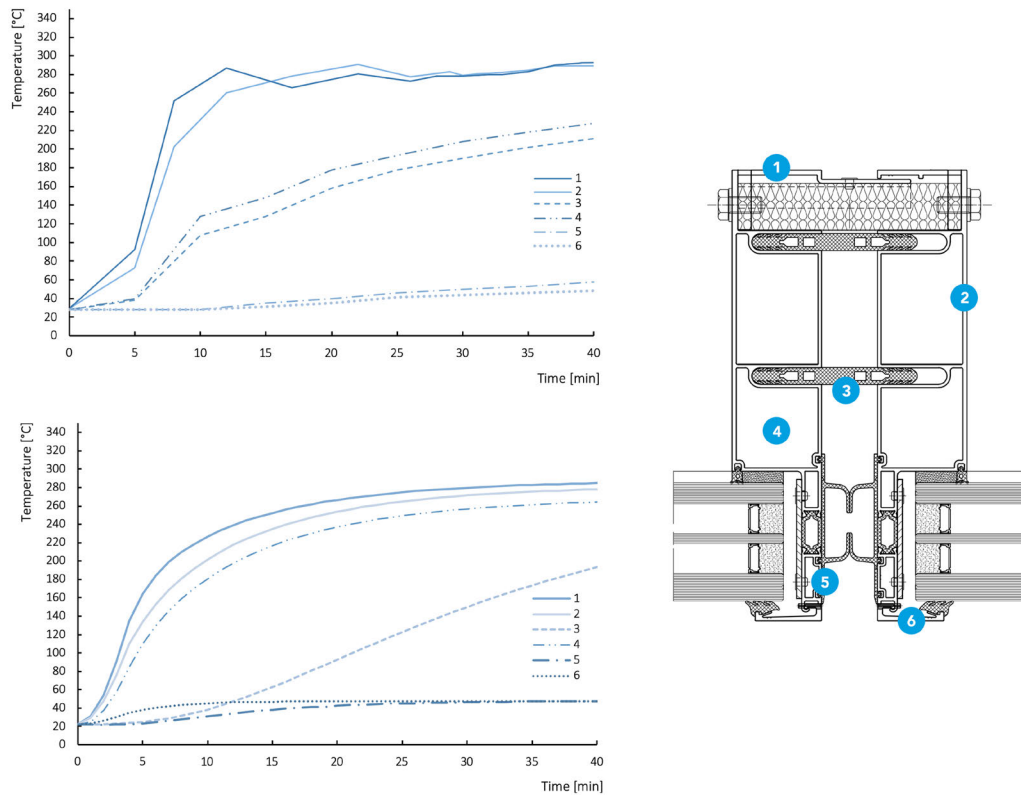


FIG. 27 Experimental test thermocouples time-temperature chart (on the top left), ANSYS sensors time-temperature (on the bottom left) and thermocouples analysed in the mullion comparison test (on the right)

TABLE 3 Summary of sensors' temperatures at 40 minutes of fire exposure

SENSOR	FIRE TEST	STRAUS7	ERROR [%]	ANSYS	ERROR [%]
1	292 °C	256 °C	12.32	284 °C	2.73
2	288 °C	242 °C	15.97	278 °C	3.47
3	211 °C	217 °C	2.84	193 °C	8.53
4	228 °C	201 °C	11.84	264 °C	15.78
5	58 °C	36 °C	37.93	47 °C	18.96
6	48 °C	36 °C	25.00	48 °C	0

The final assessment between the software and the fire test results (see Table 3) is useful to estimate the differences between them. In this regard, the overall difference with a median average is 17.65% for Straus 7 and 8.24% for ANSYS. Both simulations have a satisfactory result and are a good pre-design tool to simulate the behaviour of the mullion. ANSYS seems to give results that are closer to the real value measured during the laboratory test but, as a general remark, both software outcomes seem to be very close to the measured temperature values with an acceptable error. Once the reliability of the ANSYS model is confirmed, in case of an uncontrolled fire scenario, the time-temperature curve gives an overview of what could happen if this catastrophic case occurs.

In general terms, it is very important to set out the correct fire scenario, which clearly drives any possible consideration regarding this methodology of simulation and its potential extension to other cases. Reference fire scenarios can be found in national and international standards, but they need to be adapted to the specific design situations, involving a detailed knowledge of adopted fire prevention measures (in the case study, a sprinkler system) and architectural consideration of the building and façade details.

Façade construction details are relevant with regard to assembly and installation procedures, making a clear distinction between unitised curtain walling systems and stick construction systems. FEA analysis shows that, in terms of critical temperatures, stick systems are better performing due to a general higher thermal resistance of discrete framing (mullion and transom sections), when compared to typical coupled unitised mullions sections. In the case of unitised curtain walling systems, the presence of water and air control barriers (elastomeric EPDM gaskets, as components highlighted with number 3 in Fig. 27) represent a discontinuity in regard to temperature distribution in the framing section (see Fig. 23). On the contrary, in regard to Fig. 23, it is also very clear the importance of the thermal break made of polyamide strips, which highly reduce the heat transfer in the critical area of the curtain walling system, thus improving the mechanical glass retention (see sensors placed in 5 and 6 positions in Fig. 27). A specific consideration needs to be given in regard to the structural silicon bonding between glazing and aluminium framing. Experimental and FEA results show temperature values that are theoretically not compatible with the mechanical resistance of the bonding silicone, but no glass bonding failure occurred during the fire test. This could be explained by the local difference of temperature not recorded by the sensors (sensor no. 4 was placed inside the aluminium profile cavity and not in contact with the glass to sealant adhesion surface). In this case, a lower surface temperature could justify a residual mechanical resistance of the bonding. For sure, this specific topic requires a more detailed FEA analysis and it could be part of further investigations.

## 5 CONCLUSIONS AND FUTURE WORKS

The current tendency is to design high-rise buildings or skyscrapers with glazed façades, that involve a multidisciplinary design practice to ensure a high level of performance in terms of resistance to environmental actions (such as wind, rain, and earthquake) and to meet advanced standards of fire safety. FSE is part of the building design, but seldom is it properly considered in detail. Relevant considerations, as well as decisions, must be taken in regard to which kind of analysis is most suited to a particular project, which fire scenarios should be chosen to assess a real situation, the most appropriate safety devices to select, etc. Moreover, simulation software nowadays represents a cost-time efficient tool at a preliminary design stage, so that laboratory tests can be performed only later to validate the simulation results.

The case study presented here helps to understand how these new buildings with complex shapes can be analysed and assessed. All the studies and simulations performed (CFD, FEA, TTA) have been concluded with a valuable comparison between two different approaches, both with satisfactory results. Regarding the glazed façade, it should be considered that the SN3 represents a catastrophic scenario which is not likely to occur. It was studied to evaluate what could happen in case of a sprinkler system failure, which would also cause a general failure of the façade components. Here lies the importance of FSE, which ensures the possibility of evaluating multiple fire scenarios in a reasonable time and with good reliability, in order to give occupants and/or fire brigades the opportunity to understand how to act, thus reducing property damage, including structure, equipment, and building components.

### Acknowledgments

The authors would like to thank CityLife S.p.A. Milano, CMB (Cooperativa Muratori e Braccianti di Carpi), Focchi S.p.A., FSC Engineering Srl, UNICMI (Unione Nazionale delle Industrie delle Costruzioni Metalliche dell'Involucro e dei serramenti) and EFN (European Façade Network) for the fruitful and stimulating collaboration.

### References

- Aelenei, L., Aelenei, D., Brzezicki, M., Mazzucchelli, E.S., Rico Martinez, J., & Romano, R. (2018). *Case Studies – Adaptive Façades Network. Volume 3.1*. TU Delft Open, Delft, Netherlands.
- Anderson, J., Boström, L., McNamee, R. & Milovanović, B. (2017). Modeling of fire exposure in facade fire testing. *Fire and Materials*. doi: 10.1002/fam.2485.
- Babrauskas, V. (1998). *Glass Breakage in Fires*. The Fire Place, Washington Chapter IAAI Newsletter: 15-18.
- Bjegović, D., Pečur, I., Milovanović, B., Rukavina, M., & Alagušić, M. (2016). Comparative full-scale fire performance testing of ETICS systems. *Gradevinar 68*, vol. 5. doi: 10.14256/JCE.1347.2015.
- BS 7974:2001. *Application of fire safety principles to the design of buildings - Code of practice, British standard*.
- De la Fuente, B.J. (2019). Performance-based design for a single skin façade. *Case study: Libeskind tower in Citylife Milano*. Master's Thesis. School of Architecture Urban Planning Construction Engineering - Politecnico di Milano.
- EN 1991-1-2 (2002). *Eurocode 1: Actions on structures - Part 1-2: General actions – Actions on structures exposed to fire*.
- EN 1999-1-2 (2007). *Eurocode 9: Design of aluminium structures - Part 1-2: Structural fire design*.
- EN 1364-3 (2014). *Fire resistance tests for non-loadbearing elements - Part 3: Curtain walling - Full configuration (complete assembly)*.
- FSC Engineering Srl (2018). *Torre Tcc. Analisi del comportamento al fuoco della facciata continua [Tcc Tower. Fire behaviour analysis of the curtain wall]*. Technical report. City Life, Milano, Italy.
- Kotthoff, I., Hauswaldt, S., Riese, O., & Riemesch-Speer J. (2016). Investigations of the performance of facades made of ETICS with polystyrene under external fire exposure and fire safety measures for their improvement. 2<sup>nd</sup> International Seminar on Fire Safety of Facades, Lund, Sweden. MATEC Web of Conferences Vol. 46. doi: 10.1051/mateconf/20164602007
- Mazziotti, L., & Cancelliere, P. (2013). The Italian National Guidelines for the fire safety of facades. 1<sup>st</sup> International Seminar for Fire Safety of Facades, MATEC Web of Conferences Vol. 9. doi: 10.1051/mateconf/20130901005
- McGrattan, K., Hostikka, S., McDermott, R., Floyd, J., Weinschenk, C., & Overholt, C. (2013). *Fire Dynamics Simulator. User's Guide, v. 6*. Gaithersburg, NIST Special Publication 1019.
- McGrattan, K., Hostikka, S., McDermott, R., Floyd, J., Weinschenk, C., & Overholt, C. (2013). *Fire Dynamics Simulator. Technical Reference Guide, v. 6*. Gaithersburg, NIST Special Publication 1018.

- Mazzucchelli, E.S., Alston, M., Brzezicki, M., & Doniacovo, L. (2018). Study of a BIPV Adaptive System. Combining Timber and Photovoltaic Technologies. *Journal of Façade Design and Engineering*, vol. 6 (3), pp. 149-162, TU Delft Open, Delft, Netherlands, doi: 10.7480/jfde.2018.3.2602
- Mazzucchelli, E.S., Lucchini, A., & Stefanazzi, A. (2019). Fire safety issues in high-rise building façades. *TEMA Technologies Engineering Materials Architecture* vol. 5 n. 1, doi: 10.17410/tema.v5i1.221
- NFPA 92B - *Standard for Smoke Management Systems in Malls, Atria, and Large Spaces, 2009 Edition*. Quincy, MA, USA, National Fire Protection Association, 2009.
- Northe, C., Riese, O., & Zehfuß, J. (2016). Experimental investigations of the fire behaviour of facades with EPS exposed to different fire loads. 2<sup>nd</sup> International Seminar on Fire Safety of Facades, Lund, Sweden. MATEC Web of Conferences Vol. 46. doi: 10.1051/mateconf/20164602001
- PD 7974-1:2003. *Application of fire safety principles to the design of buildings, Part 1: Initiation and development of fire within the enclosure of origin (Sub-system 1)*, BSI reference.
- Rigone, P., & Giussani, P. (2019). Multidisciplinary approach in facade design: the upcoming role of the specialist "Façade Engineer". *Costruzioni Metalliche*, n. 2/ 2019, ISSN 0010-9673.
- Rigone, P., Mazzucchelli, E.S., & De la Fuente, B. (2020). Fire Safety Façade Design – The case study of an office tower in Milan. *Façade Tectonics 2020 World Congress*. <https://www.facadetectonics.org/papers/fire-safety-façades-design>
- Romano, R., Aelenei, L., Aelenei, D., & Mazzucchelli, E.S. (2018). What is an Adaptive Façade? Analysis of Recent Terms and Definitions from an International Perspective. *Journal of Façade Design and Engineering*, vol. 6 (3), pp. 65-76, TU Delft Open, Delft, Netherlands, doi: 10.7480/jfde.2018.3.2478
- Rukavina, M., Carevic, M., & Pečur, I. (2017). *Fire protection of façades – The guidelines for Designers, Architects, Engineers and Fire Expert*. University of Zagreb, Faculty of Civil Engineering, Zagreb, Croatia.
- Steinberg, T., Newton, B., & Beeson, H. (2000). *Flammability and Sensitivity of Materials in Oxygen-Enriched Atmospheres: Ninth Volume*. West Conshohocken, PA: ASTM International, doi: 10.1520/STP1395-EB

# A Novel Approach to Shape Memory Alloys Applied to Passive Adaptive Shading Systems

**Lorenzo Vercesi<sup>1,2</sup>, Alberto Speroni<sup>1\*</sup>, Andrea Giovanni Mainini<sup>1</sup>, Tiziana Poli<sup>1</sup>**

\* Corresponding author

1 Department of Architecture, Built Environment and Construction Engineering, Politecnico di Milano, Italy, alberto.speroni@polimi.it

2 Buro Happold, London, United Kingdom

## Abstract

*A shading device for façade application was developed by combining twisting cylindrical shading elements with the smart use of shape-memory alloy (SMA) components. These allow a dynamic behaviour of a shading device, which does not require electrical motors or manual activation, nor sophisticated electronic controls. The technical development of the system involved research of cylindrical shading geometries, which can transition from straight to hourglass configuration, given a 180° rotation, with limited mechanical movement. This is induced by the stroke of a SMA spring, which functions as both actuator and sensor. Its design is tailored to achieve a passive adaptive component that can be activated under set temperature stimuli, caused by incident solar radiation on a façade. A combination of computer simulations and physical tests were carried out to assess the optimal conditions of the SMA spring activation in a temperate climate condition (Cfa to the Koppen-Geiger classification), correlating transition temperature (50°C), incident solar radiation (>300W/m<sup>2</sup>) and the forces required to operate the cylinders. In parallel, an experimental apparatus was developed to validate the concept on a geometrical point of view, and to ensure its constraints were compatible with a SMA spring control system.*

## Keywords

*Passive adaptive, shading system, shading device, dynamic, innovative, double-skin, shape memory alloy springs, solar radiation, daylight*

DOI 10.7480/jfde.2020.1.4700

# 1 INTRODUCTION

Nowadays, building envelopes are assuming a new identity: a gradual reduction in the solid area of the façade in favour of transparent surfaces is in vogue in the context of contemporary architecture. The continuous evolution of the glazing system is not always sufficient to guarantee a dynamic behaviour that ensures users' comfort and optimal energy consumption (e.g. for cooling). Therefore, curtain walling is being progressively coupled with dynamic solar protection. An efficient solar shading system can reduce overheating in commercial buildings by about 10% to 20% (this value can change depending on several parameters such as climate, transparent surface percentage, building morphology, and shading type) (Menzies & Wherrett, 2005; Palmero-Marrero & Oliveira, 2010; Tzempelikos & Athienitis, 2007). The reduction of solar gains for fixed shading devices system is usually associated with a reduction in natural daylighting, resulting in an increase of energy consumption due to artificial lighting (Heschong, 2002). Alternatively, dynamic shading devices allow different configurations in order to respond to users' needs. In their simplest configuration, these systems can be controlled directly by the users; however, this manual mode is not efficient, since users are required to change the shading devices position periodically. The worst possible scenario results in the device being set at an extreme position permanently (i.e. completely closed or open), thus turning the system into a static solution (Wang, Pichatwatana, Roaf, Zhao, Zhu, & Li, 2014; Nielsen, Svendsen, & Jensen, 2011). A second type of dynamic shading is an automated one, where the configuration of shading devices is controlled automatically depending on environmental factors. Energy optimisation of this solution could be achieved by sensors and actuators, which can be part of the shading device or can be delocalised: sensors allow the collection of precise and localised information about physical parameters; actuators provide a dynamic response based on these parameters. The dynamic actuation is possible thanks to motors and mechanical transmission elements, through which it is possible to control multiple shading elements, in turn making the overall system more cost effective. The main issues for a dynamic shading system are a lower comfort level for users due to a diffused shading actuation, and a high risk of failure due to a wide use of mechanical parts.

The integration of smart materials (SMs) within shading systems enables an adaptive behaviour of the device and, depending on the intensity of solar radiation, reduces the system's complexity by avoiding the use of motorised mechanical parts. Direct consequences are reduced energy consumption and lower risk of failure. Fiorito et al. (2016) presented a detailed analysis of the actuation possibilities of shading systems by comparing their performances and working principles. The results highlight that SMs show the ability "to possess the characteristics to work as actuators either separated or integrated into shading components" (Fiorito et al., 2016). Within the realm of SMs, those that have been identified as suitable for this purpose, due to their durability and surety of performance, are shape memory alloys (SMAs) for the forces produced during their phase-change transition and their durability (high number of hysteresis cycle under certain condition). Like many other smart materials, SMAs require a tailor-made new shading functional model based on their material properties, which can be customised depending on the application.

A new shading device, which can change its configuration based on a passive adaptive approach, as defined by Mazzucchelli, Romano, Aelenei, and Gomes (2018), has been developed using SMA springs. These springs function as both sensor and actuator, and they change the configuration of the shading device (geometry, orientation, etc), avoiding phenomena such as overheating and glare.

The objective of this research study was to assess the mechanical and geometrical limitations of SMA springs, and to develop an innovative shading geometry that was compatible with these specific design constraints (climate, activation criteria) defined in Chapter 3.1. Once the initial parameters

had been defined, simulations and physical experiments were carried out on a number of design options (including system configuration, orientation, time over a day and a year) to correlate input stimuli on a vertical façade (incident solar radiation) with passive adaptive activation for a shading device, thus determining the range of application as a dynamic shading system.

## 1.1 BACKGROUND

Shape memory alloys (SMAs) are materials typically used in the medical and automotive sector for their reliability and integrability, as actuator or sensor. SMAs can be shaped with many geometries but their typical form is the helicoidal spring and simple wires since these geometries maximise the feature of the memory shape alloy. SMAs can be activated by temperature or electricity (via Joule effect), making them suitable for both active and passive adaptive solutions. Several shading concepts found in current literature use SMAs with different approaches. Table 1 presents different examples of SMA-based shading systems, categorised by estimated Technology Readiness Level (TRL), and by type of control and activation.

TABLE 1 SMA-Based Shading Systems. (\*Technology Readiness Level (TRL) estimated by the authors based on the information available on literature and online).

N°	SHADING SYSTEM	LITERATURE REFERENCE	SMA GEOMETRY	ESTIMATED TRL*	TYPE CONTROL	ACTIVATION STIMULUS
A1	Self-Adaptive Membrane	Decker & Yeadon, 2006	Spring	4-5	Diffuse	Temperature
A2	ADAPTIVE[SKINS]	Gonzalez, 2015	Spring	2-3	Diffuse	Temperature
A3	SmartScreen (Version C)	Luna, 2014	Spring	3-4	Diffuse	Temperature
A4	Shape Memory Alloy Responsive Façade	Adaptive Skin, 2015	Spring	3-4	Diffuse	Temperature
B1	Gill_Project	Sandoval, 2012	Wire	3-4	Local	Electrical
B2	Shutters A Permeable Surface	Coelho & Zigelbaum, 2011	Wire	2-3	Local	Electrical
B3	THE AIR FLOW(ER)	L.Architects, 2008	Wire	2-3	Local	Electrical
B4	Pixel Skin	Pixel Skin, 2006	Wire	4-5	Diffuse	Electrical

### 1.1.1 Spring-Based devices

“SmartScreen – Version C” (Decker & Yeadon, 2006), (Figure 1-A1) consists of two sliding screens, both of which comprise alternating opaque and transparent horizontal stripes. Such stripes vary their permeability by means of the shifting of the two sheets and overlapping of stripes, giving a solar permeability with an openness factor range of 50 to 100%. The control is a diffused passive type and consists of two springs (SMA r-type + standard bias) with indoor positioning. “Self-adaptive membrane” (Gonzalez, 2015), (Figure 1-A2) consists of an architectural skin with integrated passive adaptive actuators made by SMA with bias spring integrated into a transparent cylinder. The actuators change the shape of the skin locally, which increases its thickness with a low variation in its openness factor. Compared to the previous system, it is characterised by a higher number of control points that are connected in a single skin, which results in a less adaptive solution. “SMA responsive skin” (Luna, 2014), (Figure 1-A3) consists of a single small module activated passively

by a SMA spring. These modules have a central hole connected to a central axis. This axis is connected to the SMA spring that changes its shape by turning the axis, and consequently changing the openness factor of the system. "Adaptive skin" (Adaptive Skin, 2015), (Figure 1-A4) is a flexible shading material connected directly to SMA and bias springs. It is an architectural skin, therefore the variation in the position of a single module has consequences that affect the entire skin. Compared to the previous presented system, it is characterised by three SMA springs per element, which increases the possibility of control but also increases complexity and costs.

### 1.1.2 Wire-based Devices

The second type of geometry used for the SMA is the wire. The first two systems presented are "the air flower" (L.Architects, 2008), (Figure 1-B1) and "Pixel skin" (Pixel Skin, 2006), (Figure 1-B2). Both systems consist of a square element with four rigid adjustable flaps that can open/close passively, turning around the frame on the perimeter. The first of the two integrates the wire in the frame while the second one integrates the wire in the shading element.

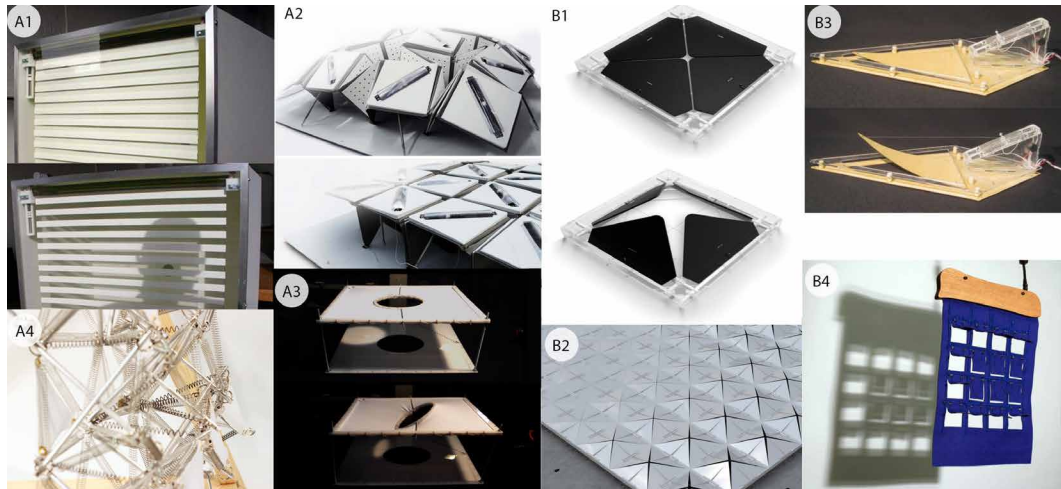


FIG. 1 [A1] SmartScreen - Version C (M. Decker, P. Yeadon). [A2] Self-Adaptive Membrane (N. Gonzales, S. More). [A3] Shape Memory Alloy Responsive Façade (I. Luna, M. Belge). [A4] ADAPTIVE(SKINS) (RatLab). [B1] THE AIR FLOW(ER) (Lift Architects). [B2] Pixel Skin (Orangevoid). [B3] Gill\_Project (J. Sandoval). [B4] Shutters A Permeable Surface (M. Coelho)

"The Gill Project" (Sandoval, 2012), (Figure 1-B3) consists of a rhomboidal opaque element that can move thanks to a SMA wire connected to the fixed part that is activated by current. This active approach allows a higher possibility of control, even if the variation of the openness factor is low. "Shutters: a permeable surface" (Coelho & Zigelbaum, 2011; Coelho & Maes, 2009), (Figure 1-B4) consists of a flexible opaque material that can change its openness factor thanks to the SMA integrated wire. The moveable shutters can assume all desired patterns, and their opening can be managed singularly. This allows the creation of many activation patterns in response to the users' requirements.

### 1.1.3 Systems Comparison

Fig. 2 presents a flexibility analysis of the shading control previously presented. By comparing the delta openness factor (variation in the percentage of the area between open and closed position) with the number of control activation points (modules per square metre), it is possible to identify the target design area with the optimum condition (high delta openness factor and high number of control points) of shading possibility and system user adaptability.

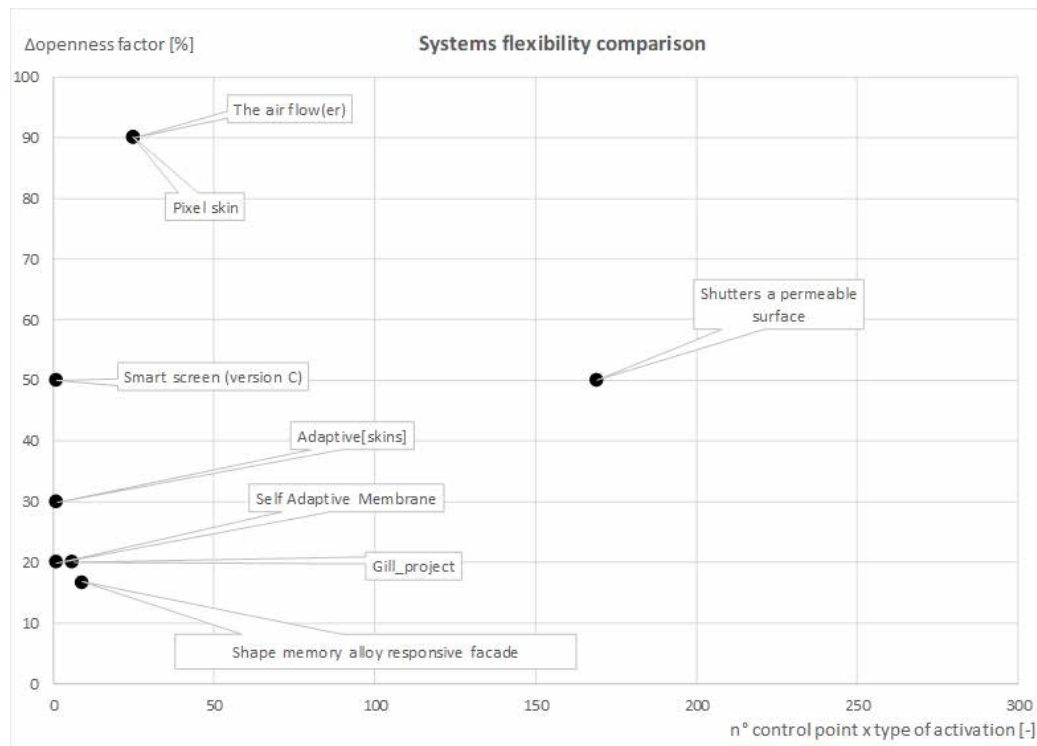


FIG. 2 Smart Shading Systems flexibility comparison

## 2 METHODOLOGY

### 2.1 SYSTEM DEVELOPMENT AND OPERATING PRINCIPLES

The shading system proposed is based on SMA springs that are activated passively. The implementation of a customised working principle allowed the optimisation of the alloy features and consequently of the shading system performance.

Fig. 3 presents the approach followed in order to design the shading system: the definition of the working principles and technology allowed to identify the preliminary information for daylighting properties, and therefore for daylighting simulations. Meanwhile, the technology has been continuously developed in order to optimise the alloy properties, making it more effective, with a detailed analysis of the moveable parts and their prototyping.

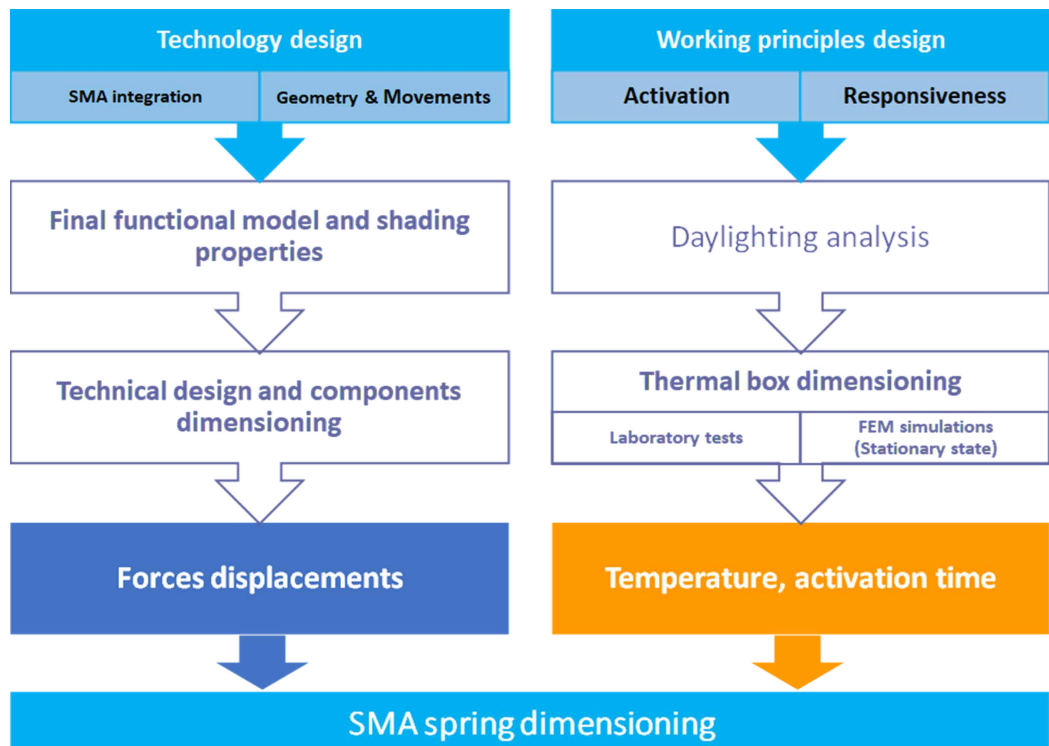


FIG. 3 Design approach description

### 2.1.1 Form Finding

The design flow started with the analysis of a cylindrical surface with top and bottom sides, which can rotate relative to each other, and the longitudinal fibres shaped around the lateral surface constrained to follow the rotation (and thus to twist). Such cylinders can be arranged parallel or orthogonal to the façade plane, and the rotation of one of the two sides (bottom or top) allows the shrinkage/elongation of the lateral surface to vary the openness factor of the shading system.

The considered arrangement was equal to a double-layer fabric. In fact, when the shadings are in the closed position and the cylinders are fully deployed, a mutual shading effect happens due to the overlap between the vertical fibres on the front and the backside of the cylinders.

A shading or privacy device comprising multiple cylinders with an axis orthogonal to the façade plane (Fig. 4, left) would allow for the local variation of the visual area, giving maximum flexibility to the users, and creating an efficient multi-zoning of the façade area: this effect, which resembles the behaviour of analogic camera shutters, could be exploited to provide effective shading to a façade, or to create visual transparency only in those areas where it is required. However, the geometrical constraints given by the thickness (height) of the cylinders, the required elongation ratio of the fibres comprising the surface of the cylinders, along with the relationship between twisting rotation and variation of visual area, were found to pose significant challenges in the development of this system.

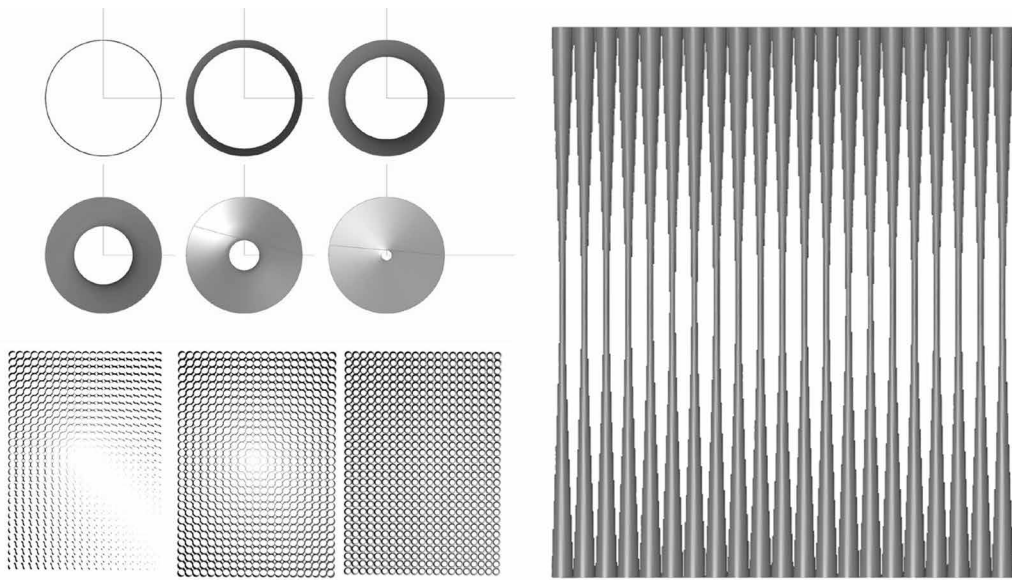


FIG. 4 [left] Cylinder's Horizontal arrangement alternative [right] Cylinder's Vertical arrangement alternative

In order to complete a full transition from transparent to fully opaque, the cylinders need to make a full 180-degree rotation, which with such proportions (e.g. with height equal to the diameter) would result in extreme elongation ratios. This magnitude of movement would be challenging to achieve with a variety of materials, and to be maintained over time, due to phenomena such as metal fatigue or creep (for polymers). To mitigate this phenomenon, cylinders would need to be taller; however, in the context of façade application, this goes against the principle of a compact façade build-up, and negates certain applications, such as inclusion within cavities of insulated glazed units. Finally, automation, transmission, and coordination of movements across an array of cylinders would be challenging, requiring several components to be connected across a single façade module: as the cylinders are perpendicular to the façade, those links or transmissions would be in sight, making a concealed mechanism harder to achieve.

Having observed the challenges of "square" cylinders, and the benefit in divorcing from small height-to-diameter ratios, slender cylinders were explored, specifically with a parallel arrangement compared to the façade (Fig. 4, right). It was found that, whilst slender cylinders limit the degree of control over the façade transparency, they require a much simpler mechanical system compared to short cylinders. A more extreme aspect ratio would also mean a much lower percentage of elongation of the fibres which, depending on the material of such elements, would also result in lower tension forces. With vertical cylinders, the variation from open to closed position places the transition zone (from open to closed) in the central part of the façade vision area, which is typically at head height on a full-height façade module; the rotating parts, instead, may be placed at the top and bottom of the panel, therefore sitting within the peripheral zone of the façade module. This allows the mechanical parts to be concealed in the panel's perimeter frame, enabling activation of multiple cylinders with a single actuator, hence reducing the complexity of the system.

Given the benefit of slender cylinders with the axis parallel to the façade plane, this solution was pursued; square, orthogonal cylinders were disregarded as they were deemed not viable in the context of mechanisation into a shading device. The slender cylinders were subject to a thorough system development process, which involved further optimisation to enhance their reliability and efficiency (Fig. 5).

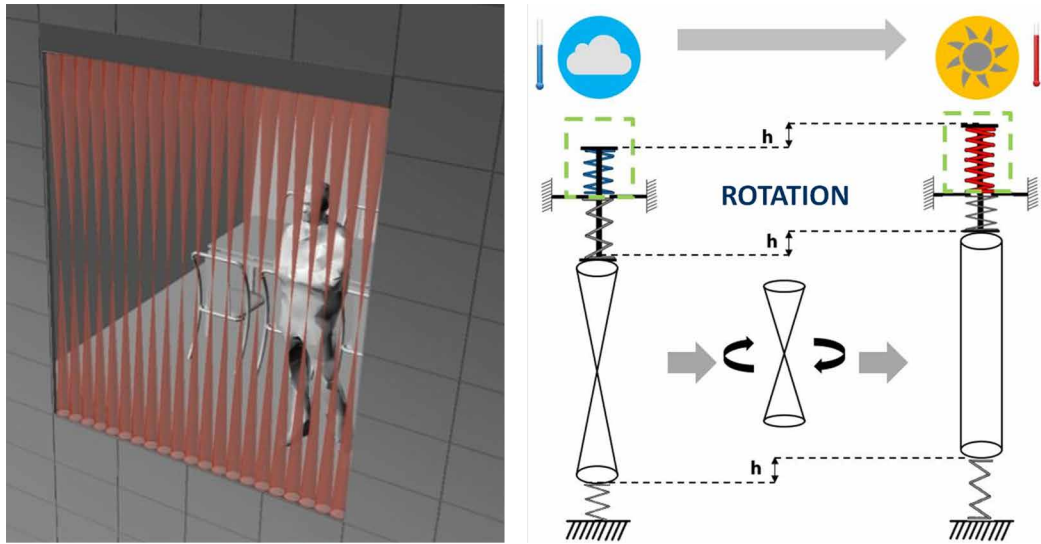


FIG. 5 [Left] System conceptual appearance. [right] Functional Model

## 2.1.2 Components Breakdown

This system comprises two main components:

- The thermal control box, where the SMA spring is placed;
- The twisting cylinders, which are the shading component of the system

The thermal box is the thermo-responsive environment, where the SMA component (in this case a spring) is thermally stressed by environmental stimuli (i.e. heat derived from incident solar radiation). As the SMA spring reaches the activation temperature, the shape memory effect takes place, modifying the shear modulus  $G$ , causing the tensile/compressive force of the spring to activate the shading device. With the solar radiation falling below a predefined threshold, the temperature progressively decreases, and the spring (coupled with the bias element) drives the system back to its initial configuration. Because of the inherent thermal inertia of the system, the deactivation temperature is not equal to the activation temperature, as the whole cycle is subject to a hysteresis phenomenon.

The key to unlocking the potential of this system is to calibrate the SMA activation temperature to match the activation (and deactivation) temperature for the system of the desired application. This can be done, to a limited extent, by choosing a SMA component with suitable chemical composition, since different SM alloys are characterised by different austenitic start temperatures. The optimal activation temperature, on the other hand, will depend on a number of factors, such as the context of application (solar orientation, climate, wind exposure, etc.), mode of activation (by solar radiation or by Joule effect with electrical current) and the overall thermal inertia of the system (insulation of the thermal box, colour, etc.).

The twisting cylinders are the visible part of the system that can have variable height and diameter depending on the requirement. These elements are characterised by two different configurations:

- “Closed”: when the top connection of the cylinder is up, the lateral surface of the cylinder is straight, and the entire visual area is shaded; this occurs when the SMA spring is above the switching temperature (activated);
- “Open”: when the top connection of the cylinder is down, the lateral surface of the cylinder has an hourglass shape. The visual open area is approximately 50%, and it is localised in the centre of a full-height glazing system, thus maximising views to the outside, which can enhance comfort parameters. This occurs when the SMA spring is below the switching temperature (not activated)

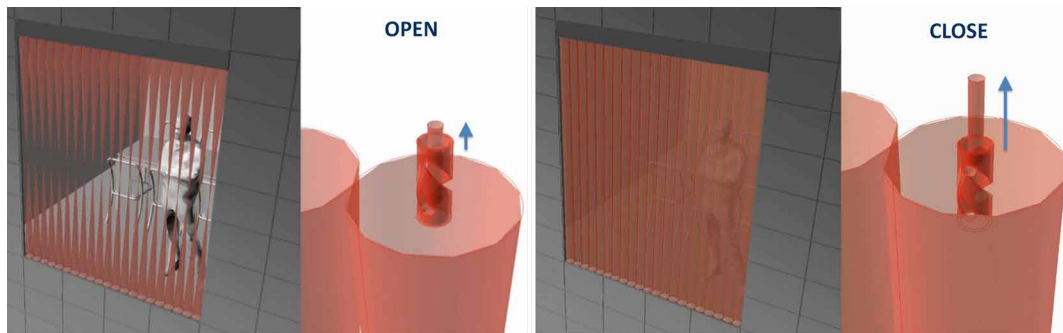


FIG. 6 System conceptual appearance in open and closed state. Focus on the axle movement

The twisting cylinders consist of three parts: top connection, shading element, and bottom connection. The top connection design is a critical part that integrates different components:

- A disk (Fig. 7, Detail 11), from which the shading component is hung, with a particular edge shape in order to fix the fabric/cords, and a tapered hollow cylinder (Fig. 7, Detail 12) in the middle with two opposite semi-helical slots that extend vertically as long as the stroke of the spring and 180° from edge to edge around the lateral surface of the tube. The inclination of the slots is designed to be 45°, so that the vertical pulling/compressing linear force can easily be transformed into a tangential force that generates a torque, thus giving rise to the rotation of the shading elements.
- An axle (Fig. 7, Detail 09) goes into the tapered hollow cylinder, and it has two horizontal pins on the external side that slide into the two semi-helical slots; the two cylinders slide one into the other, thus they are forced to relatively rotate. This axle is fixed to the upper frame from the bottom and, within this, we find the bias spring, which is a regular compressive spring capable of resetting the SMA spring as soon as the temperature drops below the activation temperature.
- A second hollow cylinder (Fig. 7, Detail 03) is fixed on the upper side of the fixed frame and contains the SMA compressive spring (Fig. 7, Detail 05), therefore it was designed to be the same length as the free length of the spring plus its typical (maximum) stroke. This cylinder has open lateral sides, to maximise heat exchange with the air contained inside the thermal box.
- An internal stick (Fig. 7, Detail 06) passes through the two springs and connects the top end of the SMA spring, which is a slider, with the bottom end of the tapered cylinder; therefore, when the SMA spring lifts the slider, the stick transmits the movement to the disk that goes up accordingly.

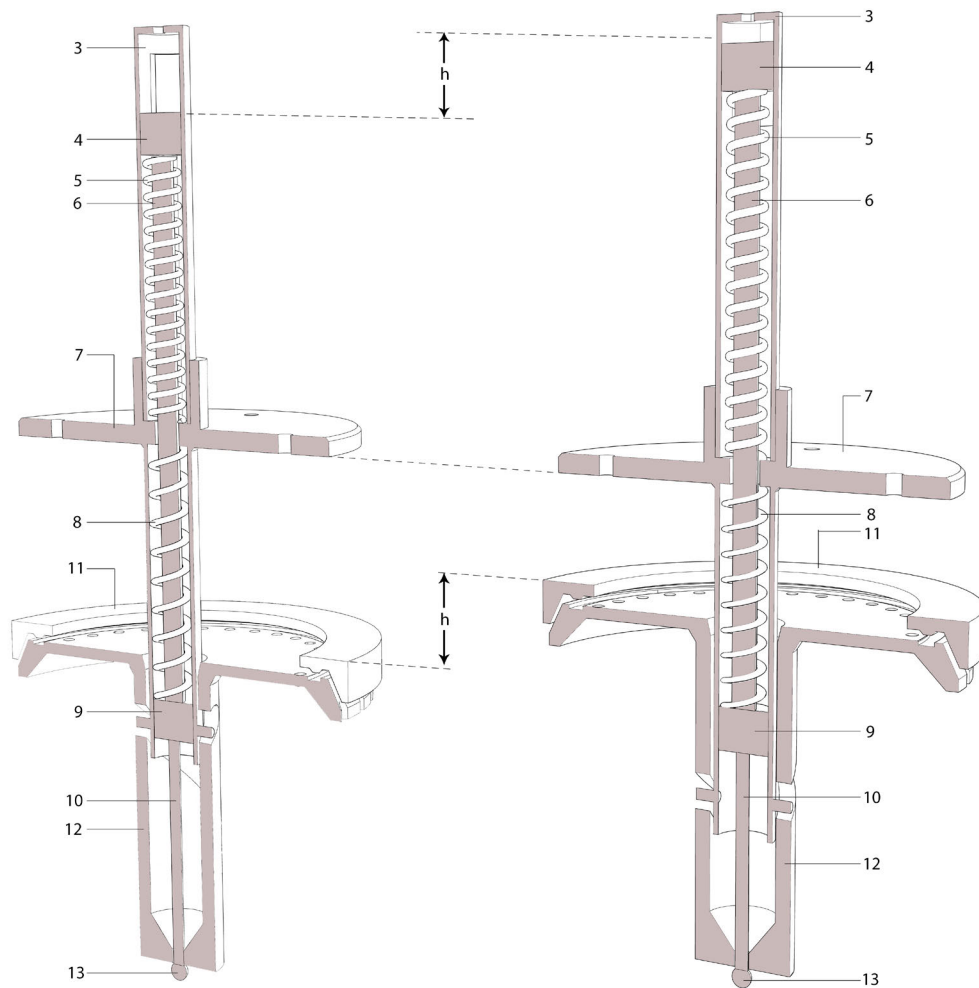


FIG. 7 The top connection Detail "Patent WP2018116102-A1"

The shading elements are the components that control solar radiation. The flexibility of the design system allows for the integration of different materials (textile, metal, plastic) with different geometry (strip, tube, cords, etc). Regarding the materiality of the cylinders, there are some restrictions on what concerns the geometry: cords and strips are better suited to accommodate the dynamic movement of the system, since they preserve a good appearance and do not ripple. This cannot be said for a continuous surface, such as a fabric: in fact, rippling can be observed in a fabric-type surface (by means of geometry modelling or even prototyping), when the cylinder transitions between its extreme states (cylinder and hourglass configuration), and this can be explained by purely comparing the surface area of the two configurations, which shrinks and causes the rippling phenomenon. Fatigue (or creep) over repeated cycles would affect the durability of the system, which in turn would have an impact on maintenance requirements.

The bottom connection is the element that keeps the shading elements in tension. Depending on the material, this disk can be fixed or moveable. The moveable configuration consists of a vertical movement (no rotation allowed) and a bias element that guarantees adequate positioning of the shading elements. 3D-printed prototypes of both top and bottom connections have also been produced (refer to Fig.10, right).

## 2.2 SMA SPRING DEFINITION

The compatible sub-components of the mechanism were designed considering transmitted force and displacement. The assumption was that the longitudinal fibres of the fabric (or the cords themselves) are of fixed length: this means that the cord length is constant, whereas the height of the cylinders varies with the rotation. Considering the longitudinal fibres inextensible is in order to avoid stress relaxation and stretching in the fibre or cords, to make the component durable. However, in order to set a full 180-degree rotation, the hollow cylinder with semi-helical slots is designed with a larger displacement, since the displacement and the radius are related.

In Fig. 8 (left and centre) a diagram of the system is presented to understand the relation between forces and displacement subsequently discussed.

Therefore, considering a commercial compressive SMA spring, a good compromise between cost and effectiveness was obtained selecting a spring with an average diameter that can fit a hollow cylinder with a mean radius,  $r$ , equal to 9 mm. Fig. 8 (right) describes in a diagram the relationship between the angle  $\beta$  and the rate of change of the forces required and displacements obtained.

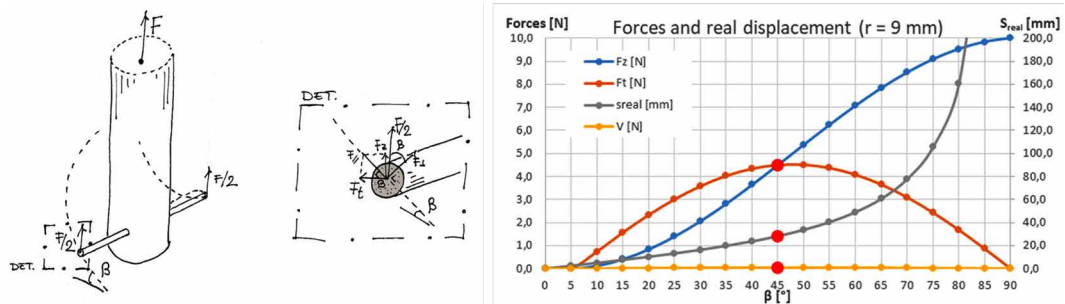


FIG. 8 Force, Displacements, and Temperatures of the compressive SMA spring. Tangential component of the forces ( $f_t$ ), tangential force ( $V$ ), real displacement ( $s_{real}$ ), Vertical component of the forces ( $F_z$ )

The force is transmitted through this component, and there is a precise rate between radius, spring pulling force and resultant vertical and torque force, due to friction and vectors components of forces.  $\beta$  is the slope angle used to split the forces over the axle in different tangential components, moreover, the higher the inclination of the slots ( $\beta$ ), the more pulling force is transmitted from the spring to the cylinder; however, the higher this angle, the higher the real displacement, so the stroke of the spring should be higher.

For a balance point of  $\beta=45^\circ$  the selected compressive SMA spring is compliant with the requirement in terms of force and displacement only within a range between  $50^\circ\text{C}$  and  $55^\circ\text{C}$ .

### 3 SIMULATIONS AND EXPERIMENT

The design workflow for the thermal control box consisted of a first phase of solar and thermal analysis, which linked a range of activation temperatures to levels of incident solar radiation, with considerations given to frequency of activation and the responsiveness of the system over the course of a year. This phase was followed by physical testing, where a prototype was tested by measuring internal temperatures reached inside a thermal box subject to pre-defined radiation levels given by an artificial source.

#### 3.1 SOLAR AND THERMAL ANALYSIS

The purpose of the solar and thermal analysis is to link temperatures reached inside the thermal box with incident solar radiation. Specifically, the aim of this analysis is to:

- Define the optimal activation temperature of the thermosensitive element (SMA Spring), contained inside the thermal box, which activates the transmission of the system and allows the movement of the shading element.
- Verify the frequency of occurrence of implementation in an annual application scenario, and to verify if the activation of the system is mainly due to combined optimal values of irradiance and external air temperature.
- Maximise the number of activation occurrences due to the incident solar radiation, and for the months (or hours) of the year, during which solar control is needed mainly to reduce primary energy for cooling (summer scenario), or to optimise daylighting (winter scenario).

Due to the significant number of variables (external temperatures, irradiance, wind, orientation, etc.), which govern the functioning of the thermal box, the solar and thermal analysis was carried out considering a specific case study, rather than a generalised scenario. The same workflow may be followed for other contexts. The selected case study comprised a thermal box located in Milan (Italy 45°28'38"28 N, 09°10'53"40 E), arranged in vertical position, and south-oriented. A realistic system was modelled, by defining a thermal box (with its own boundaries), as described in the previous paragraphs. The outer surfaces of the thermal box are thermally insulated with 3 cm of thermal insulation, except for the exposed face that consists of a glazed plane able to allow the passage of incident solar radiation. The internal surface of the thermal box, which directly receives the solar radiation, has an absorption coefficient of 0.9 and a low-emissivity value equal to 0.4. No mechanical ventilation is assumed within the box, but an infiltration rate equal to 1 ACH is considered, to allow for ventilation and imperfections in the sealing of the joints. The convective heat-exchange coefficients in the proximity of the external surfaces of the thermal box were calculated using the hourly average value of the wind speed for a north-to-south wind direction.

The summer discomfort variables considered as a reference scenario were an outdoor air temperature value of 25°C and an irradiance value on vertical surfaces of 300 W/m<sup>2</sup>.

The SMA actuator is required to self-activate with direct solar radiation on the façade surface > 300 W/m<sup>2</sup>. Whenever this value goes below this threshold, the transition temperature in the thermal box goes down accordingly and the shadings open up. For this assessment, the amount of time in one year (in hours, days, months) when the Incident solar radiation (ISR) on vertical surfaces is above 300 W/m<sup>2</sup> was calculated.

Fig. 9 shows a carpet plot of the annual distribution of the irradiance over the external surface of the thermal box. The vertical axis shows the hours in a day, whereas the horizontal axis shows the days and months over a year; the hours of the year when the air temperature is higher than 25°C are shown by means of regions bound by continuous black line.

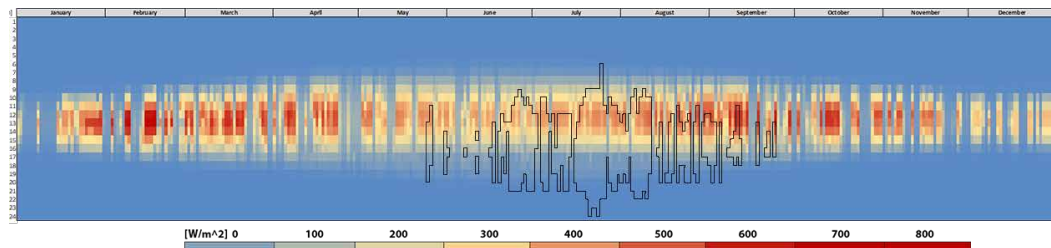


FIG. 9 Annual distribution of irradiance on a vertical unshaded surface facing south, for Milan (Italy), with hours on the vertical axis and days in one year on the horizontal axis

In reality, ISR values are probabilistic estimates, since they do not solely depend on sun path, but they are also influenced by weather conditions and urban context (mutual shadings due to geometry and context, building reflections, etc.). Milan (Italy) was considered as a case-study weather location for the test. ISR values on vertical surfaces were derived for the main orientations (east-south-west) and an in-depth analysis was done only for some representative days during the year. To predict the number of activation instances of the system, an assessment of the number of hours for each month in which ISR is above a fixed threshold (from 200 to 700 W/m<sup>2</sup>) was carried out.

### 3.2 THERMAL BOX TEST AND EXPERIMENTAL SET-UP

The analysis presented in Chapter 3.1 formed the basis on which to predict the range of ISR on a vertical surface, as well as the variability of the related outside air temperature for a selected weather location.

Considering these boundary conditions, preliminary tests of the geometry and material properties of the thermal box were performed, using simulation FEM (Finite Elements Method) software: Physibel Voltra for 3D dynamic simulation; Physibel Bisco for 2D static simulation. The limit of static thermal analyses lies in its methodology, which presents results in stationary conditions, thus mainly highlighting the peak conditions that can be reached inside the thermal box; on the other hand, dynamic simulations gave an effective prediction of the time shift and delay in temperature increase and decrease in accordance with ISR. The intermediate simulation steps, not presented in this paper, were useful to test different geometrical variants of the box, as well as the optical properties of the materials, or the expected insulation and air infiltration levels.

The analysis results were then processed, to inform the final characteristics of the responsive thermal environment (i.e. the thermal box) to host temperature-specific SMA components, with a defined austenitic start temperature (As).

Full-scale thermal box models (Fig. 10, left) were then created and tested under laboratory conditions, which were consistent with the boundary conditions set within the simulation. As a result of this validation and benchmark procedure, the dynamic behaviour of each type of thermal box was evaluated, measuring the ramps of internal temperature growth over time as a function of the ISR, as well as the temperature decrease once the radiation source was removed.

Numerous thermal box constructions were built, each featuring different characteristics: presence/absence of thermal insulation around the box (3 cm); internal surface being reflective or black painted. Each thermal box was characterised by the following dimensions: 75x110x200 mm and was subject to the same range of temperatures and radiations.

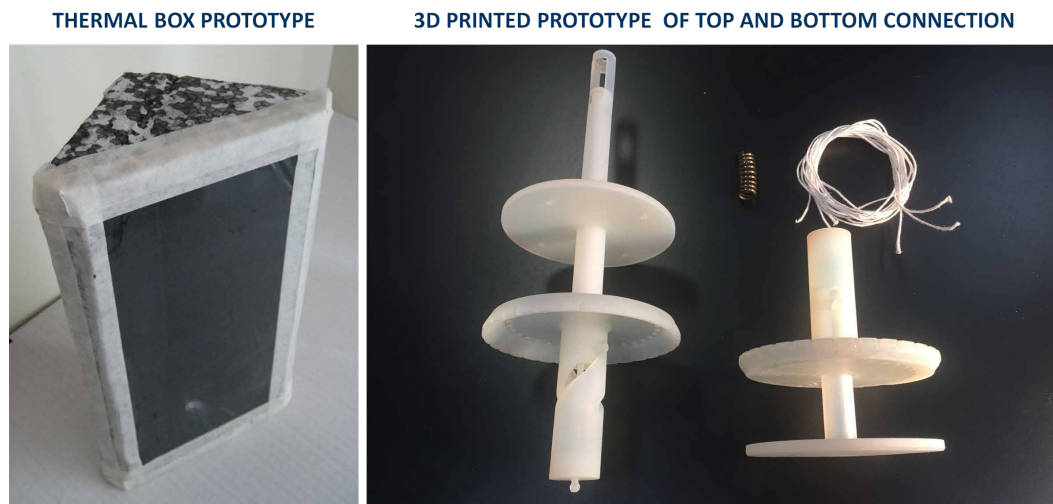


FIG. 10 Prototype of the thermal box, with external insulation and internal black paint (left) and 3D-printed prototype of the top and bottom connections (right)

The prototypes were subjected to radiation with an uncontrolled wavelength spectrum but with a set power. The experimental set-up is presented in Fig. 11.

The standard radiation level was input by means of four light bulbs, each characterised by a power  $P = 105 \text{ W}$ . The light bulbs produced a light distribution that covers the thermal box in a quasi-homogeneous fashion. The thermal box was placed on a wooden board with a rectangular hole so that the lateral sides of the box were not subject to radiation. By vertically sliding the board on different steps, the radiation level at each height was measured by a radiometer. The shorter the distance between the prototype and the lamps, the higher the radiation levels recorded. The relation between the distance and the measured radiation level was then obtained through different attempts. In fact, indoor thermal box temperature data were collected for an imposed radiation range of  $250$  to  $650 \text{ W/m}^2$ , with intermediate steps of  $300$ ,  $350$ ,  $450$  and  $550 \text{ W/m}^2$ . These were deemed suitable considering a typical application (considering the application on a vertical façade, situated in a Mediterranean region).

Each sample was equipped with 2 thermal sensors (thermocouples), glued with conductive adhesive paste on the internal surfaces of the box, one on the top side and another on the bottom side, and all the holes of the thermal box prototype were sealed to avoid air leakage.

The internal temperature was only due to surface temperatures, but the heat exchange mode influenced how fast the internal temperature increases and decreases.

The light bulbs were kept until the two measured surface temperatures stabilises, which means that from a transient scenario, a quasi-stationary heat flow was achieved, and temperature is asymptotic to a value (i.e. they can be considered stationary). In fact, temperature could rise more if the bulbs are left on; however, in reality, a higher temperature rise is balanced by external factors, such as wind and temporary external shading, therefore it was considered conservatively that the maximum reachable temperature should be estimated without letting it rise in a situation that is too constrained.

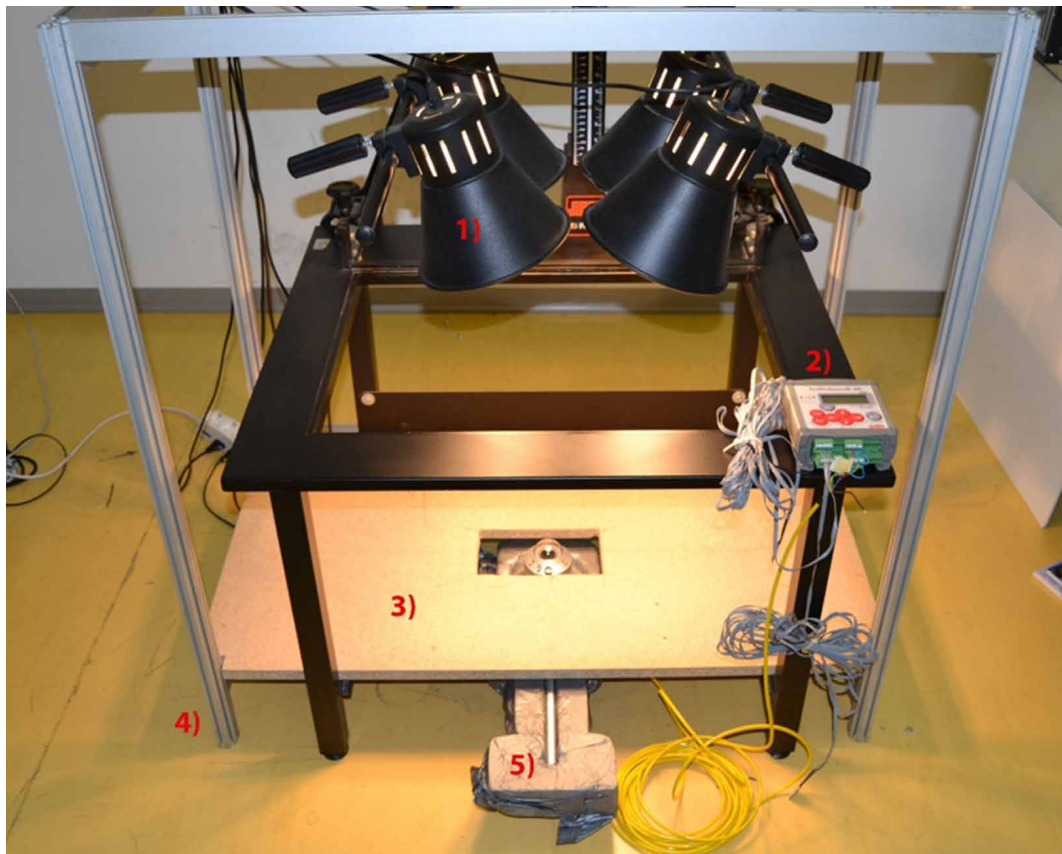


FIG. 11 Test bench: [1] Light bulbs, [2] Data Logger, [3] Timber board, [4] Reference frame [5] pyranometer

Temperatures measured by the thermocouples were registered by a data logger, which measures with a time step of 10 seconds. Therefore, every ten seconds, maximum temperature, minimum temperature, and average temperature are determined and recorded.

## 4 RESULTS

The experimental findings are summarised within this section. Firstly, the correlation between variable incident solar radiation (ISR) and the temperature inside the thermal box ( $T_{\text{box}}$ ) is shown. A further explanation of the results, in the context of variable external air temperatures ( $T_{\text{air}}$ ) and ISR levels, is given in Section 4.2. Finally, considerations on the target activation temperature ( $T_{\text{SM}}$ ) for a thermal box hosting a SMA spring actuator are presented in Section 4.3.

### 4.1 CORRELATION BETWEEN ISR AND $T_{\text{BOX}}$

The system was designed to reach a target activation temperature during a time span lower than 50 minutes and under a minimum level of ISR identified in  $300 \text{ W/m}^2$ . In Fig. 12 an explanatory diagram of temperature distribution is presented for a higher amount of available irradiance equal to  $550 \text{ W/m}^2$ . The slope describing the increase of the temperature ramp is therefore related to the amount of available ISR. The higher the amount of ISR, the shorter the time interval required to reach the target temperature. In the case of permanent solar radiation level  $T_{\text{SM}}$  increases until a stationary, balanced temperature (approximated to be equal to a quasi steady-state condition) is reached. Additionally, in this case, the maximum asymptotic temperature reached is related to the value of the imposed radiation and the balance within the thermal losses of the thermal box with the surroundings. When the radiation source is removed, the system returns to the initial conditions in half of the time, on average, that was necessary to reach the maximum registered temperature, suggesting a faster heat dissipation in comparison to the heat build-up process.

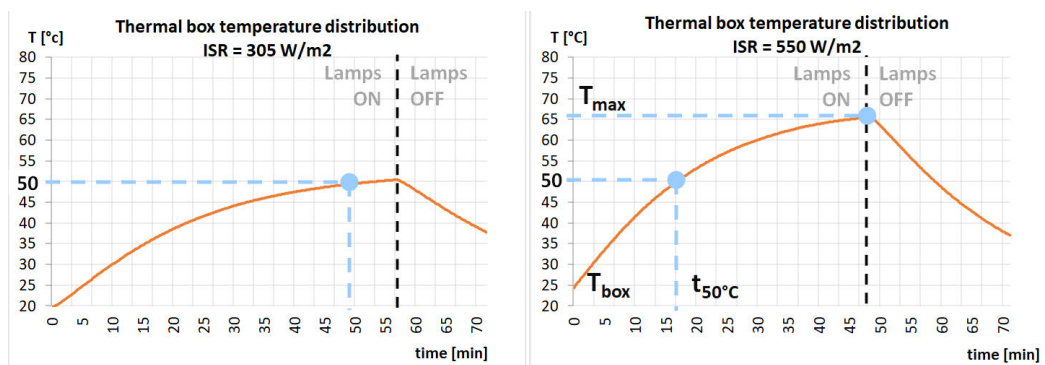


FIG. 12 Relation between temperature increase in the thermal box and exposure time to a radiant source at  $305 \text{ W/m}^2$  (left) and  $550 \text{ W/m}^2$  (right)

It is therefore possible to assume that with the same air temperature of the surrounding environment as the value of ISR incident on the surface increases, the time for which the activation of the actuator system takes place is drastically reduced. This phenomenon, however, leads to an increase in the peak temperature reached inside the thermal box, compared to the values obtained with lower ISR. This also leads to an increase in the time for effective cooling (phase delay) and return to optimal neutral, pre-activation temperature conditions.

## 4.2 DEFINITION OF $T_{SM}$

On any orientation, the hours of solar radiation higher than  $200 \text{ W/m}^2$  are lower than 30% of the total hours of the whole day (night included), which is approximately 50% of the total hours of daylight on a summer's day. The shadings are designed to self-activate when direct solar radiation on the façade surface  $> 300 \text{ W/m}^2$ ; however, while the ISR is below  $300 \text{ W/m}^2$  but still above  $200 \text{ W/m}^2$ , the internal temperature of the black box might still be above the activation threshold, avoiding the deployment of shading. The duration of the transition period was then estimated for different orientations, and it was found to be lower than one hour most of the time, which is the minimum time required to reach transition temperature. Fig. 13, presented as an illustrative example of the possible path, shows an explanatory result for a single day analysis centered on April 26<sup>th</sup> for a south-oriented façade. If hourly average values of ISR for temperature increase are considered, it is possible to observe that threshold values for ISR are sufficient to allow the system to be activated effectively in a significant range around the central hours of the day, enabling the activation of the shading system for the hours that are considered critical during the day. In addition, there are some low peaks (1 pm), probably due to temporary cloudy weather, during which, even if solar radiation is below  $300 \text{ W/m}^2$ , shading devices are still activated ("closed").

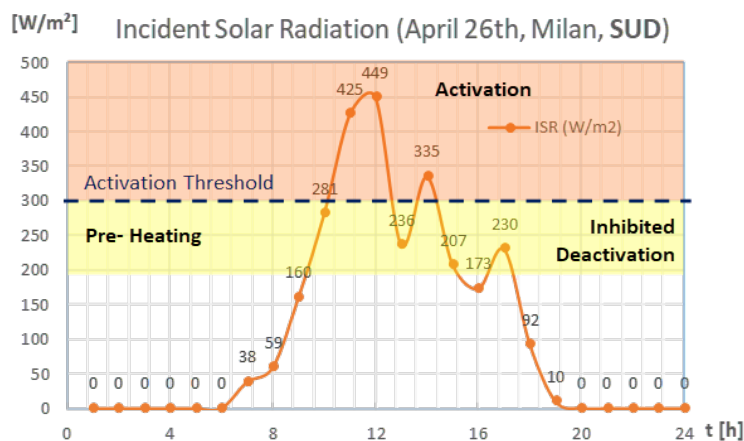


FIG. 13 Radiation Path and activation profile of the system

Whenever the temperature in the thermal box remains slightly above the activation threshold, the system is in an intermediate configuration between "open" and "closed". Whenever an external factor, such as a sudden change in ISR prevents the activation temperature from being achieved (e.g. clouds, obstructions, etc.), the shading device would remain in its intermediate position, waiting for the temperature to rise (when the shading would close) or to go down (when the shading would open). In either case, even when the shadings are not fully closed, they contribute somehow to lower the g-value of the façade system.

In a realistic scenario, the internal temperature is influenced by other factors, and the most important of those, after solar radiation, is external air temperature. When direct solar radiation hits the façade, it is expected that the air temperature inside the box is:

- higher than summer exterior temperature, so that the SMA activation occurs during direct solar presence, and not also during normal hot days with an overcast sky;
- equal to SMA activation temperature during the winter considering direct solar radiation exposition.

With regard to the semi-stationary model discussed in Section 3.1, it is possible to select for example a characteristic day (July 18<sup>th</sup>) on which the contribution of the incident solar irradiance is strongly effective in raising the temperature inside the Thermal Box ( $T_{box}$ ), reaching a maximum peak temperature of almost 70°C. Fig. 14 shows that, in accordance with the selected thresholds, an external air temperature of 25°C combined with an irradiance value equal to or higher than 300 W/m<sup>2</sup> can lead to temperature values inside the thermal box of almost 50°C. Therefore, a preliminary assessment may be made considering 50°C as activation temperature ( $T_{SM}$ ) of the SMA spring, in order to comply with the pre-defined limits as summer thermal comfort descriptors.

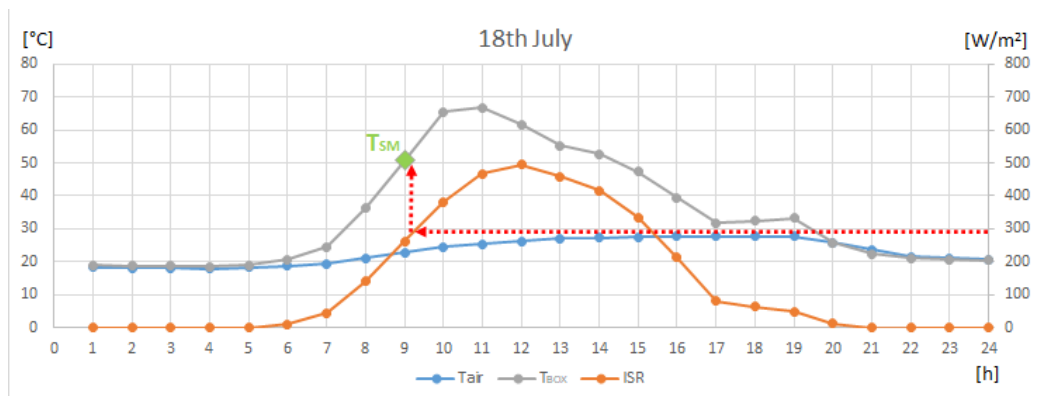


FIG. 14 Effect of solar irradiance on the temperature rise of the thermal box and definition of the activation threshold of the SMA spring element)

#### 4.3 CONSIDERATIONS ON THE ACTIVATION THRESHOLD

The question that arises spontaneously, however, and to which it is necessary to answer is how much the choice of such an activation threshold temperature for the SMA spring is optimal in optimising the passive adaptive behaviour of the shading system.

The carpet diagram presented in Fig. 15 shows the activation profile of the shading system (hours in red) for an activation temperature inside the thermal box ( $T_{SM}$ ) of 50°C. A similar activation profile is reported in Fig. 16 for  $T_{SM} = 35^\circ\text{C}$ . It is immediately understood that, as the set-point temperature decreases, there is an increase in the hours in which this activation process would take place. The increase in terms of system working hours is flat and over both winter and summer periods. However, a conservative approach, which could lead to a low set-point temperature, is likely to significantly increase the number of hours of operation, resulting in an almost constant (and potentially unwanted) activation of the system. The choice, instead, of a higher set-up activation temperature, allows the events to be located only in correspondence with the most well known summer critical periods, by means of effectively controlling and reducing the incident solar radiation over the glazed surfaces. On the other hand, during the winter hours, in which the solar radiation on vertical surfaces is severe, the system can be effective in mitigating daylight issues due to direct glare phenomena.

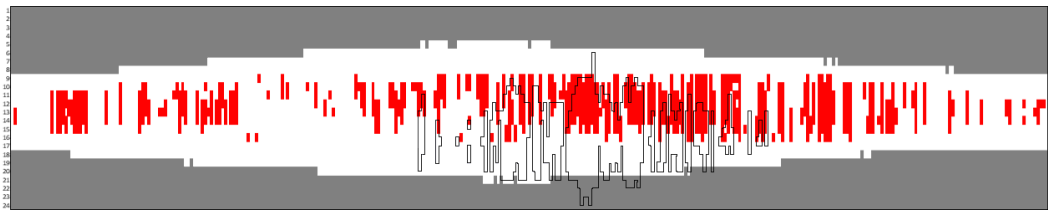


FIG. 15 Annual distribution diagram of system activation hours in SMA depending on SMA spring activation temperatures (TSM). In red the activation hours, in white the remaining daytime hours, and in grey the night-time hours. Distribution for TSM = 50°C

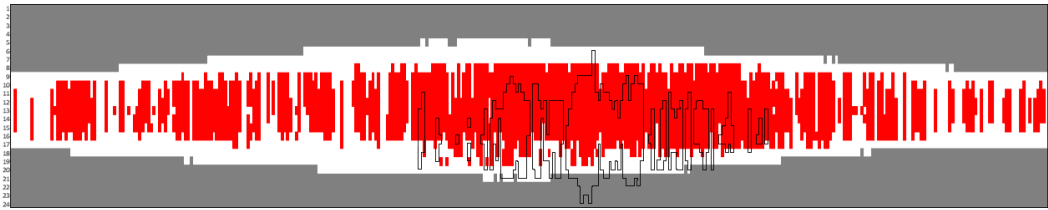


FIG. 16 Annual distribution diagram of system activation hours in SMA depending on SMA spring activation temperatures (TSM). In red the activation hours, in white the remaining daytime hours, and in grey the night-time hours. Distribution for TSM = 35°C

It is worth noting that, based on this case study, activation temperatures ( $T_{SM}$ ) below 50°C are not desirable, as they do not comply with the requirements set as part as the SMA spring definition process (refer to Chapter 2.2). Furthermore, considering standard classes of SMA springs, those with an activation temperature of 50°C or higher are typically characterised by more favourable stresses and elongation ratios (Otsuka & Ren, 2005). Finally, as explained above, the temperature inside the thermal box ( $T_{box}$ ) is also influenced by the external air temperature ( $T_{air}$ ); therefore, a higher  $T_{SM}$  will limit the influence of  $T_{air}$  on the activation of the shading.

## 5 CONCLUSIONS

The search for complex shapes and façade kinematics is associated with the concept of responsive building, characterised by complex façade systems using traditional sensor-motor actuation system. Within this context, the authors aimed to describe a workflow to provide an alternative actuation mechanism and a shading geometry, which are compatible with an adaptive passive activation process. The development of the actuators was focussed on SMA materials which could be activated by a localised temperature variation, induced by an external stimulus.

Due to the high number of varying parameters within the simulation and experiments, it was necessary to narrow down the context of the application into a specific case study, to accurately model and assess the functioning and efficacy of the system.

As outlined within Chapter 3, the context considered was a vertical façade, south-oriented, within a building situated in the Mediterranean region, specifically sourcing the environmental data (temperature, solar radiation) from Milan (Italy). This specific location was chosen as it is familiar to the authors, as well as being a good example of a humid subtropical climate (Cfa, according to the Köppen-Geiger classification), with relatively moderate external air temperatures and high levels of incident solar radiation. Within this context, a set of external air temperatures, solar irradiance values and hours of permanence of such conditions were identified, and a SMA component was tailored for the optimised functioning of the shading device.

Once the geometry of the actuator and its required force and type of displacement was defined, the analysis delved into the relationship between the optimal activation temperature and the contextual application, i.e. the expected weather scenario and its climatic variability.

It is noted that, within the commercially available SMA components, the industry is capable of manufacturing SMA springs with a wide range of characteristics: for example, given a required displacement and forces, SMA springs can be developed with different activation temperatures, depending on the desired final requirements. This is achieved by tweaking the manufacturing process, geometrical features and/or alloy composition.

The choice of enclosing the actuation system inside a thermal box allows the activation temperature of the system to be characterised, whilst maximising the effect of the incident solar radiation (ISR) for its operation. It also improves the reactivity of the system actuation by intervening on the rate of change of the indoor temperatures, thus extending the frequency of activation cycles. The temperature inside the thermal box ( $T_{\text{box}}$ ) becomes a representative index in defining the activation (and deactivation) thresholds of the system: determining the optimal value for  $T_{\text{box}}$  means capturing the effects of a change in air temperature ( $T_{\text{air}}$ ) as well as the effect of incident solar radiation (ISR) over a façade surface.

Once the maximum ISR set-point value for the desired activation was defined, it was possible to estimate the frequency distribution of  $T_{\text{box}}$  in accordance with the other outdoor weather variables.

From the simulations and experiments carried out by the authors, it is possible to conclude that:

- By means of manipulating the properties of the SMA spring and/or the thermal box, it is possible to programme the activation of these systems in accordance with a set threshold value for ISR, thus allowing activation in different seasons. The number of hours during which the system is capable of matching the imposed set point conditions also depends on the SMA activation temperature ( $T_{SM}$ ): the lower  $T_{SM}$ , the more sensitive the system becomes, resulting in higher frequency of activation, which may cause the system to activate most of the time during the year.
- The system does not adapt to all climates and orientations, and it requires a detailed design for each selected scenario. The authors defined a methodology to determine the number of activation occurrences, and therefore the optimal activation temperature of the SMA component given a specific context.
- The effect of  $T_{air}$  can interfere with ISR in raising (or lowering) the value of  $T_{box}$  above (or below) the  $T_{SM}$  threshold. This is particularly critical in those contexts that are characterised by high external temperatures and/or low solar irradiance. Such conditions could be an east-oriented SMA activated shading during a sunny afternoon, or any application during a hot but cloudy day. In this respect, manual override and/or BMS (building management system) may be considered to regulate unwanted or missed activation of the shading system.
- A static thermal simulation is deemed accurate enough to predict the maximum value for  $T_{box}$  reached by the system, as well as to define the geometry of the thermal box, its radiative properties, and its degree of thermal insulation.
- The field measurement on a physical prototype, in conjunction with dynamic analyses, is useful to verify the variation rate over time (both increase and decrease) of  $T_{box}$  and  $T_{air}$ , by capturing the effect of significant site-related variables (wind speed, cast shading, etc.) besides statistical data for ISR.
- Improving the thermal insulation of the thermal box speeds up the activation process, enhancing the temperature build-up to critical values of  $T_{box}$ ; at the same time, however, excessive values of  $T_{box}$ , if not compensated by natural or forced ventilation within the cavity, may result in prolonged activation (due to increased thermal inertia of the system), even when the system is no longer subject to target levels of ISR.
- Regarding the materiality of the twisting cylinders, the elasticity (or stiffness) of the longitudinal fibres will affect the required strength of the SMA spring, which would have an impact on the required activation stimulus (e.g. the activation temperature).

### Acknowledgements

We gratefully thank the members of SEEDlab.abc @Politecnico di Milano ([www.seed.polimi.it](http://www.seed.polimi.it)) for their support during the measurement activities and all the suggestions provided during the writing of the paper. We also thank Pa&Co architecture (<http://pacoarchitecture.com/>) for their support during the prototyping processes.

## References

- Coelho, M., & Maes, M. (2009). Shutters : A Permeable Surface for Environmental Control and Communication. *Proceedings of Tangible and Embedded Interaction (TEI '09)*, 13-18. <https://doi.org/10.1145/1517664.1517671>
- Coelho, M., & Zigelbaum, J. (2011). Shape-changing interfaces. *Personal and Ubiquitous Computing*, 15, 161-173. <https://doi.org/10.1007/s00779-010-0311-y>
- Decker, M., & Yeadon, P. (2010). SmartScreen: Controlling Solar Heat Gain with Shape Memory Systems. Decker Yeadon LLC. <https://archinect.com/news/article/88265/smart-materials-move-smartscreen>
- Fiorito, F., Sauchelli, M., Arroyo, D., Pesenti, M., Imperadori, M., Masera, G., & Ranzi, G. (2016). Shape Morphing Solar Shadings: A Review. *Renewable and Sustainable Energy Reviews*, 55, 863-884. <https://doi.org/10.1016/j.rser.2015.10.086>
- Gonzalez, N. (2015). Self-Adaptive Membrane. Retrieved from [http://www.iaacblog.com/programs/self-adaptive-membrane\\_-\\_a-passive-kinetic-system/](http://www.iaacblog.com/programs/self-adaptive-membrane_-_a-passive-kinetic-system/).
- Heschong, L. (2002). Daylighting and Human Performance. *ASHRAE Journal*, 44(6), 65-67.
- LIFT Architects (2015). The air flower. Retrieved from <http://www.liftarchitects.com/air-flower>.
- Luna, I. (2014). Shape Memory Alloy responsive façade. Retrieved from <http://www.behance.net/gallery/SMAShape-Memory-Alloy/10797251>.
- Mainini, A.G., Speroni, A., & Vercesi, L. (2018). System for shielding and controlling sun light or the light flow coming from artificial sources, especially for application to buildings. Patent n° WO2018116102-A1.
- Mazzucchelli, E. S., Romano, R., Aelenei, L., & Gomes, M.G. (2018). *Passive Adaptive Façades – Examples from COST TU1403 Working Group 1*. Delft, NL: TU Delft Open.
- Menzies, G. F., & Wherrett, J. R. (2005). Windows in the workplace: examining issues of environmental sustainability and occupant comfort in the selection of multi-glazed windows. *Energy and Buildings*, 37(6), 623-630. <https://doi.org/10.1016/j.enbuild.2004.09.012>
- Nielsen, M. V., Svendsen, S., & Jensen, L. B. (2011). Quantifying the potential of automated dynamic solar shading in office buildings through integrated simulations of energy and daylight. *Solar Energy*, 85(5), 757-768. <https://doi.org/10.1016/j.solener.2011.01.010>
- Orangevoid (2007). Pixel skin interactive façade. Retrieved from <http://fachadasmediales.blogspot.com/2007/12/pixel-skin-interactive-façade.html>
- Otsuka, K., & Ren, X. (2005). Physical Metallurgy of Ti-Ni-Based Shape Memory Alloys. *Progress in Materials Science*, 50(5), 511-678. <https://doi.org/10.1016/j.pmatsci.2004.10.001>
- Palmero-Marrero, A. I., & Oliveira, A. C. (2010). Effect of louver shading devices on building energy requirements. *Applied Energy*, 87(6), 2040-2049. <https://doi.org/10.1016/j.apenergy.2009.11.020>
- Sandoval, J. (2012). Gill\_Project performance. Retrieved from [http://www.youtube.com/watch?v=-X\\_KxijpJT0](http://www.youtube.com/watch?v=-X_KxijpJT0).
- Tzempelikos, A., & Athienitis, A. K. (2007). The impact of shading design and control on building cooling and lighting demand. *Solar Energy*, vol. 81(3), 369-382. <https://doi.org/10.1016/j.solener.2006.06.015>
- Verma, S. (2016). Adaptive Skin. Retrieved from <http://www.designboom.com/project/adaptive-skins-2/>.
- Wang, F., Pichatwatana, K., Roaf, S., Zhao, L. Zhu, Z., & Li, J. (2014). Developing a weather responsive internal shading system for atrium spaces of a commercial building in tropical climates. *Building and Environment*, 71, 259-274. <https://doi.org/10.1016/j.buildenv.2013.10.003>

# Small-scale Field Study of Window Films' Impact on Daylight Availability under Clear Sky Conditions

Júlia Pereira<sup>1\*</sup>, M. Glória Gomes<sup>1</sup>, A. Moret Rodrigues<sup>1</sup>, Henriqueta Teixeira<sup>1</sup>, Manuela Almeida<sup>2</sup>

\* Corresponding author

1 CERIS, Department of Civil Engineering, Architecture and Georresources (DECivil), Instituto Superior Técnico, Universidade de Lisboa, Lisbon, Portugal, julia.pereira@tecnico.ulisboa.pt

2 CTAC, Department of Civil Engineering (DEC), Escola de Engenharia da Universidade do Minho, Campus de Azurém, Guimarães, Portugal

## Abstract

*Daylight illuminance levels and their spatial distribution are important design elements to achieve indoor visual comfort conditions and sustainability in buildings during the operation stage. While a proper daylighting scheme increases the efficiency of the building, the excessive use of glazed surfaces can contribute to thermal and visual discomfort, hence increasing the cooling demand and use of artificial lighting. Solar control film (SCF) is a self-adhesive thin film that can be applied on glazing systems of existing buildings for retrofitting purposes to modify thermal and optical properties of the glass substrate. This paper analyses experimentally the impact of single glazing with different SCFs on the indoor illuminance levels and respective distribution on horizontal work plane by comparing the measured absolute values and the useful daylight illuminance metric. Field experiments using a small scale model with the glazing oriented to the south, in Lisbon, were performed for a 6 mm clear glass and four different SCFs applied on the external surface of the glass, under clear sky conditions during summer and winter solstice at 9h00, 12h00, and 15h00. The results show that all SCFs reduced the indoor illuminance, which demonstrate their potential for glazing refurbishment when indoor visual discomfort occurs in buildings.*

## Keywords

*Daylighting, glazing system, window films, visual comfort, scale-model*

DOI 10.7480/jfde.2020.1.4785

# 1 INTRODUCTION

Daylighting has played an essential role in the history and evolution of architecture. While the lack of natural light is known to cause negative effects on human health and mood (Potočnik & Košir, 2019), an appropriate strategy between lighting design and building project can improve the visual comfort and indoor environmental quality and the energy efficiency through the optimisation of artificial lighting, cooling, and heating energy needs (Aghemo, Pellegrino & Lo Verso, 2008; Cruz, Pereira, Gomes & Kong, 2019). Klepeis et al. (2001) showed that people spent more than 85% of their time in enclosed buildings and that daylighting is a fundamental functioning resource to be taken into account in buildings.

Computer simulations and scale models are two different approaches that can be used to accurately tackle daylighting systems in buildings exposed to lighting conditions. Both approaches can be evaluated under real sun and sky conditions or under artificial sun and sky conditions (Aghemo, Pellegrino, & Lo Verso, 2008). Software-based approaches broadened conventional practices of how daylight modelling was being performed. In the early years, this type of analysis was very time-consuming, computationally demanding, and not easy to handle. Faced with the emergence of computational modelling based on the mastery of physics involved, but not yet fully experimentally tested, building designers initially showed some reservations in integrating into their practices tools that did not allow the use and modelling by hand of the real materials involved in the lighting study to the extent that scale models did (Aghemo, Pellegrino, & Lo Verso, 2008; Ayoub, 2020). Nowadays, with higher computer power and more advanced simulation tools through the evolution of specialised hardware and development of complex algorithms (Reinhart & Fitz, 2006; Ayoub, 2020), the use of computer modelling to predict illuminance levels in the early stages of the building design has gained attention from professionals in the building sector. Different methodologies and tools to predict daylight behaviour in indoor environments have emerged, supported by sophisticated light transport algorithms that allow more accurate results within acceptable timeframes and the possibility to optimise the design of simple or complex design façades in order to promote the visual comfort and the energy efficiency of the building.

The use of scale models is widely accepted as an adequate method for daylight assessment of indoor environments of buildings (Boccia & Zazzini, 2015). While this method allows the daylight performance to be predicted in the early stages of the design process or in pre-refurbishment interventions, scale models, particularly small-scale ones, tend to overestimate the illuminance values on horizontal and vertical planes when compared to full-size buildings (Kesten, Fiedler, Thumm, Löffler, & Eicker, 2010). Studies comparing illuminance performance on the horizontal plane, measured in smallscale models and fullsize buildings, demonstrate that small-scale models outperform the real scenario or building they represent, under overcast sky conditions, by 10-30% (Reed & Nowak, 1955; Kim, Boyer, & Degelman, 1985; Love & Navvab, 1991; Cannon-Brookes, 1994, 1997). According to Cannon-Brookes (1997), errors in the physical representation of the indoor environment and difficulties in accurately defining photometric properties of materials can justify this discrepancy, as well as other physical parameters such as maintenance and dirt in the building. As underlined by Boccia and Zazzini (2015), experimental tests performed under real sky conditions produce a more realistic representation of the daylight performance when compared with tests conducted under artificial sky using sky simulators. Moreover, Kesten (2010) highlights that model scale factor is a function of the daylighting design purpose, where greater scales within 1:10 to 1:1 are appropriate to accurately assess more critical or advanced daylighting devices and useful for detailed building façades and rooms. Due to the scarcity of available information on visual performance of Solar Control Films (SCFs), the present study uses a small-scale model approach to test various SCFs with different optical properties to assess their performance when applied in singlepane glass units.

This paper aims to increase the research on solar control films (SCFs) by studying the indoor illuminance performance of office rooms with singlepane glass units without (reference scenario) and with 4 different solar control films (SCFs) – spectrally selective and reflective – for retrofitting purposes of existing buildings. This approach can be useful for refurbishment purposes in buildings with single-glazed windows in Mediterranean climates, Csa and Csb Köppen-Geiger climate classification (Rodrigues, Santos, Gomes, & Duarte, 2019), as is the case for Portugal, to increase visual comfort without having to activate shading devices or other solutions that can compromise the view to the outside (Silva, Gomes, & Rodrigues, 2015; Gomes, Rodrigues, & Bogas, 2012). In this study, illuminance levels were measured in a small-scale model 1:10 on a horizontal plane at 0.8 m (at full scale) under real sky conditions during summer and winter solstice for 5 different scenarios of the fenestration system. An analysis and discussion based on the registered absolute illuminance values and the useful daylight illuminance was performed and SCFs that presented the most suitable illuminance values to perform office activities (e.g. writing, typing, reading, data processing) were identified.

## 2 SOLAR CONTROL FILMS

Solar control film (SFC) is a thin laminate film material that can be applied to glass surfaces to alter their optical and thermal properties without having to change the type or structure of glazing systems in buildings façades (Pereira, Gomes, Rodrigues & Almeida, 2019). Nowadays, there is a high range of window films for retrofitting purposes with applications on both internal and external surfaces in glazed areas of buildings façades, appropriate for retrofitting purposes in cold and hot climates (Teixeira, Gomes, Rodrigues, & Pereira, 2020). Their efficiency is directly related to the glass substrate, solar orientation, external and internal shading conditions, airconditioning system, and local climate. Films that are applied on the external face of the glass surface present a lower durability than those applied internally due to the fact that they are exposed to weather elements and to possible damages induced by people or objects for glazing surfaces at the ground level. Also, inappropriate cleaning tasks or insufficient maintenance routines have proven to decrease the life span of the films (Pereira, Teixeira, Gomes & Rodrigues, 2019).

### 2.1 CONTEXT

The first window films were developed in the 1960s and had the main purpose of balancing heat exchanges through glass surfaces by blocking radiation across the entire range of frequencies of the electromagnetic spectrum (European Window Film Association, 2020). Although this was a major discovery with high potential to improve thermal and visual comfort in buildings, problems regarding the decrease of the external visibility (reductions in the visible light range spectrum), excessive increase of the use of artificial light and of the heating loads motivated new research and product development.

In the 1970s with the industrial revolution at its peak, new solutions and materials that improved comfort and energy efficiency in buildings were being investigated and developed. The incorporation of polyester fibres in window films produced more energy efficient films for cold climates due to the increase of the absorption coefficient and by re-irradiating long wave in the infrared electromagnetic spectrum and therefore reducing the heat losses to the outdoor environment without decreasing the visible solar transmittance through the glass surface.

Research and development of thin film materials is increasing. New innovative and more sustainable window films such as spectrally selective, adaptive, or smart films will increase their market share in future years.

## 2.2 TYPICAL CONSTITUTION

Existing window films are composed of several membranes of different materials intercalated with each other that can reach up to 8 different layers and undergo 7 different manufacturing procedures (European Window Film Association, 2020). Fig. 1 shows a standard structure of a solar control film.

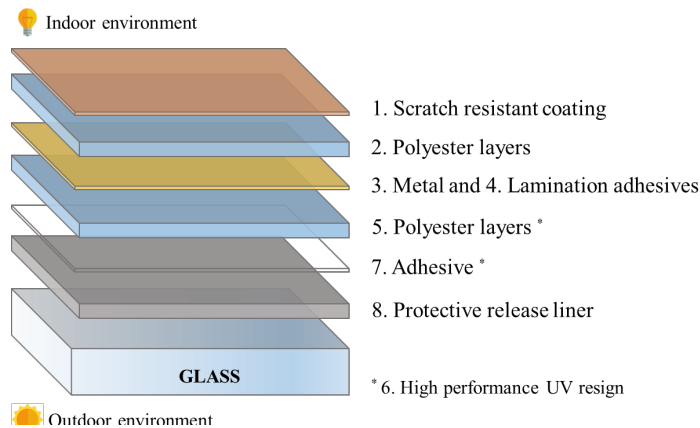


FIG. 1 Standard structure of a solar control window film with internal application on the glass surface: 1. scratch resistant coating, 2. and 5. polyester layers, 3. lamination adhesive(s), 4. metal, 6. high performance UV resin, 7. adhesive and, 8. protective release liner

As shown in Fig. 1, a typical layout of a solar control film with internal application on the glass surface can be constituted of eight different layers (European Window Film Association, 2020), namely:

- **1.** Scratch resistant coating: this hard acrylic-coated finishing layer is in contact with the indoor environment of the building and its function is to protect the film from scratching and abrasion.
- **2. and 5.** Polyester: the polyester membrane offers good optical, thermal, mechanical, physical and chemical characteristics to the film. It is very durable, resistant, and flexible and withstands high and low temperatures. It can have different types of finish, such as UV resin or adhesives. The incorporation of several layers of polyester (multi-layered structure), connected through lamination adhesives, increases the absorption and solar (front) reflectance coefficients. Many films are made with metal deposits on their polyester substrate. This type of film is in the range of solar control series due to the high solar (front) reflectance coefficient and are traditionally called reflective or metallised films.
- **3.** Metal: the oxide metals presented in the solar control films are incorporated into the polyester membrane and have the function of reducing solar gains through glazing. The metal used is usually aluminium and can reduce solar gains by about 80% and reduce visible radiation between 15% to 70%. Recent films based on nanotechnology are produced without metal oxides, resulting in thin films with combined high visible transmittance coefficients and low solar (front) reflectance coefficients.

- **4.** Lamination adhesive: joins several layers of polyester through lamination processes. Sometimes they are embedded in the polyester membranes themselves.
- **6.** High performance UV resin: blocks UV radiation and protects the polyester layers and lamination adhesives. It can be incorporated in the adhesives or in the polyester layer itself. This resin improves thermal performance by reducing the solar gains in the UV solar spectrum and protects the indoor environment content from early degradation by exposure to UV rays.
- **7.** Adhesive: there are two types of adhesives in window films - pressure sensitive and water activated adhesives. The first one adheres to the glass surface through the application of pressure forces without the need to apply any type of solvent, water, or heat. On the contrary, water activated adhesives, as the name implies, needs water to ensure correct adherence, forming chemical bonds with the glass surface which guarantees a higher durability and a more transparent appearance, though its removal or replacement can be difficult.
- **8.** Protective release liner: a film usually made of polyester that protects the adhesive from contamination before installation. It should only be removed before applying the film to the glass.

### 3 EXPERIMENTAL ANALYSIS

#### 3.1 EXPERIMENTAL SET-UP

To evaluate the daylight illuminance levels and the spatial distribution of different solar control films (SCFs) applied in singlepane glass, *insitu* measurements of indoor illuminances on a horizontal plane were carried out in a small scale model (1:10) on the rooftop of DECivil building in Instituto Superior Técnico in Lisbon, Portugal. Taking advantage of the modularity of the model, five different glazing systems were tested: a singlepane clear glass of 6 mm, taken as the reference scenario, and four solar control films applied on the external surface of a 6 mm single-pane glass (designated as SCF A, SCF B, SCF C and SCF D). Tests were conducted with the glazing system of the scale model oriented south in the summer and winter solstice under clear sky conditions at three periods of the day 09h00, 12h00 and 15h00 (True Solar Time – TST).

Fig. 2a shows the small-scale model used in this study. The model was built 30 cm high, 40 cm wide and 70 cm long (internal measurements) in compliance with the daylighting rule of thumb where the depth of the daylight area of an indoor environment is between 1 to 2 times the size of the window-head-height (Reinhart, 2005) combined with the typical geometrical representation of office rooms in buildings. The surfaces were constructed using medium density fibreboards (MDF) and, except for the floor, all surfaces have white melaminic finishing. During the construction of the model, special attention was given to possible openings in the structure that could allow radiation to enter other than from the fenestration system and therefore interfere with the results. For this reason, silicone sealant was applied in some parts of the model as a precaution. In addition, to enable a swift exchange between different glass substrates and minimise the time interval between successive measurements, the model fenestration wall was designed to be completely filled with glass, without any other parts that could make glass assembly difficult. For the tests, the model was placed over black plastic to decrease the influence of the solar reflection from the ground and to protect the materials from the floor's humidity.

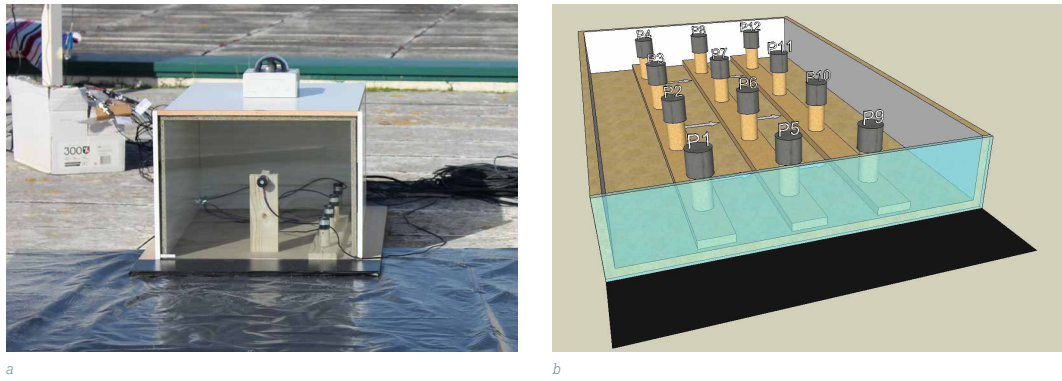


FIG. 2 [a] Small scale model (1:10) on the rooftop of DECivil building in IST, Lisbon, Portugal, and [b] position of the indoor luxmeter sensors (12 points)



FIG. 3 [a] Indoor, and [b] outdoor luxmeter sensors on horizontal plane

Illuminance values were measured with luxmeter LI-COR LI200 sensors ( $\pm 5\%$  accuracy) across a grid of 12 points (Fig. 2b) on a horizontal plane at 0.08 m (0.8 m at full scale) above the floor, corresponding to the common height of the work plane. In the small-scale model, a wooden ruler with 4 luxmeter sensors fixed on stoppers (Fig. 2b and Fig. 3a) was placed in three different positions (right, central, and left) during the measurements. The right, central, and left illuminance points were measured at different moments in time, taking about 2 minutes to record all the 12 illuminance values on the horizontal plane for each glass substrate. This timeline was tested on the rooftop in one pilot day previously to the first real measurement during the summer solstice in order to test the facility and understand the logistics of the tasks involved. Details regarding the timelines and steps of each measurement were registered and a total of 8 minutes was the time observed to place, measure, and withdraw each glass substrate, resulting in a total of 40 minutes in each of the three periods of the day (09h00, 12h00, and 15h00, TST).

As a result, all the measurements were established to start 20 minutes before and end about 20 minutes after the schedule time (09h00, 12h00, and 15h00, TST), with the following sequence being adopted: 1° SCF A, 2° SCF B, 3° SCF C, 4° SCF D, 5° clear glass. Outdoor illuminance on the horizontal plane was measured at one point in the model's exterior (Fig. 3b) at each of the three periods of the day. Additionally, photos were captured inside the model for all the 5 tested fenestration systems.

### 3.2 GLAZING SOLUTIONS

In this study, the indoor illuminance values and distribution on a horizontal plane at 0.08 m (0.8 m at full scale) above the floor was assessed for five glazing solutions: singlepane clear glass unit with 6 mm (reference glazing) and four SCFs applied on the external surface of the reference glass. Table 1 shows the main thermal and optical properties of the analysed solutions. These properties were obtained using Window and Optics tools (Curcija, Vidanovic, Hart, Jonsson, & Mitchell, 2018) which allow spectral data of combined layers of glass with applied films to be calculated. While SCFs A and B are spectrally-selective films and can be identified by their high visible transmittance (*SCF A*:  $\tau_{vis} = 39\%$ ; *SCF B*:  $\tau_{vis} = 66\%$ ; *SCF C*:  $\tau_{vis} = 16\%$ ; *SCF D*:  $\tau_{vis} = 35\%$ ), SCFs C and D are reflective films and show higher values of solar (front) reflectance (*SCF A*:  $\rho_{f,sol} = 25\%$ ; *SCF B*:  $\rho_{f,sol} = 27\%$ ; *SCF C*:  $\rho_{f,sol} = 58\%$ ; *SCF D*:  $\rho_{f,sol} = 37\%$ ).

TABLE 1 Thermal and optical characteristics of the 5 different glazing solutions: solar transmittance,  $\tau_{sol}$ , solar (front),  $\rho_{L,sol}$  and (back),  $\rho_{b,sol}$  reflectance, absorptance,  $\alpha$ , visible transmittance,  $\tau_{vis}$ , visible (front),  $\rho_{L,vis}$  and (back),  $\rho_{b,vis}$  reflectance, thermal transmittance, U, and solar factor, g

	$\tau_{sol}$ [%]	$\rho_{L,sol}$ [%]	$\rho_{b,sol}$ [%]	$\alpha$ [%]	$\tau_{vis}$ [%]	$\rho_{L,vis}$ [%]	$\rho_{b,vis}$ [%]	U [W/m <sup>2</sup> .K]	g [%]
Clear glass	85	8	8	8	90	8	8	5.73	88
SCF A	22	25	13	52	39	7	12	5.62	44
SCF B	35	27	14	36	66	12	14	5.62	51
SCF C	11	58	55	30	16	58	58	5.63	23
SCF D	25	37	38	36	35	33	37	5.63	41

### 3.3 ILLUMINANCE EVALUATION METHODS

The daylight performance was evaluated through the absolute values of indoor illuminance on the horizontal plane considering 500 lx as the recommended value for comfortable daylighting illumination for office activities (e.g. writing, typing, reading, data processing) according to EN 12464-1 (2014) and considering the illuminance range values defined in the Useful Daylight Illuminance (UDI) metric (Nabil & Mardaljevic, 2005). Results of the absolute values of indoor illuminance for the 4 SCFs were analysed and compared with those obtained for the reference glazing. Nabil & Mardaljevic (2005), developed a new concept to assess daylighting in buildings through the UDI metric. The UDI considers that values below 100 lx are insufficient and can contribute to an increase in the energy needs with artificial lighting, values between 100-300 lx require supplementary artificial lighting, and values above 3000 lx can cause thermal and/or visual discomfort and therefore values in these illuminance ranges are not considered useful. On the contrary, values between 300 lx and 3000 lx are considered useful and desirable for indoor environments.

## 4 RESULTS AND DISCUSSION

The analysis was carried out under clear sky conditions in the summer (21<sup>st</sup> June) and winter (21<sup>st</sup> December) solstice when the sun's elevation angle is at its highest and lowest, respectively, with respect to the annual solar dynamic behaviour. For both days, indoor and outdoor horizontal (h=0.8 m) illuminance values were measured at 3 different hours: 09h00 (solar radiation from the east), 12h00 (solar radiation from the south), and 15h00 (solar radiation from the west). The 12 individual data points with experimental measured illuminance values for each tested fenestration system were interpolated and extrapolated for mapping the illuminance distribution along the entire horizontal work plane area.

### 4.1 ANALYSIS OF THE DAYLIGHT AVAILABILITY BY THE ABSOLUTE ILLUMINANCE VALUES

Fig. 4 to Fig. 9 comprise the digital photos showing the indoor illuminance values on the horizontal plane at 0.8 m height at full scale (work plane) in a scale ranging from 0 to >10 klx at 9h00, 12h00, and 15h00 under clear sky conditions in both summer and winter solstices, for the 5 scenarios of the fenestration system: Clear glass; SCF A; SCF B; SCF C and; SCF D. The photos were taken from the interior of the small-scale model with a Canon EOS 600D camera, controlled remotely. The outdoor illuminance on horizontal plane,  $E_{out}$ , registered at 09h00, 12h00, and 15h00 in the summer solstice was of 72 klx, 104 klx, 116 klx, and in the winter solstice of 29 klx, 59 klx and 36 klx.

During both summer and winter seasons, all SCFs significantly reduced the indoor illuminance values, presenting in the summer solstice lower illuminance values than the ones obtained in the winter solstice. This can be explained by the higher summer sun angles and thus lower values of incident direct radiation on a south-oriented façade in the summer period when compared to the winter period (Roos, Polato, van Nijnatten, Hutchins, Olive, & Anderson, 2001). This phenomenon is also noticed in the photos captured inside the small-scale model (see Fig. 4 and Fig. 7, as examples).

At the summer solstice, illuminance values on a horizontal plane for the glass with SCFs vary between 0-1000 lx in a significant area of the horizontal working plane at 0.8 m, except for *SCF B* which is the film with the higher value of the solar transmittance. While the *clear glass* and *SCF B* showed values higher than 500-1000 lx on almost all of the total area of the work plane, SCFs *A*, *C*, and *D* showed illuminance values between 500-1000 lx on more than 50%, which results in a better visual performance by preventing possible glare situations. The *clear glass* and *SCF C* scenarios showed the highest and the lowest range of illuminance values, varying between 0.33-10 klx and 0.34-2.11 klx, respectively, which results in a higher and lower daylight availability asymmetry throughout the horizontal working plane.

In the winter solstice, as expected, the illuminance values were higher for the *clear glass* since it is the fenestration scenario with the highest solar factor, presenting illuminance values higher than 500 lx and on all of the horizontal working plane area, and above 10 klx on 50% of the horizontal working plane area. The *clear glass* scenario's results indicate that visual discomfort through the influence of glare situations can occur, making this space unpleasant or even impossible to work on without the activation of complementary shading devices. SCFs *A*, *B*, and *D* also showed values well above the recommended values of 500 lx to perform office tasks while the reflective *SCF C* showed illuminance values closer to the ones recommended during the morning and afternoon periods (09h00 and 15h00).

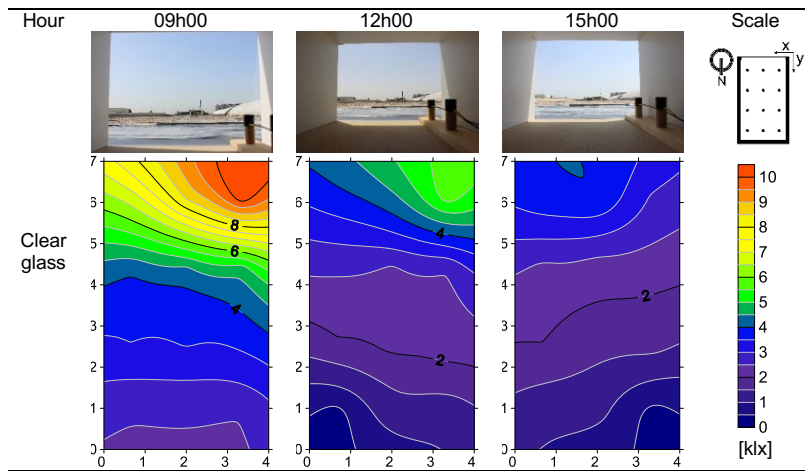


FIG. 4 Digital photos and indoor illuminance levels on a horizontal plane at 0.8 m height at 09h00, 12h00, and 15h00 at the summer solstice under clear sky conditions for the clear glass ( $E_{out}^{09h00}=72\text{klx}$ ;  $E_{out}^{12h00}=104\text{klx}$ ;  $E_{out}^{15h00}=116\text{klx}$ )

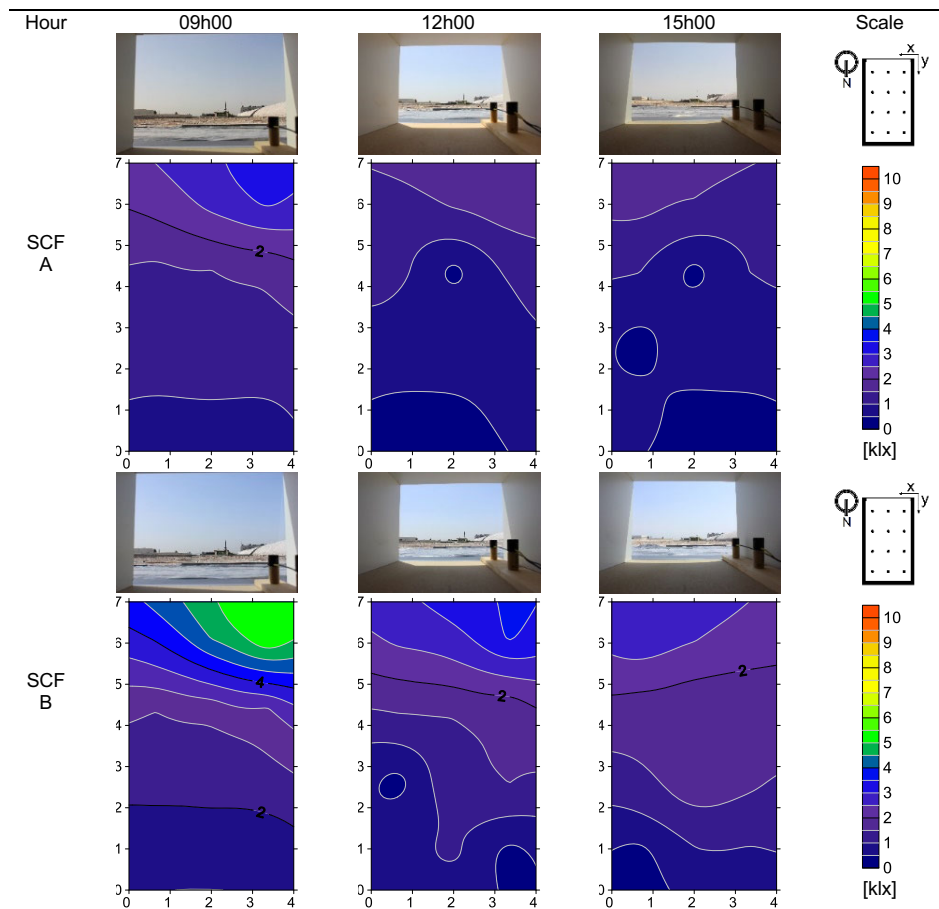


FIG. 5 Digital photos and indoor illuminance levels on a horizontal plane at 0.8 m height at 09h00, 12h00, and 15h00 at the summer solstice under clear sky conditions for the spectrally-selective films A and B ( $E_{out}^{09h00}=72\text{klx}$ ;  $E_{out}^{12h00}=104\text{klx}$ ;  $E_{out}^{15h00}=116\text{klx}$ )

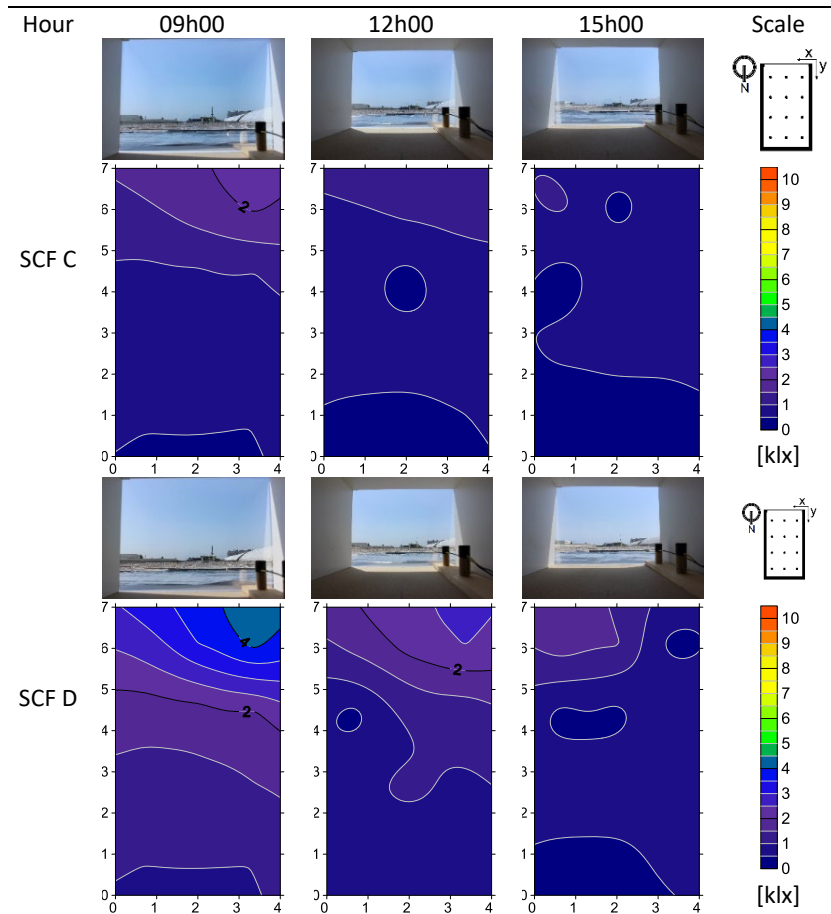


FIG. 6 Digital photos and indoor illuminance levels on a horizontal plane at 0.8 m height at 09h00, 12h00, and 15h00 at the summer solstice under clear sky conditions for the reflective films C and D ( $E_{out}^{09h00}=72\text{klx}$ ;  $E_{out}^{12h00}=104\text{klx}$ ;  $E_{out}^{15h00}=116\text{klx}$ )

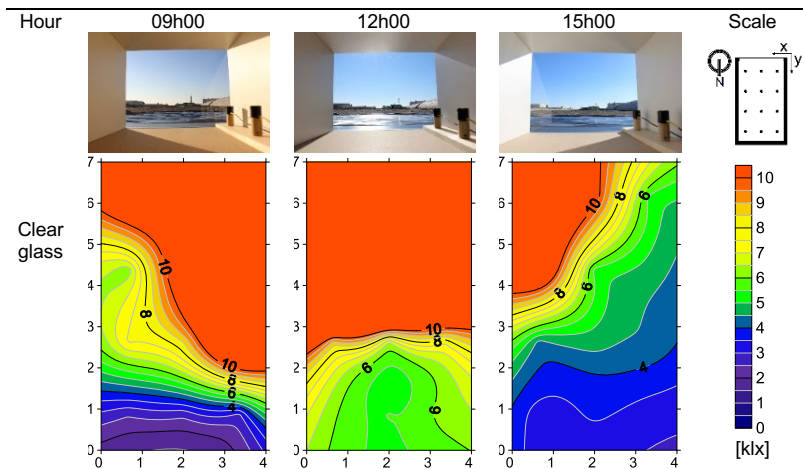


FIG. 7 Digital photos and indoor illuminance levels on a horizontal plane at 0.8 m height at 09h00, 12h00 and 15h00 at the winter solstice under clear sky conditions for the clear glass ( $E_{out}^{09h00}=29\text{klx}$ ;  $E_{out}^{12h00}=59\text{klx}$ ;  $E_{out}^{15h00}=36\text{klx}$ )

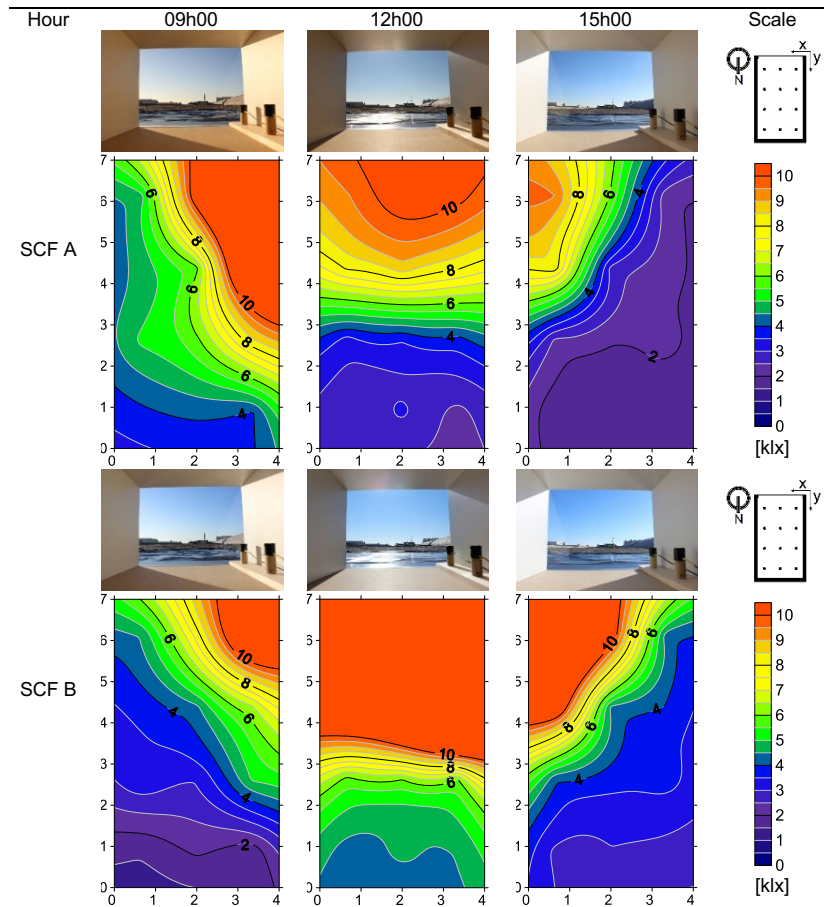


FIG. 8 Digital photos and indoor illuminance levels on a horizontal plane at 0.8 m height at 09h00, 12h00, and 15h00 at the winter solstice under clear sky conditions for the spectrally-selective films A and B ( $E_{out}^{09h00}=29klx$ ;  $E_{out}^{12h00}=59klx$ ;  $E_{out}^{15h00}=36klx$ )

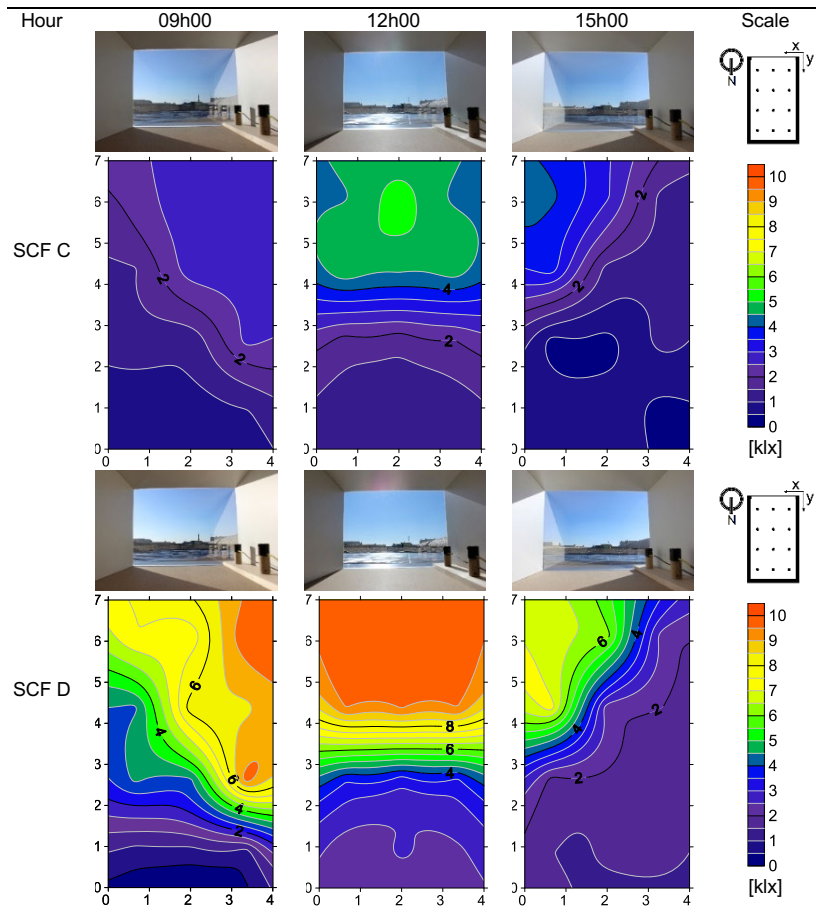


FIG. 9 Digital photos and indoor illuminance levels on a horizontal plane at 0.8 m height at 09h00, 12h00, and 15h00 at the winter solstice under clear sky conditions for the reflective films C and D ( $E_{out}^{09h00}=29klx$ ;  $E_{out}^{12h00}=59klx$ ;  $E_{out}^{15h00}=36klx$ )

## 4.2 ANALYSIS OF THE DAYLIGHT AVAILABILITY USING THE USEFUL DAYLIGHT ILLUMINANCE RANGE VALUES

Fig.10 to Fig.15 show the digital photos and indoor illuminance values at an adequate scale to analyse the areas within the range values (<100 lx insufficient, 100-300 lx supplementary artificial lighting required, 300-3000 lx useful, >3000 lx can cause thermal and visual discomfort) considered in the Useful Daylight Illuminance (UDI) metric for three hours of the day at the summer and winter solstices, respectively, under clear sky conditions for the 5 scenarios of the fenestration system: Clear glass; SCF A; SCF B; SCF C and; SCF D.

Analysing the experimental results at the summer solstice through the range values defined in the UDI metric, it is possible to conclude that the reference scenario, *Clear glass*, showed the highest area of illuminance values outside the useful range (>3 klx) which indicates that this scenario presents a high risk of causing visual discomfort conditions to perform any type of work activity. In the summer solstice, SCFs *A* and *B* showed a high area of the work plane within the useful illuminance range value, however on the winter solstice almost all the illuminance values are above the useful range. The most reflective film, *SCF C*, presented values within the useful range throughout the day on the entire area of the work plane except during the winter solstice at 12h00. *SCF D* showed medium values between the 2 spectrally selective SCFs *A* and *B*.

At the winter solstice, the results of the reference scenario, *clear glass*, presented illuminance values outside the useful range in almost all the working plane area, which indicates that from 09h00 to 15h00 the illuminance levels are so high that visual discomfort associated with glare is very likely to occur. Spectrally selective SCFs *A* and *B* showed, during the morning and afternoon periods, small areas within the useful range of illuminance values (0.3-3 klx) in the working plane area. The reflective SCFs *C* and *D* presented a higher area of the grid within the useful illuminance values, especially *SCF C* with more than 50% of the grid area within the useful values during the morning and afternoon periods. In fact, when compared to the other films, *SCF C* ( $\tau_{sol} = 11\%$ ,  $\tau_{vis} = 16\%$ ) provides the highest decrease of the illuminance values and thus is the most appropriate retrofitting scenario to prevent possible glare situations during both summer and winter seasons.

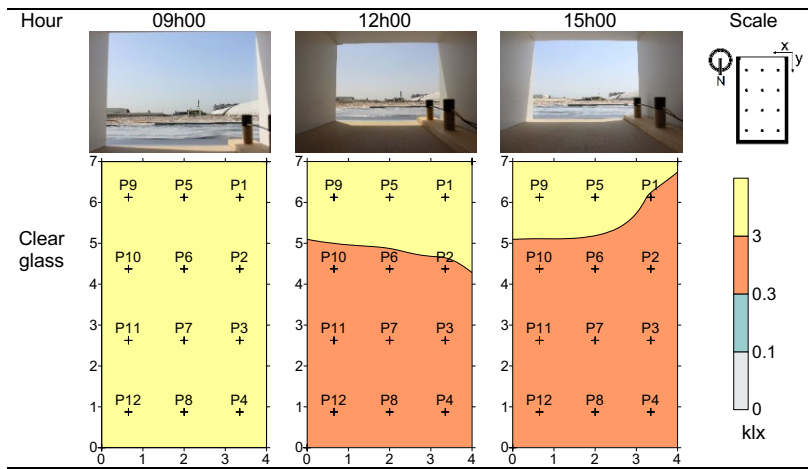


FIG. 10 Digital photos and indoor illuminance levels on a horizontal plane at 0.8 m height at 09h00, 12h00, and 15h00 at the summer solstice under clear sky conditions for the clear glass using the UDI's range values ( $E_{out}^{09h00}=72\text{klx}$ ;  $E_{out}^{12h00}=104\text{klx}$ ;  $E_{out}^{15h00}=116\text{klx}$ )

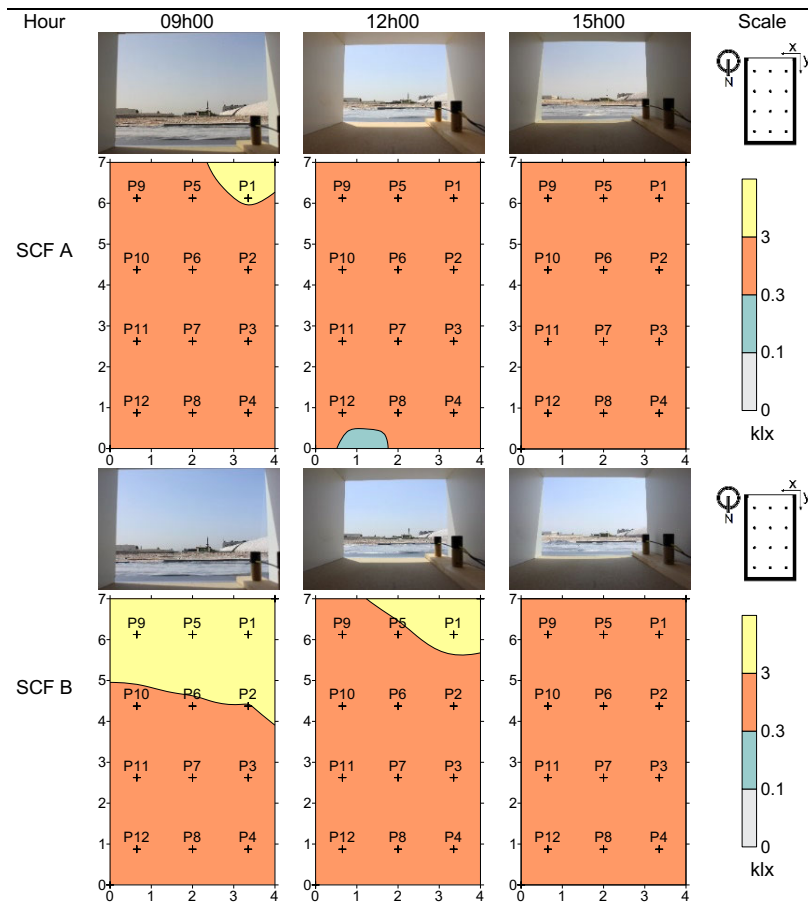


FIG. 11 Digital photos and indoor illuminance levels on a horizontal plane at 0.8 m height at 09h00, 12h00, and 15h00 at the summer solstice under clear sky conditions for the spectrally-selective films A and B using the UDI's range values ( $E_{out}^{09h00}=72\text{klx}$ ;  $E_{out}^{12h00}=104\text{klx}$ ;  $E_{out}^{15h00}=116\text{klx}$ )

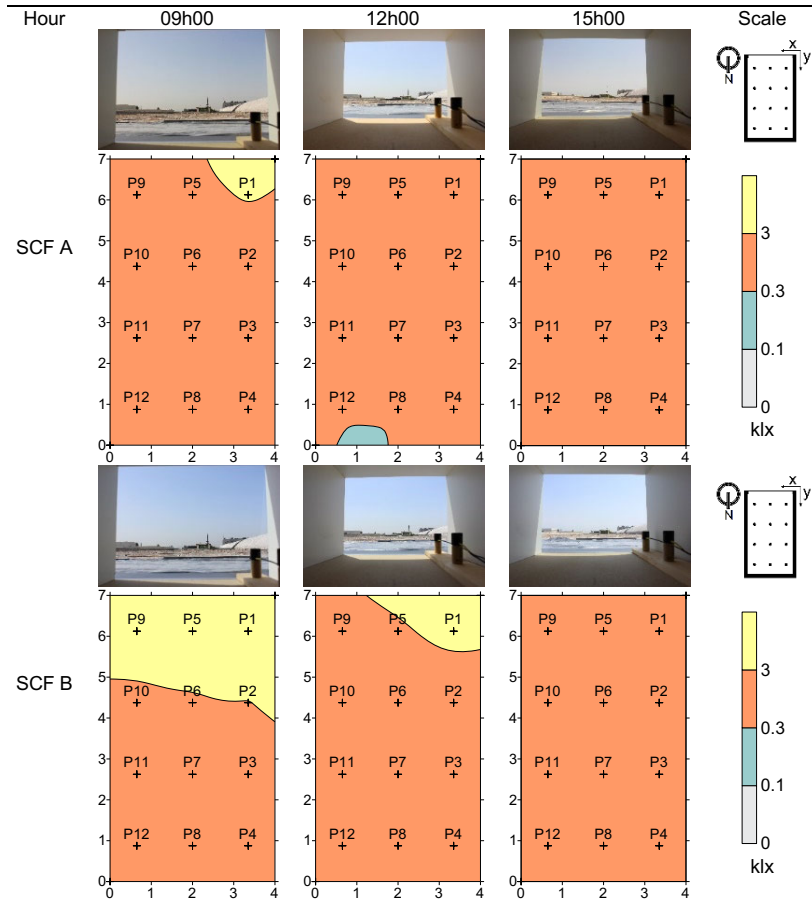


FIG. 12 Digital photos and indoor illuminance levels on a horizontal plane at 0.8 m height at 09h00, 12h00, and 15h00 at the summer solstice under clear sky conditions for the reflective films C and D using the UDI's range values ( $E_{out}^{09h00}=72\text{klx}$ ;  $E_{out}^{12h00}=104\text{klx}$ ;  $E_{out}^{15h00}=116\text{klx}$ )

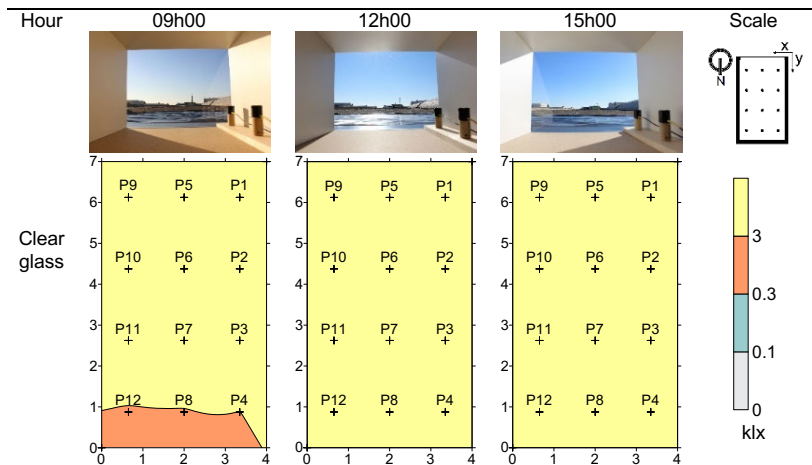


FIG. 13 Digital photos and indoor illuminance levels on a horizontal plane at 0.8 m height at 09h00, 12h00, and 15h00 at the winter solstice under clear sky conditions for the clear glass using the UDI's range values ( $E_{out}^{09h00}=29\text{klx}$ ;  $E_{out}^{12h00}=59\text{klx}$ ;  $E_{out}^{15h00}=36\text{klx}$ )

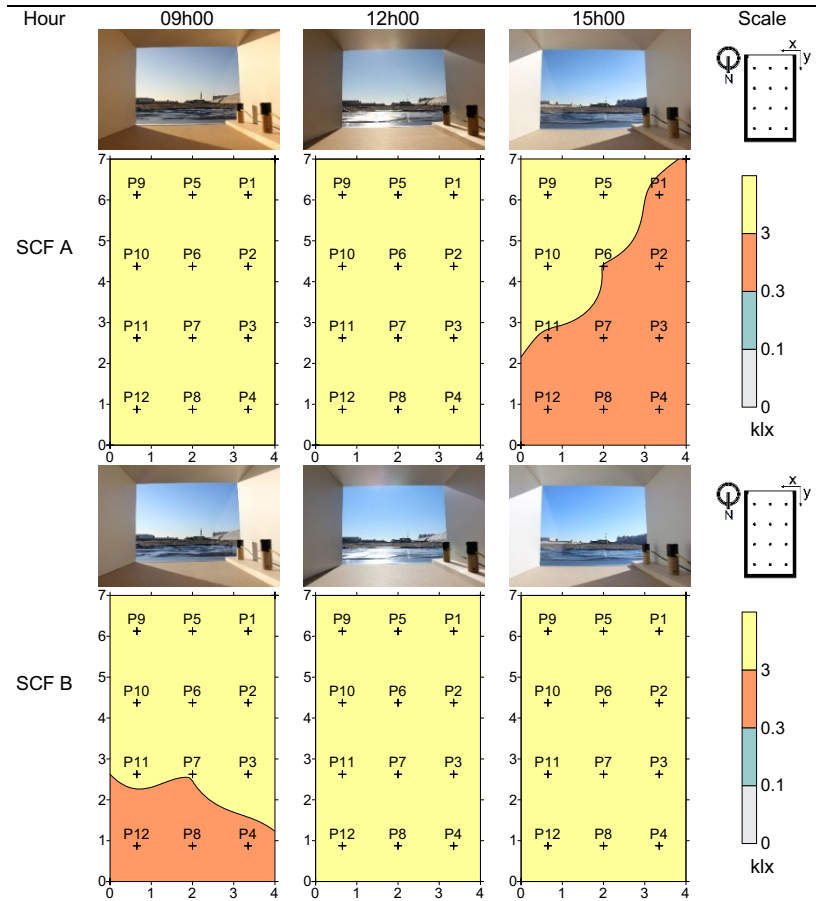


FIG. 14 Digital photos and indoor illuminance levels on a horizontal plane at 0.8 m height at 09h00, 12h00, and 15h00 at the winter solstice under clear sky conditions for the spectrally-selective films A and B using the UDI's range values ( $E_{out}^{09h00}=29klx$ ;  $E_{out}^{12h00}=59klx$ ;  $E_{out}^{15h00}=36klx$ )

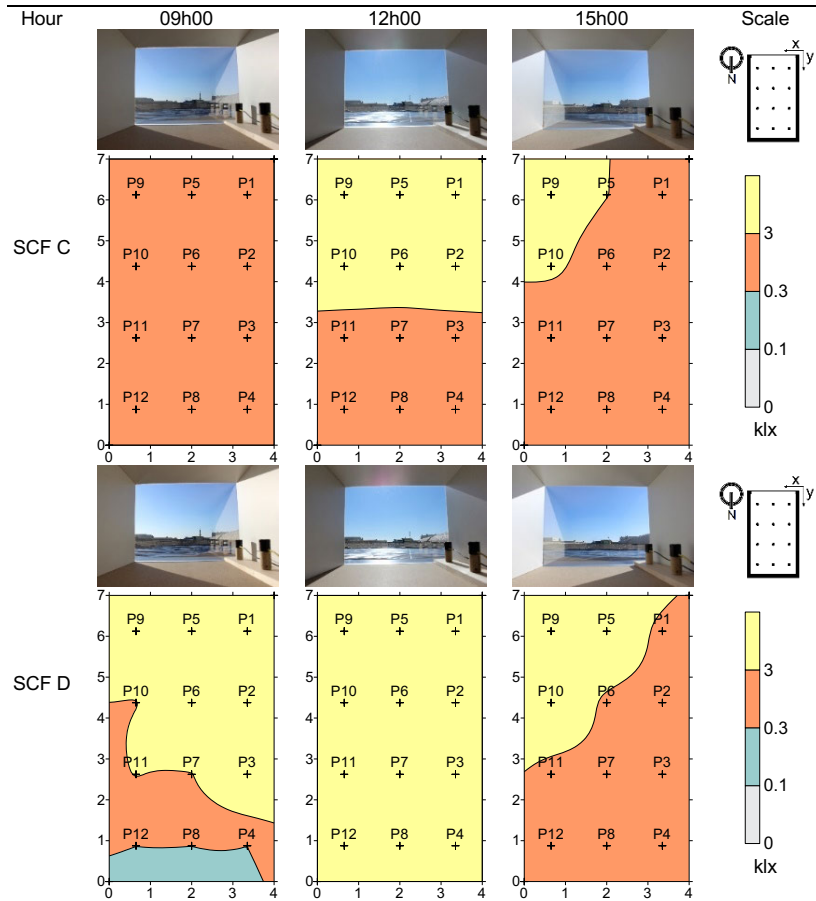


FIG. 15 Digital photos and indoor illuminance levels on a horizontal plane at 0.8 m height at 09h00, 12h00, and 15h00 at the winter solstice under clear sky conditions for the reflective films C and D using the UDI's range values ( $E_{out}^{09h00}=29klx$ ;  $E_{out}^{12h00}=59klx$ ;  $E_{out}^{15h00}=36klx$ )

## 5 CONCLUSIONS

This study shows the potential of highly reflective and spectrally selective solar control films in promoting daylight availability and limiting visual discomfort in office rooms with singlepane clear glass windows, in Mediterranean climates with predominantly clear sky conditions, by decreasing the solar gains and visible transmittance through the glazing system. The several intercalated layers of polyester with incorporated metal oxides and high-performance UV resin in the films' composition provide the thermal and optical properties that make these films a potential viable solution for the refurbishment of glazing systems. Usually, SCFs are applied on windows to improve the thermal performance of existing buildings by decreasing either the solar factor, when the aim is to prevent excessive solar gains, or the surface emissivity of the glazing, when the goal is to increase the thermal insulation of the windows (Pereira et al., 2019; Teixeira et al., 2020). For South European countries, as is the case for Portugal, window films are mainly applied to control solar gains, thereby preventing overheating and decreasing the cooling energy needs. The application of a window film may increase the thermal comfort conditions and the energy efficiency of the building, but the impact in the daylight availability due to the decrease of the visible transmittance of the glazing may be a problem that has not yet been sufficiently investigated (Cruz et al., 2019).

In this study, the indoor illuminance distribution on the horizontal work plane at 0.8 m was measured under clear sky conditions at the summer and winter solstice using a small-scale model for 5 different glazing systems. A single pane of 6 mm clear glass was tested and taken as the reference scenario. Furthermore, four different solar control films, two spectrally selective and two reflective, were applied to the external surface of a 6 mm single-pane clear glass and tested.

The results show that for single-pane glass systems, SCFs can significantly decrease the indoor daylight illuminance levels likely to cause glare problems ( $\geq 3$  klx), which is a relevant issue in locations with predominantly clear sky conditions. The application of SCF in glazing showed a greater performance in summer, when compared with single glazing without SCF, not only in decreasing the illuminance levels below the critical values (3 klx), but also in promoting a more extensive spatial distribution of acceptable levels of daylight availability (0.33 klx). In winter, the performance of these films was not as noticeable as in summer, due to the sun's lower height and greater perpendicularity of the sun's rays to the glazing surface.

The application of the spectrally selective SCFs *A* and *B* and reflective SCFs *C* and *D* on a 6 mm single pane of glass decreased the illuminance indoor values throughout the work plane, which had a positive effect in lessening possible glare situations due to the high illuminance levels, in both summer and winter seasons.

The highly reflective film, SCF *C*, which has the lowest solar and visible transmittance, was found to be the best retrofitting scenario in providing illuminance values within the useful range (0.3-3 klx) according to the UDI metric ranges in clear sky days. Therefore, this film has the highest potential to increase the visual comfort conditions in office rooms with single pane clear glass oriented to the south, showing illuminance values closer to 0.5 lx in a higher area of the work plane and preventing possible glare situations when compared to the other films, during sunny days in both summer and winter seasons. In fact, except SCF *C*, for which the area with acceptable values of illuminance during the winter is considerable, the other three SCFs lead to a higher risk of glare occurrences in the whole room extension. During the winter solstice when compared to the summer solstice under clear sky conditions, SCF *C* showed higher illuminance values across the working plane. On the one hand, this film decreased the daylight availability reducing the risk of glare occurrences during

both summer and winter seasons, and on the other hand, as the results showed, it did not decrease the daylight values to a point where supplementary artificial lighting is required for office work activities. Nevertheless, to overcome the problem with glare occurrences, movable shading devices might be considered as a feasible complementary solution, especially during the winter period under clear sky conditions.

This paper focused the analysis only on visual comfort and under clear sky conditions, which are typical of southern European countries, where summer is the dominant season. Window films, when compared to shading solutions, decrease the solar and visible transmittance of glazing systems without compromising the view to the outside, which, alongside the ease of maintenance (same as the glass without SCF) and flexibility in application, is an advantage. As a possible drawback of the films studied, that may cause suspicion in the use of window films, the lower durability of this solution is pointed out when compared to traditional ones. Depending on the type of application (on the internal or external side of the glass), the service life of these films can vary from 6 to 12 years and thus requires frequent replacements to maintain the same performance throughout the building operation stage, which can be a disadvantage of SCFs when compared to shading solutions. Another potential drawback is the decrease of the daylight availability and the heat gains during the winter season, which can lead to higher energy demand with electric lighting and heating loads.

Therefore, although these films proved to be appropriate, when the aim is to minimise the risk of visual discomfort, it is recommended in the design to extend the analysis to overcast sky conditions and to thermal comfort, even if these are not the prevailing climate conditions in southern European countries such as Portugal.

The results of this study show that SCFs are highly influential on the indoor illuminance levels and therefore the studies on visual comfort metrics and on thermal and energy efficiency indicators should not be considered separately but instead in an integrated approach that enables a better understanding of the trade-offs between the variation of solar and visible transmittance and the heat gain/losses coefficients derived from the application of the film. Additionally, a combined approach between SCFs and other shading devices should be considered to increase the visual comfort conditions when higher illuminance levels are registered.

### Acknowledgements

The authors would like to thank André Quinhones and Mário Cruz for their support during the experimental procedure. The authors would also like to extend their thanks to CERIS Research Institute and DECivil, Instituto Superior Técnico, Universidade de Lisboa, for providing the space for the experiment. The first and second authors wish to acknowledge the support of FCT (Foundation for Science and Technology) PhD Grant FCT PD/BD/127848/2016 and PD/BD/150576/2020.

### References

- Aghemo, C., Pellegrino, A., & Lo Verso, V. (2008). The approach to daylighting by scale models and sun and sky simulators: A case study for different shading systems. *Building and Environment*, 43(5), 917-927. doi: 10.1016/j.buildenv.2007.01.020
- Ayoub, M. (2020). A review on light transport algorithms and simulation tools to model daylighting inside buildings. *Solar Energy*, 198, 623-642. doi:10.1016/j.solener.2020.02.018
- Boccia, O. & Zazzini, P. (2015). Daylight in buildings equipped with traditional or innovative sources: A critical analysis on the use of the scale model approach. *Energy in Buildings*, 86, 376-393. doi:10.1016/j.enbuild.2014.10.003
- Cannon-Brookes, S. (1994). A study of the use of scale models in the daylighting design of museums. *Proc. CIBSE National Lighting Conference*, 238246. Cambridge, England (1994)
- Cannon-Brookes, S. (1997). Simple scale models for daylighting design: analysis of sources of error in illuminance prediction. *Lighting Research and Technology*, 29, 135142. doi:10.1177/14771535970290030901

- Cruz, M., Pereira, J., Gomes, M. G., & Kong, M. M. (2019). Comparative analysis of the luminous performance of fenestration with Japanese paper and glazing with a polymeric film in meditation rooms. In M. S. M. Kong, M. R. Monteiro, M. J. P. Neto (Eds.), *Intelligence, Creativity and Fantasy* (pp.555-561). Londres, Reino Unido: CRC Press. doi:10.1201/9780429297755
- Curcija, C., Vidanovic, S., Hart, R., Jonsson, J., & Mitchell, R. (2018). WINDOW Technical Documentation, *Lawrence Berkeley National Laboratory*
- European Committee for Standardisation (CEN) (2014). Light & Lighting – Lighting of Indoor Workplaces. Brussels. EN 12464-1
- European Window Film Association (2020). Knowledge about Window Films. Available on: <https://iwfa.com/ewfa/en-us/Knowledge> (consulted on 10/03/2020)
- Gomes, M. G., Rodrigues, A. M., & Bogas, J. A. (2012). Numerical and experimental study of the optical properties of venetian blinds. *Journal of Building Physics*, 36(1), 7-34. doi:10.1177/1744259112444022
- Gomes, M. G., Santos, A. J. & Rodrigues, A. M. (2014). Solar and visible optical properties of glazing systems with venetian blinds: Numerical, experimental and blind control study. *Building and Environment*, 71, 47-59, doi:10.1016/j.buildenv.2013.09.003
- Kesten, D., Fiedler, S., Thumm, F., Löffler, A., & Eicker, U. (2010). Evaluation of daylight performance in scale models and a full-scale mockup office. *Oxford University Press: International Journal of LowCarbon Technologies*, 5, 158165. doi:10.1093/ijlct/ctq023
- Kim, K.S., Boyer, L. L., & Degelman, L. O. (1985). Daylighting analysis through scale model, full scale measurements and computer analysis for Texas A&M University Campus Building. *Second Annual Symposium Improving Building Energy Efficiency in Hot and Humid Climates*, 1621
- Klepeis, N., Nelson, W., Ott, W., Robinson, J., Tsang, A., Switzer, P., Behar, J., Hern, S. & Engelmann, W. (2001). The National Human Activity Pattern Survey (NHAPS): A resource for assessing exposure to environmental pollutants. *Journal of Exposure Analysis and Environmental Epidemiology*. 11(3), 231-252. doi:10.1038/sj.jea.7500165
- Love, J. A., & Navvab, M. (1991). Daylighting estimation under real skies: A comparison of fullscale photometry, model photometry and computer simulation. *Illuminating Engineering*, 20(1), 140156
- Nabil, A. & Mardaljevic, J. (2005). Useful daylight illuminance: A new paradigm for assessing daylight in buildings. *Lighting Research and Technology*, 37(1), 41-59
- Pereira, J., Gomes, M. G., Rodrigues, A. M., & Almeida, M. (2019). Thermal, luminous and energy performance of solar control films in single-glazed windows: Use of energy performance criteria to support decision making. *Energy and buildings*, 198, 431-443. doi:10.1016/j.enbuild.2019.06.003
- Pereira, J., Teixeira, H., Gomes, M. G., & Rodrigues, A. M. (2019). Assessment of early degradation of glazing systems with damaged solar control films. *International Conference on Green Construction*. 8-9 April 2019, Cordoba, Spain
- Potočnik, J. & Košir, M. (2020). Influence of commercial glazing and wall colours on the resulting non-visual daylight conditions of an office. *Building and Environment*, 171, doi:10.1016/j.buildenv.2019.106627
- Reed, B. H., & Nowak, M. A. (1955). Accuracy of daylight prediction by means of models under an artificial sky. *Illuminating Engineering*, 50(7), 336346
- Reinhart, C. (2005). A simulation-based review of the ubiquitous window-headheight to daylight zone depth rule-of-thumb. *IBPSA 2005 - International Building Performance Simulation Association 2005*. August 2005, Montreal, Canada
- Reinhart, C. & Fitz, A. (2006). Findings from a survey on the current use of daylight simulations in building design. *Energy and Buildings*, 38(7), 824-835. doi:10.1016/j.enbuild.2006.03.012
- Rodrigues, A. M., Santos, M., Gomes, M. G., & Duarte, R. (2019). Impact of natural ventilation on the thermal and energy performance of buildings in a Mediterranean climate. *Buildings*, 9(5), 123. doi:10.3390/buildings9050123
- Roos, A., Polato, P., van Nijnatten, P. A., Hutchins, M. G., Olive, F., & Anderson, C. (2001). Angular-dependent optical properties of low-e and solar control windows: Simulations versus measurements. *Solar Energy*, 69, 15-26. doi:10.1016/S0038-092X(01)00019-6
- Teixeira, H., Gomes, M. G. Rodrigues, A. M., & Pereira, J. (2020). Thermal and visual comfort, energy use and environmental performance of glazing systems with solar control films. *Building and Environment*, 168. doi:10.1016/j.buildenv.2019.106474

# Daylight Transmittance Through Expanded Metal Shadings

Jose Miguel Rico-Martinez<sup>1</sup>, Marcin Brzezicki<sup>2</sup>, Carlos Gabriel Ruiz-Mugica<sup>1</sup>, Jakub Lech<sup>2</sup>

\* Corresponding author

1 University of the Basque Country, School of Architecture, Spain, j.rico@ehu.eus

2 Wroclaw University of Science and Technology, Faculty of Architecture, Poland

## Abstract

*Due to the substantial need for energy efficiency, the daylight performance of building envelopes is a key issue in sustainable architecture. A frequently used shading system consists of static expanded metal meshes (EM). As a very prominent textural façade element, expanded metal is widely used as both a cladding and static shading device.*

*One initial aim is to provide a sufficient description of EM, including fabrication, possible usage, and overall properties. This includes a set of parameters needed to accurately control the complex geometry of EM. These parameters are also useful in getting reliable 3D computer models of EM.*

*The main objective of this paper is to assess, describe, and compare EM light transmittance performance for a shading device. Determining the influence of parameters such as geometry, colour, position, and direction of incoming light on the shading performance were specific objectives.*

*The research is based on BSDF simulations via Radiance (Ward, Mistrick, Lee, McNeil, & Jonsson, J., 2011) and experimental data provided at a previous laboratory stage.*

*The performance of various EM shading devices has been simulated and compared for a south-facing façade in Madrid for most characteristic times of the year: solstices and equinoxes, as well as midday transmittance throughout the year.*

## Keywords

*Expanded metal, daylight transmittance, solar shading, bi-directional scattering distribution functions, angular selective shading systems*

DOI 10.7480/jfde.2020.1.4698

# 1 INTRODUCTION

## 1.1 IMPORTANCE OF BUILDING ENVELOPES

The building envelope is the first protective barrier between the building and its surroundings, which gives it immense possibilities in contributing to the building's overall performance. One of the most notable is its influence on solar energy gains and overall daylight performance. Excessive heat gains constitute a serious problem in well-lit modern buildings, leading to higher energy usage, which is a serious economic and environmental issue. On the other hand, daylighting is a key issue in terms of visual comfort and energy savings through artificial lighting. Due to these circumstances, the daylight and thermal performance of building envelopes is a key issue in sustainable architecture (Littlefair, 2001).

## 1.2 DAYLIGHT IN BUILDINGS

Daylight is the combination of all direct and indirect sunlight throughout the day. Daylight creates the healthiest visual environment in buildings and provides an appropriate amount of illumination and all necessary spectral variety (including UV light). Scattered radiation (diffused daylight) does not cause major problems because it carries a relatively small amount of energy. In contrast, direct radiation (direct solar radiation) is associated with direct high-energy flux (approx. 1000 W per sq. m. of horizontal surface depending on the angle of incidence) (Begemann, van den Beld, & Tenner, 1997).

## 1.3 IMPORTANCE OF SHADING DEVICES

Buildings harvest daylight through glazed surfaces, which work as a single direction filter for infrared radiation, producing the so-called "greenhouse effect". The infrared range, from 780 to 1060 nm, involves heat transfer and causes temperature growth in rooms that too often are serviced by energy-consuming mechanical HVAC equipment in modern buildings, and characterised by a high percentage of transparent surfaces.

In the context of climate change and the energy use reduction requirements, shading systems are one of the most important issues in façade design. Shading devices protect the internal spaces from solar radiation, and – consequently – from temperature increase, but such devices should also allow for an adequate transmittance of daylight into the interior spaces of buildings. Besides those energy-related requirements, when designing continuous translucent layers, one must consider their permeability and optical performance for an adequate outward vision and privacy protection.

Another problem to address with shading devices is the appearance of discomfort glare, related to the presence in the visual field of excess luminance differences (Perry, 1990). In urban environments, façade glare affects visual comfort (discomfort glare) and influences the thermal load of other buildings (solar radiation from more than one source) (Brzezicki, 2012). In most buildings, glare protection is necessary to maintain proper visual comfort.

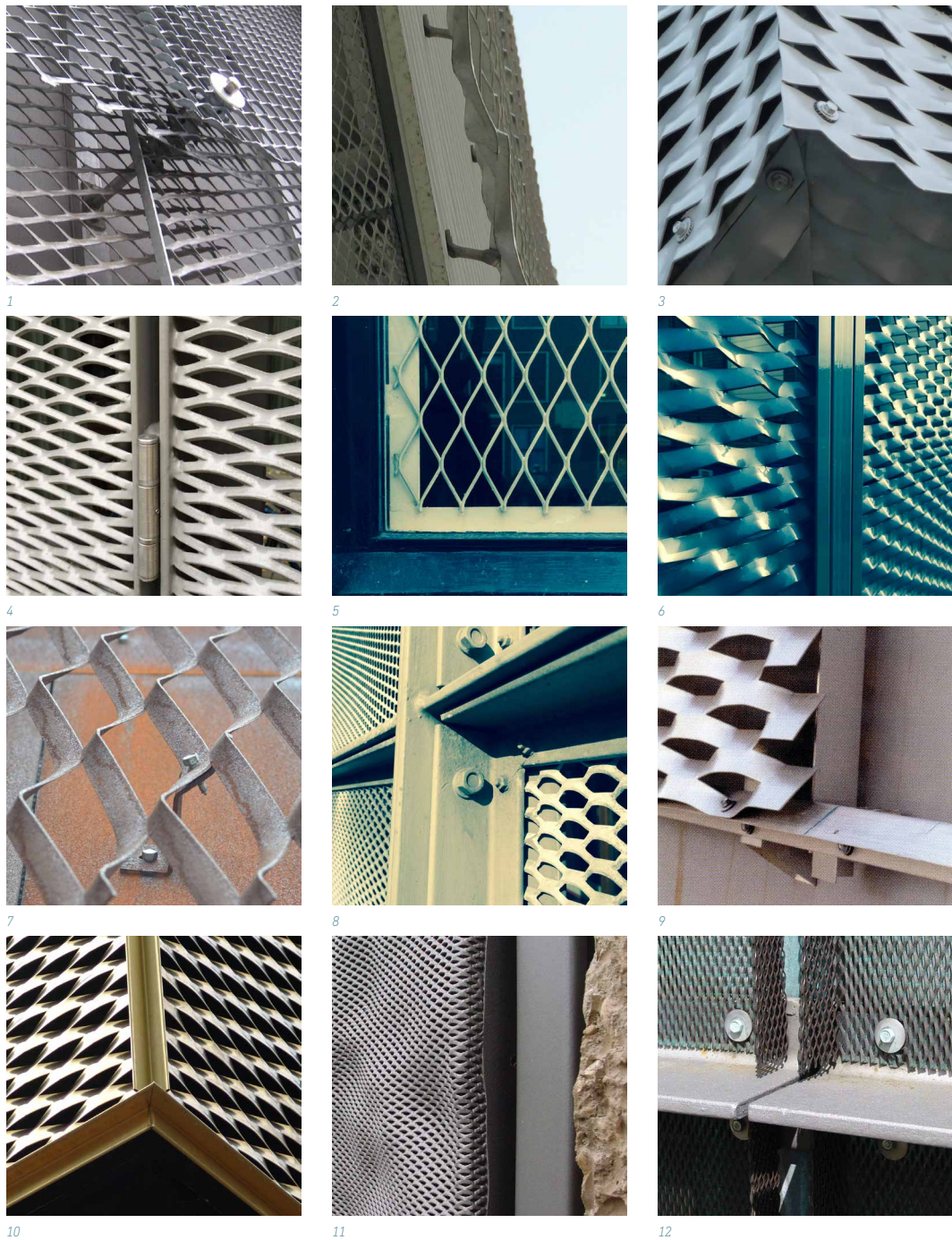


FIG. 1 Façade EM fixing solutions. Image 9 by Jesus Granada, first published in Tectonica n.22. Images 10,11,12 retrieved from <https://www.flickr.com/photos/detlefschobert/> <https://creativecommons.org/licenses/by-nd/2.0/>

As well as with other materials or products, it is common practice to use EM as a sun control layer in façades, aiming to contribute both to thermal and visual comfort. If properly designed, EM meshes may allow daylight to pass through whenever necessary, as well as reducing cooling costs when used as sunshades. While highly effective in blocking direct sunlight, such systems must allow an adequate portion of the indirect, eye-friendly daylight through.

As EM is a metal product, one might be worried about the temperature it could reach under solar radiation and the subsequent radiative effect. As an initial benefit, EM will very often reflect radiation upwards, avoiding heat transfer to the ground. We have to consider the effect of colour and finish but, in general, EM shadings do not reach very high temperatures, probably due to the high proportion of voids and its easy ventilation.

Regarding wind resistance and acoustic behaviour, EM may need further specific studies relating to its behaviour to avoid excessive deformations and noisy turbulences. Those effects could be controlled by adjusting the geometry of the shading, size of the ventilated gap, and fixing system. In relation to the fixing, the nature of the fixing system must be addressed and many options are available, all of which must allow thermal expansion in order to avoid creaking (FIG 1.).

When calculating the wind load applied to the EM surface, if the voids are small and the percentage of voids is low (below around 20-30%), the whole surface of the EM is considered to bear the wind load, as if it were an opaque plate, disregarding the voids. This is due to the effect of the wind's sudden hit and the friction created when going through the mesh voids.

We could intuitively worry about wind whistling through the EM voids but, even if we cannot entirely disregard that option, the vast experience of installed EM façades allows that concern to be relaxed.

As EM is mostly installed as the outer layer of complex fenestration systems or ventilated façades, the maintenance and cleaning factor must be considered. Due to its geometry, EM can gather dust but as it is normally glossy or lacquered and the majority of the dust is washed off by rain, it does not require extraordinary maintenance measures. Besides, photocatalytic paints can be employed to create self-cleaning surfaces that avoid dirt and stains.

## 1.4 EXPANDED METAL FAÇADES

Angular selective shading systems such as Expanded Metal (EM) block direct sunlight and admit daylight within a specific range of incident solar angles (Fernandes, Lee, McNeil, Jonsson, Nouidui, Pang, & Hoffmann, 2015). EM presents a wide range of applications in architecture and the building industry but because of its prominent textural aspect, it is widely used as a façade element, both as the cladding of opaque surfaces and as a shading device. EM is a great fit for the needs of many contemporary architectural designers seeking continuous skins that envelop the whole building, blurring the difference between hollow and solid and providing a smooth light filter (FIG 2.)

Most other contemporary shading systems are constructed mainly for the momentary reduction of the energy flux, e.g. rollers, blinds, and shades, which are frequently integrated as a part of so-called adaptive façades (Loonen et al., 2015). Contrary to many complicated, mechanised shading systems, EM skins often define the appearance of the whole building, affecting both the building's physics (heat and light transmission) and the tectonics of the envelope.

As with façade louvres, EM meshes provide different shading patterns, depending on the angle of incoming sunlight. This allows for the passive regulation of the amount of transferred daylight throughout the year. However, the choice of EM variant will strongly affect the shading performance.



FIG. 2 Example of EM continuous skin. New Museum of Contemporary Art, New York. SANAA architecture office, 2007

One of the aims of this paper is to determine which aspects of EM design and manufacture should be considered in order to fit the requirements of each architectural design. The focus is on EM as a shading device, assessing its performance as an angular selective shading system and the influence of several parameters on the resulting daylight transmittance.

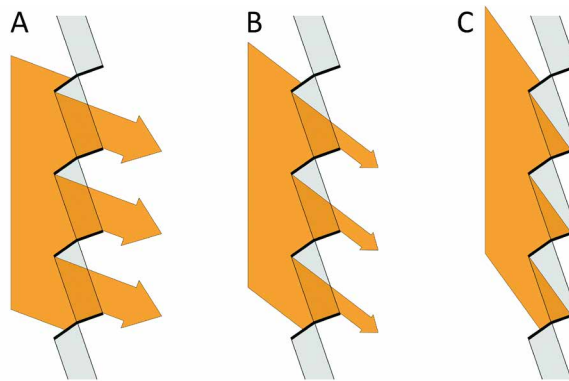


FIG. 3 EM as an angular selective shading

## 1.5 FABRICATION OF EXPANDED METAL

For an adequate understanding of the geometry of EM, which is necessary to build 3D models for simulation, an in-depth analysis of its shape and manufacturing process is needed.

EM is manufactured from metal sheets which have thicknesses usually ranging from 0.4mm to 6 mm. The manufacture consists of shearing and stretching operations in a press, leaving voids surrounded by the stretched strands of metal. Aluminium, mild steel, galvanised steel, stainless steel, copper, brass, nickel, titanium, platinum, zinc, silver, and gold are possible materials for manufacture, but companies produce 80 - 90 % in steel. Following the mechanical manufacturing operation, the resulting mesh can be coated by lacquer finishes or by galvanisation.

FIG 4. shows a sketch of the described mechanical operation. The metal sheet advances on a conveyor belt towards the press. A vertical movement of the blade (move 1) makes a row of cuts perpendicular to the advancing movement of the sheet (move 3) and simultaneously distorts the part of the sheet that has advanced beyond the cutting-line, pushing it downwards. After this first cut-and-push operation, the blade rises and moves a certain horizontal distance (move 2) perpendicular to the advancing movement of the sheet. This way, two rows of cuts end up displaced one from each other in a zigzag pattern.

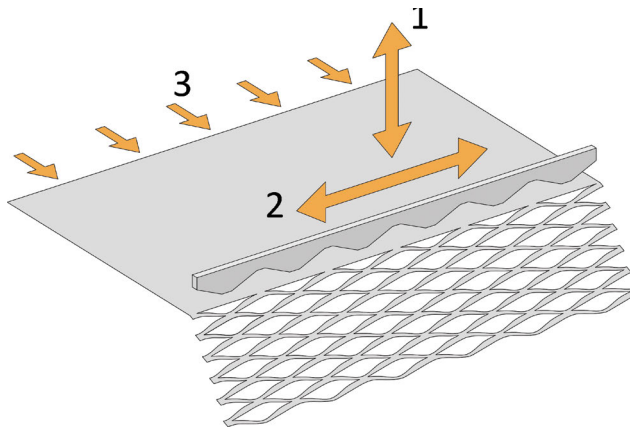


FIG. 4 The three manufacture movements

There are several kinds of EM, depending on the form and magnitude of the movements of the blade and the consequent shape of the holes. The simplest and most common type has rhomboid holes, usually known as rhombus-shaped or diamond-shaped; this will be the object of our research.

EM offers some advantages compared to other techniques: it is formed from a single piece of metal; no welding or weaving the metal is needed; neither joints nor welded knots are created and therefore there is less risk of rupture. Compared to other translucent metal screens such as perforated metal or woven metal fabrics, EM can offer greater flexural stiffness because the manufactured mesh has a larger overall thickness and therefore a better moment of inertia than the initial metal sheet. This feature of EM makes it very appropriate for installation in façades, as wind pressure is acting on them.

EM can be used for outdoor installation with different thicknesses of the departing metal coil, depending on the metal used, the geometry of the mesh, its finish and the distance between fixing points. Each mesh has a different moment of inertia (flexural strength) depending on the overall thickness the mesh achieves after expansion, which ultimately depends on the height of the peaks of each rhombus and the strand width.

In practice, designers and manufacturers do not perform such analysis to achieve a precise design, and the vast accumulated experience leads to using metal plates of minimum 2-3 mm in aluminium (depending on the alloy and geometry) and 1.5-2 mm in pre-galvanised steel. Even if these two materials are a good choice against corrosion, they are usually coated with powder paint in the case of pre-galvanised steel and powder paint or anodising in the case of aluminium. It is worth considering that for thicknesses of pre-galvanised steel lower than 2mm, the edges that become unprotected after the cutting operation are covered by the remaining rusting residues of zinc, as a kind of self-protection.

In terms of regulation, there is no specific regulation for EM. In Europe, projects have to conform to Eurocodes regarding loads and, being conservative, the aforementioned thicknesses cover almost all cases. In the USA, there is a more conservative approach and it is usual to prescribe larger thicknesses because of civil liability concerns.

## 1.6 EXPANDED METAL GEOMETRY

The geometry of a rhombus-shaped EM mesh can be described using some parameters of the mesh and press-machine shown in FIG 5: Long way mesh (LW), short way mesh (SW), strand thickness (e), strand width (w), intercut (i), cut width (c), blade bevel width (b), and blade thickness (t). The elongated metal strips that form the mesh are called strands and the joining area of four strands is called *knuckle* or *bond*.

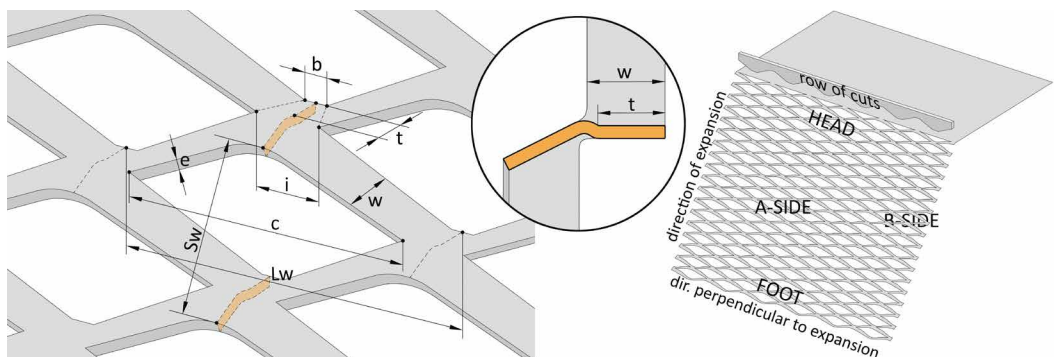


FIG. 5 A: Geometrical parameters of an EM mesh. B: Position and side-references related to the manufacturing process

Taking into consideration the available geometrical parameters and materials, one can get a countless number of different types of possible EM manufactures.

The use of EM as the external envelope in building façades has become more and more common in recent decades and designers often choose meshes with bigger nerves and holes than in other applications. Many manufacturing companies have a range of products under an architectural or decorative heading, including a wider variety of colours and sizes.

Analysis of shadow patterns cast by EM shows that those meshes with large openings are not the best option for façades of workspaces as the projected shadow patterns would involve glare and visual problems. Anyway, indoor diffusing technical sunscreens are usually used to solve this issue. Designers do install EM normally in façades of spaces used for sport, leisure, culture, commercial or circulation. EM with finer nerves offers more uniform shading patterns, but also can provide less shading performance, and therefore may be less effective in reducing overheating in the space.

EM elements shade rooms, but also act the other way round as a selective filter, that partially blocks selected parts of the field of vision. Due to EM geometry, this outward vision depends on the angle between the line of vision and the EM panel. If the observer's line of vision is perpendicular to the EM plane, the visual permeability of EM will depend on the EM mesh parameters, mainly strand width, as shown in FIG 7. With the change of this angle the permeability will show the angular selective performance of EM, meaning basically that at certain angles EM visibility will be minimised (with the observer looking down), while at the other, outward vision will be entirely blocked (with the observer looking at the steep angle up). This issue of the visibility and perforated envelope is addressed in detail in a recent PhD thesis (Alatawneh, Rosario, Germanà, & Reffat, 2016).

## 2 METHODOLOGY

Chronologically, our conducted research is divided into the following stages:

- Choice of assessment method and parameters
- Preparation of 3-d models
- Radiance simulation
- Verification of BSDF results comparing with previous lab results
- Extraction and processing of BSDF data
- Result interpretation

### 2.1 MEASUREMENT METHOD

The most popular measure of daylight performance in buildings was the daylight factor (light inside space/light outside the space ratio) (Robbins, 1985). This is quite easily measurable and provides the daylighting value at a point on a horizontal work plane in the room but does not provide any information about the direction of incident light and its distribution after transmission. Daylight factor provides information about daylight in the case of evenly overcast sky, and therefore is not suitable to assess the momentary values of the illuminance in the room resulting from direct sunlight, changing continuously according to the sun path. The development of simulation software demonstrated that more complex concepts than daylight factors were necessary.

Daylight Transmittance is the ratio of the amount of light transmitted through a window divided by the amount of light incident on its outside surface.

With Hemispherical Transmittance and Reflectance, one gets an overall amount of light going through, and reflected from the material but those magnitudes do not tell us anything about light distribution after transmission or reflection. Bidirectional Scattering Distribution Functions (Ward, Mistrick, Lee, McNeil, & Jonsson, 2011) describe the behaviour of light when reaching an opaque or translucent surface, for various angles of incidence of light on that surface and various angles of reflected and transmitted light. Based on Nicodemus and Klems' works (Klems, 1994; Nicodemus, 1965) a method was created to compile the directional behaviour of fenestration systems as regards reflection and transmission of radiation in a matrix. The BSDF of a surface is a four-dimensional function that, in simple words, describes how the surface scatters radiation. In the strict sense, the data that will be managed will be the BTDF (Bidirectional Transmittance Distribution Function) as the purpose of our work is the assessment of the daylight transmittance of EM.

Even if BSDF has the potential to provide detailed information about the way a material scatters light, the focus in this paper is not to assess the distribution of scattered light, but to assess how the overall transmittance or hemispherical transmittance is affected by different parameters of EM.

## 2.2 SOFTWARE AND SIMULATION RESULTS VERIFICATION

The 3-D models used for simulation were generated by a custom-made Grasshopper (for Rhino) algorithm, based on the parameters described in FIG 5. To ensure the high accuracy of the generated models, some of them were compared with 3-d scans of their real-life counterparts, which led to further modifications in the algorithm (Rico-Martinez, 2015).

The BSDF simulations were run via the *genBSDF* command from Radiance software (McNeil, Jonsson, & Appelfeld, 2011). This provided us with a large-size data pool, from which the data required to assess real-life daylighting situations could be later extracted.

Values from Klems-based BSDF were verified by comparison with experimental data provided at a previous laboratory assessment campaign in the context of a PhD research (Rico-Martinez, 2015). One of the main limitations of the lab setup (FIG 11.) used to measure the daylight transmittance of physical samples was the ability to measure the illuminance only in a small area and provide only specular transmittances. It was a sufficient method for measuring the direct specular transmittance, which is normally about 99% of the total, as it provided a uniformly lit constant light pattern, helped by a diffuser. However, this is a disadvantage when the indirect transmittance constitutes a more significant fraction of overall transmittance; e.g. meshes with bigger openings or extreme angles of incoming light directions, nearly parallel to the mesh plane, where interior reflections and consequent scattered light can be of greater importance.

The previous limitations are not an issue in the case of BSDF simulation, as it analyses the full spectrum of angles for both income and outcome directions.

## 2.3 PERFORMANCE COMPARISON - CHOSEN INPUT PARAMETERS

Based on the previous lab results and visual observation of various mesh variants, it was determined that the  $SW/w$  ratio or *EM opening ratio* (short way of mesh/strand width), could be used as a depictive feature of EM geometry (FIG 6.).

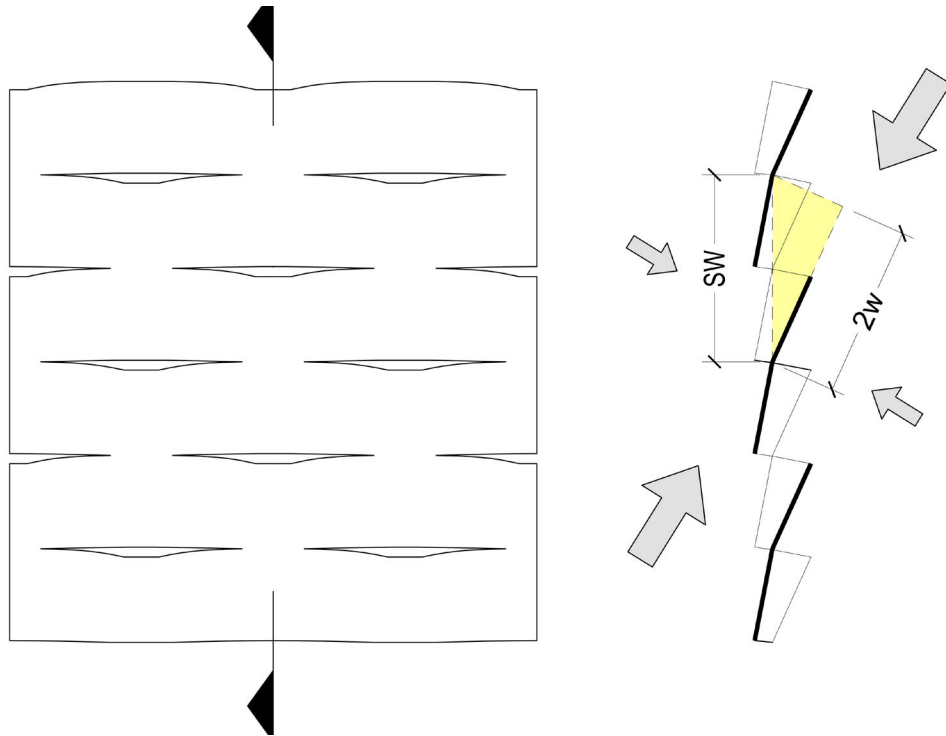


FIG. 6 Transmittance through a mesh with a low opening ratio ( $SW/w$ ) ratio

For this paper, strand width ( $w$ ) will be the main varying parameter, as it directly influences the  $SW/w$  ratio and the surface of the opaque areas of an EM mesh. All the geometrical parameters that do not rely on strand width will be kept constant, in order to allow for a reliable comparison.

### 2.3.1 Mesh type, time, position and localisation

In the presented paper, daylight transmittance through diamond-shaped EM shading devices is assessed in a vertical position with face "A" (FIG 5) on a south-facing façade, located in Madrid at most characteristic times of the year: solstices and equinoxes, as well as midday throughout the year.

- Mesh type – EM with diamond-shaped holes. Different variants of the most common EM type in building envelopes are simulated and compared.
- Position – south façade. Mesh placed in the typical, vertical position that provides the best shading performance. The south-facing position was chosen because it provides the longest sun exposure (north hemisphere).

- Location – Madrid. ( $40^{\circ} 25' N 3^{\circ} 42' W$ ). Madrid has a warm climate (annual temperature during the day:  $19.9^{\circ} C / 67.8^{\circ} F$ ) and one of the longest durations of sunshine in Europe (2769 hours per year). Latitude provides a variety of measurable sun angles throughout the whole year.

### 2.3.2 Mesh variants chosen for simulation. Strand width variation

A set of six modelled meshes (FIG 8.) was prepared, with only one differing parameter: strand width ( $w$ ).

The following three EM parameters: SW,  $d$ , and  $w$ , form a right-angled triangle. Consequently, keeping the dimension of the Short Way (SW) constant, any variation in strand width ( $w$ ) results in a change in the manufacture's blade descent ( $d$ ).

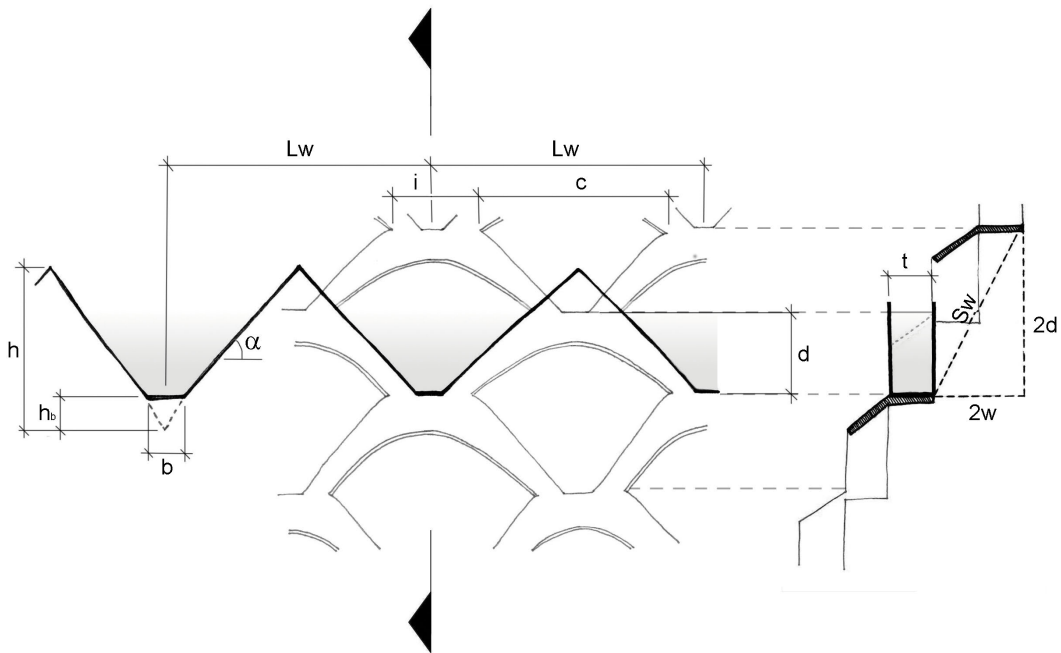


FIG. 7 Parameters of an EM mesh. Long way of mesh (LW), short way of mesh (SW), intercut ( $i$ ), cut width ( $c$ ), blade bevel width ( $b$ ), blade thickness ( $t$ ), blade descent ( $d$ ), blade tooth's height ( $h$ ), bevel's height ( $h_b$ ), blade's slope ( $\alpha$ )

Besides, the slope of the blade ( $\alpha$ ) also varies if the strand width ( $w$ ) is changed and all other parameters are fixed.

The limits for the strand width ( $w$ ) are:

- A  $w > e$ . This is an approximate limit due to fabrication conditions.
- B  $w < SW/2$ . Elsewhere, the blade does not descend; therefore, the expansion of the mesh does not occur.

The following table shows the parameters of the EM meshes assessed.

TABLE 1 Values of the geometrical parameters defining the assessed EM meshes

LW	SW	W	E	B	I	D	A	SW/W
200	73	6	1	7	33	36.00	24.23	12.17
200	73	12	1	7	33	34.47	23.31	6.09
200	73	18	1	7	33	31.75	21.65	4.06
200	73	24	1	7	33	27.50	18.97	3.05
200	73	30	1	7	33	20.79	14.57	2.44
200	73	35	1	7	33	10.36	7.38	2.09

Obviously, the increase of strand width ( $w$ ) is inversely proportional to the one of the EM opening ratio ( $SW/w$ ). This way, the thinner the EM strands, the wider the mesh expansion and, therefore, the openings are larger. Logically, high values of opening ratio should lead to high values of transmittance.

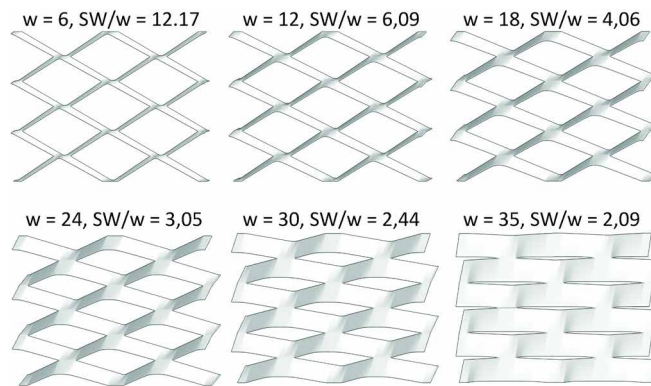


FIG. 8 Front views of EM geometrical variants used for the assessment

### 2.3.3 Mesh variants chosen for simulation. Colour variation

The impact of colour will also be considered, assessing each mesh in three colours: black, grey, and white. The same colour and reflectance values will be used, as in the previous lab assessments with real meshes. For those lacquers, the following reflectance data through spectrophotometry was obtained:

TABLE 2 Total reflectance and reflectance without specular component of analysed EM meshes finishing lacquers (measured with spectrophotometer)

COLOUR	REFLECTANCE (%)		REFLECTANCE WITHOUT SPECULAR COMPONENT (%)	
White	84.1	+/- 0.3	80.9	+/- 0.6
Grey	43.1	+/- 0.2	39.5	+/- 0.3
Black	4.4	+/- 0.1	4.2	+/- 0.1

## 2.4 EXTRACTION OF BSDF DATA FOR REAL DAYLIGHT SITUATIONS.

### 2.4.1 Data extraction

In the case of this study, the focus is on the overall percentage of transmitted rays, i.e. hemispherical transmittance (specular + scattered), which will be later referred to as *transmittance*. This paper does not differentiate scattered from specular light, as specular transmittance through EM is much higher than scattered, and hemispherical data is needed to compare the overall behaviour of different meshes at different moments.

Even if BSDF has the capacity to provide directional information about transmittance, for the aim of this paper, comparing overall data in a simplified manner is needed. Anyway, our previous experience tells us that, except for incoming light directions nearly tangential to the mesh plane, the majority of the light through the wide variety of EM meshes assessed in our computer BSDF assessment consists of specular transmittance. The rest of the values, surrounding this peak, refer to scattered transmission, which comes from the reflection of light in the mesh's strands. Among these values, we could observe some of the most significant reflection directions where transmittance values are higher. Anyway, the specular transmission takes more than 90% of the hemispherical transmission (Rico-Martinez, 2015).

In fact, we had to use a logarithmic scale (base 10) for graphs representing transmittance values in different directions because the value of the transmittance (ratio of incoming to outgoing light) in the specular direction was often bigger than 1% and lower than 0.01% for the scattering directions. The use of the logarithms of the transmittance values rather than the actual transmittance values reduces a wide range to a more manageable size. Moreover, human senses and perception are supposed to work in a logarithmic way (hearing, sight, etc.).

As the shading performance of EM is being assessed, direct sun radiation in real-life cases is assumed, i.e. one main incoming light direction.

One of the challenges was that the data about incoming light directions from BSDF simulation is related to each Klems patch and does not correspond precisely to the directions of sunlight obtained for real situations (described by linear sun paths, the daily arc-like path that the sun appears to follow across the sky). It was necessary to properly adapt the BSDF simulation data to assess the mesh's real-life performance.

BSDF data follow a coordinate system, called the Klems angle basis, which was designed specifically to simplify a matrix multiplication to model multi-layer window heat gains. The Klems angle basis has 145 input and output directions. Each direction is related to a patch of the hemisphere and all the patches have roughly the same cosine-weighted solid angle. Consistency in the cosine-weighted solid angle ensures that the contribution to hemispherical transmittance is roughly the same for all patches (McNeil, Jonsson, Appelfeld, Ward, & Lee, 2013).

Extracting the useful data meant selecting the Klems patches involving the desired sun directions. This resulted in obtaining patterns of Klems patches (FIG. 8) resembling a pixelated version of the actual sun path (FIG 9. S.P.). As the selected sun paths do not necessarily cross the centres of the patches, in some cases, it has been necessary to obtain transmittance values for additional regions (FIG 9. B) in order to calculate arithmetic averages of transmittance values of the involved patches.

The following software has been used to obtain the sun paths: Ladybug Tools (Grasshopper plugin for Rhino 5) (Sadeghipour Roudsari n.d.) and Curic Sun plugin for Sketch-Up (Curic Studio n.d.).

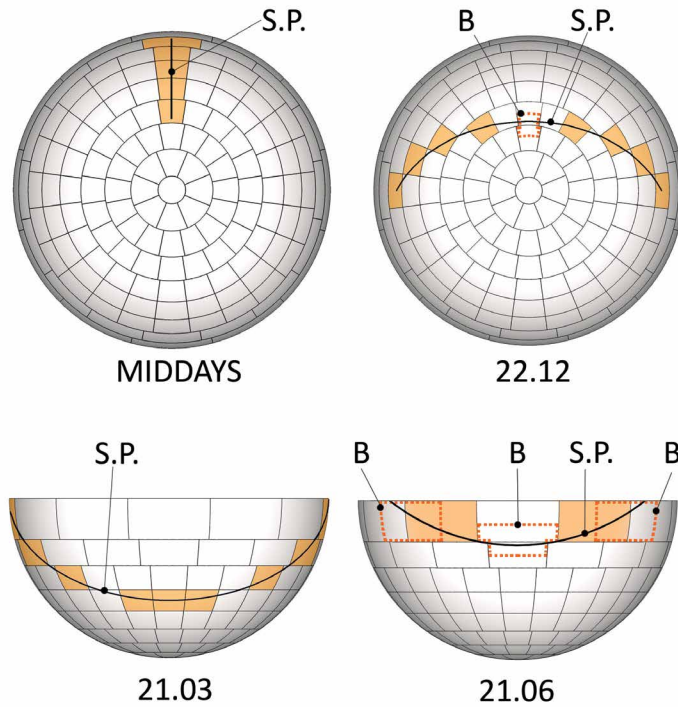


FIG. 9 Examples of sun paths (S.P.) related to patch sets on the Klems dome. Midday, winter solstice (22.12), equinox (21.03) and summer solstice (21.06)

#### Procedure for transmittance assessment throughout a day

To obtain the data about transmittance through a particular day, the geolocation and position of the mesh, as well as the date, were first specified. One could then obtain the corresponding sun-path, which describes the consecutive sun positions throughout that day.

Each Klems patch was described with the direction defined by its geometrical centre (FIG 10. C) and the closest point from each patch centre on the sun path was found. That point represents a sun position related to a daytime-value (FIG 10. C'). As a side effect, the method resulted in atypical values of daytime slots in the abscissa (e.g. 7:12, 9:36, 14:24, and 16:48) but related to quite precise transmittance values.

## Procedure for transmittance throughout a year

Likewise, midday transmittance values through the year (FIG 9. midday) were obtained considering the 365 days of the year at 12:00, picking the incident patches with centres on that longitude fragment, finding the sun positions that match with the patch centres and finally matching the date values to those points. Again, this resulted in atypical values of date slots in the abscissa (e.g. 21<sup>th</sup> January, 23<sup>rd</sup> February, 21<sup>st</sup> March, 17<sup>th</sup> April, and 24<sup>th</sup> May) but related to precise transmittance values.

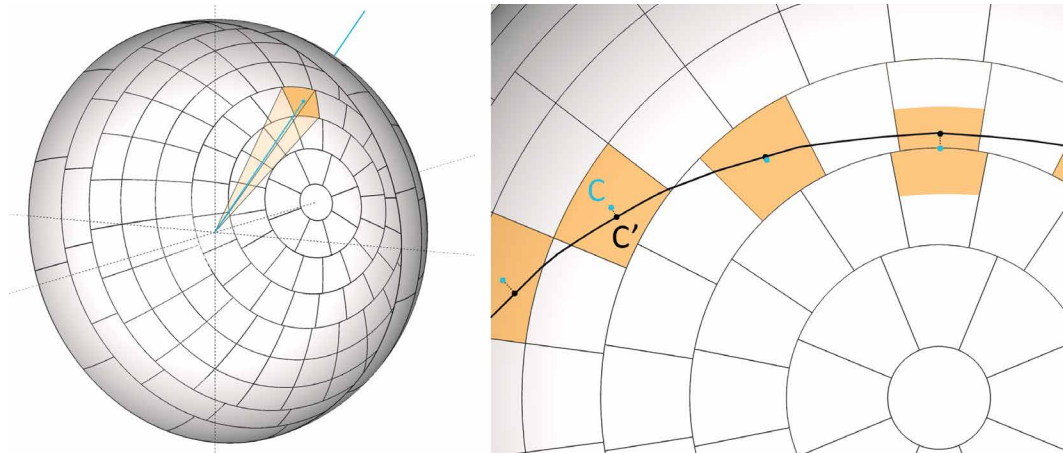


FIG. 10 Geometrical centre of a single patch. [C] patch centre [C'] the closest point on the sun path

## 3 PREVIOUS RESEARCH AND EXPERIMENT

### 3.1 COMPARISON OF LAB DATA AND BSDF SIMULATION RESULTS

In the aforementioned research (Rico-Martinez, 2015), the BSDF data running simulations were validated for models that were previously assessed in the laboratory (FIG. 11) with real samples. Overall, apart from those directions with the most extreme angles, the BSDF simulation results didn't show much deviation from lab results with an average of 4.96% (considering all incident light angles, including the most extreme, tangential ones, the overall average of deviation was 10.17%).

For those specific extreme angles, transmittance values were significantly higher for the computer simulation data and it was concluded that the physical model readings were significantly lower than the real ones, due to the lab setup limitations. However, the BSDF data obtained were consistent, as has been proven by the work and practice of many authors. (McNeil, Jonsson, Appelfeld, Ward, & Lee, 2013) (De Michele, Loonen, Saini, Favoino, Avesani, Papaiz & Gasparella, 2018) (Saini, Loonen, & Hensen, 2018).



FIG. 11 [a] Scheme of Lab assessment setup [b] Picture of the setup

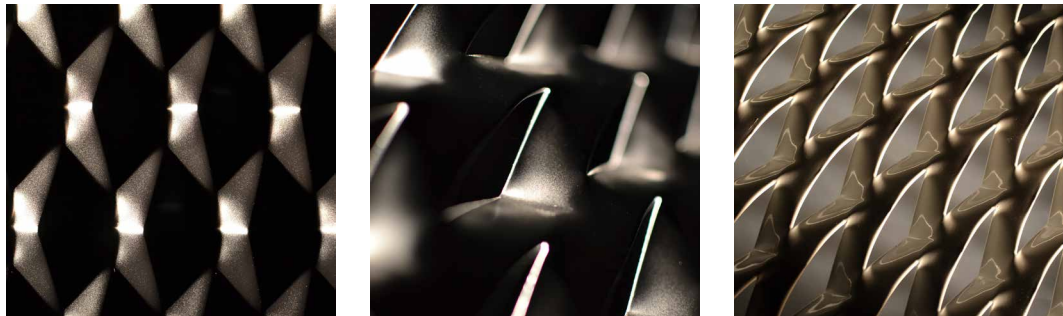


FIG. 12 Lit EM meshes in the lab setup

## 4 RESULTS AND DISCUSSION

In the following sections, the data obtained through simulation is presented in the form of graphs for the aforementioned colours, dates, and six types of EM.

The first three sets of graphs deal with the transmittance through the day.

The subsequent set of graphs shows midday transmittance values throughout the year.

Then, two sets of graphs are included using the same data but rearranging it. This way the influence of strand width on daily transmittance is described, by times of the day, and the influence of strand width on midday transmittance, by dates.

This section finishes with a table that quantifies the influence of colour on transmittance.

It is worth remembering that the following charts offer hemispherical transmittance data, the sum of scattered and specular light transmittance. For each incoming light direction, we obtain a unique value of transmittance expressed as a percentage (percentage of the incoming light transmitted through the EM mesh).

Likewise, it is important to remember that only direct incoming light is considered, i.e. clear sky conditions, which are the *raison d'être* of solar shadings.

## 4.1 TRANSMITTANCE VALUES THROUGH THE DAY BY STRAND WIDTH FOR SPECIFIC COLORS AND DATES

### 4.1.1 Winter Solstice

Besides being the shortest day of the year, the lowest solar angles are characteristic of the winter solstice (FIG 13). In such conditions, all simulated variants of EM seem to function as expected, with transmittance values dropping very slightly towards midday as solar height increases. The only visible divergence seems to be a slight increase in transmittance around midday for the 12 mm strand width mesh ( $w=12\text{mm}$ ). This can be due to the complex geometry of EM or to method inaccuracies like the ones described in 2.4.1 about the relation between the real sun path and the available light directions from the Klems basis.

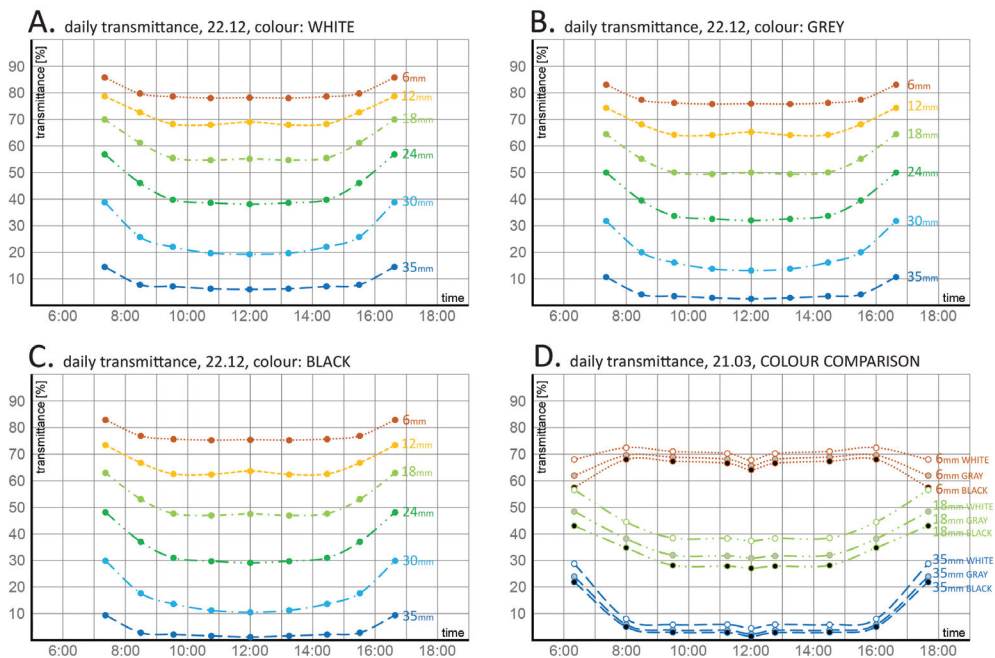


FIG. 13 Transmittance data throughout the day for the winter solstice. Each curve corresponds to a given strand-width,  $w$  (mm). The first three graphs correspond to each colour: white, grey and black. The fourth graph shows the superposition of curves for the three colours and three strand-widths: 6, 24 and 35mm

It also worth noticing, that for most of the day, the transmittance curve of  $w=35\text{mm}$  mesh seems to run almost flat, with transmittance below 10% for white and 4% for black finish.

In any case, all the curves present low amplitudes and moderate variations throughout the day due to colour. Almost all the curves show an upwards concavity with maximum values at dawn/dusk and minimum at noon. The 24 mm and 25 mm strand width meshes show the biggest amplitudes.

Bigger increases regarding noon values appear for the intermediate meshes ( $w=24$  mm,  $w=30$ mm). Those increases approach 20 percent points, whereas for the extreme meshes, with maximum and minimum translucency ( $w=6$  mm and  $w=35$ mm), those differences drop to around eight percent points.

In general, there is a great transmittance increase from  $w=35$ mm to  $w=6$ mm (around 70-75 percent points), which shows that the effect of modifying the strand width in winter is substantial.

The transmittance increase due to the colour of the mesh is greater for the intermediate meshes ( $w=24$  mm,  $w=30$ mm), which present an increase of 10 percent points at 12:00 when it changes from black to white. The difference between black and grey is low, almost half of the difference between grey and white.

### 4.1.2 Spring/Autumn Equinox

At the equinox (FIG 14.), EM meshes with strand width  $w=18$ mm and higher seem to perform as expected with lowest transmittance values at midday, and rise towards dawn/dusk. It is also worth noticing that for a significant portion of the day (even around 8:30-15:30 for 35mm mesh) transmittance values seem to remain roughly constant.

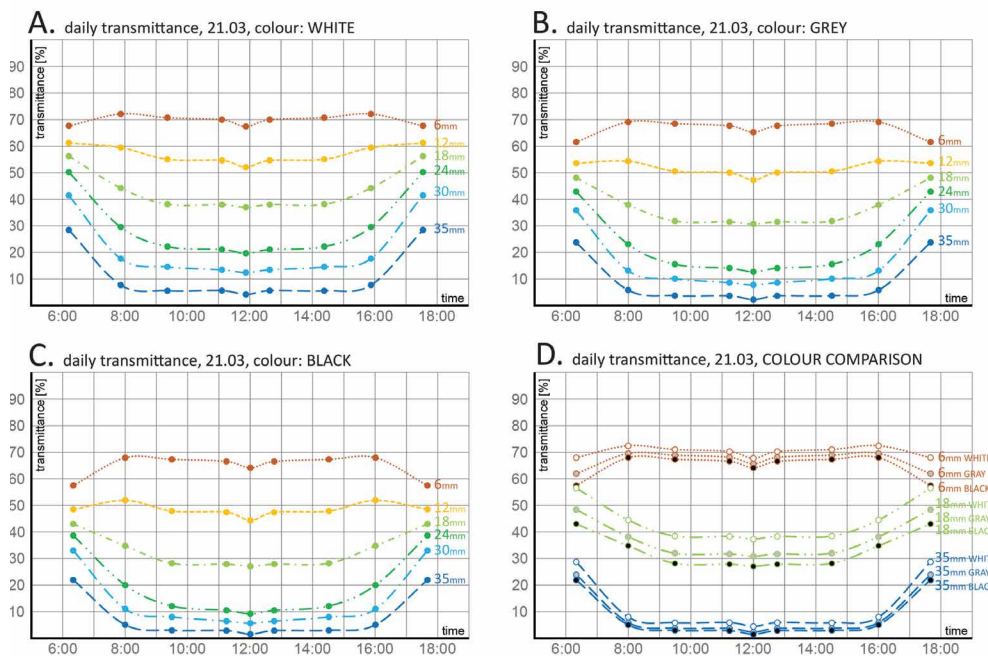


FIG. 14 Transmittance data through the day for spring/autumn equinox (21 March / 22 September). Each curve corresponds to a given strand-width,  $w$  (mm). The first three graphs correspond to each colour: white, grey and black. The fourth graph shows the superposition of curves for the three colours and three strand-widths: 6, 24, and 35mm

12mm mesh seems to maintain quite similar values throughout the day.

With the exception of the 6 mm strand width mesh, again the curves show upwards concavities but with higher differences between dawn/dusk and midday than in the winter (FIG 13.) and summer solstices (FIG 15.). The maximum amplitude is about 30 percent points. This agrees with the sun path, as it is rising towards midday and the EM strands are blocking a greater amount of rays. However, when the strand width value is low, those differences are blurred.

If one pays attention to the effect of colour, it can be noticed that it is more noticeable at dawn/dusk with a variation of around 10 percent points from black to white. This is more evident for the intermediate meshes (w=12 mm, w=18 mm, w=24 mm) and gets lower as strand width increases. For w=35 mm the colour effect is around three percent points at midday and seven points at dawn/dusk.

For the rest of the daytime, in general, the effect of colour is less evident.

No noticeable difference arises in the jumps from black to grey and from grey to white.

### 4.1.3 Summer Solstice

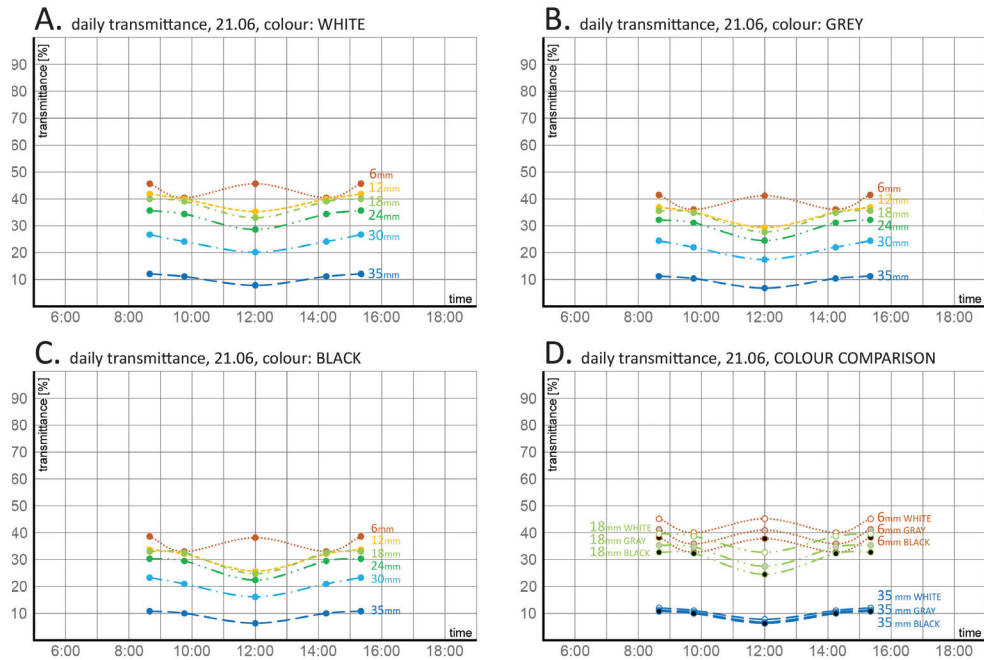


FIG. 15 Transmittance data through the day for the summer solstice (21<sup>st</sup> June). Each curve corresponds to a given strand-width, w (mm). The first three graphs correspond to each colour: white, grey, and black. The fourth graph shows the superposition of curves for the three colours and three strand-widths: 6, 24, and 35mm

Summer solstice means the highest sun angles and the longest day of the year but the shortest exposure of the southern façades. That is why the graphs (FIG 15) show quite a narrow daytime spectrum.

Besides, observing the Klems patch pattern obtained to fit the summer solstice sun path in Madrid (FIG 9.), it's evident that the sun path crosses very few patches. This is clearly one of the limitations of using the classic Klems dome method and it can be solved through the Tensor Tree method possibilities (De Michele et al., 2018).

EM meshes with strand width  $w=18$  mm and higher seem to perform as expected, with the lowest transmittance values at midday. The flattening of the curves does not appear, but that might be due to a low number of control points.

In general, the upwards concavity remains with maximum values at dawn/dusk except for the 6 mm strand width mesh. This striking inversion of curvature can be explained by the shadow patterns of the mesh for corresponding lighting directions (FIG 16A). For the direction corresponding to the hour 9:45, see-through openings constitute below 15% of the overall mesh area, while for the angle at 12:00 they occupy over 31%.

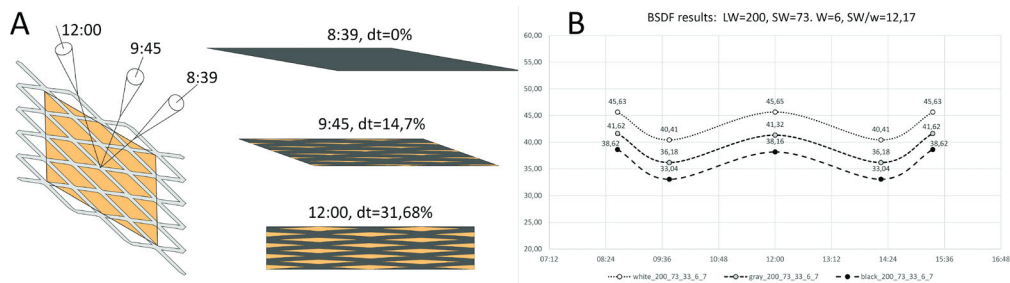


FIG. 16 [a] Shadow pattern analysis and transmittance analysis for the summer solstice (6mm strand width mesh) [b] Previously conducted lab results graph for a similar EM mesh, also showing maximum transmittance at midday.

In addition, a transmittance curve based on our physical lab measurements of a similar EM mesh seems to confirm that direct transmittance increases close to midday when it is normally expected to be at its lowest (FIG 16B)

The maximum transmittances, for white colour, were around 70%, with  $w=6$ mm in winter and 72% at the equinox. In summer, that maximum value drops to 46% due to the solar height.

The minimum values in summer are higher than in winter or the equinoxes.

The effect of the strand width is more noticeable on white coloured meshes than on black ones. For instance, at 10:00 and 14:00 the transmittance from  $w=6$ mm to  $w=35$ mm leaps 23 points on black, 27 points on grey and 30 points on white coloured meshes.

## 4.2 MIDDAY TRANSMITTANCE VALUES THROUGH THE YEAR BY STRAND WIDTH FOR SPECIFIC COLOURS

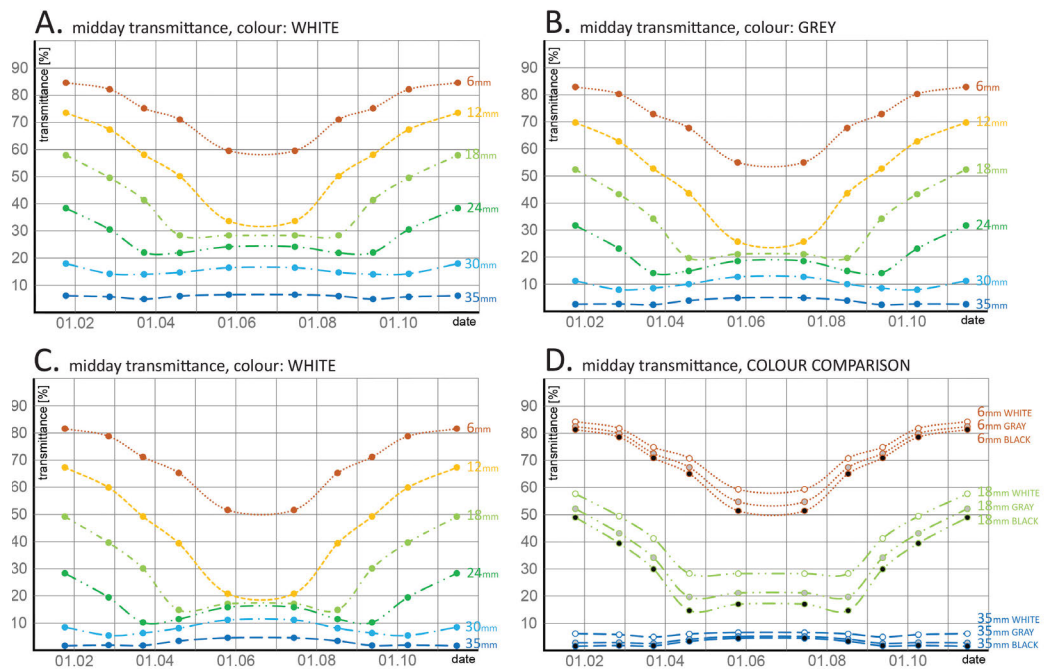


FIG. 17 Midday transmittance data throughout the year. Each curve corresponds to a given strand-width,  $w$  (mm). The first three graphs correspond to each colour: white, grey, and black. The fourth graph shows the superposition of curves for the three colours and three strand-widths: 6, 24, and 35mm

This set of graphs (FIG 17) analyses how the date of the year affects transmittance at midday (12:00).

As previously indicated (section 2.3.2), high values of opening ratio should involve bigger apertures and lead to higher transmittances and, consequently, the increase of strand width is inversely proportional to the transmittance.

The results shown here are coherent with this logic: on white meshes at the winter solstice one can observe transmittance values of 77% for  $w=6\text{mm}$  and 7% for  $w=35\text{mm}$ .

At the summer solstice, the transmittance differences drop because of the higher sun position, which reaches the façades tangentially and finds fewer openings for direct transmission.

Following the same logic, 35 mm strand width meshes show very few variations throughout the year, since their transmittance is very low.

The 6mm strand width mesh differs clearly from the rest at the summer solstice, with a transmittance nearly 25% higher than the following mesh. The transmittances of the rest of the meshes in summer show much smaller differences.

In winter, the increase of transmittance values is quite homogeneously proportional to the opening ratio.

For summer and lower opening ratios, midday-transmittances are actually higher than for winter. Similar data has been registered from lab assessment for meshes with low opening ratios as well (FIG 18). The hypothetical cause of this increase in transmittance in summer might be the additional transmission of incoming light after interior reflections on the surfaces of the mesh. The fact that darker colours of the mesh seem to amplify this trend seems to back it up.

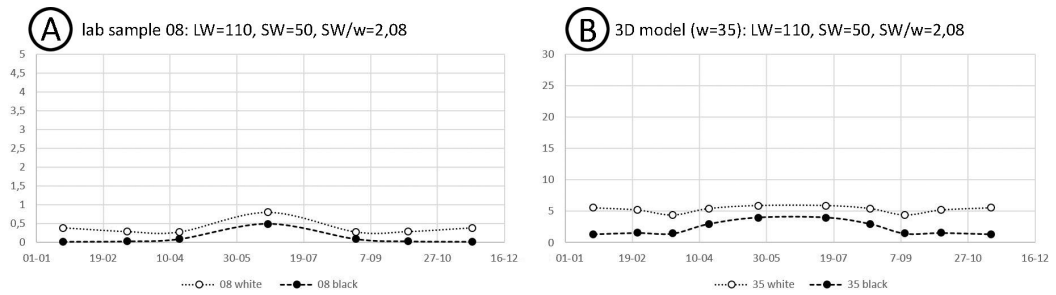


FIG. 18 Lab and BSDF results for EM meshes with similar proportions (Both meshes have an opening ratio of  $SW/w=2,08$ ) [a] Lab results [b]. BSDF results

### 4.3 INFLUENCE OF STRAND WIDTH ON DAILY TRANSMITTANCE, BY TIMES OF THE DAY, FOR DIFFERENT DATES AND WHITE COLOUR

These curves (FIG 19) have been traced in order to directly show the relation between strand width and transmittance variation. Overall, it can be stated that the relation (the slope of the curves) is similar for different daytimes except for the dawn in the equinoxes.

Coherently, the amplitude of the curves is higher for the winter solstice with big transmittance differences for different strand widths. As seen before, these differences attenuate when passing to the equinoxes and reaching the summer.

Focusing on the winter solstice and excluding the dawn (7:21) data, simplified generalist statements like the following can be done: For a south-facing mesh located in Madrid, the variation of daylight transmittance is inversely proportional to the variation of strand width. That relation is practically linear with such a slope that an increase of 5 mm in strand width implies a decrease of around 12-15% of the transmittance.

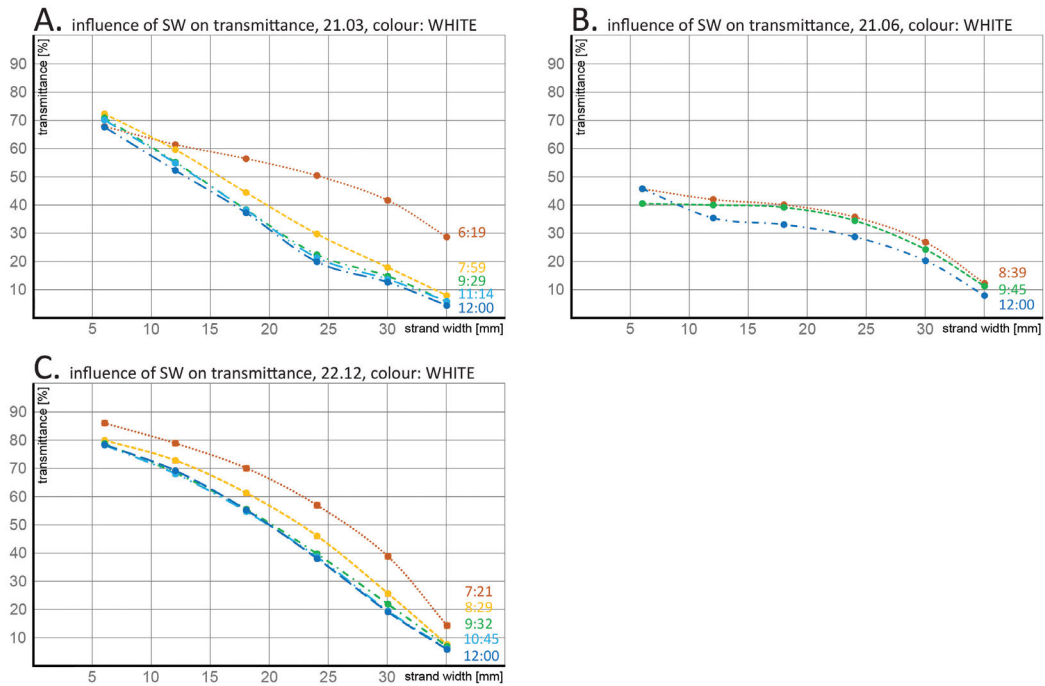


FIG. 19 Transmittance data versus EM strand width for white coloured meshes. Each curve corresponds to a given time of the day. The three graphs correspond to different dates: equinox, summer solstice, and winter solstice

#### 4.4 INFLUENCE OF STRAND WIDTH ON MIDDAY TRANSMITTANCE, BY DATE FOR SPECIFIC COLOURS

In the same direction as that of the previous graphs, the midday transmittance - strand width relation has been expressed, but collecting in each graph the curves corresponding to several dates of the year (FIG 20).

It is noticed that, for the winter dates, the decline in transmittance as strand width increases is almost linear and with a similar slope until a certain value of the strand width. From  $w=24$  mm, the curves show some curvature towards a horizontal asymptote that responds to the fact that it is getting close to zero transmittance. Nevertheless, moving away from winter, the curves show an increase of the slope (higher transmittance fall-offs for given strand width growths) and an inflection point. Getting closer to the summer, the inflection point moves to higher values of the strand width. A noticeably horizontal stretch is also observed where transmittance does not vary with the strand width. Those curves recover a certain slope to drop towards zero transmittance for high values of  $w$  (low values of the opening ratio).

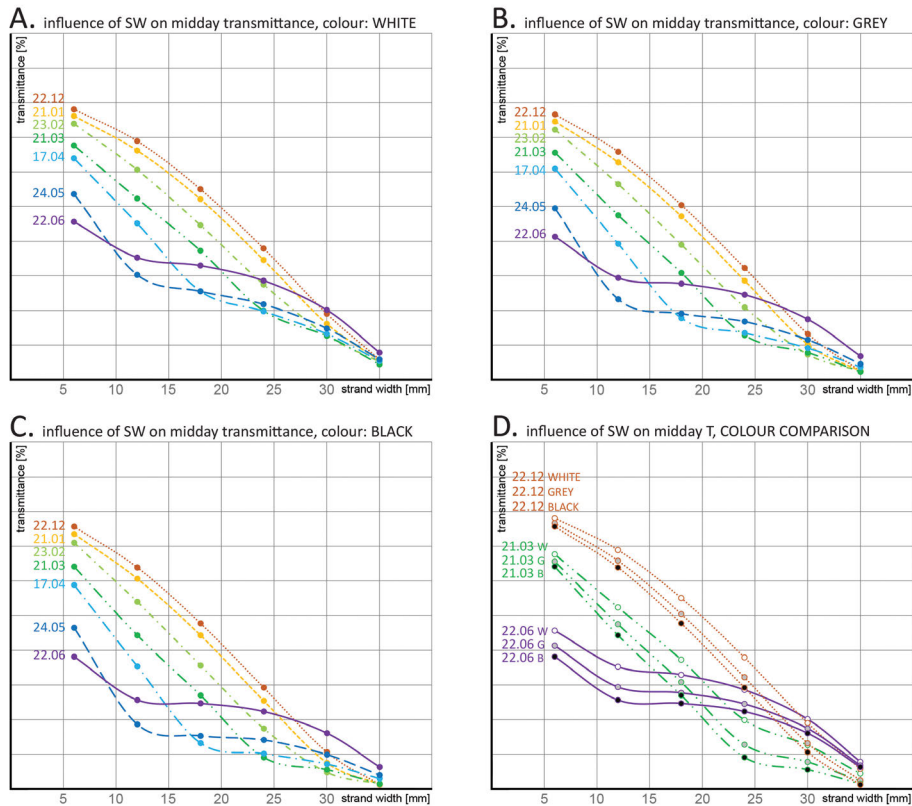


FIG. 20 Midday transmittance data versus EM strand width. Each curve corresponds to a given date. The three first graphs correspond to different colours: white, grey and black. The fourth graph shows the superposition of curves for the three colours and three dates: Winter solstice, equinox and summer solstice

## 4.5 INFLUENCE OF COLOUR ON TRANSMITTANCE

As could have been expected, the colour of the EM device affects the transmittance to a certain degree. The highest transmittance values were achieved for the white meshes and lowest for the black ones.

An overall difference of transmittance between black and white EM stayed between the range of 1.13% and 13.52%, with an average of 7.67%, which is notable. As seen in the comparison (TABLE 3), the overall influence of colour relies on the opening ratio and sun angles. One could attribute that reliance on the amount of light transmitted by interior reflections from the surface of the mesh, which varies due to the complex geometry of EM (FIG 21). Overall, for a given location, the influence of colour on transmittance seems to be the strongest for diamond shaped EM meshes with SW/w ratios between 0.25 and 0.33.

TABLE 3 Influence of colour on transmittance decrease (compared to white mesh)

DATE	22.06											
colour	grey						black					
time/w	6	12	18	24	30	35	6	12	18	24	30	35
8:39	4.01%	4.87%	4.29%	3.34%	2.23%	0.82%	7.01%	8.12%	6.95%	5.28%	3.42%	1.27%
9:45	4.24%	4.74%	4.07%	3.12%	2.06%	0.74%	7.38%	7.84%	6.53%	4.88%	3.17%	1.13%
12:00	4.33%	5.84%	5.22%	4.07%	2.70%	1.03%	7.49%	9.59%	8.26%	6.25%	4.05%	1.50%
14:15	4.24%	4.74%	4.07%	3.12%	2.06%	0.74%	7.38%	7.84%	6.53%	4.88%	3.17%	1.13%
15:21	4.01%	4.87%	4.29%	3.34%	2.23%	0.82%	7.01%	8.12%	6.95%	5.28%	3.42%	1.27%
average	4.16%	5.01%	4.39%	3.40%	2.26%	0.83%	7.25%	8.30%	7.04%	5.31%	3.44%	1.26%
summary	min	0.74%	max	5.84%	avg total	3.34%	min	1.13%	max	9.59%	avg total	5.43%

DATE	21.03											
colour	grey						black					
time/w	6	12	18	24	30	35	6	12	18	24	30	35
6:19	6.06%	7.63%	8.13%	7.34%	5.69%	4.84%	10.48%	13.04%	13.52%	11.88%	8.80%	6.85%
7:59	2.90%	5.07%	6.33%	6.53%	4.73%	2.09%	4.48%	7.84%	9.72%	9.83%	6.95%	2.98%
9:29	2.16%	4.51%	6.44%	6.80%	4.66%	2.08%	3.70%	7.48%	10.26%	10.39%	6.85%	2.90%
11:14	2.18%	4.60%	6.58%	7.18%	5.02%	2.21%	3.71%	7.53%	10.44%	10.92%	7.33%	3.06%
12:00	2.10%	4.85%	6.45%	7.09%	4.85%	2.14%	3.58%	8.04%	10.25%	10.78%	7.09%	2.98%
12:46	2.18%	4.60%	6.58%	7.18%	5.02%	2.21%	3.71%	7.53%	10.44%	10.92%	7.33%	3.06%
14:31	2.16%	4.51%	6.44%	6.80%	4.66%	2.08%	3.70%	7.48%	10.26%	10.39%	6.85%	2.90%
16:01	2.90%	5.07%	6.33%	6.53%	4.73%	2.09%	4.48%	7.84%	9.72%	9.83%	6.95%	2.98%
17:41	6.06%	7.63%	8.13%	7.34%	5.69%	4.84%	10.48%	13.04%	13.52%	11.88%	8.80%	6.85%
average	3.19%	5.38%	6.82%	6.98%	5.01%	2.73%	5.37%	8.87%	10.91%	10.76%	7.44%	3.84%
summary	min	2.08%	max	8.13%	avg total	5.02%	min	2.90%	max	13.52%	avg total	7.86%

DATE	22.12											
colour	grey						black					
time/w	6	12	18	24	30	35	6	12	18	24	30	35
7:21	1.92%	3.54%	4.80%	6.31%	6.65%	3.57%	2.58%	4.95%	6.67%	8.43%	8.64%	4.78%
8:29	1.61%	3.79%	5.42%	6.09%	5.43%	3.43%	2.51%	5.57%	7.82%	8.72%	7.80%	4.68%
9:32	1.61%	3.37%	4.82%	5.56%	5.56%	3.45%	2.58%	5.38%	7.50%	8.42%	8.04%	4.69%
10:45	1.47%	3.20%	4.70%	5.62%	5.61%	3.19%	2.43%	5.25%	7.42%	8.54%	8.12%	4.34%
12:00	1.48%	3.11%	4.61%	5.68%	5.85%	3.36%	2.43%	5.06%	7.32%	8.67%	8.43%	4.56%
13:15	1.47%	3.20%	4.70%	5.62%	5.61%	3.19%	2.43%	5.25%	7.42%	8.54%	8.12%	4.34%
14:28	1.61%	3.37%	4.82%	5.56%	5.56%	3.45%	2.58%	5.38%	7.50%	8.42%	8.04%	4.69%
15:31	1.61%	3.79%	5.42%	6.09%	5.43%	3.43%	2.51%	5.57%	7.82%	8.72%	7.80%	4.68%
16:39	1.92%	3.54%	4.80%	6.31%	6.65%	3.57%	2.58%	4.95%	6.67%	8.43%	8.64%	4.78%
average	1.63%	3.44%	4.90%	5.87%	5.82%	3.41%	2.52%	5.26%	7.35%	8.54%	8.18%	4.61%
summary	min	1.47%	max	6.65%	avg total	4.18%	min	2.43%	max	8.72%	avg total	6.08%

DATE	YEAR AVERAGE (AT NOON)											
colour	grey						black					
w	6	12	18	24	30	35	6	12	18	24	30	35
average	2.90%	4.78%	5.90%	6.11%	4.80%	2.62%	4.86%	7.77%	9.30%	9.28%	7.02%	3.65%
summary	min	0.74%	max	8.13%	avg total	4.52%	min	1.13%	max	13.52%	avg total	6.98%

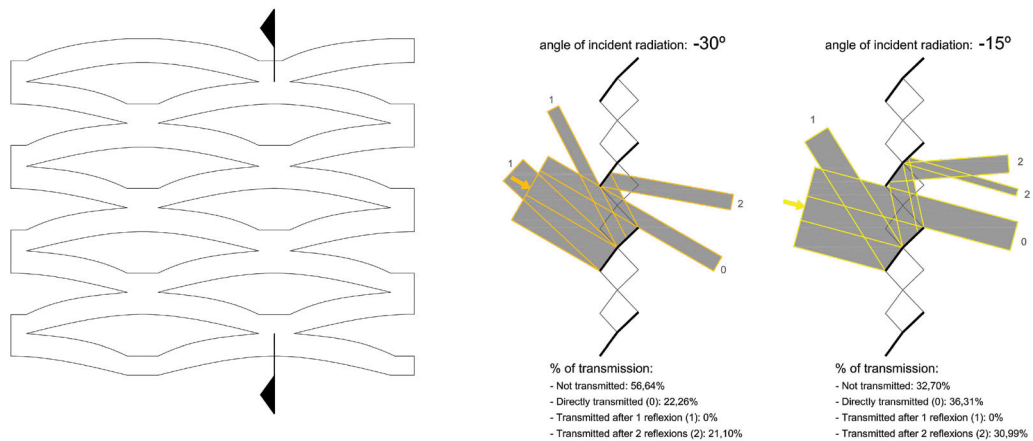


FIG. 21 Examples of simplified interior reflections (considering specular reflectance)

## 5 CONCLUSIONS

### 5.1 PARAMETERS AFFECTING TRANSMITTANCE - SUMMARY

The parameters affecting transmittance are divided into three general groups:

- EM mesh geometry: shape and proportions
- Incoming light direction (in relation to mesh face): sun azimuth (longitude) and solar height (latitude)
- EM mesh colour

To assess real-life situations it is necessary to refer the light direction to mesh localisation and position, time, and date. Overall, the impact of each parameter on transmittance depends on other parameters. As seen, transmittance depends on both mesh geometry and sun angle; it must be considered to what extent the decrease of the opening ratio ( $SW/w$ ) of Expanded Metal meshes results in lower transmittances for given solar heights.

Mesh proportions - The most significant factor in terms of mesh geometry is definitely the opening ratio ( $SW/w$ ), although, as seen in the results, this is not a linear, easy-to-describe general correlation between the opening ratio and daylight transmittance. The change of strand width also influences other proportions. It is worth remembering, those other parameters can also strongly influence the mesh geometry, affecting the shading performance. The complex geometry of the EM also makes its shading performance less predictable in terms of light direction.

In general, greater transmittance increases have been observed due to the variation of strand width of EM meshes at the winter solstice (70 to 75 percent points from  $w=35$  to  $w=6$  mm).

As stated in section 4.3, on the winter solstice, for most times of day, a south-facing mesh in Madrid presents a nearly linear variation of daylight-transmittance inversely proportional to the variation of strand width; an increase of 5 mm in strand width implies a decrease of around 12-15% of the transmittance.

It is worth mentioning that low values of the opening ratio lead to meshes that almost totally prevent direct vision through them. This is a very limiting condition for an element to be included in a complex fenestration system.

### Solar Height

This is the most obvious and one of the most important factors affecting the transmittance values. As a rule, the higher the position of the sun, the lower the transmittance. However, as seen on the graphs that show transmittance throughout the year (section 4.2), the relationship is not linear and once the solar height and SW/w ratio are high enough, an inversion of the curvature may occur.

Solar height is related to the season, of course.

The maximum transmittances, for white colour, were around 70% with  $w=6\text{mm}$  in winter and 72% at the equinox. In summer, that maximum value drops to 46% of the solar height.

The minimum values in summer are higher than in winter or the equinoxes. Minimum summer transmittance with black colour is around 7%, while at the equinox it drops to 2% and in winter to 1%. These values always appear at midday.

### Sun Azimuth

Similarly to the solar height, the transmittance is at its maximum when the sun azimuth is perpendicular to the mesh plane and decreases as it moves towards the mesh plane. Although, in general, solar height seems to be slightly more influential on the transmittance, overall sun direction is always a sum of both latitude and longitude. This sometimes leads to counterintuitive outcomes, such as the temporary rise of transmittance towards midday, as seen for the summer solstice in FIG 15.

### Colour

Colour influences the indirect transmittance (transmittance through internal reflection). Therefore, the influence of colour relies on SW/w and the direction of incoming light. As expected, darker colours led to a decrease of transmittance.

## 5.2 GENERAL ASPECTS FOR FAÇADE DESIGNERS.

### 5.2.1 Position and tilt of the building envelope

The data shown in this paper relates to an envelope facing directly south, and perpendicular to the ground. Change of either orientation or tilt of the EM's surface obviously changes the relative sun angles, strongly affecting the performance. Therefore, it is essential to consider each aspect. In general, an upwards tilt of the envelope usually causes an increase of transmittance while a downward tilt decreases it. A change of orientation for the façade changes the timeslot in which the direct sunlight reaches it, which, of course, also affects the performance.

### 5.2.2 The necessity of detailed research and on purpose simulation

Due to the multiple variable conditions of the issue it is not possible to state strictly linear relations between any particular parameter (or group of parameters) and the shading performance of EM. While most assumptions about the influence of those parameters are correct, they are too general to reliably predict the real-life performance. For proper assessment, it is necessary to run a specific simulation, which takes into account the specific mesh model and colour, as well as its position and location.

### 5.2.3 Presence of shadow patterns

Due to the visible shading patterns, EM meshes are generally not suitable for any spaces in which precision work is done, such as labs, workshops, or offices. For such spaces, it is recommended to use either fine (densely distributed, small openings) EM meshes, or an additional layer of diffuse material.

### 5.2.4 The complexity of façade systems

It is worth remembering that EM meshes are usually just a part of a façade/fenestration system, with its different layers working as a whole. Therefore, to analyse the whole behaviour it is necessary to include all layers and elements of the façade. Furthermore, to obtain real-life performance it is also crucial to take into account the environmental data, such as the intensity of light, or amount of incoming diffused light. Only then can the illumination of the building's interior and solar energy gains be closely predicted and balanced.

## 5.3 OBSERVATIONS ON BSDF DATA FOR REAL LIFE DAYLIGHT TRANSMITTANCE ASSESSMENT.

### 5.3.1 Potential usage

Thanks to previously conducted lab measurements (Rico-Martinez, 2015), statements that one could intuitively predict, without analysis, were proved valid and expressed measurably.

In particular, the ratio SW/w appeared as a depictive feature of EM meshes. However, they have also shown that it is difficult to predict and summarise transmittance behaviour for EM and one cannot relate it simply and directly to geometrical mesh features such as SW/w ratio or the surface of the openings. Therefore, to predict the EM performance more closely it is necessary to consider tools that take into account multiple factors such as specific geometry and outside finish of mesh or specific directions of incoming light. One of the advantages is that, once the simulation for a particular EM shading is done and saved, it provides a large database, allowing the device shading performance to be simulated for every possible position or location. Such data can also be part of more in-depth analysis, considering the complete complex fenestration and façades systems, diffused light transmittance, and the influence of other environmental factors to allow for detailed and accurate performance analysis. Even as is, the data can be useful for designers needing to choose adequate EM shading systems.

### 5.3.2 Usage of classic Klems dome as a source of inaccuracies

In the classic Klems pattern, each patch represents a range of directions and transmittance values are calculated for the sum of those directions. Decreasing the size of the patches as with Tensor tree BSDF (Ward, Kurt, & Bonneel, 2012) would also reduce the inaccuracies (the lower the patch, the more accurate the results). Another option could be to use custom ray-tracing simulations for particular directions.

#### Acknowledgments

We want hereby to acknowledge:

- The support of the Environment, Territorial Planning and Housing of the Basque Government.
- The support of the Architecture Department of the University of the Basque Country
- The advice of Xavier Ferrés (Doctor Architect - Façade Consultant), Zigor Marroquin (Façade Engineer) and Patxi Rubin (Engineer - Technical Director of Industrias Imar S.A.).

In this paper, the SDC (sequence-determines-credit) approach for the authors order has been followed.

## References

- Alatawneh, B.M.K., Nobile, M.R., Germanà, M.L., & Reffat, R.M. (2016). *THE PERFORATED BUILDING'S ENVELOPE: GUIDING THE EARLY DESIGN PHASES*. 317.
- Begemann, S. H. A., van den Beld, G. J., & Tenner, A. D. (1997). Daylight, Artificial Light and People in an Office Environment, Overview of Visual and Biological Responses. *International Journal of Industrial Ergonomics* 20(3):231–39.
- Brzezicki, M. (2012). The influence of reflected solar glare caused by the glass cladding of a building: application of caustic curve analysis. *Computer Aided Civil and Infrastructure Engineering*, 27(5), 347-357.
- Curic Studio. n.d. 'Curic Sun | SketchUp Extension Warehouse'. Retrieved 21 May 2020 (<https://extensions.sketchup.com/extension/49b56362-ada6-4bde-8213-8c68eb7763d1/curic-sun>).
- De Michele, G., Loonen, R., Saini, H., Favoino, F., Avesani, S., Papaiz, L., & Gasparella, A. (2018). Opportunities and challenges for performance prediction of dynamic Complex Fenestration Systems (CFS). *Journal of Façade Design and Engineering*, 6(3), 101-115.
- Fernandes, L. L., Lee, E.S., McNeil, A., Jonsson, J.C., Nouidui, T., Pang, X., & Hoffmann, S. (2015). Angular Selective Window Systems: Assessment of Technical Potential for Energy Savings. *Energy and Buildings* 90:188–206.
- Klems, J. H. (1994). New Method for Predicting the Solar Heat Gain of Complex Fenestration Systems- 2. Detailed Description of the Matrix Layer Calculation. *ASHRAE Transactions* 100(1):1073–1086.
- Littlefair, P. (2001). Daylight, Sunlight and Solar Gain in the Urban Environment. *Solar Energy* 70(3):177–85.
- Loonen, R.C.G.M, Rico-Martinez, J. M., Favoino, F., Brzezicki, M., Menezo, C., La Ferla, G., & Aelenei, L. (2015). Design for Façade Adaptability—Towards a Unified and Systematic Characterization. Pp. 1274–84 in *Proc. 10<sup>th</sup> Energy Forum-Advanced Building Skins, Bern, Switzerland*.
- McNeil, A., Jonsson, C. J., Appelfeld, D., Ward, G., & Lee, E. S. (2013). A Validation of a Ray-Tracing Tool Used to Generate Bi-Directional Scattering Distribution Functions for Complex Fenestration Systems. *Solar Energy* 98:404–14.
- McNeil, A., Jonsson, J., & Appelfeld, D. (2011). *Validation of GenBSDF. 10<sup>th</sup> International Radiance Workshop*.
- Michele, De., G., Loonen, R., Saini, H., Favoino, F., Avesani, S., Papaiz, L., & Gasparella, A. (2018). Opportunities and Challenges for Performance Prediction of Dynamic Complex Fenestration Systems (CFS). *Journal of Façade Design and Engineering* 6(3):101–15.
- Nicodemus, F. E. (1965). 'Directional Reflectance and Emissivity of an Opaque Surface'. *Applied Optics* 4(7):767–773.
- Perry, M. J. (1990). Mechanisms of Discomfort Glare. *Lighting Research & Technology* 22(3):159–159.
- Rico-Martinez, J. M. (2015). *Methods and Tools for the Assessment of Daylight Transmittance through Expanded Metal Meshes*. University of the Basque Country, Donostia-San Sebastian.
- Robbins, C. L. (1985). *Daylighting. Design and Analysis*.
- Sadeghipour Roudsari, Mostapha. (n.d). 'Ladybug Tools | Ladybug'. *Ladybug*. Retrieved 21 May 2020 <https://www.ladybug.tools/ladybug.html>.
- Saini, H., Loonen, R. C. G. M, & Hensen, J.L.M. (2018). Simulation-Based Performance Prediction of an Energy-Harvesting Façade System with Selective Daylight Transmission. Pp. 213–19 in *VIII International Congress on Architectural Envelopes*.
- Ward, G., Mistrick, R., Lee, E. S., McNeil, A., & Jonsson, J. (2011). Simulating the Daylight Performance of Complex Fenestration Systems Using Bidirectional Scattering Distribution Functions within Radiance. *LEUKOS* 7(4):241–61.
- Ward, G., Kurt, M., & Bonneel, N. (2012). *A Practical Framework for Sharing and Rendering Real-World Bidirectional Scattering Distribution Functions*. LBNL--5954E, 1172245.

# Assessing Self-shading Benefits of Twisting Towers

**Nebojsa Jakica\***, Mikkel K. Kragh

\* Corresponding author  
University of Southern Denmark, nja@iti.sdu.dk

## Abstract

*Over the last number of decades, tall building geometries have been shifting from rectangular boxes towards shapes that are defined through geometrical transformations such as twisting. While, from an aesthetical point of view, these twisting geometries make tall buildings appear contemporary and iconic, from an environmental point of view, however, the benefits are not as straightforward. They may vary significantly based on climatic loads and urban conditions, among others.*

*This study aims to assess the self-shading benefits of twisting geometries by finding a correlation between floor-to-floor rotation and façade solar irradiation across climates, primarily focusing on hot ones, where self-shading is used as a passive solar design strategy. The study analysed three types of irradiation studies: Cumulative Annual Irradiation, Cumulative Harmful Irradiation during Cooling Design Day, and lastly, Solar Irradiation Self-Shading Balance. The latter compares beneficial and harmful solar irradiation during Hot and Cold Degree Days to quantify the impact of floor-to-floor rotation on optical and thermal performance. The study explored hundreds of possible scenarios across different climates and various floor-to-floor rotation angles, revealing a variety of positive, negative, and neutral situations. The study recommends careful examination of environmental conditions via a combination of multiple irradiation studies, particularly in the case of a smooth façade scenario.*

## Keywords

*Climate, energy and sustainable building façades, self-shading, solar radiation benefit, passive solar design, twisting towers*

DOI 10.7480/jfde.2020.1.5043

# 1 INTRODUCTION

There are currently more than 1600 completed skyscrapers in the world, more than 500 under construction, and more than 1800 proposed and envisioned ones (CTBUH, 2020). These numbers are always on the rise, especially over the last decade, with an almost exponential progression of the number of skyscrapers and an increased pace of breaking world height records, with the current record now approaching 1km (CTBUH, 2019). Since increased height imposes an exponential increase of wind loads, most of the skyscrapers' volumes tend to soften the edges and reduce size with increasing altitude. The volume reduction is usually achieved in the form of tapering or the setting back of volumes to reduce wind pressure on façades or due to the right to light regulations, and consequently to minimise vortex shedding and swaying. Yet, the most effective technique in channelling wind flows and reducing wind pressure and swaying is via twisting. The twisting method has been known to engineers for a long time, for example, in industrial chimneys and antennae. However, the first building tower to implement twisting technique was Turning Torso in Malmö, Sweden, designed by Santiago Calatrava Architects in 2005 – just 15 years ago – Fig. 1 and Fig. 5. Since then, many skyscrapers have followed this idea. For some, it was due to performance concerns, while others mainly used it due to the aesthetics.

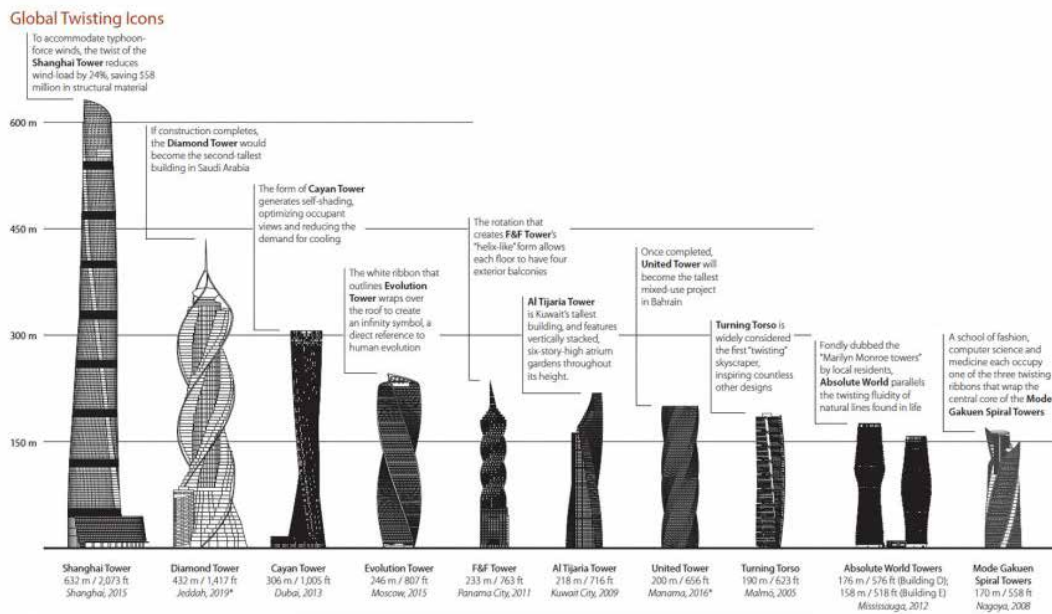


FIG. 1 Global twisting icons by height (CTBUH, 2016)

Recognising this trend, CTBUH made a report (CTBUH, 2016) that analysed 28 twisting towers across the globe and their respective average floor rotations as well as total rotations (Fig. 2). They defined the twisting building as "one that progressively rotates its floor plates or its façade as it gains height". With a 5.9° rotation, F&F Tower in Panama holds the record for the maximum floor to floor rotation, while the diamond tower will be the only twisting tower with a 360° total rotation (Fig. 1). The report demonstrates the growing trend for twisting towers that is "creating a new generation of iconic buildings throughout the world".

No.	Building	City	Country	Completion Year	Architectural Height (m)	Floor Count	Average Floor Rotation	Total Rotation
1	Shanghai Tower	Shanghai	China	2015	632	128	0.938°	120°
2	Lakhta Center	St. Petersburg	Russia	2018 (expected)	462	86	1.047°	90.0°
3	<b>Diamond Tower</b>	Jeddah	Saudi Arabia	2019 (expected)	432	93	3.871°	<b>360°</b>
4	Ocean Heights	Dubai	United Arab Emirates	2010	310	83	0.482°	40.0°
5	Cayan Tower	Dubai	United Arab Emirates	2013	306	73	1.233°	90.0°
6	Supernova Spira	Noida	India	2017 (expected)	300	80	1.825°	146°
7	Evolution Tower	Moscow	Russia	2015	246	55	2.836°	156°
8	<b>F&amp;F Tower</b>	Panama City	Panama	2011	233	53	<b>5.943°</b>	315°
9	Al Majdoul Tower	Riyadh	Saudi Arabia	2016 (expected)	232	54	2.500°	135°
10	Al Tjaria Tower	Kuwait City	Kuwait	2009	218	41	1.951°	80.0°
11	United Tower	Manama	Bahrain	2016 (expected)	200	47	3.830°	180°
12	Al Bidda Tower	Doha	Qatar	2009	197	44	1.364°	60.0°
13	SOCAR Tower	Baku	Azerbaijan	2015	196	40	0.500°	20.0°
14	Turning Torso	Malmö	Sweden	2005	190	57	1.580°	90.0°
15	Trump International Hotel & Tower Vancouver	Vancouver	Canada	2016 (expected)	188	63	0.714°	45.0°
16	Generali Tower	Milan	Italy	2017 (expected)	185	44	1.127°	49.6°
17	Absolute World Building D	Mississauga	Canada	2012	176	56	3.732°	209°
18	Mode Gakuen Spiral Towers	Nagoya	Japan	2008	170	38	3.000°	114°
19	Absolute World Building E	Mississauga	Canada	2012	158	50	4.000°	200°
20	Baltimore Tower	London	United Kingdom	2017 (expected)	149	44	2.182°	96.0°
21	Avaz Twist Tower	Sarajevo	Bosnia and Herzegovina	2008	142	39	1.539°	60.0°
22	The Point	Guayaquil	Ecuador	2014	137	36	5.833°	210°
23	Sichuan Radio & TV Centre	Chengdu	China	2010	136	31	2.903°	90.0°
24	PwC Tower	Midrand	South Africa	2018 (expected)	106	26	1.154°	30.0°
25	Xiamen Suiwa Tower	Xiamen	China	2016 (expected)	100	22	4.091°	90.0°
26	Grove at Grand Bay North Tower	Miami	United States of America	2016 (expected)	94	21	1.843°	38.7°
27	Grove at Grand Bay South Tower	Miami	United States of America	2016 (expected)	94	21	1.843°	38.7°
28	Tao Zhu Yin Yuan	Taipei	Taiwan	2016 (expected)	93	21	4.286°	90.0°

FIG. 2 Global twisting icons – list (CTBUH, 2016)

The report also noticed that “Aided by new technologies assisting architectural and structural design, a proliferation of tall twisting towers is now spreading across the globe”. Finally, the report tackled performance aspects as well: “A stunning variety of textures, view angles, and ripple effects result from these manipulations, making these ‘twisters’ some of the world’s most iconic buildings – and in many cases, aerodynamic and energy-efficient.” From an aesthetical point of view, these twisting geometries make tall buildings appear fluid and contemporary. From an environmental point of view, however, the benefits are not as straightforward and may vary significantly, based on climatic loads and urban conditions. Some cases have proven, through simulations and testing, that twisting may lead to reduced wind loads and consequent savings on structural weight and costs. On the other hand, other environmental aspects such as energy savings, daylighting potential, glare control, and views are poorly documented.

Since the impact of twisting on building performance was never examined in detail and on a global scale, this research aims to address the benefits of twisting building geometries from a holistic perspective. It analyses a global potential for self-shading of twisting towers, mainly focusing on environmental performance in hot climates where self-shading has the highest potential to be used as a very effective passive solar design strategy. This study assesses the self-shading benefits of twisting geometries, analysing how climatic conditions, floor-to-floor rotation, as well as façade smoothness, influence building performance. In particular, the study performed three types of irradiation studies: Cumulative Annual Irradiation; Cumulative Harmful Irradiation during Cooling Design Day, and lastly; Solar Irradiation Self-Shading Balance compares beneficial and harmful solar irradiation during Hot and Cold Degree Days. This comparative approach provides resourceful and specific data for effectively quantifying the twisting impact on optical and thermal performance. A global potential with particular recommendations for twisting and façade smoothness offers a useful resource for all stakeholders to be used in early-stage design discussions on twisting strategies.

## 2 CASE STUDIES

As shown in the CTBUH report, there are many twisting towers in the world, with some claiming performance improvements with twisting. This section aims to demonstrate a range of benefits that some of the case studies have achieved, ranging from structural, wind, and energy efficiency, among others.



**AGORA GARDEN, TAIPEI, TAIWAN**  
VINCENT CALLEBAUT ARCHITECTURES  
(FREARSON A., 2013)



**ABSOLUTE TOWERS, MISSISSAUGA, CANADA**  
MAD ARCHITECTS  
IMAGE CREDITS: AARON LEDESMA AT UNSPLASH.COM



**EVOLUTION TOWER, MOSCOW, RUSSIA**  
RMJM, TONY KETTLE, PHILIPP NIKANDROV (GORPROJECT)  
(CTBUH, 2016)

FIG. 3 Twisting towers case studies

### *Agora Garden, Taipei, Taiwan by Vincent Callebaut Architectures.*

"The tower is a prototype of Carbon-Absorbing Green Building, and it will carry 23,000 trees planted on the ground and balconies, which can absorb 130 tonnes of CO<sub>2</sub> annually in Taipei. The sunlight, thermal, and wind analyses have enabled us to improve the bioclimatic design of the project" (Vincent Callebaut Architectures, 2020). The project received LEED Gold green certification from US Green Building Council, as well as Diamond Level from Low Carbon Building Alliance. However, apart from hand sketches, there was no demonstrated evidence of the impact of twisting on performance improvement (Fig. 3).

### *Absolute Towers, Mississauga, Canada by MAD architects.*

This is one of the few examples in which twisting was very loose, and instead of being very regular, in combination with smooth slabs/balconies, it created a fluid volume. Besides its unique shape, balconies were used to improve energy performance. Still, no specific quantitative value has been provided: "Besides providing every resident with a nice exterior place to enjoy views of Mississauga, the balconies naturally shade the interior from the summer sun while soaking in the winter sun, reducing air conditioning costs." (Frearson, 2012) (Fig. 3).

Evolution Tower, Moscow, Russia by RMJM, Tony Kettle, Philipp Nikandrov (GORPROJECT).

One of the juries of CTBUH said of the tower: "The world has seen an increasing number of twisting towers in the last decade or so, but Evolution Tower takes the record for the most extreme twist" (CTBUH, 2016). The main reason for such an extreme twist is purely aesthetical. "The sculptural DNA-shaped twisting tower symbolises the evolution spiral with the white façade ribbon wrapping over the roof in the form of a 90-degree twisting infinity symbol, which speaks of the philosophical concept of evolution and celebrates the development of human civilisation. From spiralling onion domes of St. Basil to the iconic Tatlin Tower concept the Russian architecture was obsessed with the idea of a spiral." (Nikandrov, 2020) (Fig. 3).

Tore Banke - PhD Thesis "Parametri i praksis - Generativ performance i arkitektur"  
(Parametric design in practice - Generative performance in architecture).

The last case study is the most documented in terms of the environmental benefit of twisting towers. The towers have a star-like floor plan with smooth corners that rotate 2 degrees floor to floor (Fig. 4). The author of this work has demonstrated 11.4% of cumulative irradiation reduction over the year (Banke, 2013). Yet, as it is shown in the results part of this research, such a parameter is not enough to prove to what extent this irradiation was harmful or beneficial. Moreover, it does not reflect the seasonal and daily dynamic of solar radiation and its combination with the external temperature that produces a specific thermal load on a building envelope.



FIG. 4 Twisting towers case studies (Banke, 2013)

As demonstrated in most of the described cases, if authors emphasised performance improvement, they mostly used the twisting effect to improve wind flows and consequently, structural performance. In some of the cases, blocking solar radiation was mentioned with minimal reference to the location-specific climatic loads and estimated energy savings. Therefore, since there was no significant evidence to conclude how twisting impacts performance on a global level, this paper uses a methodology based on simulations.

### 3 METHODOLOGY

The methodology of this paper uses an automated assessment procedure which utilises the simulation of solar radiation on façade surfaces to estimate the global self-shading potential of twisting forms, considering twisting angle and façade smoothness. Like similar methodologies used in green building certifications (US Green Building Council, 2014), the study used a baseline geometry in the form of a simple box obtained via vertical extrusion from a square rectangle. The baseline tower had four planar façades facing four cardinal directions. The study continued with gradually introducing and consequently increasing the twisting angle clockwise in increments of  $1^\circ$  up to  $10^\circ$ . Since the case study research revealed two façade cases, smooth/continuous, and discreet, the methodology assessed the solar self-shading potential for both façade options. For every twisting angle, an automated script developed explicitly for this study recorded results of each of the two façade states and repeated the process for all climates. Three different analyses process and extract quantitative data that is relevant to this study. Results of all three studies of self-shading potential are then summed up in tables with both absolute values and relative improvement compared to the baseline. The following paragraphs provide more detail of the sub-processes.

#### 3.1 GEOMETRY AND TWISTING

The twisting tower has a  $40 \times 40 \text{m}$  square floor shape that could rotate as it gained height. The testing building volume had 90 floors with  $4 \text{m}$  floor-to-floor height. Twisting has floor-to-floor rotation angle covering a range from  $0^\circ$  to  $10^\circ$  for the baseline tower, with continuous planar façade surfaces and maximum twisting tower, respectively. The direction of the twist was addressed in the preliminary analyses, where the design variable showed no influence on overall results.

Since irradiation on the surface was highly dependent on the angle setting and shading overhang, two different façade types were analysed. The first one represents a continuous, smooth façade without overhangs. The second one represents a discretised façade with all vertical surfaces and slabs that behaved as overhang shadings. The façade surface of each floor was tessellated into a  $2 \times 2 \text{m}$  mesh grid that represented an optimal spatial resolution to provide reasonable accuracy vs computation time trade-off. Moreover, this spatial resolution was able to account for relatively small shaded areas below the slabs, particularly at small twisting angles. Examples of two façade types at an  $8^\circ$  floor-to-floor rotation angle are shown in Fig. 5.

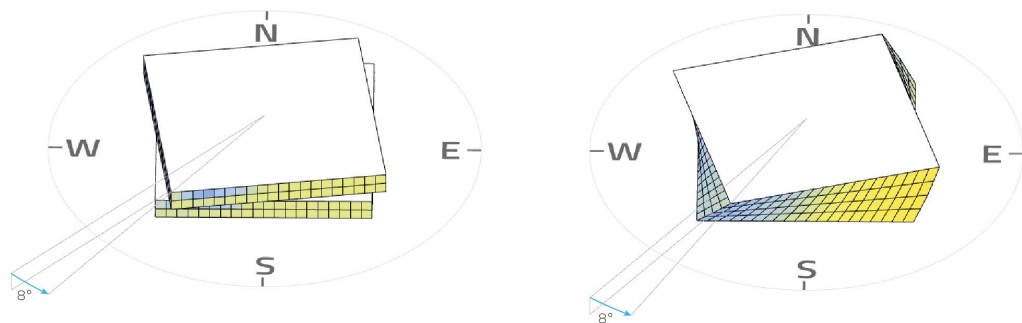


FIG. 5 Two façade types at  $8^\circ$  floor-to-floor rotation angle

## 3.2 CLIMATES

To address a full range of possible scenarios, this paper analysed twisting towers in all 17 different climates according to the ASHRAE (ASHRAE, 2013) and IECC climate classifications (ICC, 2000) (Fig. 6).

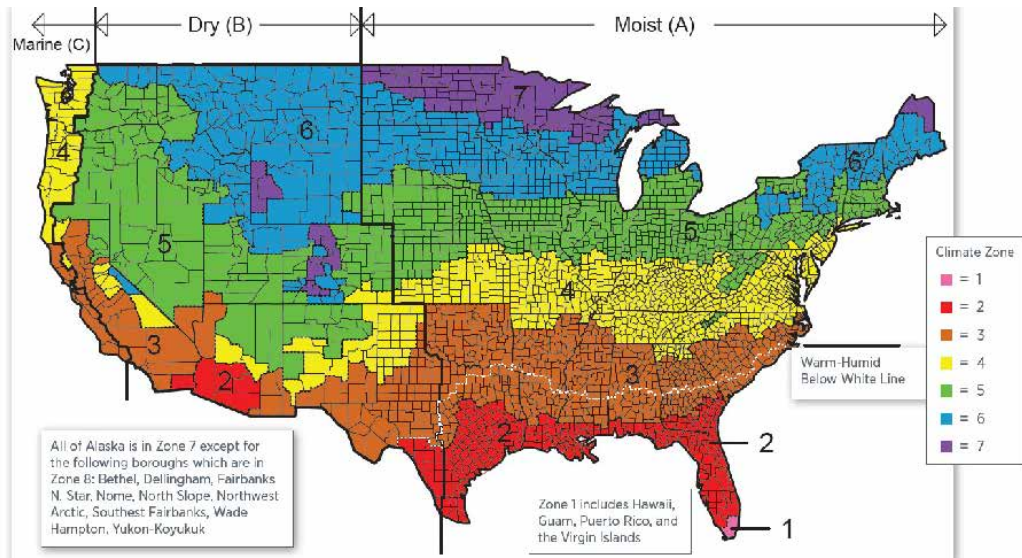


FIG. 6 ASHRAE and IECC climate classifications

Each of the climates had its specific combination of ASHRAE Cooling and Heating Degree Days that are used to estimate thermal loads on the building and give an estimate on HVAC sizing. A list of cities, representing each climate from the set, is shown in Table 1, along with climatic and site parameters extracted from (ASHRAE, 2013).

TABLE 1 A list of climates with the most relevant climatic parameters (Skalko et al., 2013)

ZONE NUMBER	ZONE NAME	THERMAL CRITERIA (SI UNITS)	LOCATION	LATITUDE	SHGC	HARMFUL IRRADIATION THRESHOLD [WH/M2]
1A	Very Hot - Humid	5000<CDD10°C	Miami, USA	25.82	0.25	380
1B	Very Hot - Dry	5000<CDD10°C	Dubai, UAE	25.25	0.25	380
2A	Hot-Humid	3500<CDD10°C≤5000	Houston, USA	29.97	0.25	380
2B	Hot - Dry	3500<CDD10°C≤5000	Phoenix, USA	33.43	0.25	380
3A	Warm - Humid	2500<CDD10°C≤3500	Atlanta, USA	33.65	0.25	380
3B	Warm - Dry	2500<CDD10°C≤3500	El Paso, USA	31.77	0.25	380
3C	Warm - Marine	CDD10°C≤2500 AND HDD18°C≤2000	San Francisco, USA	37.62	0.25	380
4A	Mixed - Humid	CDD10°C≤2500 AND HDD18°C≤3000	New York, USA	40.78	0.40	237.5
4B	Mixed - Dry	CDD10°C≤2500 AND HDD18°C≤3000	Albuquerque, USA	35.05	0.40	237.5
4C	Mixed - Marine	2000<HD-D18°C≤3000	Seattle, USA	47.45	0.40	237.5
5A	Cool - Humid	3000<HD-D18°C≤4000	Chicago, USA	41.78	0.40	237.5
5B	Cool - Dry	3000<HD-D18°C≤4000	Denver, USA	39.76	0.40	237.5
5C	Cool - Marine	3000<HD-D18°C≤4000	Vancouver, CAN	49.18	0.40	237.5
6A	Cold - Humid	4000<HD-D18°C≤5000	Minneapolis, USA	44.88	0.40	237.5
6B	Cold - Dry	4000<HD-D18°C≤5000	Helena, USA	46.60	0.40	237.5
7	Very Cold	5000<HD-D18°C≤7000	Duluth, USA	46.83	0.45	211.1
8	Subarctic	7000<HDD18°C	Fairbanks, USA	64.82	0.45	211.1

### 3.3 IRRADIATION ANALYSES

The methodology analyses irradiation on the façade surface using the raytracing method within the Ladybug tools plug-in for grasshopper and Rhino. Solar radiation is considered as one of the most critical parameters in passive solar design techniques for estimating energy balance and solar shading potential (Olgay & Olgay, 1957; Olgay et al., 1963; Givoni, 1969). For every climate, one sky-matrix was produced, combining both direct and diffuse solar radiation components for all 8760 hours of the year. An intersection matrix was used to compute irradiance falling on each of the 14,400 mesh faces at each timestep for both façade types, twisting state, and climate. In total, 126,144m data points were computed for each of the 374 design states (2 façade types x 11 twisting

angles x 17 climates). Simulations excluded multiple reflections as this would drastically increase the time for an already highly demanding computation. Moreover, solar radiation analyses neglected indoor and material-specific parameters of the façade such as thermal conductivity, building energy systems, and HVAC. These parameters would impose many additional climate-specific criteria and therefore, drastically increase discrepancies of results between climates.

Irradiation data were processed and analysed in three different ways. The first analysis was the most common cumulative annual irradiation that integrated all timesteps and produced a cumulative irradiation value for each mesh face. An average irradiation value was recorded for every twisting state and both façade types. This analysis was capable of quantitatively demonstrating an increase or decrease of average irradiation levels for different twisting states (Fig. 7). However, climate conditions differ significantly, ranging from the extreme cold to hot environments. Therefore, assuming that irradiation is always harmful is far from accurate. Yet, the primary purpose of this analysis is to show a correlation between higher temporal resolutions used in this study with the lower temporal resolutions commonly used in passive solar design.

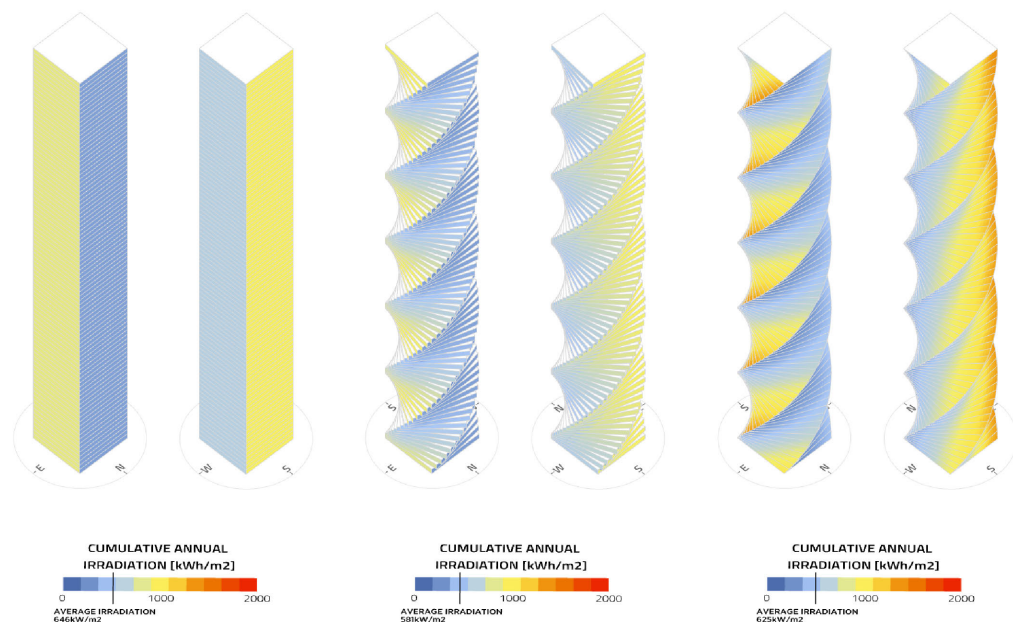


FIG. 7 Cumulative Annual Irradiation Analysis

To be able to quantify harmful and beneficial radiation throughout the year, it was necessary to consider dry bulb temperature to determine whether irradiation would improve or reduce thermal balance for every time step. The analysis assumed that solar radiation might contribute to the thermal load balance between indoor and outdoor environments in both negative and positive ways. "The following sources of heat flow are typically considered in buildings: conduction through walls and windows, infiltration and ventilation, solar as well as internal heat gains for occupants, equipment and electric lighting. ... For all buildings, there is a temperature range at which these heat flows cancel each out over the day, keeping the building within a desired interior temperature range without the need for active heating and cooling. This temperature range is called the balance point temperature range of the building." (Reinhart, 2014). The authors used the following assumptions to calculate the balance point temperature range:

Indoor environments have constant internal heat gains from occupants for a standard office that is the sum of the mean occupancy load (13.5 W/m<sup>2</sup>), the mean lighting load (10.1 W/m<sup>2</sup>) and the mean equipment load (8 W/m<sup>2</sup>). Solar gains for mid-latitudes in June are roughly 2.9 kWh/m<sup>2</sup>. Ventilation losses were set to 0.5h<sup>-1</sup> ACH (air changes per hour) and forced ventilation for a fresh air supply rate of 10l/s per occupant during office hours (8 am - 6 pm). Conduction losses were set to 0.391 W/m<sup>2</sup>K for walls and 1.6 W/m<sup>2</sup>K for windows with a glazing ratio of 40%.

Assuming the desired temperature range from 20°C to 26°C, the authors calculated the balance point temperature to be 8-14 °C for June for mid-level latitudes. These temperatures may seem quite low, yet it shows that an internal load-dominated space such as the reference office tends to receive more internal and solar gains than it loses through the building envelope.

To compute the exact balance temperature point, it was necessary to calculate solar heat gains and heat losses for every mesh face throughout every time step. This would provide different balance point temperatures across the façade surface and different seasons. Since this was not practical, and the study was focused on overall building performance, this analysis assumed a unique balance point temperature of 12°C and a balance temperature range of 8-14°C. The fluctuation of balance point temperature throughout the seasons and in different climates was set to ±2°C. It could have been expected that this approximation could introduce an error range that was estimated to be within a 10% range.

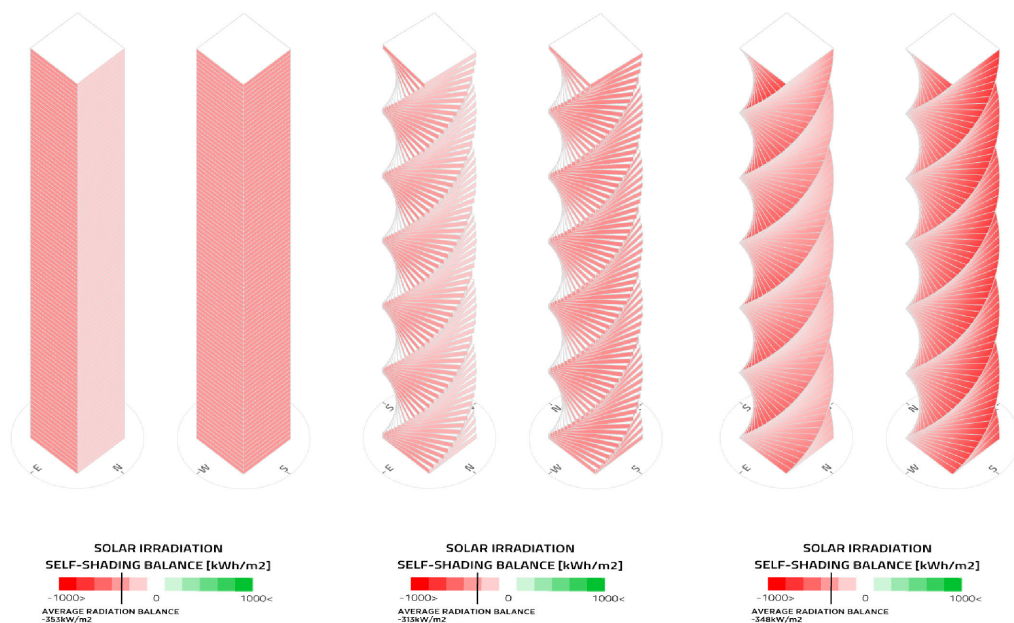


FIG. 8 Solar Irradiation Self-Shading Balance Analysis

For every time step, the algorithm checked if outdoor dry bulb temperature was above or below the balance point temperature range and the irradiance of this time step was classify into two sets of sky matrices. Whenever outdoor dry bulb temperature was above the balance point temperature, it sorted irradiance for that time step into a harmful irradiation set, as this irradiation would likely decrease thermal comfort by adding more heat. Harmful irradiation was presented as negative. On the contrary, if outdoor dry bulb temperature was below the balance point temperature, it

classified irradiance for that time step into beneficial irradiation, as this irradiation will likely increase thermal comfort by adding more heat. Beneficial irradiation was presented as positive. At the end of the hour classification, two lists of hours of the year were created and two irradiation values were integrated for every mesh face, beneficial and harmful cumulative irradiation. These two cumulative values were then summed up. If harmful (negative) values prevailed, additional shading would be needed. On the other hand, if beneficial irradiation prevailed, more solar heat gain would be required to heat the space and reduce energy consumption for heating passively. By considering both beneficial and harmful radiation at the same time, it was possible to estimate the impact of self-shading across climates, including both hot and cold extremes. Performance improvement of twisting was confirmed if the overall sum of irradiations approached 0 in comparison to the baseline. In this sense, zero represented an irradiation balance point in which shading was neither beneficial nor harmful (Fig. 8).

The third type of analysis focused on hot climates and considered cumulative irradiation to estimate a self-shading potential on a Cooling Design Day, as this day is commonly used to determine cooling loads and HVAC sizing. The increase of irradiation above a threshold was considered as being always harmful, and therefore increased average irradiation represented a decrease in performance. In other words, negative values represent decreased performance as harmful irradiation increases (Fig. 9). The transmitted luminous intensity threshold was set to  $95\text{W/m}^2$  (Skalko et al., 2013), which, in combination with the prescribed Solar Heat Gain Coefficients (SHGC) from Table 5.5-1 – 5.5-8 Building Envelope Requirements for Climate Zones 1-8 (SI) of the same document, for different climates, produced different irradiance thresholds (Table 1).

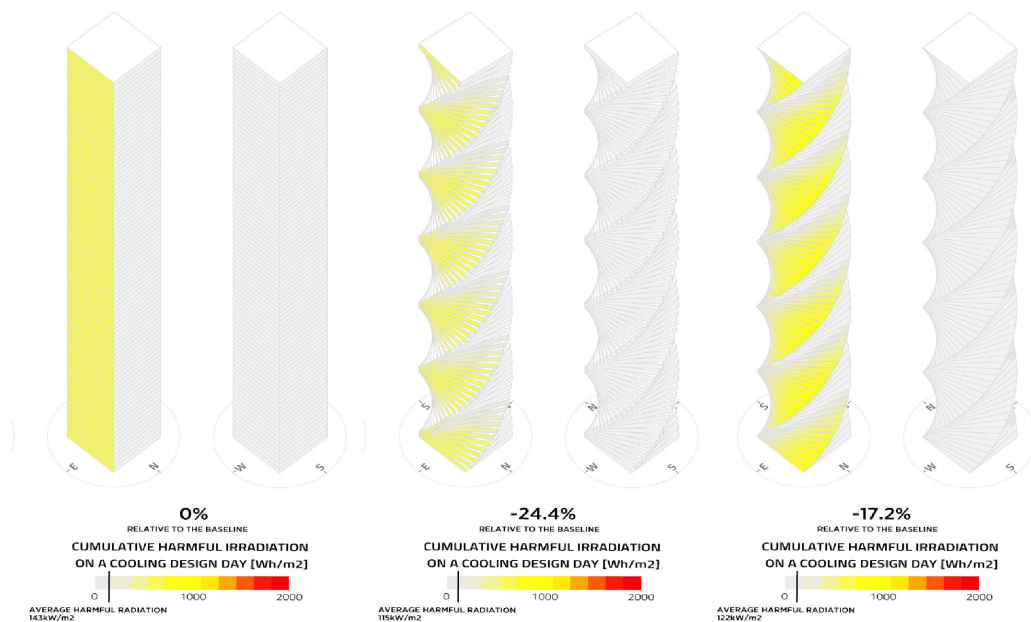


FIG. 9 Cumulative Harmful Irradiation during Cooling Design Day Analysis

## 4 RESULTS

The automated script calculated all twisting states in all the climates for both façade types and all three analyses. The results of this assessment are summarised in 6 charts. Cumulative Annual Irradiation for smooth façades (Fig. 10) shows differences in average baseline irradiation levels of around 300kWh/m<sup>2</sup>. In most of the climates, twisting reduces irradiation levels by up to 80kWh/m<sup>2</sup>. However, results exhibit a small anomaly in the lower twisting angle range, where the irradiation first slightly increases and then gradually drops. This trend is present in all climates but more dominant in hot ones.

SMOOTH - Cumulative Annual Irradiation [kWh/m <sup>2</sup> ]																	
Rotation	1A	1B	2A	2B	3A	3B	3C	4A	4B	4C	5A	5B	5C	6A	6B	7	8
0	665	788	635	885	646	863	747	551	888	572	652	830	597	705	719	672	530
1	670	796	641	896	652	871	754	554	895	576	657	837	603	709	724	676	532
2	666	792	638	892	649	867	750	551	891	574	654	832	600	706	721	673	529
3	662	787	634	885	645	861	745	547	885	569	650	826	595	701	716	668	526
4	656	780	628	878	639	854	738	542	877	564	644	819	590	694	709	662	521
5	649	772	622	868	632	845	730	537	868	558	637	810	583	687	701	655	515
6	642	763	614	858	625	835	721	530	857	551	629	800	576	679	693	647	509
7	634	753	606	847	617	824	712	523	846	544	621	790	568	670	684	638	502
8	625	743	598	836	609	813	703	516	835	536	613	779	560	660	674	629	494
9	616	732	589	823	600	801	692	508	822	528	603	767	552	650	664	620	486
10	605	720	579	809	589	787	681	500	809	520	593	754	543	639	653	609	478

FIG. 10 Cumulative Annual Irradiation Analysis Results for a Smooth Façade

Cumulative Annual Irradiation for the discrete façade (Fig. 11) shows similar trends in baseline irradiance but has slightly greater irradiance reduction of up to 100kWh/m<sup>2</sup> with twisting. Similarly, it exhibits the same small increase in the lower twisting angle range, but with a limited effect. As expected, it was proven wrong to assume that the irradiance reduction is always beneficial. Furthermore, it would be impossible to make a clear division of climates into two groups, hot and cold climates, and assume irradiance reduction is beneficial for one group and harmful for the other. Instead, irradiation assessment would be much more meaningful with an increased temporal resolution in which irradiation is assessed concerning the temperature for every time step, as shown in the second analysis.

DISCRETE - Cumulative Annual Irradiation [kWh/m <sup>2</sup> ]																	
Rotation	1A	1B	2A	2B	3A	3B	3C	4A	4B	4C	5A	5B	5C	6A	6B	7	8
0	665	788	635	885	646	863	747	551	888	572	652	830	597	705	719	672	530
1	668	794	639	894	651	870	753	553	894	576	657	836	602	709	724	676	532
2	657	781	630	882	641	857	742	546	882	569	649	826	596	701	717	669	528
3	643	763	616	864	628	840	726	535	865	559	637	810	586	689	705	658	522
4	625	742	600	842	612	819	707	522	844	546	622	792	573	675	691	644	513
5	609	722	584	822	596	799	689	510	825	534	608	774	561	661	677	631	505
6	594	703	570	802	581	780	672	498	805	523	595	756	549	647	663	618	496
7	581	688	557	785	569	763	657	487	789	513	583	741	539	635	651	607	488
8	568	673	546	769	557	748	643	478	773	503	572	726	529	624	639	597	481
9	559	661	537	757	547	736	632	470	760	495	563	714	521	614	630	588	474
10	547	647	525	741	536	720	618	460	745	485	552	700	511	602	618	577	466

FIG. 11 Cumulative Annual Irradiation Analysis Results for a Discrete Façade

As explained, the self-shading benefit analysis shows results with much higher resolution and therefore, more reliable data. Regarding baseline irradiation balance for the smooth façade, results show high levels of excessive irradiation in hot climates on average. On the contrary, irradiation is

not sufficient in cold climates. Fig. 12 shows that twisting generally improves performance in all climates to a variable degree. However, the effectiveness of the self-shading is almost negligible for a range of moderate to cold climates, 4A to 8. Moreover, the real effect may be seen only in hot climates where reduction of irradiance can be up to 70kWh/m<sup>2</sup> on average. Similarly to the previous analyses, small twisting angles tend to slightly decrease performance, while higher angles always improve the balance.

SMOOTH - Self-shading Balance [kWh/m <sup>2</sup> ]																	
Rotation	1A	1B	2A	2B	3A	3B	3C	4A	4B	4C	5A	5B	5C	6A	6B	7	8
0	-650	-786	-529	-774	-353	-585	-444	-173	-344	-238	-165	-195	-210	-126	-103	49	19
1	-655	-794	-536	-787	-362	-600	-451	-178	-360	-241	-172	-206	-215	-133	-109	43	19
2	-652	-790	-534	-784	-360	-597	-448	-177	-358	-240	-171	-205	-213	-132	-108	43	19
3	-647	-785	-530	-778	-358	-593	-445	-175	-355	-238	-170	-204	-212	-131	-107	43	19
4	-642	-778	-526	-771	-355	-588	-441	-174	-352	-236	-168	-202	-210	-130	-106	42	19
5	-635	-770	-520	-763	-352	-582	-437	-172	-349	-233	-167	-200	-207	-129	-105	42	18
6	-628	-761	-514	-754	-348	-575	-432	-170	-345	-231	-165	-198	-205	-127	-104	41	18
7	-620	-751	-508	-745	-343	-568	-426	-169	-341	-228	-163	-196	-202	-126	-103	40	18
8	-611	-741	-501	-735	-339	-561	-421	-167	-337	-225	-161	-194	-200	-125	-101	39	18
9	-602	-730	-493	-724	-334	-553	-415	-164	-333	-222	-159	-191	-197	-123	-100	38	17
10	-592	-718	-485	-712	-329	-543	-408	-162	-327	-218	-157	-188	-194	-121	-99	38	17

FIG. 12 Solar Irradiation Self-Shading Benefit Analysis Results for a Smooth Façade

On the other hand, discrete façade analysis shows slightly different results (Fig. 13). In all climates except 7 and 8, twisting improves irradiation balance in general. The baseline comparison reveals that hot climates have proportionally higher irradiance levels in contrast to the hot ones that are closer to the balance point as climates become colder. This implies that all irradiation in colder climates can be considered beneficial and there is no risk of excessive radiation and therefore no need for self-shading. A similar bump of adverse effect from twisting is visible when a small amount of twisting is applied. Values first go off the balance point and then get closer. In that sense, the baseline and 4° twisting solutions have almost equal performance.

DISCRETE - Self-shading Balance [kWh/m <sup>2</sup> ]																	
Rotation	1A	1B	2A	2B	3A	3B	3C	4A	4B	4C	5A	5B	5C	6A	6B	7	8
0	-650	-786	-529	-774	-353	-585	-444	-173	-344	-238	-165	-195	-210	-126	-103	49	19
1	-653	-791	-535	-786	-361	-598	-449	-177	-358	-241	-172	-206	-214	-133	-108	43	19
2	-643	-779	-526	-774	-354	-587	-441	-173	-349	-237	-167	-199	-211	-128	-105	45	19
3	-628	-761	-513	-756	-344	-572	-428	-167	-338	-230	-161	-191	-205	-122	-99	48	21
4	-611	-740	-499	-736	-333	-555	-415	-160	-325	-223	-154	-181	-198	-116	-93	50	23
5	-595	-720	-486	-717	-322	-539	-402	-154	-313	-216	-148	-173	-192	-110	-87	52	24
6	-580	-701	-473	-699	-313	-525	-390	-149	-303	-210	-143	-166	-186	-105	-83	53	26
7	-567	-685	-462	-683	-305	-512	-380	-144	-294	-204	-138	-160	-181	-101	-79	54	27
8	-555	-671	-452	-669	-297	-501	-371	-140	-286	-199	-134	-154	-176	-97	-75	55	27
9	-546	-659	-444	-657	-292	-491	-363	-137	-280	-195	-131	-150	-173	-94	-72	56	28
10	-534	-644	-434	-643	-285	-480	-354	-134	-273	-190	-127	-145	-168	-91	-69	56	29

FIG. 13 Solar Irradiation Self-Shading Benefit Analysis Results for a Discrete Façade

The last analysis is more relevant for hot climates as it shows a self-shading benefit on the Cooling Design Day. All results are normalised, and positive values represent an increase in harmful irradiation, whereas negative values represent decreased irradiation. Fig. 14 shows results for the smooth façade with high variability of results across climates. Only climates 1A and 3A show self-shading potential for all twisting angles. In climates 1B, 2A, 2B, 3B, and 3C, twisting angles up to 4° - 5° show self-shading potential, while larger twisting angles exhibit a linear increase of harmful

irradiation. Climate 4A is quite neutral, showing the only slight benefit of twisting. Climates 4B to 8 show a slight increase of harmful radiation, but these climates are less relevant for this analysis.

SMOOTH - Harmful Radiation during the Cooling Design Day relative to Baseline [%]																	
Rotation	1A	1B	2A	2B	3A	3B	3C	4A	4B	4C	5A	5B	5C	6A	6B	7	8
0	0	0	0	0	0	0	0	0	0	0	0	0	0	0	0	0	0
1	-15.6	-43.5	-12.9	-16.3	-10.4	-14.1	-14.1	-2	6.7	4.3	0	4.8	2.3	0.1	3.9	1.6	-2.1
2	-15.7	-34.5	-9.8	-13.1	-11.1	-10.3	-11	-2	8.4	4.4	0.5	5.3	2.5	0.4	4	1.8	-1.7
3	-15.8	-22.1	-5.2	-8.6	-12.1	-5.7	-6.5	-2	10.4	4.6	1.6	6	2.7	0.8	4	2	-1.2
4	-15.7	-9.1	0.2	-3.9	-13.5	-0.7	-1.8	-2	12.4	4.9	3	6.7	3	1.4	3.9	2.1	-0.7
5	-15.4	2.3	5.5	0.4	-15.2	4	2.5	-1.9	14	5.4	4.7	7.2	3.3	2	3.8	2.3	0
6	-14.9	11.3	10.2	4	-17.2	8.2	6.4	-1.7	15.2	5.7	6.2	7.6	3.5	2.6	3.6	2.4	0.9
7	-14.3	18.2	14.2	7	-19.2	11.8	9.8	-1.5	15.9	5.9	7.5	7.8	3.6	3.1	3.3	2.5	1.9
8	-14	23.2	17.4	9.5	-20.9	14.6	12.3	-1.3	16.2	5.9	8.5	7.9	3.4	3.5	2.9	2.4	2.7
9	-13.7	26.8	20	11.6	-22.5	16.7	14.3	-1.3	16.3	5.7	9.2	7.8	3.1	3.6	2.3	2	3.1
10	-14	28.8	21.4	12.5	-24.3	17.8	15.2	-1.7	15.6	5.1	9.1	7.2	2.4	3.3	1.5	1.4	3.1

FIG. 14 Cumulative Harmful Irradiation during Cooling Design Day Analysis Results for a Smooth Façade

Lastly, Fig. 15 shows different behaviour in comparison to Fig. 14. For a discrete façade type, all climates from 1A to 4A demonstrate a decrease up to approximately 50% of harmful irradiation on a Cooling Design Day with almost linear progression. Only climate 1B shows huge potential in reduction with a decrease up to 118% for the maximum twisting angle.

SMOOTH - Harmful Radiation during the Cooling Design Day relative to Baseline [%]																	
Rotation	1A	1B	2A	2B	3A	3B	3C	4A	4B	4C	5A	5B	5C	6A	6B	7	8
0	0	0	0	0	0	0	0	0	0	0	0	0	0	0	0	0	0
1	-15.6	-43.5	-12.9	-16.3	-10.4	-14.1	-14.1	-2	6.7	4.3	0	4.8	2.3	0.1	3.9	1.6	-2.1
2	-15.7	-34.5	-9.8	-13.1	-11.1	-10.3	-11	-2	8.4	4.4	0.5	5.3	2.5	0.4	4	1.8	-1.7
3	-15.8	-22.1	-5.2	-8.6	-12.1	-5.7	-6.5	-2	10.4	4.6	1.6	6	2.7	0.8	4	2	-1.2
4	-15.7	-9.1	0.2	-3.9	-13.5	-0.7	-1.8	-2	12.4	4.9	3	6.7	3	1.4	3.9	2.1	-0.7
5	-15.4	2.3	5.5	0.4	-15.2	4	2.5	-1.9	14	5.4	4.7	7.2	3.3	2	3.8	2.3	0
6	-14.9	11.3	10.2	4	-17.2	8.2	6.4	-1.7	15.2	5.7	6.2	7.6	3.5	2.6	3.6	2.4	0.9
7	-14.3	18.2	14.2	7	-19.2	11.8	9.8	-1.5	15.9	5.9	7.5	7.8	3.6	3.1	3.3	2.5	1.9
8	-14	23.2	17.4	9.5	-20.9	14.6	12.3	-1.3	16.2	5.9	8.5	7.9	3.4	3.5	2.9	2.4	2.7
9	-13.7	26.8	20	11.6	-22.5	16.7	14.3	-1.3	16.3	5.7	9.2	7.8	3.1	3.6	2.3	2	3.1
10	-14	28.8	21.4	12.5	-24.3	17.8	15.2	-1.7	15.6	5.1	9.1	7.2	2.4	3.3	1.5	1.4	3.1

FIG. 15 Cumulative Harmful Irradiation during Cooling Design Day Analysis Results for a Discrete Façade

## 5 DISCUSSION

Presented results reveal how temporal resolution impacts the quality of results. It confirmed that cumulative annual irradiation should not be used to quantify the self-shading benefit, unless for very hot climates, where there are no Heating Days so it can be assumed that all irradiation is harmful. For all other cases, there may be some percentage of beneficial radiation that increases as climates have more Heating Days. For general purposes, the Solar Irradiation Self-Shading Benefit analysis that calculates irradiation balance should be used as it provides much more granularity and precision. This is demonstrated in Fig. 14. and Fig. 15. The discrepancy between discrete and smooth façade types can be assigned to several causes. Firstly, the angle setting of smooth façade panels follows the twisting curvature and therefore they have a low sun incidence angle. The reflection of coated glass at a low incidence angle is relatively small in comparison to the reflection of the glass above 56 degrees incidence angle, which is very high due to the exponential behaviour defined by the

cosine law. Therefore, façade panels with low sun incidence angles are much more exposed to solar radiation. Secondly, self-shading at meso-level caused by floor volumes in a discrete façade scenario significantly reduces direct solar radiation in the upper part of the glazing that causes a drop in harmful irradiation levels. However, this analysis also has limitations as it is impractical to compute balance points for all façade points and all hours of the year. Therefore, the approximation increases simulation errors, but still provides a reasonable accuracy.

However, it is realistic to assume that these types of studies are practical for understanding trends, while more accurate simulations should be used on the narrow design search set. Moreover, for each specific case, a set of simulations could be extended to daylighting and whole building energy to provide more details on the behaviour of twisting geometries.

Regarding self-shading benefit, results have shown that claiming that twisting is a priori beneficial is not reasonable, as benefits may be highly sensitive to the climatic conditions and twisting angles, as well as façade type. In general, the discrete façade provides more benefit of twisting as it offers more floor-to-floor self-shading while the smooth façade only provides building volume self-shading.

## 6 CONCLUSION

The study demonstrates hundreds of possible scenarios of twisting towers with a relatively high sensitivity of self-shading benefits across different climates and various floor-to-floor rotation angles, revealing a variety of positive, negative, and neutral scenarios. Therefore, the study provides useful insights into a true global self-shading potential of twisting. It is recommended that all environmental conditions be carefully examined via irradiation studies, instead of automatically assuming self-shading benefits, particularly in the case of a smooth façade scenario.

### References

- ASHRAE (2019). Standard 90.1. Energy Standard for Buildings Except Low-Rise Residential Buildings
- ASHRAE (2013). ASHRAE/IES Standard 90.1-2013--Energy Standard for Buildings Except Low-Rise Residential Buildings. American Society of Heating, Refrigerating, and Air-Conditioning Engineers Inc., Atlanta.
- Banke, T. (2013). Parametri i praksis: Generativ performance i arkitektur [Parametric design in practice - Generative performance in architecture]. (1 ed.). Retrieved from [http://issuu.com/parametri/docs/afhandling\\_tore\\_banke\\_web/3?e=9673948/5357075](http://issuu.com/parametri/docs/afhandling_tore_banke_web/3?e=9673948/5357075)
- Capeluto, G. (2003). Energy performance of the self-shading building envelope. *Energy and Buildings*. 35. 327-336. 10.1016/S0378-7788(02)00105-6.
- CTBUH (2016). Twisting Tall Buildings. *International Journal on Tall Buildings and Urban Habitat*, (III).
- CTBUH (2019). Year in Review - The Skyscraper Center. Retrieved from <http://www.skyscrapercenter.com/year-in-review/2019/> (Accessed: 28 March 2020).
- CTBUH (2020). The Skyscraper Center. Retrieved from [http://www.skyscrapercenter.com/compare-data/submit?-type%5B%5D=building&base\\_region=0&base\\_country=0&base\\_city=0&base\\_height\\_range=4&base\\_company=All&base\\_min\\_year=2010&base\\_max\\_year=9999&comp\\_region=0&comp\\_country=0&comp\\_city=0&comp\\_height\\_range=4&comp\\_c](http://www.skyscrapercenter.com/compare-data/submit?-type%5B%5D=building&base_region=0&base_country=0&base_city=0&base_height_range=4&base_company=All&base_min_year=2010&base_max_year=9999&comp_region=0&comp_country=0&comp_city=0&comp_height_range=4&comp_c) (Accessed: 28 March 2020).
- Frearson, A. (2013). Agora Garden by Vincent Callebaut. Retrieved from Dezeen <https://www.dezeen.com/2013/04/05/agora-garden-by-vincent-callebaut/>, (Accessed on 20 June 2020)
- Frearson, A. (2012). Absolute Towers by MAD. Retrieved from Dezeen <https://www.dezeen.com/2012/12/12/absolute-towers-by-mad/> (Accessed: 05 March 2020)
- Givoni, B. (1969). *Man, climate, and architecture*. Amsterdam; London; New York: Elsevier Publishing Company Limited.
- International Code Council (ICC), Building Officials, Code Administrators International, International Conference of Building Officials, & Southern Building Code Congress International. (2000). *International energy conservation code*. International Code Council.
- Nikandrov, P. (2020). Philipp Nikandrov. Retrieved from <https://www.philippnikandrov.com/evolution-tower> (Accessed: 05 March 2020)

- Olgay, A., & Olgay, V. (1957). Solar control and shading devices. Princeton: Princeton University Press.
- Olgay, V. (1963). Design with climate : bioclimatic approach to architectural regionalism. Princeton: Princeton University Press.
- Reinhart, C. F. (2014). Daylighting handbook I: fundamentals, designing with the sun. Building Technology Press. ISBN 069220363X
- US Green Building Council (2014). LEED v4 for building design and construction. USGBC Inc.
- Vincent Callebaut Architectures (2020). Retrieved from Vincent Callebaut Architectures: [http://vincent.callebaut.org/object/190320\\_taozhuyinyuansite/taozhuyinyuansite/projects](http://vincent.callebaut.org/object/190320_taozhuyinyuansite/taozhuyinyuansite/projects) (Accessed: 05 March 2020)
- Vollers, K. J. (2005). High-Rise Buildings with Twisted Façades. CTBUH 2005 7<sup>th</sup> World Congress. New York.

# Design and Experimental Proof-of-concept of a Façade-integrated Solar Thermal Venetian Blind with Heat Pipes

**Simon Frederik Haeringer<sup>1\*</sup>, Paul-Rouven Denz<sup>2</sup>, Puttakhun Vongsingha<sup>2</sup>, Bruno Bueno<sup>1</sup>, Tilmann E. Kuhn<sup>1</sup>, Christoph Maurer<sup>1</sup>**

\* Corresponding author

<sup>1</sup> Fraunhofer Institute for Solar Energy Systems ISE, Energy Efficient Buildings, Germany, simon.haeringer@ise.fraunhofer.de

<sup>2</sup> Priedemann Façade-Lab GmbH, Germany

## Abstract

*Solar thermal venetian blinds (STVB) pursue the goal of reducing the primary energy demand of buildings with highly transparent façades during operation. They can provide solar control and daylighting functions and at the same time function as a solar thermal collector. A technical overview of STVB based on a design parameter space, which can be used as guideline for the design of STVB, is presented. It is then applied to develop a first actual-size test sample of STVB. The design principle, based on heat pipes and a switchable thermal coupling for heat transfer between the slats and a header tube, allows the STVB to be tiltable and retractable. The key characteristics of the built STVB test sample are: (1) integrated in a double skin façade element; (2) conventional absorber sheet with diagonally mounted heat pipe; (3) switchable thermal coupling with mechanism using springs and solenoids; (4) a multi-port header tube. Outdoor measurements have been carried out and are discussed, demonstrating the technical feasibility of the concept. In the end, design choices for architects and planners for the STVB system and possible installation processes are presented, and recommendations for further developments are assessed.*

## Keywords

*Multifunctional façade, solar control, double skin façade, BIST, design parameter space, heat pipes*

DOI 10.7480/jfde.2020.1.4796

# 1 INTRODUCTION

Many contemporary buildings employ large proportions of glazing in their façades, due to the opportunities that glass offers for daylighting and visual contact with the outside, combined with aesthetic considerations that aim for maximum transparency as proclaimed by modernism (Murray, 2013). At the same time, the drive for green and sustainable buildings with reduced primary energy demand is a current topic of discussion (Mays, 2019). As transparent façade areas cannot be used to install opaque energy-harvesting systems, such as building-integrated solar thermal collectors (BIST) or building-integrated photovoltaic systems (BIPV), new technical solutions are desirable. The solar thermal venetian blind (STVB) represents a novel BIST technology which can turn a venetian blind into an energy-harvesting building component which supplies solar thermal heat to the technical building services. At the same time, the STVB can control and lower passive solar heat gains through the façade by extracting excess heat from the façade thus lowering cooling loads. Like venetian blinds, they provide further adaptive solar control functionalities such as glare control (Kuhn, 2017). The synergy of lowering cooling loads and supplying heat to the technical building services has the potential to lower the overall energy demand of buildings equipped with STVB compared to conventional venetian blinds.

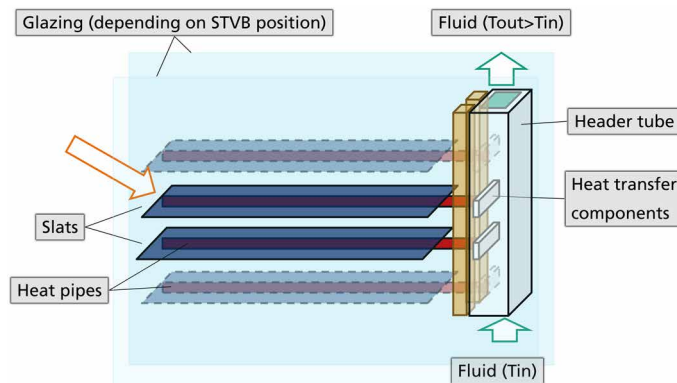


FIG. 1 Main components of a solar thermal venetian blind positioned between an outer and an inner glazing pane. The increase between fluid inlet temperature  $T_{in}$  and fluid outlet temperature  $T_{out}$  illustrates the harvesting of solar thermal heat. The blind mechanism for retracting and tilting the slats is not shown.

The technological approach of the studied STVB is to incorporate heat pipes or closed two-phase thermosiphons<sup>1</sup> into the slat and transfer the absorbed heat via a dry connection to a header tube which transports the heat to the technical building services (cf. Fig. 1). This is advantageous compared to having pipes with flowing fluid incorporated into the slats because no flexible piping is needed. Flexible pipes need space to fold when the slats are retracted and have a higher risk of leakage. The slats of the solar thermal venetian blind need to be movable like a conventional venetian blind to provide adaptive solar control functionalities, i.e. the slats can be tilted, and retracted or lowered. There are several approaches to realising this as will be discussed, one being a “switchable thermal coupling”.

1

In the solar industry, the term “heat pipe” is often used for heat pipes working with capillary forces to return the fluid from the condenser to the evaporator part, as well as for two-phase thermosiphons returning the fluid by gravity. This paper refers to the term “heat pipe” as a generic term for both heat transfer devices whenever no clear declaration is needed.

## 1.1 STATE OF THE ART

Using the building envelope to harvest solar thermal heat was proposed over a century ago (US246626, 1881) and semi-transparent solar collector windows have also been previously presented (Fuschillo, 1975). To date, there are some examples of research projects and products dealing with semi-transparent BIST (Abu-Zour, Riffat, & Gillott, 2006; erfis GmbH; L. Li, Qu, & Peng, 2017; Maurer et al., 2014; Molter, Wolf, Reifer, & Auer, 2017; Palmero-Marrero & Oliveira, 2006; EP1376026B1, 2002; Siebert, 2018). A review of building-integrated solar thermal collectors including semi-transparent BIST was presented in Maurer, Cappel, and Kuhn (2017). Because all of the above-mentioned semi-transparent solutions are static, they are either limited to the parapet areas of the façade or undesirably reduce the visual contact to the exterior (i.e. transparency) and daylight availability. The latter is problematic especially on overcast days with low irradiance. Additionally, they only provide limited control of passive solar heat gains and limited glare protection, as they cannot actively adapt to changing weather conditions, e.g. the position of the sun or heating versus cooling season. Glare issues were reported for a semi-transparent BIST consisting of vacuum tubes and a perforated mirror due to partial shading resulting in dark and bright spots in the field of view of users and reflection of direct sunlight (Molter, Wolf, Reifer, & Auer, 2017). For these reasons, semi-transparent BIST have thus far rarely been used in modern architecture (Cappel et al., 2015).

To address these opposing requirements, many buildings use venetian blinds on transparent areas of the building envelope as an adaptive solar control device to reduce the energy demand for cooling and provide visual comfort (e.g. daylight availability, glare protection, visual contact to the exterior). An extensive review on solar control devices and a design method can be found in Kuhn (2017). In double-skin façades, box-type windows, and closed-cavity façades (CCF), blinds are often installed in the cavity between outer and inner glazing. One problem that can arise in this configuration is the overheating of the cavity (Gratia & Herde, 2007a; Lutz, 2012). Approaches to mitigate this overheating, such as the proper positioning of the blind (Gratia & Herde, 2007b) or integrating phase-change material into blinds (Li, Darkwa, Kokogiannakis, & Su, 2019) were studied.

Solar thermal venetian blinds, as a multifunctional combination of venetian blinds and BIST, have been described in several patents (DE 102006000668 B4, 2006; US4143640 A, 1977). However, none of these patents discusses STVB, which are both tiltable and retractable. A solar thermal venetian blind for the purpose of heating air was presented in US4002159 (1975). A master's thesis on STVB presented both simulation results as well as proposing technical solutions for a STVB design (Cruz Lopez, 2011). This study assumes that heat pipes that work on the horizontal orientation are available for the application in STVB. As will be discussed in Section 2.1, heat pipes suitable for horizontal orientation are not yet available. The study seems to disregard previous studies on BIST and on building energy performance simulations. It uses a simple calculation method for simulation of the STVB which neglects the coupling between STVB and building regarding heating and cooling loads. Furthermore, the presented technical solution for the heat transfer from the heat pipe condenser to the header tube should be investigated experimentally to prove that it functions reliably and efficiently. Theoretical studies and simulations of STVB application in the Mediterranean climate were presented in Guardo, Egusquiza, Egusquiza, and Alavedra (2015); and Velasco, Jiménez García, Guardo, Fontanals, and Egusquiza (2017) without presenting technical solutions. The effect of cooling the slats of venetian blinds in a double skin façade by embedding pipes into the slat through which water is circulated was studied in Jiang, Li, Lyu, and Yan (2019); and Shen and Li (2016) and related studies. The proposed "pipe-embedded" blind is shown to reduce overheating of the cavity and passive solar heat gains. The studies focus on static blinds which cannot be lifted and tilted, thus significantly reducing the visual contact to the exterior as well as daylight availability.

Additionally, photovoltaic venetian blinds and their effect on the thermal performance of double-skin façades have been studied (Luo et al., 2017). They act as shading device-like conventional venetian blinds but cannot remove excess heat like a solar thermal venetian blind. Due to their high absorptivity they could even increase overheating problems.

There are other approaches for fully transparent BIST system, which use fluid between glass panes to remove the heat (InDeWag, 2017; Heiz, Pan, Lautenschlager, Sirtl, Kraus, & Wondraczek, 2017; Li & Tang, 2020; Stopper, 2018, 2019; Stopper, Boeing, & Gstoehl, 2013). With these approaches, ensuring glare protection is challenging and combination with solar control devices such as textile screens is necessary.

It is concluded that a detailed technical overview for designing movable (retractable and tiltable) STVB and an experimental proof of feasibility have not been published yet. Within this publication, a detailed design parameter space for development of *STVB with heat pipes* will be presented. This design parameter space can be helpful for the design of STVB as it gives a detailed overview of the technological options. It was used to guide the development of a first actual-size test sample of a façade element with integrated STVB. The technical performance of this test sample with regard to solar thermal and solar control functionality is subsequently evaluated based on results of calorimetric measurements, to prove the general feasibility of the technological approach. Later, the STVB system is discussed regarding its potential for customisation and from the context of façade construction. Finally, recommendations for further developments are assessed based on expert feedback and on the conclusions drawn from the investigated test sample. As the focus of the paper is the design and proof-of-concept, the energy savings potential by STVB in buildings is not evaluated in detail. This should be part of future studies based on building performance simulations using an experimentally validated simulation model of STVB. The paper at hand lays the foundation for further in-depth performance evaluations.

## 2 DESIGN OF SOLAR THERMAL VENETIAN BLINDS

A detailed design parameter space (DPS) is developed to give an overview of the technical design options and is then used to create a full-scale test sample of a STVB. The design parameter space is divided into different categories (such as different subassemblies of the STVB). For each category the relevant components and their different design choices, named design parameters, are listed. The design parameter space provides a detailed technological overview to engineers and researchers designing and constructing STVB with heat pipes. It can thus help to create new variants of the STVB and continue its development.

### 2.1 DESIGN PARAMETER SPACE

The STVB must simultaneously function as a building-integrated solar thermal collector and as solar control device. For the design parameter space presented here, *STVB with heat pipes* are defined as venetian blinds with horizontal, tiltable and retractable slats that incorporate a heat pipe along their lengths. The heat pipe is responsible for the heat transfer from the slat to the fluid in a header tube, thus providing solar thermal heat. The STVB is defined as the venetian blind with all elements relevant for heat transfer, including the header tube, but without the surrounding or adjacent façade element and glazing (cf. Fig. 1). As such, the STVB is then mounted as part of the façade.

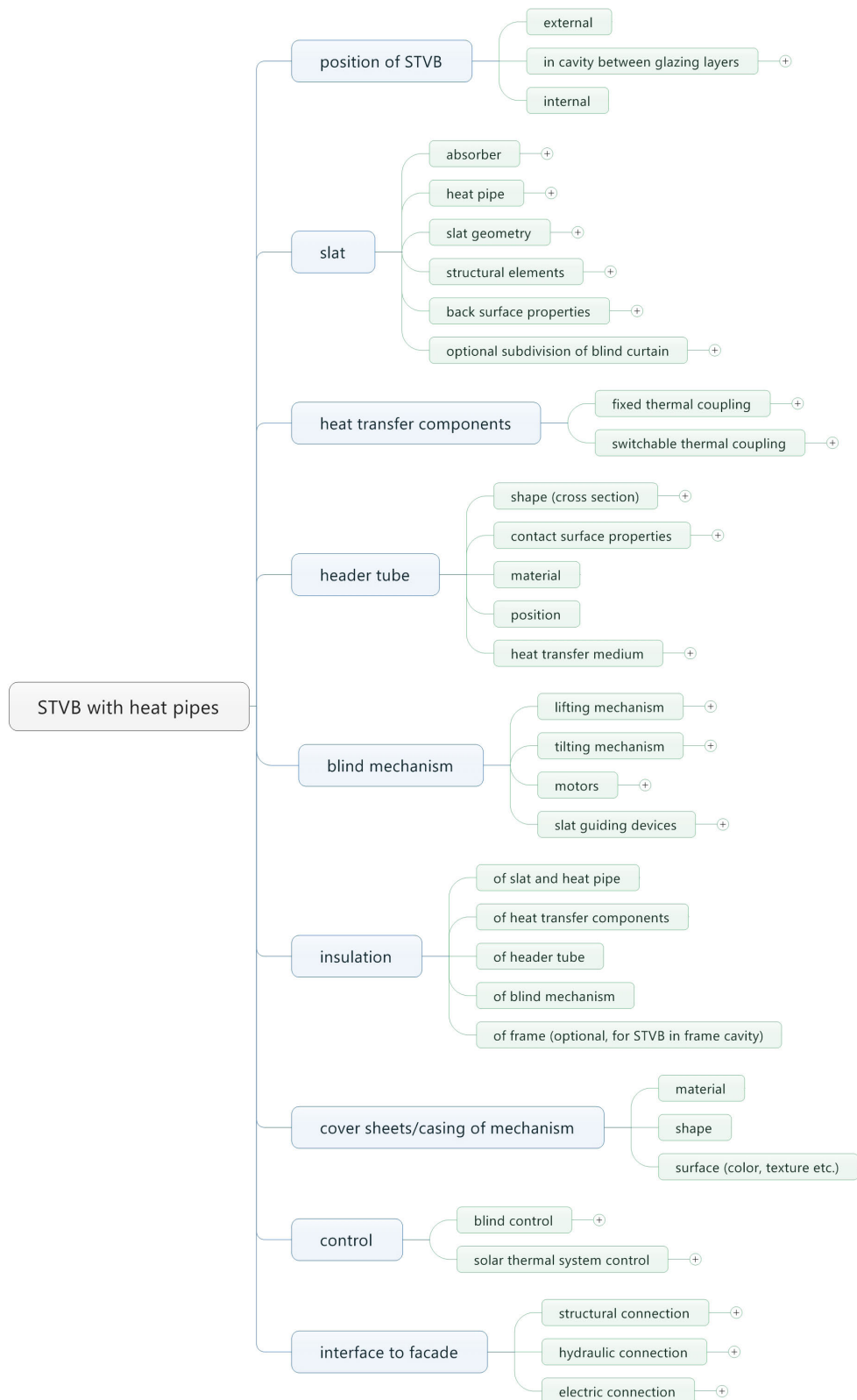


FIG. 2 First and second level of the design parameter space of solar thermal venetian blinds with heat pipes. The full design parameter space is provided as a supplementary file.

An overview of design parameters for BIST collectors and a design parameter space for solar control devices were published in Cappel, Kuhn, and Maurer (2015); and Maurer, Cappel, and Kuhn (2015); and Kuhn (2017), respectively. Following the above-mentioned definition of *STVB with heat pipes*, the STVB design parameter space was compiled to give a complete insight into all design choices that play a role when designing, engineering, and developing a solar thermal venetian blind. As a starting point, the essential functional elements of STVB were analysed. For each of these, the different technical possibilities and design choices were analysed. Each branch of the DPS in Fig. 2 thus presents a different main category. For each main category the relevant design parameters are presented, sometimes grouped into sub-categories (cf. full DPS as Supplementary File). The DPS is considered to include all relevant design parameters at the time of writing; nonetheless, new developments and technologies might alter it in the future.

When using the DPS, an option has to be chosen for each design parameter in each category. The design parameters are not linear independent, i.e. changing one parameter can influence other parameters. The DPS provides exemplary options for each design parameter but does not claim to include all possible options. The DPS is not intended to evaluate the resulting STVB variants, but rather to give a detailed overview to help the understanding of the relevant design parameters of STVB.

The first two levels of the DPS, which represent the main functional elements and main design choices of STVB, are now discussed in detail. Subsequently, examples of the application of the DPS to develop a STVB concept are shown in Section 2.2. This STVB concept has been realised as a functional actual-size test sample.

### Position of STVB

The STVB can be positioned *externally* on the façade, or inside the building (*internal*). In double skin façades, box-type windows, or closed-cavity façades, the STVB can be mounted *in a cavity between glazing layers* where conventional venetian blinds would be mounted as well.

### Slat

*The absorber*, i.e. the top surface of the slat, and the heat pipe have a large influence on solar thermal performance, solar control functions (e.g. passive solar gains and daylighting), and aesthetic appearance. The absorber can range from grey, that is diffusely reflecting, or light guiding as known from conventional slats, to dark blue and highly absorbing with low emissivity as known from solar thermal collectors (called spectrally selective coating). In addition, more sophisticated coatings with high absorption and yet a broader range of colours (Bläsi et al., 2017) or spectrally selective coating with IR absorption and diffuse reflection in the visual range (Lang, 2007) can be used. Absorber thickness and material influence the heat transfer to the heat pipe as well as slat weight and stability. The bulk material of the absorber sheet should ideally be the same as the heat pipe material to handle thermal expansion. In fact, the combination of an aluminium absorber with a copper heat pipe, though common in solar thermal collectors, could lead to aesthetically undesirable deformations and waviness of the absorber sheet due to different thermal expansion coefficients.

The *heat pipes* are responsible for the heat transfer from absorber to header tube. Most commercially available heat pipes for the application in solar thermal collectors have a cylindrical cross section.

The maximum amount of power they can transfer, called operating limit, depends to some degree on a sufficiently large diameter and on its angle of inclination. The operating limit of the chosen heat pipe has to be higher than the maximum amount of absorbed solar radiation, while maintaining a low thermal resistance. The thermal performance is known to decrease with decreasing diameter (Jack & Rockendorf, 2013). This is a limiting factor in achieving thin slats for STVB. Other cross-sectional shapes, such as oval or rectangular, could better suit the application in STVB but are much less common. Moreover, due to the horizontal slats, the heat pipes have to function at small angles of inclination. To be more precise, the operating limit of the selected heat pipe has to be sufficiently high for all possible tilt angles of the slat. Two technological approaches can be used for heat pipes to achieve this good thermal performance at or near horizontal orientation of the heat pipe: mesh or sintered heat pipes using capillary forces to return the fluid from the condenser to the evaporator part (Reay, Kew, & McGlen, 2014) or "overfilling" of closed two-phase thermosiphons (Bezrodny & Podgoretskii, 1994; Morawietz, Paul, & Schnabel, 2018). The topic of heat pipes in horizontal orientation for the application in solar thermal collectors is still the subject of ongoing research. Special attention has to be paid to the case of the condenser being lower than the evaporator, i.e. for negative operating angles. This could happen due to the orientation of an individual slat, of the STVB element, or the mounting in the façade. In this case the heat pipe would have to work against gravity to return the condensed fluid back to the evaporator part and the resulting operating limit is lower. Besides the important topic of the operating limit, the maximum and minimum ambient and operating temperatures have to meet the application in a STVB, i.e. typically, the heat pipe would have to withstand freezing temperatures for its application in the façade as well as high temperatures above 100°C for its application in a solar thermal collector. The outer material of the heat pipe needs to be compatible with the other components of the slat and based on availability.

*Slat geometry* such as cross-sectional shape, edges, etc. can be chosen, taking into consideration the absorber and heat pipe properties as well as the requirements of architectural design and solar control properties. One important characteristic is the slat thickness in packed position. The packed slats will be an opaque area of the façade, which should be minimised for highly transparent façades and/or needs to coincide with opaque areas of the façade such as floor slabs. Furthermore, the projected slat thickness of the lowered blind as seen from an observer inside the room is important as it influences the visual contact to the exterior. *Structural elements* of the slat have to be designed carefully to deal with the increased mass of the slat due to heat pipe, absorber and other components. *Back surface properties* need to be considered as they influence daylighting, could cause glare if not chosen well, and influence the overall appearance of the blind curtain. Finally, different slat types can be chosen for parts of the blind curtain, e.g. using light redirecting slats for the top part and STVB slats below, leading to an *optional subdivision of blind curtain*.

### Heat Transfer Components

The *heat transfer components* include all elements and mechanisms involved in the heat transfer between heat pipe condenser and header tube. Two main approaches were identified. *Fixed thermal coupling* means that the connection between heat pipe and header tube is fixed except for the movement necessary for the slat. An example can be found in Cruz Lopez (2011), where the heat is transferred via overlapping of fin-type heat sinks mounted onto the heat pipe condenser and header tube without direct contact or only a sliding contact between the elements. *Switchable thermal coupling* is a concept that was filed for a patent and in which the thermal and mechanical contact between heat pipe condenser and header tube can be switched (Haeringer, Abderrahman, Vongsingha, Camarena Covarrubias et al., 2017). In the closed position the heat is transferred via

conduction, while in the open position the slats can be moved freely. For the switchable thermal coupling, a mechanism including actuators is necessary to switch from closed to open position and back. To ensure a good heat transfer across the switchable thermal contact, the contact pressing force of the mechanism has to be sufficiently high (Bahrami, Yovanovich, & Culham, 2004). Additionally, the heat transfer from heat pipe to header tube can be enhanced using elements such as an adapter around the heat pipe condenser, special condenser geometries and/or heat transfer films. As this heat transfer is crucial for the solar thermal performance and the control of passive solar heat gains, detailed simulations or experiments are recommended when comparing different concepts (Haeringer, Abderrahman, Vongsingha, Camarena Covarrubias et al., 2017).

### Header Tube

The *header tube* needs to transfer the heat into a *heat transfer medium* such as water or solar fluid (a water-glycol mixture), which then transports the heat to the technical building services. The heat transfer to the header tube is influenced both by the design of the *heat transfer components* as well as the *contact surface properties* of the header tube. The heat transfer into the fluid is mainly influenced by the *shape (cross section)* and *material* of the header tube. For example, multi-port pipes or fins inside the header tube can be used to create a large contact area and high heat transfer coefficients between fluid and header tube (Schiebler, Giovannetti, Schaffrath, & Jack, 2018). Mechanical strength, with regard to the pressing force of a switchable thermal coupling and against deformation due to the inner fluid pressure of the system, is important and influenced mainly by the cross-sectional geometry. Another parameter is the *position*: The header tube would typically be at the side of the element, but the orientation relative to the heat pipe condenser can be chosen (Haeringer, Abderrahman, Vongsingha, Camarena Covarrubias et al., 2017).

### Blind Mechanism

To move the slats, a *blind mechanism* has to be designed. The main components include the *lifting mechanism* and the *tilting mechanism* responsible for retracting and lowering the blind curtain and changing the slat tilt angle with the help of *motors*. Furthermore, *slat guiding devices* can be used such as guiding rails or guiding ropes. Regarding costs, it is preferable to use conventional components (motors, gears, lifting tapes etc.) which use a single motor for lifting and tilting. However, the increased weight of the blind curtain and potentially higher temperatures need to be taken into consideration. Additionally, the alignment between the slats and the header tube is critical for the *heat transfer components*, especially for the *switchable thermal coupling*. Therefore, elongation of the elements connecting the motors and bottom bar or slats, caused by the suspended load, has to be considered. Conventional lifting tapes and tilting cords are based on textile material. To improve their strength and reduce the elasticity modulus, these textile elements can be fibre-reinforced or replaced by metal elements (e.g. steel). Plastic tape reels, conventionally used for tilting and lifting of venetian blinds with one motor, can typically carry up to 5 kg of weight each. With heavier STVB slats a larger number of tape reels must be used to carry the additional weight, or they have to be replaced by a more robust alternative. Commercially available all-metal blinds use a system of scissor chains for tilting and a chain mechanism for lifting (Griesser AG, n.d.; Griesser AG, 1979; Schenker Storen, n.d.) achieving a precise, reliable positioning of heavy slats but requiring regular maintenance.

## Insulation

*Insulation* can and should be applied in various locations to increase solar thermal yield and lower passive solar heat gains by lowering heat losses. Additionally, *cover sheets* can be used to hide elements such as the blind mechanism and the mechanism of switchable thermal coupling for aesthetic reasons. The design of the STVB allows architectural design freedom such as using a shadow box technique or glass fritting when positioning the STVB between two glazing layers. Cover sheets and many other elements allow for individual architectural designs.

## Control

In operation, different *control* strategies can be applied. The *blind control* could be manual or automated. Due to the multifunctionality, it is highly advisable to employ an automated control strategy that considers both passive solar gains, solar thermal energy harvesting and user comfort. Automated controls could prioritise, for example, user comfort (e.g. thermal comfort, glare control or daylighting) or solar thermal yield, and allow overriding by the user. The extent of overriding by the user might have to be limited, to not compromise the overall performance of the system especially regarding solar thermal yields. Advanced control strategies with optimisation routines could be adapted to balance the different demands and provide a robust system (Katsifaraki, Bueno, & Kuhn, 2017).

The *solar thermal system control* includes control of mass flow and fluid inlet temperature or target outlet temperature. This greatly depends on the intended use of the solar thermal heat and the building service system. In general, applications requiring lower fluid temperatures are preferable, such as low temperature radiant heating or as a source for heat-pumps. With lower fluid temperatures, the solar thermal efficiency is higher (due to reduced losses to the ambient) and passive solar heat gains are lower (due to reduced secondary heat gains). At times when the heat demand of the building is significantly lower than the heat provided by the STVB, stagnation can occur (e.g. in summer, as in a conventional solar thermal system). The design of the STVB, overall façade system, and the integration into the building service system therefore has to ensure that the control of passive solar heat gains and prevention of overheating is guaranteed during stagnation or that stagnation is prevented.

## Interface to the Facade

Taking the *position of the STVB* into account, the *interface to the facades* has to be defined including the *structural, hydraulic, and electric connections*. Considerations for the interfaces during the installation process are presented in Section 4.2.

## 2.2 DESIGN AND CONSTRUCTION OF A FIRST SOLAR THERMAL VENETIAN BLIND TEST SAMPLE

The presented design parameter space was used to develop a detailed concept of a STVB, which then was realised as actual-size test sample. This publication discusses the design parameter categories *position of the STVB* and *slat*, as they are relevant to architectural appearance. The design considerations are done for the most part on a qualitative level for the design and realisation of the

first STVB test sample but can be extended to quantitative comparison using detailed simulation models or extensive testing. Criteria to evaluate solar control functionality including visual comfort and daylighting of solar control devices were presented in Kuhn (2017). The general evaluation criteria for building-integrated solar thermal systems *functionality, aesthetics, ecology, economy,* and *feasibility* were presented in Maurer, Cappel, and Kuhn (2015). The main technical evaluation criteria used for the design process of the STVB test sample are *solar thermal yield* and *solar control functionality*, especially *passive solar heat gain control* (g-value). The main aim of the presented STVB concept is maximising solar thermal yield.

### 2.2.1 Position of the Solar Thermal Venetian Blind

Mounting the STVB *in a cavity between glazing layers* as in double-skin façades (DSF) (or box-type windows or closed-cavity façades) protects it from wind, dust, and human contact (Knaack, Bilow, Klein, & Auer, 2014), leading to longer life expectancy, reduced maintenance, and the capacity to function in strong winds. A higher solar thermal yield can be achieved, when compared to *external* or *internal* mounting, as fewer heat losses to the surroundings via convection and radiation occur, especially for non-ventilated DSF (e.g. closed-cavity façades CCF). Mounting the STVB within the cavity between two glazing layers resembles the situation of a conventional flat plate collector, where a front glass pane covers the absorber and the back is insulated. The test sample was therefore constructed as a double-skin element façade, identified as a suitable façade type for STVB.

### 2.2.2 Slat Design

The slats have a significant influence on solar thermal performance, aesthetic appearance, and structural stability. The slat developed for the STVB test sample is shown with its individual components in Fig. 3. Conventional copper-based collector absorber sheets with spectrally selective coating (i.e. high absorptivity in solar range, low emissivity in the IR range) were used aiming to maximise solar thermal yield. The influence on the passive solar heat gain is not clear without in-depth analysis due to two opposing effects:

- higher absorptivity leads to higher secondary heat gains, due to increased temperatures of the absorber
- lower reflectivity leads to a lower effective transmission of solar radiation through the STVB layer into the building (i.e. less radiation is reflected from the slat into the building, especially for small slat tilt angles)

For the designed STVB, commercially available cylindrical mesh heat pipes with 8 mm diameter and copper as the outer material were chosen. Alcohol as working fluid is used to withstand temperatures below 0°C. The selected heat pipe works at an almost horizontal orientation, but the thermal performance increases with increasing operating angle (if angles near 0° are considered). For this reason, the heat pipe is mounted diagonally behind the absorber sheet. A geometric analysis of the heat pipe inclination in correlation with the slat dimensions and slat tilt angle was carried out in TABLE 1. The slats dimensions are length  $l = 1020 \text{ mm}$ , width  $w = 93.8 \text{ mm}$ , and thickness  $t = 10.6 \text{ mm}$  with a vertical slat distance of  $d = 83.4 \text{ mm}$ . The absorber area per slat is  $A_{\text{abs,slat}} = (1004.72 \text{ mm}^2) = 0.072 \text{ m}^2$ . The absorber and heat pipe were assembled using laser-welding, which

is established for solar collectors and is less visible than, for example, ultra-sonic welding (Cappel et al., 2015). The bond from laser welding is nonetheless slightly visible on the front surface of the absorber sheet in Fig. 3.

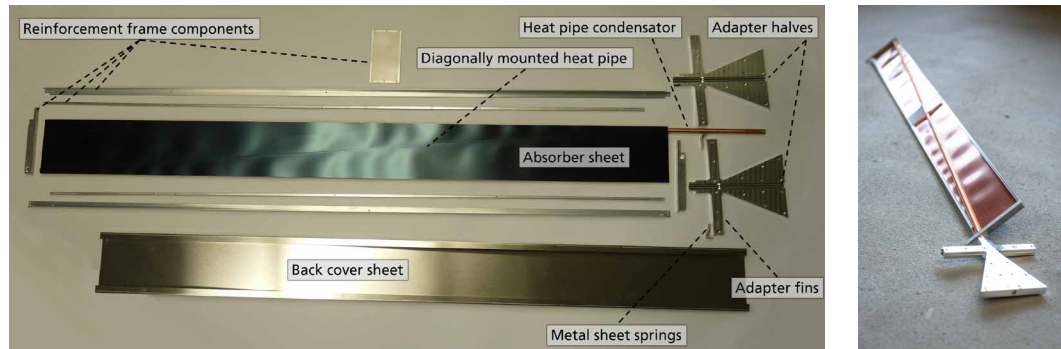


FIG. 3 Left: Slat components. Right: Back surface of a slat with diagonally mounted heat pipe and triangular adapter in the foreground (back cover sheet removed).

TABLE 1 Heat pipe inclinations in correlation with slat dimension and slat tilt angle.

SLAT SIZE	SLAT TILTING ANGLE $\beta$	HEAT PIPE INCLINATION
1020 x 94 mm	5°	0.4°
	10°	0.8°
	45°	3.1°
	82° (closed)	4.3°

The slat geometry was chosen to be flat as the heat pipe is mounted diagonally along the length of the absorber sheet. Curved absorber sheets would require a curved heat pipe. This is technically feasible but results in a more costly manufacturing process. Taking into account the slat thickness  $t$  and vertical slat distance  $d$ , 12% of the visual contact to the exterior is blocked in the horizontal viewing direction for slats in a horizontal position. Reducing the slat thickness would improve the visual contact to the exterior and reduce the opaque area for the retracted slats.

As both the heat pipe and absorber sheet itself are structurally weak, reinforcement is needed to deal with the weight of the heat pipe, absorber sheet, and adapter, which is used for heat transfer to the header tube. For the test sample, a reinforcement frame assembled out of commercially available aluminium profiles was designed to support the perimeter of the absorber sheet. The aim was to achieve structural strength while keeping a low overall slat weight. The reinforcement frame elements on the short, lateral edges are slightly thicker than the rest of the slat. They act as spacers between the slats, when they are in a packed position, to protect the absorber coating from damage. The back and sides of the slats are covered using a thin aluminium back cover sheet resulting in a plain slat appearance. In mass production, an aluminium frame profile that supports the absorber and heat pipe, and functions as back cover sheet, could be manufactured cost-effectively via extrusion moulding. The absorber and heat pipe could then be inserted easily in a simple assembly process.

For the first test sample, no subdivision of the blind curtain was employed for simplicity and cost reasons. In a more advanced STVB, the upper part of the blind curtain could use light-redirecting slats to provide daylight to the depth of the room.

### 2.2.3 Overall Concept of the Test Sample

The overall design of the test sample, an actual-size double skin façade element with integrated solar thermal venetian blind, is shown in Fig. 5. The heat transfer from heat pipe condenser to the header tube is achieved using an adapter and a switchable thermal coupling mechanism as shown in Fig. 4. The adapter is mechanically fixed to the heat pipe condenser to increase the contact surface area to the header tube (cf. Fig. 3). The switchable thermal coupling mechanism employs springs and solenoids. The springs press each adapter against the header tube to achieve the heat transfer, while the solenoids open the coupling when blind movement is necessary (cf. Fig. 4 and Fig. 5). The pressing force between each adapter and the header tube is approximately 10-15 N. The development of a first switchable thermal coupling as *heat transfer component* was presented in Haeringer, Abderrahman, Vongsingha, Camarena Covarrubias et al. (2017). A video demonstrates the movement of the switchable thermal coupling and the ability of the test sample to tilt and retract the slats (Fraunhofer ISE, 2018). The *header tube* is based on a multi-port profile, which has a large contact surface with the fluid for heat transfer, while its structural strength minimises deformation due to internal fluid pressure (see Fig. 4). Deformations would lead to a reduced contact between the adapter and the header tube. The *blind mechanism* employs rigid steel ropes for lifting, and steel scissor chains to connect the slats for tilting. Using steel was necessary to achieve the high precision in positioning the slat and adapter perpendicular to the header tube surface.

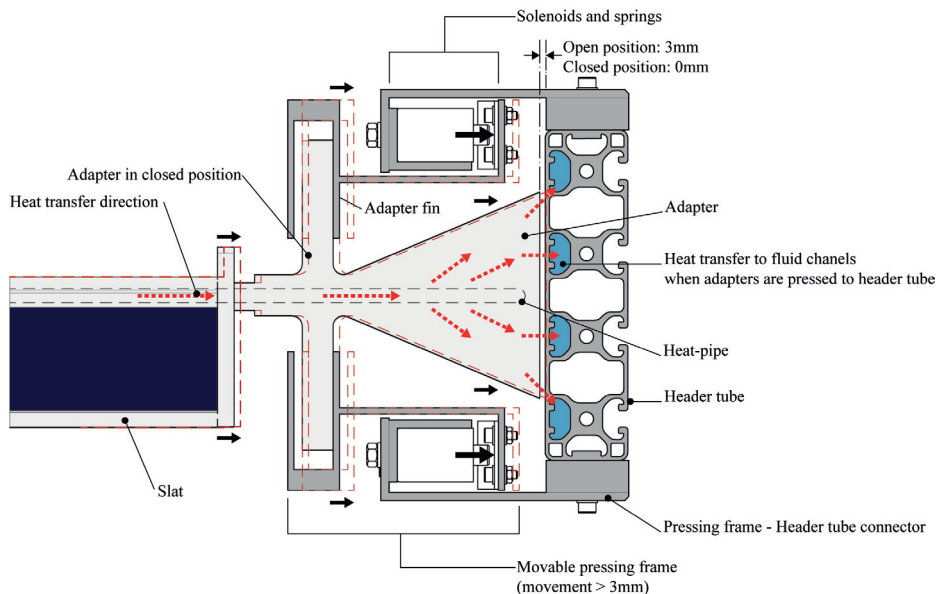


FIG. 4 Schematic horizontal cross-section of the switchable thermal coupling mechanism used as heat transfer component in the STVB test sample. Red arrows indicate the heat flow from slat through heat pipe and adapter to the fluid in the header tube. Black arrows indicate the movement of the switchable thermal coupling mechanism from open to closed position. The dashed red lines indicate the position of slat, adapter, and movable pressing frame when the switchable thermal coupling is closed.

The outside of the façade element is fully glazed and the overall active slat absorber area is  $A_{abs,tot} = 37 \cdot A_{abs,slat} \approx 2.67 \text{ m}^2$ , out of the overall gross façade element area  $A_{gross} = 5.0 \text{ m}^2$ . The exterior glazing layer is 8mm low-iron single-pane toughened safety glass with a solar transmission of  $t_g = 0.89$ . The interior glazing has an area of  $2.9 \text{ m}^2$ , i.e. about 60% of the façade element is transparent from the inside. It is a conventional insulating double-glazed unit with single low-e coating and argon filling with  $t_g = 0.52$ , solar heat gain coefficient  $g = 0.60$  and  $U = 1.1 \text{ W}/(\text{m}^2\text{K})$ . Plain steel sheets cover the remaining area of the back surface of the façade element. The cavity between the exterior and interior glazing layer is 31 cm in depth and has no ventilation openings (but it is not hermetically sealed). Slats, header tube, and mechanism of the STVB are all placed in this cavity. A detailed description of the overall test sample has already been published in Haeringer et al. (2018); and Haeringer, Denz, Vongsingha, Delgado, and Maurer (2019).



FIG. 5 Left: Test sample of double skin façade element (1.4 m x 3.6 m) with integrated solar thermal venetian blind seen from the exterior side. Right: Switchable thermal coupling mechanism with springs and solenoids mounted in the test sample, upper part covered with cover sheets.

### 3 EXPERIMENTAL PROOF OF CONCEPT

The STVB test sample that was developed based on the presented design parameter space has been characterised using calorimetric measurements on an outdoor test facility for solar active building envelope elements. Based on these results, the technical performance of the test sample has been evaluated with regard to solar thermal performance and solar control functionality. The overall goal was to prove the technical feasibility of the chosen STVB concept, i.e. to show the simultaneous functioning as solar control device and as solar thermal collector.

#### 3.1 METHODOLOGY

The experiments were carried out at an outdoor test facility for real-size building envelope elements (Haeringer, Denz, Kuhn, & Maurer, 2019; Maurer, Amann et al., 2015). The measurements report the energy flux through the façade element as well as renewable energy performance, specifically the solar thermal yield. Thus, solar heat gain coefficients ( $g$ ) and solar thermal efficiency  $\eta$  can be calculated. The measurement of the energy flux through the element relies on a “cooled plate method” as discussed in detail for indoor laboratory conditions in Kuhn (2014).

The operation parameters varied during the measurements as shown in TABLE 2 are:

- blind curtain extension  $BE$ , with  $BE = 1$  for fully lowered blind and  $BE = 0$  for fully retracted blind
- slat tilt angle  $\beta$ , with  $\beta = 82^\circ$  representing fully closed slats
- collector fluid inlet temperature  $T_{in}$ , covering the whole working temperature range

The solar irradiances  $G_h$  (total hemispherical irradiance on the collector plane),  $E_d$  (horizontal diffuse irradiance), and ambient temperature  $T_{amb}$  vary naturally. The sample was placed in the vertical position with the façade azimuth angle tracking the sun, i.e. the sample receives the irradiance with changing solar altitude angles  $\theta$  and constant zero azimuth angle. The collector fluid mass flow was set to  $\dot{m} \cong 0.02 \text{ kg}/(\text{m}^2/\text{s}) \cdot A_{abs,tot} = 0.054 \text{ kg}/\text{s}$  following the standard test conditions of (ISO 9806, 2017), but using the absorber area  $A_{abs,tot}$  instead of the gross collector area  $A_{gross}$ . For all measurements the interior temperature was set to  $T_{int} = 22^\circ\text{C}$  to approximately match  $T_{amb}$ .

TABLE 2 Design of experiments for calorimetric measurements of STVB test sample.

DESCRIPTION		$BE$	$\beta [^\circ]$	$T_{in} [^\circ\text{C}]$
<b>Slats lowered &amp; closed</b>	with low fluid temp.	1	82	21
	with medium fluid temp.	1	82	55
	with high fluid temp.	1	82	90
<b>Slats lowered &amp; 45°</b>	with low fluid temp.	1	45	21
<b>Slats lowered &amp; opened</b>	with low fluid temp.	1	10	21
<b>Slats halfdown &amp; closed</b>	with low fluid temp.	0.5	82	21
	with medium fluid temp.	0.5	82	55
<b>Slats halfdown &amp; 45°</b>	with low fluid temp.	0.5	45	21
	with medium fluid temp.	0.5	45	55
<b>Slats halfdown &amp; opened</b>	with low fluid temp.	0.5	10	21

The main measurement results are solar thermal yield  $Q_{use}$  and the local solar energy fluxes  $q_{SHG,i}$  to the building interior for each individual measurement situation. The instantaneous hemispherical solar thermal efficiency  $\eta = Q_{use} / (G_h \cdot A_{ref})$  at the present operation and boundary conditions is calculated using the overall absorber  $A_{abs,tot} \approx 2.67 \text{ m}^2$  as reference area  $A_{ref}$  (cf. Fig. 6). In contrast to conventional opaque collectors, the STVB can offer partial transparency, and thus visual contact to the exterior, while harvesting solar thermal energy. To take into account this multifunctionality of the STVB, the total projected area of the slats on the front glass pane  $A_{proj} = l \cdot (t \cos \beta + w \sin \beta) \cdot 37 \cdot BE$  can be used as reference area  $A_{ref}$  as shown in Fig. 6. This is the opaque area in the normal viewing direction (neglecting the blind pack). This area reaches its maximum at  $A_{proj,max} = 3.15 \text{ m}^2 \cdot BE$  for slat tilt angles  $\beta \geq 56^\circ$  where the transparent area in normal viewing direction disappears. For  $BE = 1$  this is the total venetian blind area. Achieving a similar ratio of transparency in normal viewing direction for an opaque solar thermal collector would result in an absorber with area  $A_{proj}$ .

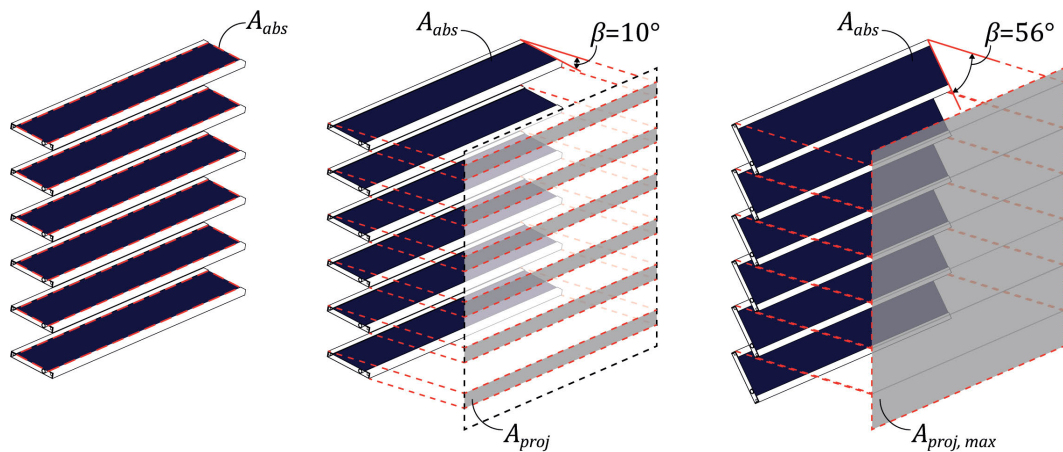


FIG. 6 Different areas that can be used as reference area  $A_{ref}$  to calculate the solar thermal efficiency  $\eta$ . Left: Overall slat absorber area  $A_{abs,tot} \approx 2.67 \text{ m}^2$ . Centre: Projected slat area  $A_{proj}$  for exemplary slat tilt angle of  $\beta = 10^\circ$ . Right: Maximum projected slat area  $A_{proj,max} = 3.15 \text{ m}^2 \cdot BE$  for slat tilt angles of  $\beta \geq 56^\circ$ .

The local solar heat gain coefficient  $g_i$  of the test sample (i.e. of the façade element including the STVB) is calculated with  $q_{abs,i}$ ,  $G_h$ ,  $T_{int,i}$ ,  $T_{amb}$  and the  $U$ -value (Kuhn, 2014). In this paper, only the centre-of-glazing solar heat gain coefficient  $g_{cg}$  is presented. It is important to note that the solar heat gain coefficient  $g$  of transparent BIST, like the STVB, varies with the collector operating conditions (Maurer & Kuhn, 2012). Semi-stationary conditions can be defined for times when efficiency and solar heat gain coefficient  $g$  are stationary. This requires fairly constant irradiance and ambient temperature. Using azimuth tracking increases the time with constant irradiance to reach these conditions.

Under the condition of  $T_{int} \approx T_{amb}$ , the solar thermal performance of the STVB test sample, which is a BIST collector, can be evaluated like conventional solar thermal collectors according to Quasi-Dynamic Testing (QDT) as defined in ISO 9806 (2017) and setting  $a_s$ ,  $a_d$ ,  $a_g$ ,  $a_7$  (artificial wind source) and  $a_8$  (non-concentrating collector) to zero in equation (13) of ISO 9806 (2017). As direct irradiance  $G_b$  and diffuse irradiance  $G_d$  on the collector plane are not directly measured by the test facility, they are calculated based on  $G_h$ ,  $E_{gt}$ ,  $\theta$  and a ground reflectance of 0.2 estimated for the test site. For the conversion, the isotropic sky model and the general relationship  $G_h = G_b + G_d$  have been used (Duffie & Beckman, 2013). The flat plate collector model is used for the incidence angle modifier  $K_b(\theta)$

for closed slats with slat tilt angle  $\beta = 82^\circ$  under azimuth tracking (ISO 9806, 2013). The resulting efficiencies can be compared to efficiency curves of conventional solar thermal collectors to evaluate the technical feasibility of the STVB concept.

### 3.2 RESULTS AND DISCUSSION

The measured solar thermal yield  $Q_{use}$ , showed that the STVB test sample operates as a solar thermal collector for all tested cases of TABLE 2. This proves that the conversion of irradiation into heat by the absorber sheets, as well as the heat transfer via heat pipe and switchable thermal coupling to the header tube, are working. The first aspect (conversion of solar irradiation into heat) was expected because the absorber sheets are the same as those used in conventional solar thermal collectors. The second aspect (heat transfer via heat pipe and switchable thermal coupling) thus proves that the heat pipe operates properly at all slat tilt angles, and that the heat transfer across the switchable thermal coupling is working.

Stationarity of  $\eta$  was found on clear days roughly between 12:00 and 17:00. On overcast days with highly varying irradiance, semi-stationary conditions were not achieved. The QDT method was applied for  $BE = 1$ ,  $\beta = 82^\circ$  with results in TABLE 3 and efficiency curve in Fig. 7. Efficiency curves represent the efficiency  $\eta$  as a function of the so-called "reduced temperature difference", which is the temperature difference between mean fluid temperature  $T_m$  and ambient temperature  $T_{amb}$  divided by the irradiance  $G_h$ . Hence, it can be used to evaluate the solar thermal performance at different fluid temperature levels and/or irradiances. The application of the QDT approach for the STVB measurements, the resulting efficiency curve, and all comparisons to conventional solar thermal collectors are valid only for  $T_{int} \approx T_{amb}$  and zero azimuth angle, as discussed. The QDT evaluation and the efficiency in semi-stationary conditions for  $BE = 1$ ,  $\beta = 82^\circ$  match well. Comparing the performance of half-lowered slats ( $BE = 0.5$ ) with fully lowered slats ( $BE = 1$ ) shows a lower efficiency for  $BE = 0.5$  where only 18 slats are fully exposed to the sun.

TABLE 3 Collector parameters of STVB for  $T_{int} \approx T_{amb}$  obtained via QDT compared to a research flat plate collector with heat pipes - FPC-HP - (Schiebler et al., 2018) and a commercially available flat plate collector - FPC - (DIN CERTCO, 2015). Reference area  $A_{abs,total} = 2.67 \text{ m}^2$  used for the STVB.

	STVB $BE = 1$ $\beta = 82^\circ$	FPC-HP	FPC
$\eta_0$ [1]	0.307±0.010	0.733	0.842
$a_1$ [W/m <sup>2</sup> K]	3.07±0.16	3.562	3.620
$a_2$ [W/m <sup>2</sup> K <sup>2</sup> ]	0	0.017	0.016
$a_3$ [kJ/m <sup>2</sup> K]	138±12	-	6.8
$b_0$ [1]	0.12±0.11	-	0.13
$K_d$	0.88±0.13	-	-

To learn more about the quality of the heat transfer and heat losses in the STVB test sample, the efficiency parameters in TABLE 3 are compared to a commercially available flat plate collector (DIN CERTCO, 2015) and a flat plate collector with heat pipes developed in a research project (Schiebler et al., 2018), which resembles the STVB more closely in terms of the heat transfer principle. The peak

collector efficiency  $\eta_0$  of the STVB test sample is much lower than  $\eta_0$  of these reference collectors. The collector heat transfer coefficient  $a_1$  is comparable. The maximum reachable fluid temperature  $T_m$  for given ambient temperature  $T_{amb}$  and irradiance  $G_h$  are considerably lower for the STVB than for the references, as can be seen from Fig. 7. It is important to note that the possibility to tilt and retract the slats offers the possibility for transparency, which is inherently not possible with conventional solar thermal collectors. Using the projected slat area  $A_{proj} = 1.01 \text{ m}^2$  instead of  $A_{abs,total}$  as a reference area for  $\beta = 10^\circ$  at  $BE = 1$  to judge this multifunctionality would increase the calculated efficiency by a factor of 2.6. An efficiency of  $\eta_0 \approx 0.3$  would thus become  $\eta_{0,proj} \approx 0.8$ . This efficiency is comparable to a conventional solar thermal collector. Conclusively, the STVB can already provide solar thermal yields at  $\eta_0$ -conditions similar to a conventional collector with a comparable transparent percentage of 68%, as achieved for  $\beta = 10^\circ$ ,  $BE = 1$  for the venetian blind area. Because the heat loss coefficient  $a_1$  increases by a factor of 2.6 for the area conversion as well, the STVB efficiency drops much more quickly than a conventional collector for higher temperature differences  $T_m - T_{amb}$ .

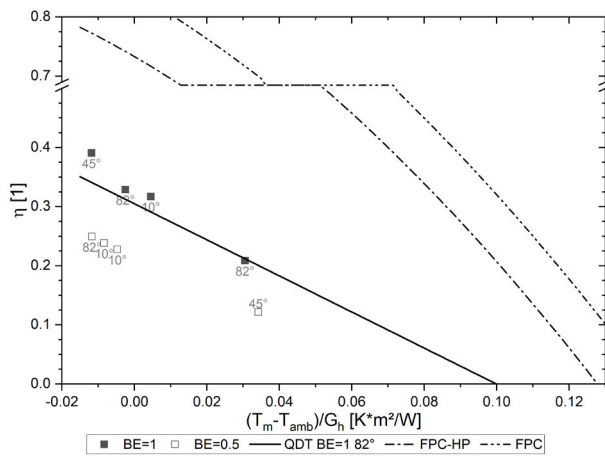


FIG. 7 Efficiency curves  $\eta$  of STVB test sample for  $T_{int} \approx T_{amb}$  as function of mean fluid temperature  $T_m$ , ambient temperature  $T_{amb}$ , and hemispherical irradiance  $G_h$  compared to reference collectors (cf. TABLE 3). Slat tilt angles  $\beta$  noted as label for each data point. Reference area  $A_{abs,total} = 2.67 \text{ m}^2$  used for the STVB.

The measured solar heat gain coefficients of the test sample with closed and lowered slats ( $\beta = 82^\circ$ ,  $BE = 1$ ) are in the range of  $g_{cg} \approx 0.1$ . The solar heat gain coefficient  $g_{cg}$  increases relatively by approximately 50%<sub>rel</sub> with increasing fluid temperatures of the solar thermal system from  $T_{f,in} = 21^\circ\text{C}$  to  $90^\circ$ . Due to the overall low solar heat gain coefficient of the tested STVB façade element, this change is not considered critical to the control of passive solar heat gains. Nonetheless, operating the STVB at lower fluid temperatures would be beneficial with regard to lowering the cooling demand of a building. Considering that towards the interior only conventional double glazing is used (cf. Section 2.2.3), the measured solar heat gain coefficients are sufficiently low, even for highest fluid temperatures, and the solar control functionality is provided for all cases.

Based on the presented measurement results, it is concluded that both the solar thermal functionality and the solar control functionality of the test sample have been demonstrated successfully. Despite the need for technical improvement, especially with regard to solar thermal efficiency, this first STVB test sample therefore proves the technical feasibility of the concept of STVB with heat pipes and switchable thermal coupling. It also shows its potential due to its multifunctionality allowing transparency.

## 4 ARCHITECTURAL IMPLEMENTATION OF THE STVB SYSTEM

The concept of STVB has been evaluated regarding its applicability in architecture and façade construction. Design choices by architects, planners and building owners regarding the STVB system and their relation to the design parameter space are discussed in this section on a conceptual level. Possible installation processes are presented and recommendations for further developments of STVB are identified with the help of industry experts.

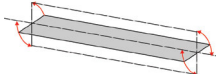
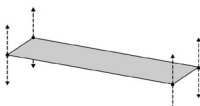
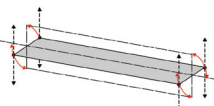
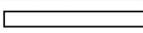
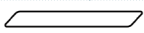
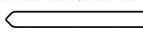
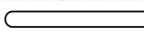
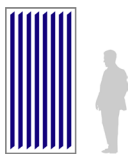
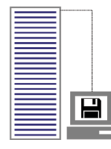
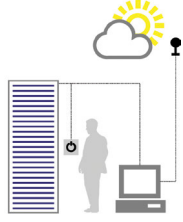
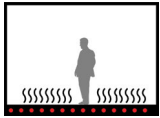
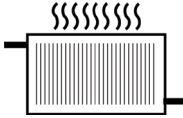
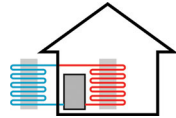
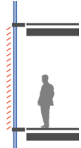
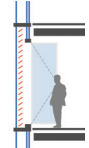
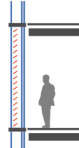
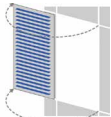
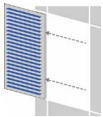
### 4.1 CUSTOMISATION OF STVB DESIGN

The functional and architectural potential of the STVB concept has been presented and reviewed at several trade fairs (BAU 2017, BAU 2019, and glasstec 2018 (Horn & Block, 2018)), and conferences (Denz, Maurer et al., 2018; Denz, Vongsingha et al., 2018; Haeringer, Abderrahman, Vongsingha, Kuhn et al., 2017). The variety of the STVB design parameter options allows for customisation of the STVB for individual building projects, e.g. concerning slat colour (*absorber*), shape (*slat geometry*), and *position* of the STVB. As the STVB can be combined with various different façade typologies, this leads to different potential adaptations of the STVB system. Changing these parameters influences the technical performance, especially solar thermal and solar control functionality. Finding a meaningful STVB concept therefore depends on the individual requirements of the building project and can require compromises, e.g. between technical performance and architectural intent.

The architect, specialist planner, or building owner can thus make different design choices. TABLE 4 provides an overview of the most important design options for the STVB system and its integration into the technical building plant. These design choices are conceptual and require experimental or theoretical validation before being applied in real buildings. The scope of the design choices in TABLE 4 is broadened compared to the DPS in Fig. 2, which explicitly focuses on technical aspects for horizontal, fully movable STVB. For example, TABLE 4 includes choices with reduced slat movement (i.e. less complexity), which could be beneficial to solving the issues with heat transfer from heat pipe to header tube and thus improving the solar thermal efficiency compared to the test sample (cf. Section 3.2). The design choice map is not as detailed as the DPS, so architects and planners can use it during conceptual and design phases when applying the STVB to an individual building project. From the design choices, the technical requirements need to be defined and solutions can be found with the help of the DPS.

Based on this overview, STVB can be seen as a slat-type solar control and solar thermal system that can be adapted to meet different architectural and constructional requirements. This customisation enables design possibilities as required for façade application of newly developed solutions (Klein, 2013). Furthermore, a reduction of the complexity can be achieved to enable application in first building projects with low risks, for example by focusing on tiltable slats, which cannot be retracted. The blind mechanism becomes simpler and the number of components is reduced. The *heat transfer components* from slat to header tube could be modified as the full movement of each slat is not required anymore. This could lead to a better heat transfer and thus a higher solar thermal efficiency. TABLE 4 therefore serves as an outlook to further development paths of the STVB and to potential adaptations of the STVB in first building projects.

TABLE 4 Design choices and options for solar thermal venetian blind systems

DESIGN CHOICE	OPTIONS				
Degree of slat movement	 Fixed	 Tiltable	 Retractable	 Tiltable & retractable	
Absorber surface	 No coating	 Colour coating (painted, anodized, powder coated)	 Spectrally selective coating	 PVT (combination with PV cells)	
Slat shape					
Slat width	Large slats (>100 mm width)			Venetian blind slats (~60-100 mm width)	
Façade pattern width & slat length	Conventional (~1.35 m)			Long (>1.5 m)	
Slat orientation	 Vertical slats			 Horizontal slats	
Blind control	 Manual control	 Central control	 Fully automated control with optional overriding by user		
Use of solar thermal heat	 Domestic hot water preparation	 Low-temperature radiant heating	 Space heating with radiators	 Source for heat-pump or to regenerate geothermal probes	 Solar dehumidification / Solar cooling
Position of STVB and façade type	 Exterior application (arbitrary façade type)	 Inside cavity of box-type window or double skin façade		 Inside cavity of closed cavity façade	
Degree of STVB element movement	 Fixed element	 Window shutter type		 Sliding shutter type	

## 4.2 INSTALLATION PROCESS OF STVB

Due to the vast variety of façade construction typologies in the market, the installation concept of STVB should be adaptable to different façade construction and installation types. The basic installation scenarios that are investigated, under consideration of the surrounding and support components, are:

- Scenario 1: The STVB is installed on site into a façade system that provides the structure to carry and position the STVB components.
- Scenario 2: The STVB is a pre-fabricated unit supporting itself, installed in a façade system that provides supporting points only, such as brackets.

Scenario 1 mostly applies to window (or box-type window) units in a punctuated façade as well as stick-system façades like multi-storey ventilated double skin façades (see Fig. 8). In this scenario, the STVB is installed directly to the existing structures on site, which support the components of the STVB structurally. During the installation, the STVB requires temporary installation support elements – e.g. to hold all STVB components in place during transportation and mounting. The temporary elements are removed when the STVB is adjusted to site tolerances and fixed to the main structure in the correct position. This method would require a long installation process on site. Depending on weather and location, the installation could therefore become rather difficult.

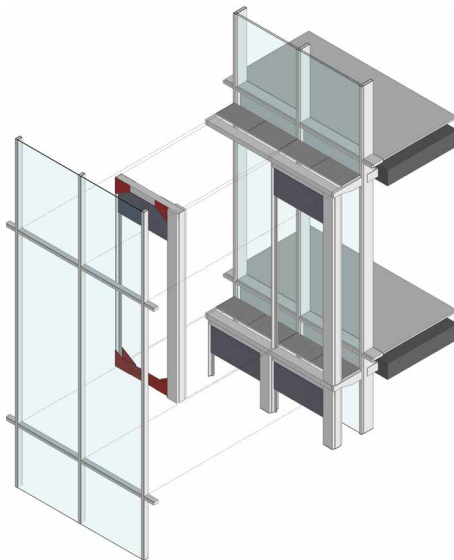


FIG. 8 STVB installation in Scenario 1 on a multi-storey ventilated double-skin façade

In Scenario 2, the STVB itself comes with a rigid frame as standalone unit to be added externally to an existing façade or as an integrated part of a unitised façade system. In this scenario, the STVB is completely assembled at the workshop before being delivered and mounted to the building. This method allows better quality control because the crucial process is done in a controlled environment thus shortening the installation process on site.

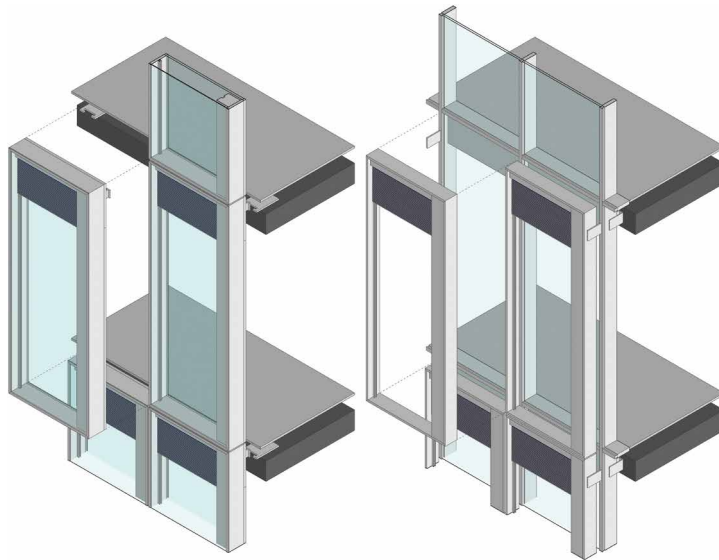


FIG. 9 STVB installation in Scenario 2 as part of double skin unitised façade (left); as an additional stand-alone element on an existing unitised or stick façade system (right)

As in any general construction process, the façade and other exterior surfaces have to be completed first, before the construction of the interior spaces, including the building service system, can start. The installation of STVB needs to be considered as part of both processes: façade construction and building service construction. After its installation as part of the façade, the STVB needs to be checked by a building service specialist who will review the inlet and outlet pipes of the solar thermal unit and carry out a leak test. After the test, the pipes need to be sealed, if the installation of building service has not yet started. Once the building envelope is fully closed and interior finishing starts, the STVB can be connected to building service piping and be put into operation.

### 4.3 RECOMMENDATIONS FOR FUTURE DEVELOPMENTS AND APPLICATIONS

Based on a detailed review of the developed STVB test sample and with input from trade fairs and conferences, a SWOT analysis was carried out underlining strengths as well as weaknesses of the STVB approach (Denz, 2019). To review the main benefits of STVB and guide the direction of further developments, feedback from external stakeholders was gathered in a lead-user workshop (Hippel, 2005). Experts with backgrounds such as façade system fabricator, sun-shading fabricator, project developer, specialist planner on climate engineering, and architects from both practice and academia were identified as lead users and took part in a workshop (Beucker, 2020). The participants discussed and evaluated the STVB test sample and its proposed benefits. Together with the lead users, relevant requirements and recommendations for future STVB developments were specified and weighted. The most important results are summarised in TABLE 5.

TABLE 5 Main requirements and recommendations for future developments of STVB as stated during the lead-user workshop.

<b>Design requirements</b>	– Visually reduced and unobtrusive slat design
<b>Technical requirements</b>	– Reduction of mechanical complexity – Reduction of the size of the heat transfer components (switchable thermal coupling mechanism and header tube) – Accessibility for maintenance and cleaning
<b>Commercial requirements</b>	– Focus on promoting the reduction of the solar heat gain by the STVB while maintaining high visual transparency of the glazing as a unique selling point – Suitable types of buildings are hospitals, hotels, restaurants, representative building of companies, offices, ministries etc. – Improve the cost-benefit ratio
<b>User requirements</b>	– High reliability during the service life

These results show that the main concern is the current complexity of the STVB, which presumably would result in a laborious production process, high cost, and high maintenance, or low reliability during operation. This assessment matches the review of the built STVB test sample and the SWOT analysis (Denz, 2019). Reducing the complexity as discussed in Section 4.1 could deal with these concerns and improve the cost-benefit ratio if reduced functionality is sufficient for the actual building project. In order to simplify the system, the existing components could furthermore be redesigned by applying industrial production and installation methods. For example, as suggested in Section 2.2.2, aluminium extrusion could reduce cost and time of manufacturing and assembly of the slats by reducing the amount of components.

The participants of the lead-user workshop listed the feature of STVB to reduce the thermal load within a double skin façade as well as the  $g$ -value, while allowing high visual transparency as one of its major strengths. Following this concept, STVB could be further developed by focusing on its application as an adaptive solar control system, which aims to control and reduce the solar heat gain coefficient  $g$  rather than focusing on maximising the solar thermal yield. Optimising the STVB to reduce the solar heat gain could enable future building projects with fully glazed façades, even in corner situations, while still preventing overheating of the room in summer, as required by energy efficiency and building codes such as EnEV (2007).

## 5 CONCLUSIONS

Solar thermal venetian blinds present a novel, multi-functional, and adaptive solar control device with solar thermal functionality, fully integrated into glazed areas of the building envelope. They can simultaneously fulfil the functions of a solar thermal collector and of a solar control device as has been demonstrated experimentally with the designed test sample. The presented design parameter space for STVB gives a complete overview of possible variants of STVB with horizontal, tiltable and retractable slats that incorporate a heat pipe. Engineers and researchers can use it as guideline for future technical developments. Guided by the design parameter space, a STVB test sample with heat pipes and fully movable slats was developed. Its key design features are: (1) STVB positioned within the cavity of a double-skin façade element, (2) conventional absorber sheet with diagonally mounted cylindrical heat pipe, (3) heat transfer between heat pipe condenser and header tube via switchable thermal coupling using an adapter with an optimised shape and a mechanism using springs and self-latching solenoids, (4) a multi-port header tube. Alternative concepts with different absorber coatings, heat pipes, slat geometries, and alternative mechanisms for the switchable

thermal coupling can be designed based on the design parameter space. Outdoor experiments on the STVB test sample proofed the technical performance of the studied STVB concept in terms of solar thermal efficiency  $\eta$  and control of passive solar heat gains ( $g$ -value). It was found that the solar thermal performance leaves significant room for improvement. However, when considering the multifunctionality, namely transparency, the STVB already performs comparably to conventional solar thermal collectors.

The design parameter space, various design choices, and integration into different façade systems allow architects and specialist planners to adapt the STVB to individual building projects. The installation processes for two different mounting scenarios were discussed and recommendations by industry experts for future developments were evaluated. The proposed customisation of STVB and the recommendations by the lead users will be used to guide further developments aiming at the first implementation of the STVB in a building project. Future research will investigate the effects of technical improvements and of different design variants and assess the overall energy savings potential in simulation studies using an experimentally validated model of the STVB.

### Acknowledgements

The authors would like to thank Ulrich Amann and Johannes Hanek for carrying out the calorimetric measurements and the mechanical workshop at Fraunhofer ISE for manufacturing components of the test sample. The authors would like to thank Paolo di Lauro, Katharina Morawietz, Alberto Delgado, Mohamad Haidar, Sören Nungesser, Krutarth Panchal, Ikbel Abderrahman, Csaba Jozsef, Achim Rastelli, Sven Fahr, Andreas Piekarczyk and Josef Steinhart, current and former colleagues at Fraunhofer ISE, for their contribution and hands-on support within the research project. The authors would like to thank Johannes Pellkofer and Stefan Robanus of IBK2, University of Stuttgart and Severin Beucker, Borderstep Institute for Innovation and Sustainability, for their contributions within the research project.

The authors gratefully acknowledge the financial support within the ArKol research project (grant number: 0325857 A/B/C) by the German Federal Ministry of Economic Affairs and Energy (BMWi) based on a decision by the German Bundestag.

## References

- Abu-Zour, A. M., Riffat, S. B., & Gillott, M. (2006). New design of solar collector integrated into solar louvres for efficient heat transfer. *Applied Thermal Engineering*, 26(16), 1876–1882. <https://doi.org/10.1016/j.applthermaleng.2006.01.024>
- Angilletta, D. J. (1975). US4002159.
- Bahrami, M., Yovanovich, M. M., & Culham, J. R. (2004). Thermal Joint Resistances of Conforming Rough Surfaces with Gas Filled Caps. *Journal of Thermophysics and Heat Transfer*, 18(3), 318–325. <https://doi.org/10.2514/1.5480>
- Beucker, S. (2020). *Auswertung von Produkt- und Vermarktungsoptionen für architektonisch integrierte Fassadenkollektoren im Projekt ArKol [Evaluation of product and marketing options for architecturally integrated façade collectors within the ArKol project]: Internal project report*. Berlin.
- Bezrodny, M. K., & Podgoretskii, V. M. (1994). Flooding and heat transfer limits in horizontal and inclined two-phase thermosiphons. *Experimental Thermal and Fluid Science*, 9(3), 345–355. [https://doi.org/10.1016/0894-1777\(94\)90037-X](https://doi.org/10.1016/0894-1777(94)90037-X)
- Bittmann, M. (2006). DE 102006000668 B4.
- Bläsi, B., Kroyer, T., Höhn, O., Wiese, M., Ferrara, C., Eitner, U., & Kuhn, T. E. (2017). Morpho Butterfly Inspired Coloured BIPV Modules. Advance online publication. <https://doi.org/10.4229/EUPVSEC20172017-6BV.3.70>
- Cappel, C., Kuhn, T. E., & Maurer, C. (2015). Research and development roadmap for façade-integrated solar thermal systems. Retrieved from <http://publica.fraunhofer.de/documents/N-349494.html>
- Cappel, C., Streicher, W., Hauer, M., Lichtblau, F., Szuder, T., Kuhn, T. E., & Maurer, C. (2015). "AktiFas" Fassadenintegrierte Solarthermie: Bestandsaufnahme und Entwicklung zukunftsfähiger Konzepte [AktiFas" façade integrated solar thermal systems: review and development of future-proof concepts]: Final Project Report. Freiburg. Retrieved from Fraunhofer ISE website: <http://publica.fraunhofer.de/dokumente/N-349495.html>
- Cruz Lopez, P. B. (2011). *Solar Thermal Collector in Façades: Collecting Solar Thermal Energy for Heating and Cooling Purposes* (Master Thesis). TU Delft, Delft. Retrieved from <http://repository.tudelft.nl/islandora/object/uuid:1c-da81f7-c889-447b-9759-7b774cc7fece?collection=education>
- Denz, P.-R. (2019). Solar Thermal Venetian Blinds. In International Energy Agency (Ed.), *State-of-the-art and SWOT analysis of building integrated solar envelope systems: Deliverables A.1 and A.2* (pp. 93–95): IEA Solar Heating and Cooling Technology Collaboration Programme (IEA SHC). Retrieved from <https://doi.org/10.18777/ieashc-task56-2019-0001>
- Denz, P.-R., Maurer, C., Vongsingha, P., Haeringer, S. F., Hermann, M., Seifarth, H., & Morawietz, K. (2018). Solar Thermal Façade Systems – an interdisciplinary approach. In *Advanced Building Skins Conference*, Bern, Switzerland.
- Denz, P.-R., Vongsingha, P., Haeringer, S. F., Maurer, C., Hermann, M., Seifarth, H., & Morawietz, K. (2018, October). Solar thermal energy from opaque and semi-transparent façades – current results from R&D project ArKol. In *Engineered Transparency 2018*. Berlin: Ernst & Sohn.
- DIN CERTCO (2015). *Summary of EN 12975 Test Results, annex to Solar KEYMARK Certificate: Licence number: 011-7S1404 F*. Berlin. Retrieved from <https://www.dincertco.tuv.com/registrations/60072471?locale=en>
- Duffie, J. A., & Beckman, W. A. (2013). *Solar engineering of thermal processes* (4<sup>th</sup> ed.). Hoboken: Wiley.
- EnEV (2007). *Verordnung über energiesparenden Wärmeschutz und energiesparende Anlagentechnik bei Gebäuden (Energieeinsparverordnung - EnEV) [German Energy Saving Regulations]: Bundesgesetzblatt Teil 1; Nr. 34, Seiten 1519 - 1563*. Retrieved from [http://www.gesetze-im-internet.de/enev\\_2007/index.html](http://www.gesetze-im-internet.de/enev_2007/index.html)
- Erfis GmbH. Erfitherm. Retrieved from <http://www.erfis.de/ff/produkte/erfitherm/>
- Fraunhofer ISE (2018). Forschungsprojekt »Arkol« – Flexible Fassadenkollektoren für solare Architektur [Research project "Arkol" – Flexible façade collectors for solar architecture]: Demonstration video on YouTube. Retrieved from <https://www.youtube.com/watch?v=6BlwtcDmkH8>
- Fuschillo, N. (1975). Semi-transparent solar collector window systems. *Solar Energy*, 17(3), 159–165. [https://doi.org/10.1016/0038-092x\(75\)90054-7](https://doi.org/10.1016/0038-092x(75)90054-7)
- Gratia, E., & Herde, A. de (2007a). Greenhouse effect in double-skin façade. *Energy and Buildings*, 39(2), 199–211. <https://doi.org/10.1016/j.enbuild.2006.06.004>
- Gratia, E., & Herde, A. de (2007b). The most efficient position of shading devices in a double-skin façade. *Energy and Buildings*, 39(3), 364–373. <https://doi.org/10.1016/j.enbuild.2006.09.001>
- Griesser AG. (n.d.). Metalunic. Retrieved from <https://www.griesser.de/en/products/external-venetian-blinds/all-metal-external-venetian-blind/metalunic>
- Griesser AG (1979). CH635164A5.
- Guardo, A., Egusquiza, M., Egusquiza, E., & Alavedra, P. (2015). Preliminary results on the assessment of using Venetian blinds as a solar thermal collector in double skin façades in Mediterranean climates. In *10<sup>th</sup> Energy Forum on Advanced Building Skins*, Bern; Switzerland.
- Haeringer, S. F., Abderrahman, I., Vongsingha, P., Camarena Covarrubias, S., Amann, U., Kuhn, T. E., ... Maurer, C. (2017). Solar Thermal Venetian Blind - Development and Evaluation of a Switchable Thermal Coupling. In OTTI e.V. (Chair), *27. Symposium Thermische Solarenergie*, Bad Staffelstein, Germany.
- Haeringer, S. F., Abderrahman, I., Vongsingha, P., Kuhn, T. E., Denz, P.-R., & Maurer, C. (2017). Solar Thermal Venetian Blinds – Transparency, User Comfort and Solar Energy in one! In *Passive Low Energy Architecture (Chair), Proceedings of 33<sup>rd</sup> PLEA International Conference - Design to Thrive*, Edinburgh, Scotland.
- Haeringer, S. F., Delgado, A., Di Lauro, P., Vongsingha, P., Haidar, M., Panchal, K., ... Maurer, C. (2018). Raumhohes Ganzglas-Fassadenelement mit solarthermischer Jalousie. In *Conexio GmbH (Chair), Symposium Solarthermie*, Bad Staffelstein, Germany.
- Haeringer, S. F., Denz, P.-R., Kuhn, T. E., & Maurer, C. (2019). Solar thermal venetian blind as synergetic and adaptive sun protection device in double skin façades - Characterization via calorimetric measurements. In *14<sup>th</sup> Conference on Advanced Building Skins* (pp. 282–291). Lucerne (Switzerland): Advanced Building Skins GmbH.

- Haeringer, S. F., Denz, P.-R., Vongsingha, P., Delgado, A., & Maurer, C. (2019). Arkol – Development and Testing of Solar Thermal Venetian Blinds. In T. Auer, U. Knaack, & J. Schneider (Eds.), *Powerskin Conference: Proceedings* (pp. 195–207). Delft: TU Delft Open. Retrieved from [https://books.bk.tudelft.nl/index.php/press/catalog/book/isbn\\_9789463661256](https://books.bk.tudelft.nl/index.php/press/catalog/book/isbn_9789463661256)
- Heiz, B. P. V., Pan, Z., Lautenschlager, G., Sirtl, C., Kraus, M., & Wondraczek, L. (2017). Ultrathin Fluidic Laminates for Large-Area Façade Integration and Smart Windows. *Advanced Science (Weinheim, Baden-Württemberg, Germany)*, 4(3), 1600362. <https://doi.org/10.1002/advs.201600362>
- Hippel, E. von (2005). *Democratizing innovation*. Cambridge: Creative Commons / The MIT Press. Retrieved from <http://web.mit.edu/evhippel/www/democ1.htm>
- Horn, B., & Block, E. (2018). *VISIONS: GLASS TECHNOLOGY LIVE - THE HUB @ GLASSTEC*. Düsseldorf. Retrieved from Messe Düsseldorf website: [https://www.glasstec.de/de/glass\\_technology\\_live/Visions\\_auf\\_glass\\_technology\\_live](https://www.glasstec.de/de/glass_technology_live/Visions_auf_glass_technology_live)
- InDeWag: Industrial Development of Water Flow Glazing Systems (2017). Retrieved from <http://indewag.eu/>
- ISO 9806 (2013). *Solar energy - Solar thermal collectors - Test methods (DIN EN ISO 9806:2014-06)*. (ISO, 9806): International Organization for Standardization.
- ISO 9806 (2017). *Solar energy - Solar thermal collectors - Test methods (ISO 9806:2017)*. (ISO, 9806): International Organization for Standardization.
- Jack, S., & Rockendorf, G. (2013). *Wärmerohre in Sonnenkollektoren - Wärmetechnische Grundlagen und Bewertung sowie neue Ansätze für die Integration: Abschlussbericht zum Vorhaben (Heat pipes in solar collectors - Thermal engineering basics and evaluation as well as new approaches for integration: Final project report); Kurzbezeichnung: HP-Opt; Laufzeit: 01.06.2010 - 31.05.2013*. <https://doi.org/10.2314/GBV:788667017>
- Jiang, S., Li, X., Lyu, W., & Yan, S. (2019). Numerical analysis on the load reduction of a pipe-embedded window with different water temperatures and structures under different climates. *Science and Technology for the Built Environment*, 25(9), 1187–1198. <https://doi.org/10.1080/23744731.2019.1642094>
- Katsifaraki, A., Bueno, B., & Kuhn, T. E. (2017). A daylight optimized simulation-based shading controller for venetian blinds. *Building and Environment*, 126, 207–220. <https://doi.org/10.1016/j.buildenv.2017.10.003>
- Klein, T. (2013). *Integral façade construction: Towards a new product architecture for curtain walls*. *Architecture and the built environment*.
- Knaack, U., Bilow, M., Klein, T., & Auer, T. (2014). *Façades: Principles of construction* (Second and revised edition). Basel: Birkhäuser Verlag. Retrieved from <http://search.ebscohost.com/login.aspx?direct=true&scope=site&db=nlebk&AN=852547>
- Kuhn, T. E. (2014). Calorimetric determination of the solar heat gain coefficient g with steady-state laboratory measurements. *Energy and Buildings*, 84, 388–402. <https://doi.org/10.1016/j.enbuild.2014.08.021>
- Kuhn, T. E. (2017). State of the art of advanced solar control devices for buildings. *Solar Energy*. Advance online publication. <https://doi.org/10.1016/j.solener.2016.12.044>
- Lang, U. (2007). Energieeffizienz durch selektiven Sonnenschutz [Energy efficiency through selective sun protection]. *RTS Magazin*, 52(2), 31–33. Retrieved from <https://www.rts-magazin.de/heftarchiv/rts-magazin/2007/item/639-ausgabe-02-2007.html>
- Li, C., & Tang, H. (2020). Evaluation on year-round performance of double-circulation water-flow window. *Renewable Energy*, 150, 176–190. <https://doi.org/10.1016/j.renene.2019.12.153>
- Li, L., Qu, M., & Peng, S. (2017). Performance evaluation of building integrated solar thermal shading system: Active solar energy usage. *Renewable Energy*, 109, 576–585. <https://doi.org/10.1016/j.renene.2017.03.069>
- Li, Y., Darkwa, J., Kokogiannakis, G., & Su, W. (2019). Phase change material blind system for double skin façade integration: System development and thermal performance evaluation. *Applied Energy*, 252, 113376. <https://doi.org/10.1016/j.apenergy.2019.113376>
- Luo, Y., Zhang, L., Wang, X., Xie, L., Liu, Z., Wu, J., . . . He, X. (2017). A comparative study on thermal performance evaluation of a new double skin façade system integrated with photovoltaic blinds. *Applied Energy*, 199, 281–293. <https://doi.org/10.1016/j.apenergy.2017.05.026>
- Lutz, M. (2012). Die Closed-Cavity-Fassade. *Stahlbau*, 81(S1), 268–278. <https://doi.org/10.1002/stab.201290070>
- Maurer, C., Amann, U., Di Lauro, P., Hanek, J., Fahr, S., Kramer, K., & Kuhn, T. E. (2015, March 31). "GWert-Tracker": Neues Verfahren zur Outdoor-Charakterisierung von Fassadenkollektoren und BIPV. *Schlussbericht ["G-Value-Tracker": new method for outdoor characterisation of façade collectors and BIPV. final report]*. Freiburg. Retrieved from Fraunhofer ISE website: <http://publica.fraunhofer.de/dokumente/N-366874.html>
- Maurer, C., Cappel, C., & Kuhn, T. E. (2015). Methodology and first results of an R&D road map for façade-integrated solar thermal systems. *Energy Procedia*, 70, 704–708. <https://doi.org/10.1016/j.egypro.2015.02.179>
- Maurer, C., Cappel, C., & Kuhn, T. E. (2017). Progress in building-integrated solar thermal systems. *Solar Energy*, 154, 158–186. <https://doi.org/10.1016/j.solener.2017.05.065>
- Maurer, C., Gasnier, D., Pflug, T., Plešec, P., Hafner, J., Jordan, S., & Kuhn, T. E. (2014). First Measurement Results of a Pilot Building with Transparent Façade Collectors. *Energy Procedia*, 48, 1385–1392. <https://doi.org/10.1016/j.egypro.2014.02.156>
- Maurer, C., & Kuhn, T. E. (2012). Variable g value of transparent façade collectors. *Energy and Buildings*, 51, 177–184. <https://doi.org/10.1016/j.enbuild.2012.05.011>
- Mays, J. C. (2019, April 25). De Blasio's 'Ban' on Glass and Steel Skyscrapers Isn't a Ban at All. *The New York Times*. Retrieved from <https://www.nytimes.com/2019/04/25/nyregion/glass-skyscraper-ban-nyc.html>
- Molter, P., Wolf, T., Reifer, M., & Auer, T. (2017). Integration of technology components in cladding systems. In T. Auer, U. Knaack, & J. Schneider (Eds.), *Powerskin Conference: Proceedings* (pp. 171–178). Delft: TU Delft Open.
- Morawietz, K., Paul, T., & Schnabel, L. (2018). Experimental investigation of horizontal and slightly inclined closed two-phase thermosyphons and heat pipes for solar façade integration. In *Joint 19<sup>th</sup> International Heat Pipe Conference and the 13<sup>th</sup> International Heat Pipe Symposium*.

- Morse, E. S. (1881). US246626.
- Murray, S. (2013). *Translucent building skins: Material innovations in modern and contemporary architecture*. London: Routledge.
- Palmero-Marrero, A. I., & Oliveira, A. C. (2006). Evaluation of a solar thermal system using building louvre shading devices. *Solar Energy*, 80(5), 545–554. <https://doi.org/10.1016/j.solener.2005.04.003>
- Pierce, N. T. (1977). Massachusetts Institute of Technology US4143640 A.
- Reay, D. A., Kew, P. A., & McGlen, R. J. (2014). *Heat pipes: Theory, design and applications* (Sixth edition). Amsterdam: Elsevier.
- Robin, J.-M. (2002). Jean-Marc Robin EP1376026B1.
- Schenker Storen (n.d.). All-metal blinds GM 100. Retrieved from <https://de.schenkerstoren.com/en/products/all-metal-blind-gm-100>
- Schiebler, B., Giovannetti, F., Schaffrath, W., & Jack, S. (2018). *Kostengünstige und zuverlässige Solarsysteme durch neuartige Wärmerohr-Kollektoren: Abschlussbericht zum Vorhaben*. Kurztitel: HP-Koll, Laufzeit: 01.09.2014-31.03.2018. Emmerthal. Retrieved from Institut für Solarenergieforschung Hameln (ISFH) website: <https://www.tib.eu/de/suchen/id/TIBKAT%3A1048288684/Kosteng%C3%BCnstige-und-zuverl%C3%A4ssige-Solarsysteme-durch/>
- Shen, C., & Li, X. (2016). Thermal performance of double skin façade with built-in pipes utilizing evaporative cooling water in cooling season. *Solar Energy*, 137, 55–65. <https://doi.org/10.1016/j.solener.2016.07.055>
- Siebert, J. (2018, June 4). Powered by Shade | Ingenieurbüro für Regenerative Energiesysteme Dipl.-Ing. (FH) Joachim Siebert. Retrieved from <http://erneuerbare-energien-ostsachsen.de/index.php/produkte/powered-by-shade>
- Stopper, J. (2018). *FLUIDGLAS - Flüssigkeitsdurchströmte Fassadenelemente: Anwendbarkeit von flüssigkeitsdurchströmten, transparenten Fassadenelementen zur Kontrolle der Energietransmission von Gebäuden in der Gebäudehülle (FLUIDGLAS – fluid flow through façade elements: usability of fluid flow through, transparent façade elements for energy transmission control of buildings within the building envelope)*. München: Universitätsbibliothek der TU München. Retrieved from <http://nbn-resolving.de/urn/resolver.pl?urn:nbn:de:bvb:91-diss-20180425-1430706-1-4>
- Stopper, J. (2019). Fluidglass – The Energy Efficient Glass Façade. In T. Auer, U. Knaack, & J. Schneider (Eds.), *Powerskin Conference: Proceedings* (pp. 223–233). Delft: TU Delft Open.
- Stopper, J., Boeing, F., & Gstoehl, D. (2013). Fluid glass façade elements: Influences of dyeable liquids within the fluid glass façade. In *8<sup>th</sup> Energy Forum*, Bressanone; Italy.
- Velasco, A., Jiménez García, S., Guardo, A., Fontanals, A., & Egusquiza, M. (2017). Assessment of the Use of Venetian Blinds as Solar Thermal Collectors in Double Skin Façades in Mediterranean Climates. *Energies*, 10(11), 1825. <https://doi.org/10.3390/en10111825>





# JOURNAL OF FAÇADE DESIGN & ENGINEERING

VOLUME 8 / NUMBER 1 / 2020

v **Editorial**

001 **Additive Manufacturing of Ceramic Components for Façade Construction**

Paulo J.S. Cruz, Bruno Figueiredo, João Carvalho, Tatiana Campos

021 **Fire Safety Façade Design and Modelling**

Enrico Sergio Mazzucchelli, Paolo Rigone, Blanca Judith De la Fuente, Paolo Giussani

043 **A Novel Approach to Shape Memory Alloys Applied to Passive Adaptive Shading Systems**

Lorenzo Vercesi, Alberto Speroni, Andrea Giovanni Mainini, Tiziana Poli

065 **Small-scale Field Study of Window Films' Impact on Daylight Availability under Clear Sky Conditions**

Júlia Pereira, M. Glória Gomes, A. Moret Rodrigues, Henriqueta Teixeira, Manuela Almeida

085 **Daylight Transmittance Through Expanded Metal Shadings**

Jose Miguel Rico-Martinez, Marcin Brzezicki, Carlos Gabriel Ruiz-Mugica, Jakub Lech

115 **Assessing Self-shading Benefits of Twisting Towers**

Nebojsa Jakica, Mikkel K. Kragh

131 **Design and Experimental Proof-of-concept of a Façade-integrated Solar Thermal Venetian Blind with Heat Pipes**

Simon Frederik Haeringer, Paul-Rouven Denz, Puttakhun Vongsingha, Bruno Bueno, Tilmann E. Kuhn, Christoph Maurer

TU DELFT OPEN

ISSN PRINT 2213-302X

ISSN ONLINE 2213-3038